Feathers by day, membranes by night - Aerodynamic performance in bird and bat flight

Muijres, Florian

2011

[Link to publication](#)

Feathers by day, membranes by night

Aerodynamic performance in bird and bat flight

Abstract

The efficiency and performance of a flying animal is directly related to the aerodynamics around its body and flapping wings. Here, I have developed methods for quantifying the wake dynamics around a flying animal. The results are used to estimate the aerodynamic performance of flapping flight. Using these methods, I have studied flight of the Pied Flycatcher (*Ficedula hypoleuca*), the Pallas' Long-tongued bat (*Glossophaga soricina*) and the Lesser Long-nosed Bat (*Leptonycteris yerbabuenae*).

In paper I, the aerodynamics close to the wing surface of slow flying *G. soricina* bats was studied, showing that bats use a Leading Edge Vortex (LEV) to enhance lift with up to 40% of the total. LEVs are known to be used by insects, but here I have shown that also larger vertebrates can use LEVs. In paper II, the aerodynamics close to the wing surface of a slow flying Pied Flycatcher was studied. This results showed that Pied Flycatchers generate LEVs with similar strength as in *G. soricina*, but the LEV structure is significantly different from that of bats and insects. In paper III, a new high-speed stereoscopic Particle Image Velocimetry (PIV) system for studying animal flight was introduced. Using this system, the wakes of the two bat species were captured, and new methods for visualizing and analyzing wake data were introduced. In paper IV, the wake dynamics and aerodynamic performance of flapping flight for the two bat species was studied. Although the wake dynamics for the two species was similar, maximum aerodynamic performance was achieved at a significantly higher speed for the highly mobile and migratory *L. yerbabuenae* than for the non-migratory *G. soricina*. In paper V, I introduced an actuator disk model for analyzing time-resolved PIV data of flapping flight. Analysis of the wake data for the two bat species showed that the model can be used to compare flight efficiency of different animal species. In paper VI, the wake dynamics in flycatchers was studied. The results showed that the wake of slow flying flycatchers is more similar to that of fast flying passerines than to that of hummingbirds, and that flycatchers are probably aerodynamically more efficient than hummingbirds. In paper VII, the wake dynamics and aerodynamic performance for the three studied species was compared. This showed that birds outperform bats in aerodynamic efficiency, which could be ascribed to differences in aerodynamic function of the body and of the wing upstroke, and which were proposed to be a result of differences in phylogenetic constraints between birds and bats.

Keywords: animal flight, aerodynamics, vortex wake, actuator disk, flight performance, span efficiency, bird, bat, wind tunnel, PIV, Pied Flycatcher, *Glossophaga soricina*, *Leptonycteris yerbabuenae*.

Feathers by day, membranes by night

Aerodynamic performance in bird and bat flight

Florian T. Muijres

Dissertation 2011

A doctoral thesis at a university in Sweden is produced either as a monograph or as a collection of papers. In the latter case, the introductory part constitutes the formal thesis, which summarizes the accompanying papers. These have either already been published or are manuscripts at various stages (in press, submitted or in ms).

Contents

This thesis is based on the following papers:

Paper I, III , IV and V are reprinted with permission from the publishers.

Feathers by day, membranes by night

Aerodynamic performance in bird and bat flight

Facts are the air of scientists. Without them you can never fly.

Dr. Linus Pauling

Included papers are referred to by roman numerals (I-VII). Technical terms are explained in the glossaty

1 Introduction

Active flight has evolved independently at least five times in the animal kingdom. More than 300 million years ago insects were the first to conquer the skies; 225 million years ago the now extinct pterosaurs were the first vertebrates to evolve active flight; 150 million years ago birds took to the sky; the oldest bat fossils are about 50 million years old; and finally just a 100 years ago suddenly humans started to fly. Although humans need tools to fly, the underlying evolutionary pressures that made men use flight as a mode of locomotion are probably very similar to that in all the previous cases.

The independent evolution of active flight has resulted in very different types of flying animals (Fig. 1), ranging from tiny insects such as the extremely steadily hovering hoverfly to large birds such as swans, from night-active echo-locating bats with great manoeuvrability to aerodynamically efficient soaring albatrosses. However, one thing all these flying animals have in common is that they have wings to produce a lift force required for weight support and a thrust force to overcome drag (Alexander 2004, Fig. 2). Lift production in animal wings is relatively similar to that in aircraft wings, but thrust is produced in a completely different way. All animals produce thrust by flapping their wings up and down, which tilts the net aerodynamic flight force forward to give a thrust component (Fig. 2). Especially at low flight speeds, wing flapping also increases the effective wing

speed resulting in an increase of the total flight force (Fig. 2). This is how animals are able to hover: the body does not move, but the wings certainly do.

Although all flying animals use wings to fly, the basic wing design or body plan for the three taxa of extant actively flying animals differ (Fig. 3). Bird wings have evolved from feathered forelimbs in small theropod dinosaurs (Qiang et al. 1998, Hedenström 2002). The resulting feathered wings can be morphed by spreading the wing feathers or by sliding the feathers over each other (Videler 2006). This enables birds to optimize wing surface area (Lentink et al. 2007, Fig. 3), to improve flight efficiency by generating slotted wingtips (Tucker 1993), and bird wings can be made aerodynamically inactive by spreading the wing feathers enabling air to flow through the gaps (Norberg 1985).

Bat wings have probably evolved from webbed fingers of a small arboreal quadruped (Teeling 2005), resulting in an extremely compliant wing consisting of skin membrane stretched between elongated finger bones (Swartz et al. 1996, Pennycuick 2008a, Fig. 3). The surface area of bat wings cannot be varied as much as in bird wings, because the membranous wing will go slack when reducing the wing span too much (Pennycuick 1971). Also, a membranous wing cannot be made inactive as easily as the feathered bird wing because air cannot flow through the solid membrane. Bats can however control the shape and position of their membranous wings very precisely

Fig. 1 Bats, birds and insects, the three extant groups of active flying animals. The species are the Big Eared Townsend Bat *Corynorhinus townsendii*, Shy Albatross *Thalassarche cauta* (image by Glen Fergus), Marmalade Hoverfly *Episyrphus balteatus* (photo by André Karwath).

using separately controllable digits and muscle fibres in the wing membrane (Macalister 1872, Norberg 1970, Norberg 1990). This enables bats to optimize wing profile shape and angle-of-attack throughout the wingbeat (Wolf et al. 2010, paper I).

Insect wings have probably evolved from specialized tracheal gills extending from the body (Marden and Kramer 1994). The earliest flying insects had four separate wings as in dragonflies (Davis et al. 2010, Fig. 3) and fossil mayflies (Wootton 1981). In most modern insects, though, the two wings on each side are connected or, as in diptera, one wing has reduce into a haltere, resulting in a functionally two wing configuration (Dudley 2002, Fig. 1). Insect wings are stiff compared to bird and bat wings, and can not be morphed actively by the animal, although passive deformations are of importance (e.g. Young et al. 2009). However, insects can turn the wing upside down during the upstroke to generate equal lift forces during downstroke and upstroke (Weis-Fogh 1973).

Thus, these extremely different wing types generate flight forces in substantially different ways, and one can assume that this will be reflected in differences in relative flight performance. Since flight is energetically one of the most costly activities found in nature (Schmidt-Nielsen 1972), one can assume that evolution should optimize flight performance, which in turn can be assumed to be limited by basic wing design or body plan, the so called phylogenetic constraints (Lauder 1996).

Within a single taxa the flight apparatus design can also vary much, compare for example an albatross (Fig. 1) with a hummingbird. These differences can be explained by differences in ecological requirements (Norberg 1990). The ecological requirements for a certain species set the position of the optimum within the flight performance parametric space, which is then favoured by evolutionary selection. A typical ecological requirement relevant for this thesis is that a migrating bird should minimize energy required per distance travelled, while a foraging bird should rather minimize energy required per unit time (Hedenström and Alerstam 1995).

To summarize, optimum flight performance for a certain species depends on the ecological requirements of that species (Norberg 1990), but the attainable maximum performance is limited by phylogenetic constraints based on the body plan of the flight apparatus (Lauder 1996). Although this is theoretically

a simple relation, to test it in practice is not an easy feat. Since biological systems are very complex it is impossible to identify and quantify all the ecological requirements and phylogenetic constraints.

In this thesis I investigate how aerodynamic performance of flapping flight varies between one bird species and two bat species, and I relate this to differences in ecological requirements and phylogenetic constraints. To do this I have developed aerodynamic models based on empirical wake dynamics data of free flying animals in a wind tunnel. These models are used to objectively quantify aerodynamic flight performance, and the results for the different studied species are compared among each other. This gives us a first glance on how flight performance differs between species due to ecology and morphological constraints. Yet, we are still far from a general theory. For this we should increase the amount of species studied, and possibly improve the here developed flight performance models.

2 Animals studied

In this thesis three species of flying animals are studied, being one bird and two bat species (Fig. 4). The bird is the Pied Flycatcher (*Ficedula hypoleuca*), and the bats are the Pallas' Long-tongued bat (*Glossophaga soricina*) and the Lesser Long-nosed Bat (*Leptonycteris yerbabuenae*). These three animals were chosen because they are similar in size and because they all are well adapted to hovering and slow flight. The flycatcher is an insectivorous bird that hovers and flies slowly when catching insects on the wing, while the bats are nectar feeders that feed from flowers by hovering in front of them.
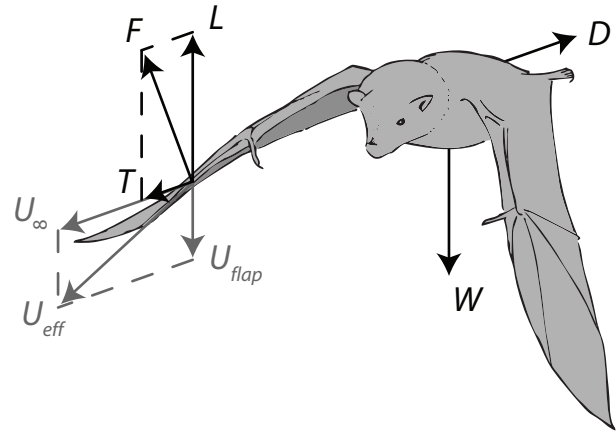
Fig. 2 An animal flaps its wings to generate both lift *L* and thrust *T*, which compensate for weight *W* and drag *D*, respectively. The forward velocity (U_∞) and flapping velocity (U_{flap}) of the wing together result in an effective velocity (U_{eff}). Perpendicular to U_{eff}, the wing produces the aerodynamic flight force *F* with a streamwise lift component *L* and vertical thrust component *T*.

2.1 Pied Flycatcher
2.1.1 Ecology

The pied flycatcher is a small (body mass 14 g) insectivorous migratory passerine (Fig. 4). When hunting, flycatchers commonly take-off from a perch to capture insects in mid air, after which they return back to the perch (Davies 1977). These flight manoeuvres are very elegant and controlled, and although they look very fast, it are mainly the accelerations that are high while maximum flight speeds during such manoeuvres are probably relatively low. Therefore, flycatchers can be assumed well adapted to hovering and slow flight.

Flycatchers are long-distance migrants; they migrate annually from breeding sites in northern Europe and Asia to wintering grounds in central and western Africa. When migrating, flycatchers are expected to fly much faster than while hunting, and based on predictions from Pennycuick's flight program Flight 1.22 (Pennycuick 1989), their average migratory

Table 1 Morphological data and efficiency factors for the animals used for this thesis (average ± standard deviation). The morphological data consists of mass *M*, wing span *b*, wing surface area *S*, mean cord length *c = S/b*, aspect ratio *AR = b²/S* and wing loading *Q = Mg/S*, with *g* the gravitational constant. The efficiency factors are the average span efficiency (e_i) and flap efficiency (e_f) for the measured flight speed range.

Species	*M* (g)	*b* (cm)	*S* (cm²)	*c* (cm)	*AR* (-)	*Q* (N/m²)	e_i (-)	e_f (-)
G. soricina	10.2±0.5	23.8±0.6	90.3±8.2	3.8±0.3	6.3±0.6	11.2±0.9	0.81±0.03	0.64±0.04
L. yerbabuenae	22.6±1.4	32.9±0.8	155.3±3.3	4.7±0.0	7.0±0.2	14.3±1.2	0.79±0.03	0.62±0.09
F. hypoleuca	14.2±0.6	23.5±0.1	106.0±1.0	4.5±0.0	5.2±0.0	13.1±0.6	0.90±0.03	0.82±0.04

Glossary

Actuator disk model: aerodynamic model for estimating lift and induced power produced by a rotating or flapping wing based on the induced air flows generated by the wing.

Aerodynamic performance: certain extreme quantities in fluid forces or power production required for a specific flight movement, e.g. minimum aerodynamic power required per distance travelled.

Angle-of-attack: the angle between the wing chord and the effective velocity vector. Generally, flight forces produced by a wing increase with increasing angle-of-attack up to a point when stall occurs.

Body plan: the blueprint of an organismal design, which sets limitations to evolutionary changes for that body.

Bound circulation: circulation bound to a lift producing wing. Thus, bound circulation moves with the wing and induces a downwash behind the wing, which results in lift.

Drag D: the aerodynamic forces generated in free-stream velocity direction, consisting of friction and pressure drag.

Ecological requirements: requirements that an animal should fulfil based on the ecological conditions for that animal, and which are enforced by evolutionary selection pressure.

Effective velocity: the velocity vector resulting from the vector sum of the forward flight speed (wind tunnel velocity) and the velocity due to wing flapping. Generally, fight forces scale quadratically with the effective velocity.

Flap efficiency: ratio between the induced power required to generate a specific wingbeat average lift force with a certain temporal and spanwise downwash distribution within the wingbeat, and the corresponding minimum induced power to generate the same lift based on a uniform downwash.

Hovering: flying at a zero forward flight speed.

Induced drag: when a wing produces lift it induces a downwash at the wing. This downwash causes the local effective oncoming flow to have a vertical downward velocity component, which tilts the lift force backwards, resulting in a (induced) drag component.

Inviscid vortex dynamics: the collection of laws that describe the fluid dynamics of vortices when ignoring viscous (friction) forces.

Leading Edge Vortex (LEV): If air flowing over a wing separates from the wing at its leading edge and re-attaches to the wing before reaching the trailing edge, a separation bubble is generated. Due to friction forces, the air within this separation bubble will start to rotate resulting in a LEV. The low pressure area in the LEV will result in LEV lift.

Lift L: the aerodynamic flight force produced perpendicular to the free-stream velocity, required to balance weight during steady flight.

Lift-to-drag ratio (L/D): ratio between lift forces required to fly and drag forces associated with the cost of flight.

Parasite drag: drag produced by the non-lifting body of a flying animal.

Particle Image Velocimetry (PIV): a non-intrusive experimental technique for measuring the airflow velocity distribution within, typically, a two-dimensional plane.

Phylogenetic constraints: Limitations in potential evolutionary solutions due to the evolutionary history of a species.

Power curve: a curve showing the relation between power required for flight and forward flight speed.

Propulsion system: the system responsible for thrust production, in airplanes it is the propeller, while in flying animals it is the flapping wing.

Reynolds number Re: a measure for the ratio of inertial forces to viscous forces on a body moving through a fluid, quantifying the relative importance of these two types of forces on that body. Birds and bats operate at a Re range where the airflow is very sensitive to small changes in wing shape, wing attitude and environmental conditions.

Span efficiency: ratio between the induced power required to generate a specific lift force with a certain spanwise downwash distribution, and the corresponding ideal power required to generate the same lift based on a spanwise uniform downwash.

Stall: When the angle-of-attack of a wing increases stall occurs when flow separates and drag increases significantly.

Thrust T: the aerodynamic flight force produced in the opposite direction of the free-stream velocity, required to overcome drag and to accelerate.

Vortex circulation: the integrated vorticity within a vortex area.

Vorticity: twice the angular velocity of a fluid element.

Wing camber: the ratio between the maximum deviation of a wing profile from the cord line and the local cord length. Flight forces typically increase with increasing wing camber.

Wing chord: a straight line from the leading edge to the trailing edge of a local wing section, its length is called the local chord length. The mean chord length is defined as the wing surface area divided by the wing span.

Wingbeat kinematics: the way a wing moves and deforms throughout a wingbeat.

Fig. 3 (top) an alpine swift in a turn. During this maneuver, the bird slides the feathers of wing and tail over each other to optimize wing shape and surface area (Lentink et al. 2007, photo by Mark Kilner). (bottom left) *G. soricina* **bat flying away from the feeder in the Lund wind tunnel. The bat morphes its extremely flexible wings separately from each other, to optimize wing profile shape and orientation throughout the wingbeat (Wolf et al. 2010, photo by Anders Hedenström). (bottom right) Dragonflies have four reltively stiff wings that they can flap independantly from each other, enabling them to switch between wingbeat kinematics with high maneuverability and with high energetic flight efficiency (Usherwood & Lehmann 2008 , photo by Boris Krylov).**

flight speed should be around 10 m/s.

Thus, flycatchers are subject to selection for efficient slow flight as well as efficient cruising flight. One can assume that there should be some kind of trade-off between these two selection pressures, but how this is manifested is not yet known.

2.1.2 Wing morphology and kinematics

The basic wing morphology of flycatchers is typical for that of a small passerine. Table 1 shows the basic morphological characteristics of the flycatchers used, which have been determined using the routine described by Bowlin (2007), except that a 'body-box' was added (Pennycuick 1989).

The wingbeat kinematics of a hovering flycatcher was studied by Norberg (1975) and by Norberg (1985), while the wingbeat kinematics in forward flight is described in this thesis (paper VI). In Norberg (1975), the wingbeat kinematics is used to get a first order estimation of the flight forces required for weight support. The results show that hovering flycatchers require some unsteady aerodynamic mechanism to generate enough lift to stay aloft, which is identified in this thesis as a Leading Edge Vortex (LEV) (paper II). In Norberg (1985) wing deformations in hovering flycatchers are discussed. When flapping, the primary and secondary feathers of a flycatcher wing deform significantly throughout the wingbeat. During the downstroke, the wingtip and wing trailing edge bend up as a result of feather flexibility, while during the upstroke the wing is greatly retracted and primary feathers are separated. This enables air to flow through the gaps, making the wing aerodynamically inactive during the upstroke. These wingbeat kinematics are regarded as typical for slow flying passerines, while faster flying birds can have a more active upstroke, where the wing generates both positive lift and negative thrust (Spedding et al. 2003a, Hedenström et al. 2006).

2.2 Glossophaga soricina
2.2.1 Ecology

Glossophaga soricina (Fig. 4) is a new world small (10 g) nectivorous bat of the family Glossophaginea, living in the tropical rainforests of South and Central America, where it commonly roosts in trees (Norberg and Rayner 1987). *G. soricina* feeds from flowers by hovering in front of them, although it occasionally eats fruit and small insects (Heithaus et al. 1975). *G. soricina* has a very small home range where it both feeds and roosts, since mean recapturing distances for *G. soricina* are only about 200 m (Heithaus et al. 1975). Therefore, *G. soricina* can be assumed primarily adapted to hovering and flying at low flight speeds.

2.2.2 Wing morphology and kinematics

The basic wing morphology characteristics for *G. soricina* are shown in Table 1. *G. soricina* has a relatively low aspect ratio wing (low wing slenderness), which is assumed a result of it living in dense rainforests and being well adapted to hovering flight (Norberg and Rayner 1987).

The wingbeat kinematics of *G. soricina* is well described by both Lindhe Norberg and Winter (2006) and Wolf et al. (2010). Based on the angles-of-attack of the wings during the downstroke (Wolf et al. 2010), *G. soricina* is assumed to generate unsteady aerodynamics in hovering and at low flight speeds, which is confirmed in paper I.

During the upstroke, bats in general do not retract their wings as much as birds do, which is probably because in that case the membranous bat wing would go slack (Pennycuick 1971). So, *G. soricina* has a much more active upstroke than for example the flycatcher. During hovering and slow flight, *G. soricina* flips its outer wing upside down during the upstroke, and moves it backwards faster than the forward flight speed (Helversen von 1986, Wolf et al. 2010). This results in positive lift production during the upstroke. At high flight speeds though, the wing is not flipped over but is moved upwards with a negative angle-of-attack (Hedenström et al. 2007, Wolf et al. 2010), which would result in negative lift production (a downwards force), but also in positive thrust production. The resulting flight forces are determined in paper IV.

2.3 Leptonycteris yerbabuenae
2.3.1 Ecology

Leptonycteris yerbabuenae (formerly considered a subspecies of *Leptonycteris curasoea*) is, as *G. soricina*, a new world nectar feeding bat of the family Glossophaginea (Norberg and Rayner 1987, Fig. 4). With a body mass of around 20 g it is twice the weight of *G. soricina*, and can be regarded as a medium sized bat (Norberg and Rayner 1987). *L. yerbabuenae* feeds primarily from flowers of columnar cacti by hovering in front of them, so *L. yerbabuenae* can be regarded as a hovering specialist. The home-range of *L. yerbabuenae* is much larger than that of *G. soricina*, since it makes long commuting flights between its day roost site (generally a cave), night roost sites and different feeding patches, travelling around 100 km every night (Horner et al. 1998). Also, *L. yerbabuenae* migrates annually 1000 to 1600 km between Mexico and the southern United States (Wilkinson and Fleming 1996). Thus next to being a hovering specialist, *L. yerbabuenae* should also be under selection for efficient cruising flight.

The migratory route for *L. yerbabuenae* would be regarded as a short distance migratory route for birds, but it is among the longest migratory routes for bats (Fleming and Eby 2003). In paper VII, I show that this difference in migration distances between birds and bats could be related to differences in flight performance.

2.3.2 Wing morphology and kinematics

The basic wing morphology characteristics for *L. yerbabuenae* are shown in Table 1. *L. yerbabuenae* has a higher aspect ratio wing and a higher wing loading than *G. soricina*, which could be related to the requirement for *L. yerbabuenae* to fly more efficient while commuting and migrating. The wingbeat kinematics of *L. yerbabuenae* is described by von Busse (2011), and is similar to that of *G. soricina*. *L. yerbabuenae* has an active upstroke, where it generates positive lift during slow flight and generates negative lift in combination with positive thrust at high flight speeds. The resulting flight forces are determined in paper IV.

Fig. 4 the three species studied in this thesis. (top left) the Pied Flycatcher (photo by Adrian Dancy), (top right) *Glossopaga soricina (***photo by L. Christoffer Johansson), and (bottom)** *Leptonycteris yerbabuenae (***photo by Anders Hedenström)**

3 Experimental setup and procedure

3.1 Wind tunnel

Flight studies are preferably performed in wind tunnels, because this provides easy access and data collection (the air is moving instead of the studied object) and because the environmental conditions, such as air pressure, temperature and of course air speed, can be monitored and/or controlled in detail. A drawback of studying animal flight in a wind tunnel is that the conditions the animal experiences in a wind tunnel can be very different from that in free flight, most importantly the animal is flying in a confined space

instead of the open air. This could result in the animal behaving significantly different in the wind tunnel compared to flight in their natural environment, and which could also influence flight performance. These effects are probably relatively small for the animals studied here since they are used to flying in confined spaces. Although, *G. soricina* did not want to fly faster than at a wind tunnel speed of 7 m/s, while it is able to fly at speeds up to 10 m/s (Winter 1999).

For my studies I used the Lund University low-speed, low-turbulence, wind tunnel, which is specially designed for animal flight studies (Pennycuick et al. 1997). It has an octagonal test section, 1.22 m wide and 1.08 high. The contraction ratio of the tunnel is

12.25, which results in very low turbulence levels in the wind tunnel (~0.05%), making the wind tunnel suitable for studies at Reynolds numbers relevant for animal flight (Spedding et al. 2008).

3.2 Experimental animals

For this thesis six individuals of each species were trained to fly in the wind tunnel, and for the different experiments we selected the individuals that were easiest to handle and flew most steadily. We used three *G. soricina* for paper I, two flycatchers for paper II, two *G. soricina* and two *L. yerbabuenae* for paper III to V, three flycatchers for paper VI, and three flycatchers, two *G. soricina* and two *L. yerbabuenae* for paper VII. The bats were all provided by York Winter, Humboldt University, Germany. They were kept in a sea container (5.9 x 2.3 x 2.3 m³, length x width x height), which was kept at a temperature of at least 25°C and humidity of at least 50%. The bats were fed honey water supplemented with milk powder and Nektar plus ©, pollen and occasionally fruit. The bats were clock shifted 12h, so their night active period coincided with office hours. During the experiments, the bats roosted on a net in the settling chamber of the wind tunnel. When a bat got hungry, it would fly into the test section, make a U-turn and approach a tube-like feeder from the downstream direction. When the bat was flying steadily at the feeder, it was provided with honey-water and experimental measurements were performed. After feeding, the bat would fly back into the settling chamber.

The flycatchers were caught in the wild at the Falsterbo bird observatory, southwest Sweden. They were kept in aviaries in the wind tunnel building, where they were fed meal worms and water (at regular intervals supplemented with vitamins). For the experiments, the flycatchers were trained to perch on a hand held stick in the test section of the wind tunnel. When the perch was lowered the bird would take off. If the bird would fly steadily at the position above the perch, experimental measurements were performed and the stick was presented again. If the bird would fly away, the perch was not presented until the bird would return to its original position. In this way, the animal was conditioned to fly steadily at the right position. After all the experiments were done, the birds were released back into the wild.

The animal keeping and all the experiments were approved by the Lund University ethical board.

3.3 Flow visualization

To study the aerodynamics of animal flight we use a particle image velocimetry (PIV) system. A PIV system enables you to determine the air velocities within a two-dimensional measurement plane. For this technique, the wind tunnel is filled with a thin fog (~1μm particle size). A laser sheet lights up these fog particles in a plane, and light reflection from the particles are captured by camera(s). A PIV camera takes two snapshots of the fog particles closely after each other (~100μs time difference), and a correlation routine is used to determine local particle displacements, resulting in a velocity vector field of the air in the measurement plane.

For this thesis, two PIV systems were used: for paper I a two-dimensional PIV system was used which measured in-plane velocities at 10Hz (for details see Spedding et al. 2003b and paper I), while for the other papers a high-speed (200Hz) stereo PIV system was used. This system used two synchronized PIV cameras to perform stereo measurements, resulting in three-component velocity vectors, including the out-of-plane velocity component. The wake is sampled at 200Hz, and since the bats and bird species flap their wings at frequencies in the order of 10 Hz, the 200Hz wake dynamics measurements can be considered time resolved (for details see paper III).

The PIV measurements can be divided into two types: on-wing PIV measurements (paper I and II), and near-wake PIV measurements (paper III to VII).

For the on-wing PIV measurements, the PIV image plane was positioned in a vertical streamwise position, and the laser light was coming from above (see paper I and II). The animal was positioned in such a way that the laser was shining onto the wing. This enabled us to measure the fluid dynamics close to the wing surface, which gave very exciting results. Since the laser light was positioned close to the animal, their eyes needed protection. This was done by adding side plates made of red light filter material to the bat feeder (paper I), and by providing the birds with goggles custom-made from red filter material (paper II, Fig. 6).

For the near-wake PIV measurements, the PIV image plane was positioned in a vertical transverse position closely behind the animal (~10 cm). This setup was used to measure the time-resolved aerodynamic wake dynamics for flapping flight across a range of flight speeds, and the data is
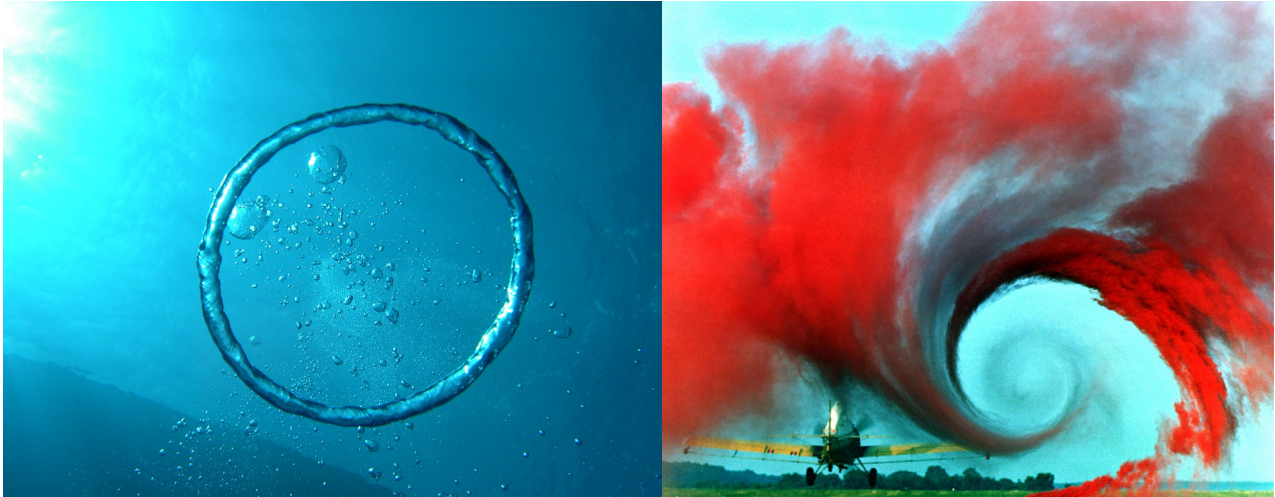
Fig. 5 basic vortex dynamics principles: (left) the most fundamental vortex structure, a vortex ring; (right) a tip vortex behind an airplane wing

used to estimate the aerodynamic performance of flapping flight, as described below.

3.4 Wingbeat kinematics

Wingbeat kinematics was studied by filming the animals with high-speed cameras. Data from a single camera was used to estimate simple variables, such as wing surface area (e.g. see paper III), local angle-of-attack (paper I and II), and to monitor the flight behaviour of the animal. To determine detailed three-dimensional kinematics, two synchronized high-speed cameras (250Hz frame rate) were used in a stereo setup. All kinematics measurements were performed using infra-red illumination to reduce interference with the PIV system, and to reduce disturbance for the night-active bats.

The stereoscopic wingbeat films were analyzed using a custom-made Matlab program (Matlab 7.7.0.471 R2008a). In this program the required wing and body markers were manually digitized and converted into three-dimensional positions using direct linear transformation (Christoph Reinschmidt Matlab routines), based on a calibration cube.

The wingbeat kinematics data were used to quantify the aerodynamic regime the animals operate in (e.g. to determine the effective Reynolds number Re_{eff} and downstroke based strouhal number St_{ds}), as input for the aerodynamic models, and to correlate kinematics with aerodynamic wake data (for details see paper I-VII).

4 Aerodynamic models

When a flying animal moves through the air, air particles are accelerated in different directions by the animal's body and wings. As a reaction to these fluid movements the animal experiences aerodynamic forces (Newton's third law). Thus, by capturing induced air movements around a wing or in the wake of a flying animal one can estimate the flight forces the animal experiences.

In this thesis I use two aerodynamic models to estimate flight forces from wake dynamics, a vortex circulation based model (paper I to IV; VI and VII) and an impulse based model (paper V to VII). Each model was used to estimate a different aspect of aerodynamic performance in flapping flight.

4.1 Vortex circulation model and L/D for locomotion

The vortex circulation model is based on the fact that the lift force produced by a wing is proportional to the circulation about the wing (Anderson 1991, Spedding et al. 2003a). This circulation can consist of so called bound circulation as a result of wing camber and angle-of-attack, and circulation of any attached vortex, e.g. an attached leading edge vortex (LEV) (Lehmann 2004). By measuring this LEV circulation and the circulation in the wake the relative contribution of the LEV to the total lift production can be estimated (paper I and II).

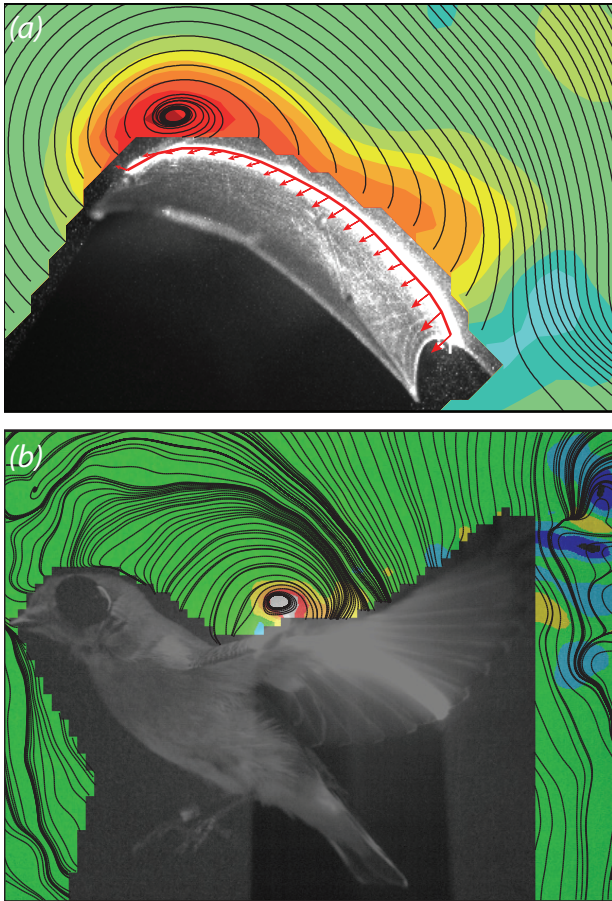Flight forces can also be estimated from the near-

Fig. 6 attached leading edge vortices above the wing of a slow flying *G. soricina* (*a*) and Pied Flycatcher (*b*). For details see paper (I) and (II), respectively

wake PIV, but to explain how this is done, I need to give a short introduction into basic inviscid vortex dynamics (Anderson 1991, Saffman 1995). We assume the fluid to be inviscid because for the spatial and temporal scales of the near wake of flying vertebrates viscous dissipation is negligible (Nieuwstadt 1998).

Kelvin's theorem states that in a closed inviscid vortex system, the total sum of circulation is constant. Hence, the circulation about a wing has the same strength but opposite spin as the circulation in its wake (Anderson 1991). Thus, when the lift production by a wing changes, it will shed a start vortex with the same amount of circulation but opposite spin as the change in bound circulation. Also, according inviscid vortex dynamics, each vortex must form a closed loop (Fig. 5) or terminate at a solid surface. Therefore, each shed start vortex will initially connect to the wing surface, forming streamwise vortices, such as the well known 'tip vortex' (Fig. 5). By measuring the circulation

in these streamwise vortices the instantaneous lift and thrust forces can be estimated (see paper IV for details). By integrating lift (vertical vortex forces) and thrust (horizontal vortex forces) throughout the wingbeat, the effective lift-to-drag ratio L/D is estimated (in steady flight thrust equals drag).

This effective L/D is our first aerodynamic performance parameter, which is an estimate for the efficiency of locomotion, since it is the ratio between the required force for flight (lift required to balance weight), and the resulting costs of flight (drag). For example, the locomotion power P_{loc} required for an animal with weight W to fly at a flight speed U_∞ is $P_{loc} = W\,U_\infty\,/\,(L/D)$. Note that P_{loc} does not include power required by the 'propulsion system', which in this case are the flapping wings, but it is purely the power required for locomotion.

4.2 Actuator disk model and span efficiency

The second aerodynamic wake model is termed the 'actuator disk model for flapping flight'. As stated before, it is based on the impulse which is generated by the downward deflected air. The actuator disk is a highly simplified model to determine thrust and induced power production by a constant rotating propeller or helicopter rotor (Gessow and Myers 1952), but which has also been adapted for animal flight studies (Pennycuick 1968). In paper V I show how the general actuator disk can be modified to model flapping flight more in detail, based on time-resolved near-wake PIV data. The spanwise downwash distributions in the wake of a flying animal are used to determine instantaneous lift production, the required induced power for flapping flight P_i, and the wingbeat average span efficiency e_i. In this case P_i does include power required by the propulsion system, as it is equivalent to the shaft power in propellers. It is therefore significantly higher than P_{loc}.

The span efficiency factor is our second aerodynamic performance parameter. It is a value for the efficiency of lift production, describing the deviation from a uniform spanwise downwash. This uniform spanwise downwash would result in the lowest required power for generating a certain lift force, called the ideal power $P_{i\;ideal}$. Thus, span efficiency is defined as $e_i = P_{i\;ideal}\,/\,P_i$ (Spedding and McArthur 2010).

Note that e_i is based only on the deviation from a spanwise uniform downwash (Spedding and McArthur

Fig. 7 vortex wake structure around the wings at mid downstroke of a slow flying *G. soricina* (*a*) and flycatcher (*b*). For details see paper (I) and (II), respectively

(*a*)

(*b*)
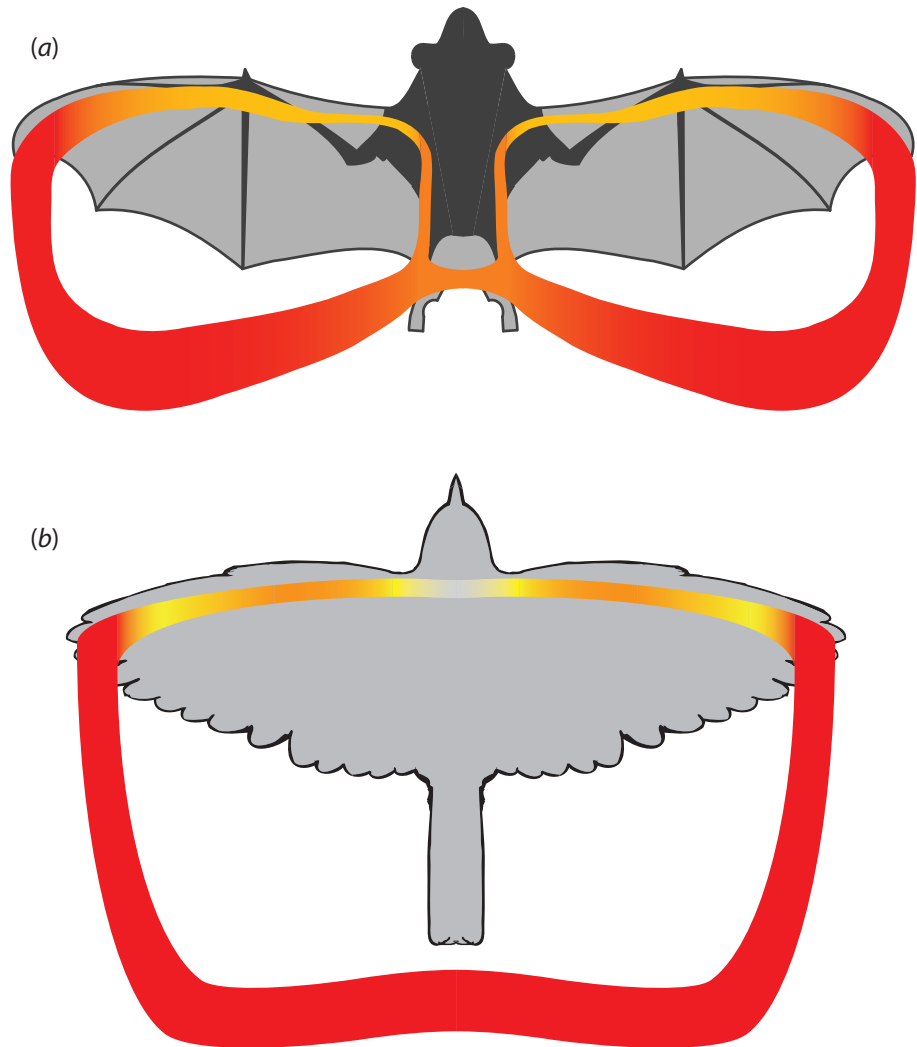
2010), while the absolute minimum required power would be for the case where the downwash is constant throughout the complete wingbeat. This purely hypothetical case would result in the absolute minimum required power for weight support ($P_{i\,min}$). The corresponding efficiency factor I will call flap efficiency ($e_f = P_{i\,min} / P_i$), since it incorporates power losses as a result of the time-varying lift production due to the flapping motion.

5 Results and discussion
5.1 Leading edge vortex

On-wing PIV measurements were performed for *G. soricina* (paper I) and a flycatcher (paper II) at a flight speed of 1 m/s, showing that both species use LEVs to enhance lift during slow flight (Fig. 6) similar to what have previously been shown for insects (Ellington et al. 1996, Sane 2003). The relative strength of the LEV is similar in the bats and bird, where the LEV

enhances lift with 40% and 49% of the total lift in *G. soricina* and flycatcher, respectively. These are both significantly stronger than in hummingbirds, of which the LEV enhances lift with only 16% (Warrick et al. 2009), which could be related to hummingbirds generating more lift during the upstroke than *G. soricina* and the flycatcher (Warrick et al. 2005). Thus, *G. soricina* and the flycatcher need to compensate for this by generating stronger LEVs.

The spanwise LEV structure is very different between the bat and bird (Fig. 7). For the bat, the LEV increases towards the wingtip, while for the flycatcher LEV circulation is maximum at mid-wing and lowest near the wingtip.

The bat LEV structure (Fig. 7a) is similar to LEV structures found in most insects (Sane 2003, Bomphrey et al. 2005), plant seeds (Lentink et al. 2009) and in a model of a gliding swift (Videler et al. 2004). For the bats, both the angle-of-attack and wing camber

are relatively constant along the wingspan, while the wing speed increases towards the tip, which explains why LEV strength also increases towards the wingtip. It is still amazing that the airflow is nicely attached at the trailing edge of the highly cambered high angle-of-attack bat wing. Since the membranous bat wing is very compliant and its shape and attitude can be controlled actively and precisely by the bat, the LEV production could be actively controlled by the bat by optimizing wing camber and angle-of-attack.

The flycatcher LEV structure (Fig. 7b) is similar to that found in a mechanical bird flapper (Hubel and Tropea 2010). For the mechanical flapper the reduction in LEV strength at the outer wing is a result of LEV bursting and separation (Lentink and Dickinson 2009), while that is certainly not the case for the flycatcher, where the LEV at the outer wing is attached and has a coherent structure (paper II). The reduction in LEV strength at the outer wing of the flycatcher can be explained by a reduction in local angle-of-attack at the outer wing, which is a result of wing twist and bending up of the feathers at the trailing edge. I hypothesize that the reduction in LEV strength near the wingtip is a LEV stabilizing mechanism to prevent LEV bursting or separation as found in a rigid bird wing model (Hubel and Tropea 2010). This LEV stabilizing mechanism is strikingly similar to the mechanism described for flexible mechanical insect wings (Zhao et al. 2010).

Both birds and bats require some kind of lift enhancing mechanism to be able to hover or fly slowly, and both use an attached LEV with surprisingly similar strength. Still, the LEV structure is very different between birds and bats, which can be ascribed to differences in body plan. For example, the wing stabilizing mechanism found in the flycatcher where the feathers bend up at the trailing edge is not found in bats, and which is maybe not possible for membranous bat wings, since these requires a relatively stiff trailing edge for manipulating wing profile shape. Thus, although LEV dynamics is very different between the bird and bats and these differences are correlated with differences in morphology, it does not look like there is any difference in limitations for LEV production in birds and bats at the measured flight speed.

5.2 Wake dynamics

Using the transverse near-wake PIV data the wake dynamics for a single wingbeat of the bird and bats was visualized as iso-surfaces of streamwise vorticity and the downwash distribution throughout the actuator disk surface (Fig. 8, paper VII). Both the bird and bats generate strong 'tip vortices' during the downstroke. Between the tip vortex and body, the bats also generate a relatively strong 'root vortex' (Hedenström et al. 2007), while the bird generates hardly any root vorticity at all (Johansson and Hedenström 2009). During the upstroke, the wake structure is very different between bird and bats. The bird generates a narrow wake consisting of only 'tail vortices', while the bats generate a 'reversed vortex loop' behind each wing (Hedenström et al. 2007, Johansson et al. 2008). See paper VII for details.

Thus, the wake dynamics for the bird is clearly different from that of the bats, and these differences can be ascribed to differences in morphology. For example, the fact that the bird generates hardly any root vorticity, resulting in an almost uniform spanwise downwash, is probably due to lift production by the body and tail of the bird (paper VI). The bats, on the other hand, have a significant reduction in downwash behind the body as a result of low body lift (paper V). Thus, the birds generate more body lift than the bats, which could be a result of birds having a larger tail and a more streamlined body than bats, partly because bats require protruding ears for echolocation (paper VII).

During the upstroke, the bird is able to make its wings aerodynamically inactive by retracting them close to the body and spreading the wing feathers (Norberg 1985). This is not possible for the membranous bat wing, both because bats cannot retract the wing as much as birds without the membrane going slack (Pennycuick 1971), which would significantly increase drag, and air cannot flow through the solid wing membrane. As a result of this, the bird generates only body/tail lift during the upstroke, resulting in tail vortices, while the bats use their wings actively during the upstroke, moving them upwards at a negative angle-of-attack, producing thrust in combination with negative lift, and resulting in the reversed vortex loops (Hedenström et al. 2007, Wolf et al. 2010, paper IV).

Thus, due to a different body plan, the bird and bats are limited in the possibilities of flight force production, resulting in different wake dynamics.

5.3 Aerodynamic performance

A central question in this thesis is if the different wake dynamics due to differences in phylogeny and ecological requirements also result in different limitations in flight performance. To investigate this, we have estimated the lift-to-drag ratio for locomotion (paper IV and VI for bats and birds, respectively), and the span efficiency for flapping flight (paper V and VI for bats and birds, respectively).

Span efficiencies for birds and bats are compared to the equivalent flap efficiencies (Table 1 and Fig. 9a), showing that, as expected, the span efficiency is higher than the flap efficiency. I would argue to carefully distinguish e_f and e_p since these two efficiency factors are often mixed up in the scientific literature. For example, Norberg et al. (1993) estimates the flap efficiency for a hovering *G. soricina*, rather than the span efficiency, since the deviation from wingbeat uniform downwash was determined. Also, when calculating the power curve for flapping flight using Pennycuick's flight model (Flight 1.22, Pennycuick 1989), the variable 'Induced power factor' is equal to the inverse of the flap efficiency ($k=1/e_f$) rather than the inverse of the span efficiency. It is still striking how similar the flap efficiency determined here for the flycatcher (e_f=0.82±0.04) is to the inverse of induced power factor used as default in Flight 1.22 (k = 1.2; 1/k = 0.83).

In paper IV, I have compared the lift-to-drag ratio for locomotion between *G. soricina* and *L. yerbabuenae*, and related that to differences in ecological requirements. The performance results showed that, although L/D_{max} is similar for both species, the speed at which L/D_{max} occurs is significantly higher for *L. yerbabuenae* than for *G. soricina*. This could be explained by differences in movement ecology, where *L. yerbabuenae* is a more mobile species than *G. soricina*. The here found differences in optimum flight speed between *L. yerbabuenae* and *G. soricina* are not captured by the current commonly used flight performance models, which are based purely on morphological data such as body weight, wing span and wing surface area (Pennycuick 1968, Pennycuick 2008b, Rayner 1979) .

The lift-to-drag ratio for locomotion and span efficiency in the birds and bats are compared in paper VII. Both aerodynamic performance values are significantly higher for the birds than for the bats.
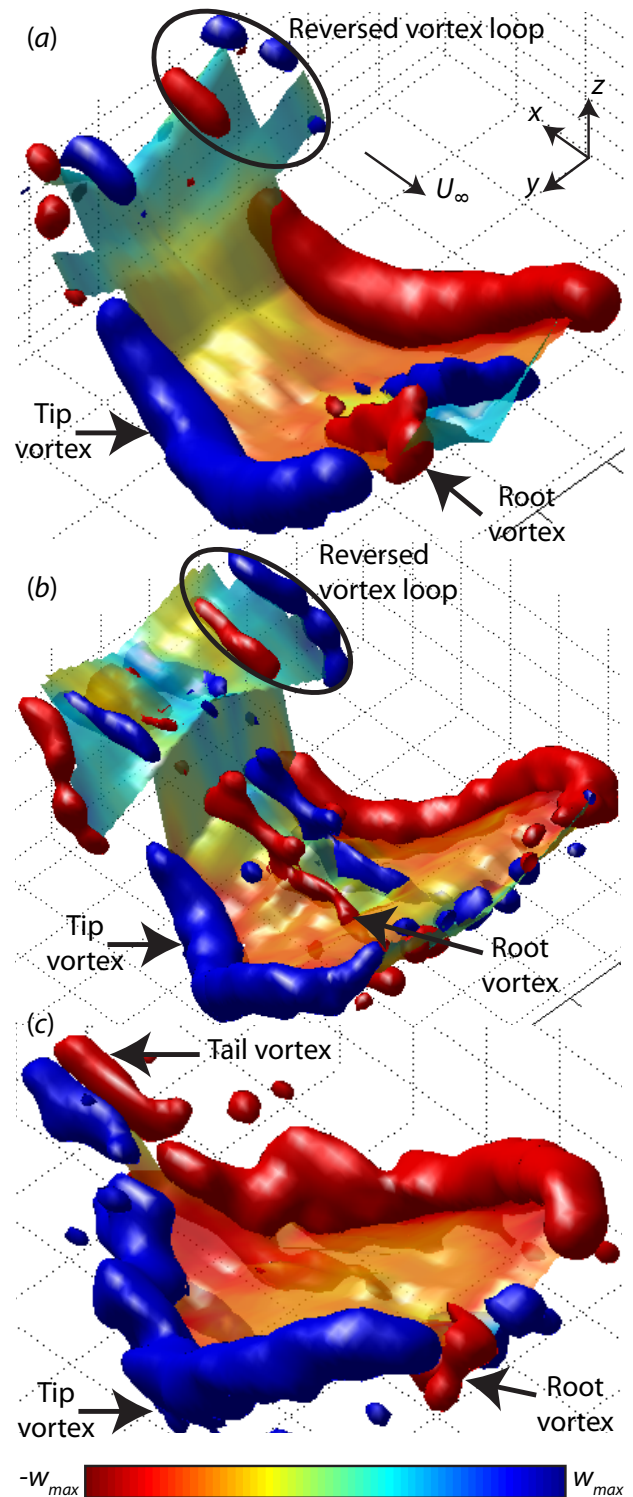

Fig. 8 vortex structure and downwash distribution in the wake of (*a*) *G. soricina*, (*b*) *L. yerbabuenae* and (*c*) Pied Flycatcher, flying at a speed of 4 m/s. See paper (VII) for details.

Span efficiency is higher in birds than bats as a result of higher body/tail lift in birds, resulting in a more uniform spanwise downwash. This is probably a result of birds having a larger tail and a more streamlined body than bats. The difference in body streamlining between birds and bats is partly due to the presence of protruding ears required for echolocation in bats. Since concave shapes, such as these ears, are known to be the highest drag producing bluff bodies (Hoerner 1965), they can also be assumed to generate high body drag.

Thus, the difference in *L/D* between the birds and bats can at least partly be related to variation in body streamlining, where the more streamlined bird body results in both less induced drag and less parasite drag. One possible positive effect of the lower body lift in bats could be that as a result of this, the wake dynamics for each wing is more independent from the other wing. This could result in the bats being more manoeuvrable, because it is easier to independently vary flight forces for the separate wings (Fig. 3).

Hall and Hall (1996) and Hall et al. (1998) used a viscous extension of the Betz criterion for optimal propellers to find the minimum power required for a flapping wing generating a prescribed lift and thrust. They showed that there is a trade-off between efficient thrust production, which increases with flapping amplitude, and efficient lift production, which decreases with flapping amplitude. The optimal flap kinematics together with the resulting force distribution was explicitly describe for two cases, being a case with a relatively low thrust requirement (high *L/D*=10), and a case with relatively high thrust requirement (low *L/D*=5). The *L/D* values for these two cases (*L/D*=10 and *L/D*=5) are similar to those determined for the birds and bats, respectively.

For the *L/D*=10 case positive lift should be produced throughout the complete wingbeat. This is also found in the flycatcher, although the flycatcher makes its wings inactive during the upstroke, which could not be modelled by Hall et al. (1998). For the case with *L/D*=5 the outer wing should generate thrust and negative lift during the upstroke, by moving the wing upwards at a negative angle of attack. This is strikingly similar to the upstroke dynamics found in bats, where the bats generate a reversed vortex loop behind each wing, resulting in the production of thrust and negative lift.

Thus, birds and bats operate close to the optimum kinematics for their relative flight efficiency regime. This suggests that the phylogenetic constraints for flight are significantly different between birds and bats, giving birds the potential to reach higher aerodynamic performance.

Based on the lift-to-drag ratio for locomotion I have estimated the weight specific power for locomotion ($P^*_{loc} = U_\infty /(L/D)$) for the studied species throughout the measured flight speed range (Fig. 9), resulting in a mechanical power curve for locomotion for each studied species. Comparing the bats, shows that at low flight speeds P^*_{loc} is lower for *G. soricina* than for *L. yerbabuenae*, while at high flight speeds P^*_{loc} is lowest for *L. yerbabuenae*. This agrees well with the results from paper IV.

Comparing the birds and bats, shows that throughout the complete flight speed range P^*_{loc} is lower for the flycatcher than for the bats. But also the shape of the power curve is different between the bird and bat species. The bats have a single optimal flight speed for minimum energy required per unit distance travelled (the tangent to the power curve going through the origin, Hedenström and Alerstam 1995), while the flycatcher has two local optima, one at a low flight speed (U_∞ ~3 m/s) and one close to the highest measured flight speed (U_∞ =7m/s). This could indicate that the flycatcher can fly relatively efficient when hunting (low speed optimum) and at cruising flight speeds (high speed optimum). At the transition between the low-speed and high-speed optima, I did not find any abrupt change in kinematics or wake dynamics (paper VI), suggesting that these two optima cannot be regarded as separate gaits (Spedding et al. 2003a).

To determine the exact location of the high speed optimum for the flycatchers, one should perform additional experiments at higher speeds than 7 m/s. We did not do this because the bats were not able to fly faster than 7 m/s in the wind tunnel.

Wild *L. yerbabuenae* fly slightly faster than 7 m/s when commuting over sea (U_∞ = 7.8 m/s), while flight speeds when commuting over land were lower (U_∞ = 4.3 m/s) (Horner et al. 1998). The maximum flight speed of *G. soricina* flying through a 50 m long flight corridor was on average 7.3 m/s (Winter 1999). Migrating flycatchers, on the other hand, can be assumed to fly faster than the bats (Pennycuick 1972, Alerstam 1993). These differences in maximum observed flight speeds in the bird and bats can be

explained by the differences in power curves. At the highest measured flight speed, P^*_{loc} increases rapidly for the bats, while for the flycatcher P^*_{loc} levels off locally. The fact that birds can fly faster and more efficiently at high flight speeds than bats, could help explain why bats migrate less and shorter distances than birds (Fleming and Eby 2003).

5.4 Concluding remarks

In this thesis I have estimated aerodynamic flight performance for one bird species and two bat species, and compared the results among them, showing that flight performance differs between the two bat species (paper IV), and between the bird species and the bats (paper VII). These differences are not captured by the current, commonly used flight performance models (Pennycuick 1968, Rayner 1979) and could at least largely be related to differences in evolutionary history and ecology. However, considering the small number of species studied here, we caution against over-generalizing our results.

While the interaction between relative flight performance and ecological requirements for the two bat species (paper IV) is based on universal selection pressure laws, the exact location of the flight performance optimum depends on a range of ecological factors, and can therefore be very different for other species of flying animals. However, the methods developed here provide a way towards understanding the aerodynamic costs associated with different wing shapes, which are correlated to different habitats (Norberg and Rayner 1987). To be able to generalize these results, one needs to study the flight performance of many more species, and develop a method to quantify relative ecological requirements relevant for flight, which could then be added as variables to the current flight performance models (Pennycuick 1968, Rayner 1979).

The here found difference in flight performance between birds and bats (paper VII) are supported by results from various previous studies (Hedenström et al. 2009, Johansson et al. 2010). Next to this, the wakes of the here studied bat species are strikingly similar to that of a larger bat species (Hubel et al. 2010), while the wake of the flycatcher is more similar to that of other passerines (Spedding et al. 2003a, Hedenström et al. 2006, Johansson and Hedenström 2009) and the highly aerial common swift *Apus apus* (Henningsson et al. 2010). Also, *L/D* values estimated using the same method as used in this thesis for blackcaps
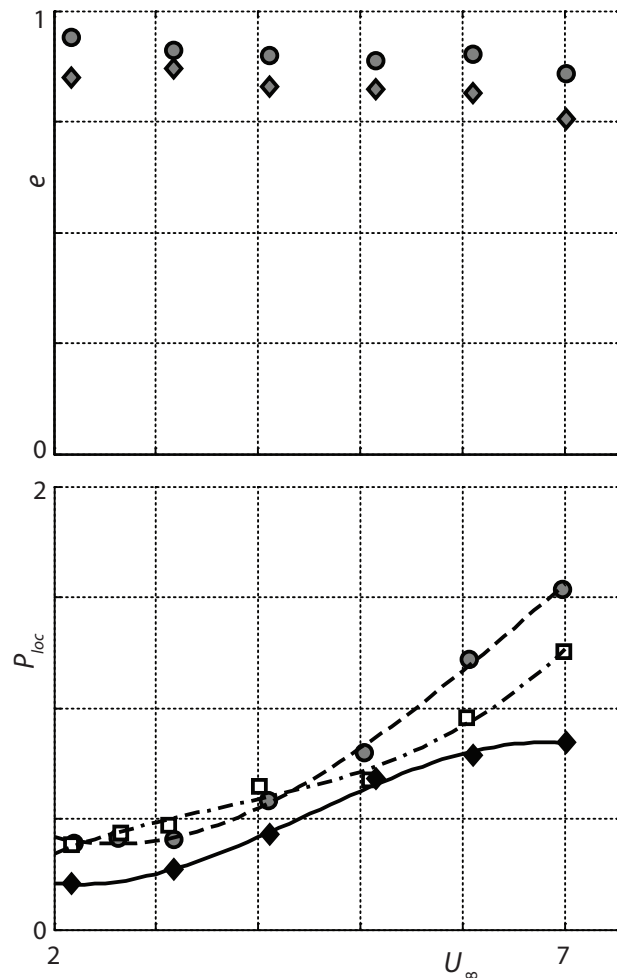
Fig. 9 Aerodynamic performance parameters throughout the measured flight speed range. (*a*) the efficency factors span efficiency e_i (circles) and flap efficiency e_f (diamonds) for the Pied Flycatchers. (*b*) the weight specific power required for locomotion (P^*_{loc}) together with the corresponding weight specific power curves for locomotion (third order trendlines) for the Pied Flycatcher (black diamonds with solid lines), *G. soricina* (grey circles dashed line) and *L. yerbabuenae* (white squares with dot dash lines) .

Sylvia atricapilla (Johansson and Hedenström 2009, paper VII) and for the swift (Henningsson et al. 2010) are more similar to that of the flycatcher than to that of the bats. Taken together, the difference in aerodynamic performance found for the here studied bird and bats can be assumed typical for small to medium sized bats, passerines and even the highly aerial swift. And since one can assume that flight performance should be optimized by evolution due to the high cost of flight, the difference in performance in birds and bats may be explained by differences in phylogenetic constraints.

These results might help explain general differences between birds and bats in relative size and migratory behaviour (Fleming and Eby 2003).

On a more practical note, the results show that migratory flight models developed and adapted to bird flight (e.g. Pennycuick's flight program Flight 1.22) should not directly be used to model bat migration. A good starting point for adapting Flight 1.22 to estimate power curves for bats better is to increase the variable 'body drag coefficient', and set the variable 'induced power factor' to the inverse of the flap efficiency for bats ($k=1/e_f = 1.59$). I do not dare to give a recommendation for the body drag coefficient of bats, since there is already much controversy about body drag coefficients of birds (Hedenström and Liechti 2001, Pennycuick et al. 1996), and I do not want to add another controversial number to the scientific literature.

Next to this, I have shown that Leading Edge Vortices, which are known to be used by many species of insect to enhance lift production (Sane 2003, Lehmann 2004), are also used by slow flying bats and birds. The LEV thus seems to be the most common lift enhancing mechanism in the animal kingdom. The differences in LEV structure between birds and bats are related to the relative wing plan form and differences in kinematics, but it looks like LEV production and stability is not limited by these constraints for neither the bird nor the bats, at least not at 1 m/s forward flight. It could be, though, that generating stable attached LEVs will be more problematic at higher flight speeds (higher *Re* and lower *St*), and it would be very informative to investigate this further. This could potentially demonstrate the limitations of LEV production in birds and bats, but also how birds or bats use LEV stabilizing mechanisms to push beyond these boundaries.

References

Alerstam, Thomas. 1993. *Bird migration*. Cambridge University Press, Cambridge.

Alexander, David E. 2004. *Nature's Flyers: Birds, Insects, and the Biomechanics of Flight*. JHU Press, London

Anderson, John D. 1991. *Fundamentals of Aerodynamics*. McGraw-Hill, New York.

Bomphrey, Richard J., N.J. Lawson, N.J. Harding, G.K. Taylor, and A.L.R. Thomas. 2005. The aerodynamics of *Manduca sexta*: digital particle image velocimetry analysis of the leading-edge vortex. *J Exp Biol* 208: 1079-1094.

Bowlin, Melissa S. 2007. Sex, Wingtip Shape, and Wing-Loading Predict Arrival Date at a Stopover Site in the Swainson's Thrush (*Catharus ustulatus*). *The Auk* 124: 1388-1396.

Busse von, Rhea. 2011. *The trinity of energy conversion - kinematics, aerodynamics and energetics of the lesser long-nosed bat (*Leptonycteris yerbabuenae*)*, PhD thesis.

Davies, N. B. 1977. Prey selection and the search strategy of the spotted flycatcher (*Muscicapa striata*): A field study on optimal foraging. *Animal Behaviour* 25: 1016-1033. doi:10.1016/0003-3472(77)90053-7.

Davis, R. B, S. L Baldauf, and P. J Mayhew. 2010. Many hexapod groups originated earlier and withstood extinction events better than previously realized: inferences from supertrees. *Proceedings of the Royal Society B: Biological Sciences* 277: 1597.

Dudley, Robert. 2002. *The biomechanics of insect flight: form, function, evolution*. Princeton University Press, New Jersey.

Ellington, C.P., C. van den Berg, A.P. Willmott, and A.L.R. Thomas. 1996. Leading-edge vortices in insect flight. *Nature* 384: 626.

Fleming, T. H., and P. Eby. 2003. Ecology of bat migration. *Bat ecology. University of Chicago Press, Chicago, Illinois, USA*: 156–208.

Gessow, Alfred, and Garry C. Myers. 1952. *Aerodynamics of the helicopter*. F. Ungar Pub. Co., New York.

Hall, K. C, S. A Pigott, and S. R Hall. 1998. Power requirements for large-amplitude flapping flight. *Journal of Aircraft* 35: 352–361.

Hall, Kenneth C., and Steven R. Hall. 1996. Minimum Induced Power Requirements for Flapping Flight. *Journal of Fluid Mechanics Digital Archive* 323: 285-315. doi:10.1017/S0022112096000924.

Hedenström, Anders. 2002. Aerodynamics, evolution and ecology of avian flight. *Trends in Ecology and Evolution* 17: 415-422.

Hedenström, Anders, L.C. Johansson, M. Wolf, R. von Busse, Y. Winter, and G.R. Spedding. 2007. Bat Flight Generates Complex Aerodynamic Tracks. *Science* 316: 894-897.

Hedenström, Anders, and F. Liechti. 2001. Field estimates of body drag coefficient on the basis of dives in passerine birds. *Journal of Experimental Biology* 204: 1167–1175.

Hedenström, Anders, M. Rosén, and G. R Spedding. 2006. Vortex wakes generated by robins Erithacus rubecula during free flight in a wind tunnel. *Journal of The Royal Society Interface* 3: 263-276.

Hedenström, Anders, and Thomas Alerstam. 1995. Optimal Flight Speed of Birds. *Philosophical Transactions of the Royal Society of London. Series B: Biological Sciences* 348: 471 -487. doi:10.1098/rstb.1995.0082.

Hedenström, Anders, L. Christoffer Johansson, and Geoffrey R. Spedding. 2009. Bird or bat: comparing airframe design and flight performance. *Bioinspiration & Biomimetics* 4.

Heithaus, E. R, T. H Fleming, and P. A Opler. 1975. Foraging patterns and resource utilization in seven species of bats in a seasonal tropical forest. *Ecology* 56: 841–854.

Helversen von, O. 1986. Blotenbesuch bei Blumfledermäusen. *Bat Flight, Biona Report 5, W. Nachtigall, Ed.*

Henningsson, P., F. T. Muijres, and A. Hedenström. 2010. Time-resolved vortex wake of a common swift flying over a range of flight speeds. *Journal of The Royal Society Interface.* doi:10.1098/rsif.2010.0533.

Hoerner, S.F. 1965. *Fluid-dynamic drag; practical information on aerodynamic drag and hydrodynamic resistance.* Cambridge University Press, Cambridge.

Horner, M. A., T. H. Fleming, and C. T. Sahey. 1998. Foraging behaviour and energetics of a nectar-feeding bat, *Leptonycteris curasoae* (Chiroptera: Phyllostomidae). *Journal of Zoology* 244: 575-586. doi:10.1111/j.1469-7998.1998.tb00062.x.

Hubel, Tatjana Y., Daniel K. Riskin, Sharon M. Swartz, and Kenneth S. Breuer. 2010. Wake structure and wing kinematics: the flight of the lesser dog-faced fruit bat, *Cynopterus brachyotis*. *J Exp Biol* 213: 3427-3440. doi:10.1242/jeb.043257.

Hubel, Tatjana Y., and Cameron Tropea. 2010. The importance of leading edge vortices under simplified flapping flight conditions at the size scale of birds. *J Exp Biol* 213: 1930-1939. doi:10.1242/jeb.040857.

Johansson, L. Christoffer, and A. Hedenström. 2009. The vortex wake of blackcaps (Sylvia atricapilla L.) measured using high-speed digital particle image velocimetry (DPIV). *J Exp Biol* 212, no. 20 (October 15): 3365-3376. doi:10.1242/jeb.034454.

Johansson, L. Christoffer, Marta Wolf, Rhea von Busse, York Winter, Geoffrey R Spedding, and Anders Hedenström. 2008. The near and far wake of Pallas' long tongued bat (*Glossophaga soricina*). *J Exp Biol* 211: 2909-2918.

Johansson, L. Christoffer, Marta Wolf, and Anders Hedenström. 2010. A quantitative comparison of bird and bat wakes. *Journal of The Royal Society Interface* 7: 61-66. doi:10.1098/rsif.2008.0541.

Lauder, G. V. 1996. The argument from design. In *Adaptation*, Academic press, San Diego: 55–91.

Lehmann, F.-O. 2004. The mechanisms of lift enhancement in insect flight. *Naturwissenschaften* 91: 101.

Lentink, David, and M. H Dickinson. 2009. Rotational accelerations stabilize leading edge vortices on revolving fly wings. *Journal of Experimental Biology* 212: 2705.

Lentink, David, W. B. Dickson, J. L. van Leeuwen, and M. H. Dickinson. 2009. Leading-Edge Vortices Elevate Lift of Autorotating Plant Seeds. *Science* 324: 1438-1440. doi:10.1126/science.1174196.

Lentink, David, U.K. Muller, E.J. Stamhuis, R. de Kat, W. van Gestel, L.L.M. Veldhuis, P. Henningsson, A. Hedenström, J.J. Videler, and J.L. van Leeuwen. 2007. How swifts control their glide performance with morphing wings. *Nature* 446: 1082.

Macalister, A. 1872. The myology of the Cheiroptera. *Philosophical Transactions of the Royal Society of London* 162: 125–171.

Marden, James H., and Melissa G. Kramer. 1994. Surface-Skimming Stoneflies: A Possible Intermediate Stage in Insect Flight Evolution. *Science* 266: 427-430. doi:10.1126/science.266.5184.427.

Nieuwstadt, Franciscus Theodorus Marie. 1998. *Turbulentie: inleiding in de theorie en toepassingen van turbulente stromingen*. Epsilon Uitgaven, Utrecht.

Norberg, R. A. 1985. Function of vane asymmetry and shaft curvature in bird flight feathers; inference on flight ability of Archaeopteryx. In *The beginnings of birds. International Archaeopteryx Conference in Eichstätt*: 303–318.

Norberg, Ulla M. 1970. Functional osteology and myology of the wing of Plecotus auritus Linnaeus (Chiroptera). *Ark. Zool* 33: 483–543.

Norberg, Ulla M., and J. M. V. Rayner. 1987. Ecological Morphology and Flight in Bats (Mammalia; Chiroptera): Wing Adaptations, Flight Performance, Foraging Strategy and Echolocation. *Philosophical Transactions of the Royal Society of London. B, Biological Sciences* 316: 335-427. doi:10.1098/rstb.1987.0030.

Norberg, Ulla M. 1975. Hovering flight in the pied flycatcher (*Ficedula hypoleuca*). *Swimming and Flying in Nature* 2: 869-888.

Norberg, Ulla M., T.H. Kunz, J.F. Steffensen, Y. Winter, and O. von Helversen. 1993. The cost of hovering and forward flight in a nectar-feeding bat, Glossophaga soricina, estimated from aerodynamic theory. *J Exp Biol* 182: 207-227.

Norberg, Ulla M. 1990. *Vertebrate flight: mechanics, physiology, morphology, ecology and evolution*. Springer-Verlag, Heidelberg.

Norberg, Ulla M. Lindhe, and York Winter. 2006. Wing beat kinematics of a nectar-feeding bat, Glossophaga soricina, flying at different flight speeds and Strouhal numbers. *J Exp Biol* 209: 3887-3897. doi:10.1242/jeb.02446.

Pennycuick, C. J. 1989. *Bird flight performance: a practical calculation manual*. Oxford University Press, Oxford.

Pennycuick, C. J. 1971. Gliding Flight of the Dog-Faced Bat Rousettus Aegyptiacus Observed in a Wind Tunnel. *J Exp Biol* 55: 833-845.

Pennycuick, C. J., T. Alerstam, and A. Hedenström. 1997. A new low-turbulence wind tunnel for bird flight experiments at Lund University, Sweden. *J Exp Biol* 200: 1441-1449.

Pennycuick, C. J., M. Klaassen, A. Kvist, and A. Lindström. 1996. Wingbeat frequency and the body drag anomaly: wind-tunnel observations on a thrush nightingale (*Luscinia luscinia*) and a teal (*Anas crecca*). *Journal of Experimental Biology* 199: 2757–2765.

Pennycuick, C.J. 1968. Power Requirements for Horizontal Flight in the Pigeon Columba Livia. *J Exp Biol* 49: 527-555.

Pennycuick, C.J. 2008a. Chapter 6 The Membrane Wings of Bats and Pterosaurs. In *Modelling the Flying Bird*, Elsevier, Amsterdam: 135-160.

Pennycuick, C.J. 2008b. *Modelling the Flying Bird*. Elsevier, Amsterdam.

Pennycuick, C.J. 1972. *Animal flight*. Edward Arnold, London.

Qiang, Ji, Philip J. Currie, Mark A. Norell, and Ji Shu-An. 1998. Two feathered dinosaurs from northeastern China. *Nature* 393: 753-761. doi:10.1038/31635.

Rayner, Jeremy M. V. 1979. A New Approach to Animal Flight Mechanics. *J Exp Biol* 80: 17-54.

Saffman, P. G. 1995. *Vortex dynamics*. Cambridge University Press, Cambridge.

Sane, S.P. 2003. The aerodynamics of insect flight. *J Exp Biol* 206: 4191-4208.

Schmidt-Nielsen, K. 1972. Locomotion: energy cost of swimming, flying, and running. *Science* 177: 222–228.

Spedding, G. R., A. Hedenström, and L. C. Johansson. 2008. A note on wind-tunnel turbulence measurements with DPIV. *Experiments in Fluids* 46: 527-537. doi:10.1007/s00348-008-0578-1.

Spedding, G. R., and J. McArthur. 2010. Span Efficiencies of Wings at Low Reynolds Numbers. *Journal of Aircraft* 47: 120-128. doi:10.2514/1.44247.

Spedding, G. R., M. Rosén, and A. Hedenström. 2003a. A family of vortex wakes generated by a thrush nightingale in free flight in a wind tunnel over its entire natural range of flight speeds. *J Exp Biol* 206: 2313-2344. doi:10.1242/jeb.00423.

Spedding, G.R., A. Hedenström, and M. Rosén. 2003b. Quantitative studies of the wakes of freely flying birds in a low-turbulence wind tunnel. *Experiments in Fluids* 34: 291.

Swartz, S.M., M.S. Groves, H.D. Kim, and W.R. Walsh. 1996. Mechanical properties of bat wing membrane skin. *J. Zool.* 239: 357-378.

Teeling, E. C. 2005. A Molecular Phylogeny for Bats Illuminates Biogeography and the Fossil Record. *Science* 307: 580-584. doi:10.1126/science.1105113.

Tucker, V.A. 1993. Gliding Birds: Reduction of Induced Drag by Wing Tip Slots between the Primary Feathers. *J Exp Biol* 180: 285-310.

Usherwood, J. R, and F. O Lehmann. 2008. Phasing of dragonfly wings can improve aerodynamic efficiency by removing swirl. *Journal of The Royal Society Interface* 5: 1303.

Videler, J.J., E.J. Stamhuis, and G.D.E. Povel. 2004. Leading-Edge Vortex Lifts Swifts. *Science* 306: 1960-1962.

Videler, John J. 2006. *Avian Flight*. Oxford University Press, Oxford.

Warrick, Douglas R., B.W. Tobalske, and D.R. Powers. 2005. "Aerodynamics of the hovering hummingbird." *Nature* 435: 1094.

Warrick, Douglas R., Bret W. Tobalske, and Donald R. Powers. 2009. "Lift production in the hovering hummingbird." *Proceedings of the Royal Society B: Biological Sciences* 276: 3747-3752. doi:10.1098/rspb.2009.1003.

Weis-Fogh, T. 1973. Quick Estimates of Flight Fitness in Hovering Animals, Including Novel Mechanisms for Lift Production. *J Exp Biol* 59: 169-230.

Wilkinson, G. S., and T. H. Fleming. 1996. Migration and evolution of lesser long-nosed bats *Leptonycteris curasoae*, inferred from mitochondrial DNA. *Molecular Ecology* 5: 329–339.

Winter, Y. 1999. Flight speed and body mass of nectar-feeding bats (Glossophaginae) during foraging. *J. Exp. Biol.* 202: 1917-1930.

Wolf, Marta, L. Christoffer Johansson, Rhea von Busse, York Winter, and Anders Hedenström. 2010. Kinematics of flight and the relationship to the vortex wake of a Pallas' long tongued bat (*Glossophaga soricina*). *J Exp Biol* 213: 2142-2153. doi:10.1242/jeb.029777.

Wootton, R. J. 1981. Palaeozoic insects. *Annual Review of Entomology* 26: 319–344.

Young, John, Simon M. Walker, Richard J. Bomphrey, Graham K. Taylor, and Adrian L. R. Thomas. 2009. Details of Insect Wing Design and Deformation Enhance Aerodynamic Function and Flight Efficiency. *Science* 325: 1549-1552. doi:10.1126/science.1175928.

Zhao, Liang, Qingfeng Huang, Xinyan Deng, and Sanjay P. Sane. 2010. Aerodynamic effects of flexibility in flapping wings. *Journal of The Royal Society Interface* 7: 485-497. doi:10.1098/rsif.2009.0200.

Feathers and membranes

Popular scientific summary

The figures and glossary can be found in the introduction

Animal flight has always intrigued people, and different aspects of animal flight have therefore widely been studied by biologists, physicists and engineers. At least to me, the aspect concerning the aerodynamics of animal flight in particular is very interesting because of the complex temporal varying wake dynamics as a result of continually wing morphing in flapping flight. This puts aerodynamics of animal flight among the most complex and intriguing phenomena in fluid dynamics.

Within the animal kingdom, there is a large diversity of flying animals, ranging from large soaring albatrosses to tiny hovering insects, which can be explained by two factors, namely ecological requirements and phylogenetic constraints.

The variation between the different taxa of flying animals (birds, bats and insects) is due to the fact that flight has evolved independently for each flying taxa. This has resulted in very different body plans of the flight apparatuses, for example birds have feathered wings and bats have membranous wings. These different body plans set different limitations to the flight dynamics for each taxa, and ultimately limits flight performance. These limitations to evolutionary change are called phylogenetic constraint.

The morphological differences between species within a certain taxa, for example between an albatross and a hummingbird, can primarily be explained by differences in ecological requirements. The ecological requirements for a certain species set the optimum flight performance for that species, and this is enforced by evolutionary selection pressure. In fact, the albatross in the example above is a result of nature's attempt to make an efficiently gliding sailplane based on a bird body plan (Fig. 1), resulting in the well known landing and take-off problems. On the other hand, the hummingbird is nature's attempt to make an insect out of a bird.

To summarize, optimum flight performance for a certain species is set by its ecological requirements, while the acquired maximum performance is limited by the phylogenetic constraints for that species. In this thesis I investigate how the relative flight performance in two bat species and one bird species differ and how these differences depend on their ecology and evolutionary history. For this I have developed methods for visualizing and quantifying the wake dynamics behind a flying animal in a wind tunnel, and which is used to quantify aerodynamic flight performance.

I have studied flight in two species of nectar feeding bats: the Pallas' Long-tongued bat (*Glossophaga soricina*) and the Lesser Long-nosed Bat (*Leptonycteris yerbabuenae*). Both species feed from flowers by hovering in front of them, so both may be regarded as hovering specialists. Next to this, *L. yerbabuenae* is a highly mobile species, since it migrates annually up to 1600 km from Mexico to Arizona (USA), and it flies around 100 km every night between its roosting sites and different feeding patches. *G. soricina*, on the other hand, does not migrate and has an extremely small home-range where it both roosts and feeds from flowers (recapturing distance for wild *G. soricina* is only 200 m).

The studied bird is a typical small insectivorous passerine, the Pied flycatcher (*Ficedula hypoleuca*).

It habitually hovers and flies slowly when catching insects on the wing, and it migrates annually from northern Europe to western Africa. Thus, flycatchers are expected to be well adapted to efficient slow flight as well as efficient cruising flight.

I studied the aerodynamics of flight for these species in a wind tunnel. In a wind tunnel the air moves instead of the animal, which enables me to study flight from up close in a controlled environment. The wake dynamics is studied using a technique called Particle Image Velocimetry (PIV). This technique allows visualization and measurement of air movements within a defined plane, by tracking fog particles illuminated by a laser sheet. I did two types of measurements: streamwise PIV measurements close to the wing surface, called on-wing PIV; and PIV measurements in a cross-stream plane closely behind the flying animal, called near-wake PIV.

For the PIV analysis, I developed a method for visualizing (fig 6 and 8) and quantifying the fluid dynamics around and behind a flying animal. The wake dynamics is quantified by converting the vortex strength and downwash in the wake into flight forces. These flight forces are then used to estimate the aerodynamic performance for flapping flight.

I have defined two aerodynamic performance measures, being the lift-to-drag ratio L/D and the span efficiency e_i. L/D is a value for the efficiency of locomotion since the lift force L is the force required to stay up in the air and drag D is the force related to the cost of flight (Fig. 2). e_i is a value for the efficiency of lift production, where a high e_i means low power required to generate lift.

As explained above, both bat species studied are hovering specialist, but their movement ecology is very different: *L. yerbabuenae* flies much longer distances than *G. soricina*. This means that *L. yerbabuenae* should be more adapted to efficient flight at cruising flight speeds than *G. soricina*. In this thesis, I compare these differences in ecological requirements with differences in aerodynamic performance. It turns out that L/D is similar between the two bat species, but the speed at which L/D is maximum (highest efficiency) is close to cruising flight speed for *L. yerbabuena* , while this speed is much lower for *G. soricina*. Thus, both bats fly most efficient at the speed at which they fly most of the time.

Both the bird and bat generate a Leading Edge Vortex (LEV) (Fig. 6 and 7), which is an unsteady vortex structure commonly used by insects to enhance lift. In this thesis, I show for the first time that also vertebrates use LEVs. The strength of the LEV is very similar in birds and bats, adding 49% and 40% of the total lift produced, respectively, but the LEV structure is very different between bird and bats. In bats the LEV strength increases along the wing span from low close to the body to high near the wingtip. This LEV structure similar to that for insects. The flycatcher, on the other hand, produces a LEV that is strongest at mid wingspan, and weakest near the wingtip. The reduction in LEV near the wingtip is probably a result of upwards bending of feathers near the tip. This is probably a mechanism to stabilize the relatively strong LEV in birds.

The wake dynamics behind the flying birds and bats differ significantly (Fig. 8), which is a result of the fact that birds and bats have both a very different body shape and wingbeat upstroke.

Birds use a so called a feathered upstroke, where they retract the wings close to the body and spread the wing feathers. This enables air to flow through the gaps between the feathers, making their wings aerodynamically inactive during the upstroke (Fig. 8*c*).

Bats cannot do this since air cannot flow through the solid wing membrane, and if a bat would retracts its wings too much the membrane would go slack, resulting in uncontrolled fluttering. Therefore, bats have an active upstroke where they move the wing upwards at a negative angle-of-attack generating thrust and negative lift. This results in the production of a 'reversed vortex loop' in the wake behind each wing (Fig. 8*a-b*).

Throughout the complete wingbeat, the birds generate more body lift than the bats, which suggests that bird bodies are more streamlined than bat bodies. This could be partly due to bats having more blunt shaped bodies and protruding ears required for echolocation. Concave shaped structures such as bat ears are known to be among the most drag producing bluff bodies.

All these differences together result in both higher L/D and span efficiency for the birds than for the bats, suggesting that birds outperform bats in aerodynamic flight performance. Still it looks like the wake dynamics for both birds and bats are optimal for their relative

flight performance regime (for the *L/D* regime they operate at). This suggests that evolution has adapted the wingbeat kinematics for birds as well as for bats to optimize their flight performance, although differences in their basic body plan (e.g. bird wings have feathers and bats wings consist of membranes) has resulted in a higher maximum performance in birds.

All in all, I have shown that aerodynamic flight performance depends strongly on the ecology and evolutionary history of a specific species. The currently used flight performance models, though, do not capture variation in flight performance due to these detailed characteristics. The here found results can be used as a starting points to improve these animal flight models. This would enable us to tailor flight performance estimates better for a specific species.

Thanks!

First of all, I would like to thank my advisors, Anders and Christoffer, for your help and support throughout my PhD studies. Anders, thank you for believing in me and inviting me to come to Sweden. I learned a lot from you, ranging from writing manuscripts to migration ecology. It's amazing how much you know about our research field, and it really helped me to put my research into context. This made me develop from an aerospace engineer into a biologist, or at least something in between. Let's call it a 'scientist'. Christoffer, you are one of the most involved advisors I can imagine. I could always just drop by to discuss my results or research in general. Your feedback on analyses and manuscripts were always very detailed and constructive. You are a great advisor, colleague and friend. I hope that we can keep working together like this.

I would also like to thank my colleagues from the 'Lund Animal Flight Lab' without whom this thesis could not exist and who made work so much fun! Lets start furthest away… geographically speaking. Geoff, it was great to work with you on various papers. Although you were only able to visit us a few times, your lectures, being in a presentation, as comments on various manuscripts, or via the phone were very interesting and instructive, especially the validation monologue… I hope to continue learning from you in the future. Rhea, you are the colleague I worked wost with in the wind tunnel and those sessions were very nice. Per, you are the colleague I am closest to from a personal point-of-view. You are a great friend, and I regard myself very fortunate to work directly with you on a couple of very successful studies. Let's continue the good work! Melissa, it was great that you came to Lund for a postdoc project. We have very different backgrounds, you being a biologist and me being an engineer. But our skills complemented each other perfectly and this made working with you and learning from you very interesting and fun. Marta and Sophia, you are a great colleagues, and it was nice to work with you.

Thanks to the rest of the people from Theoretical ecology. It was fun to learn about traits like fur length… or was it beak size? And how fortunate was I to have such skilled statisticians like Jonas or Jörgen two doors down the hall. Thank you to Kristina and Lena for being such nice roommates. Martin, isn't it fun that we both start and finish our PhD studies at the same day? Thank you for our memorable discussions concerning ecology and countless other topics. People from the ecology building, and in particular from CanMove and the Migration Group, thank you for the interesting talks and discussions. During my PhD studies I was fortunate to work with and advise a couple of great and enthusiastic students. Ryan, Roel, Marco, Melanie and Gide. Marco, I am happy that you will continue your research in our lab for your PhD studies.

Friends from Sweden, thank you for making me feel so much at home. Friends from Holland. Despite the distance I feel still very close to you, and your numerous visits to Sweden were unforgettable.

My sister Eva. It was great that you came to Lund University for an Erasmus exchange programme! Living together here at Filippavägen was fun. Playing poker for who would have to cook and who would have to do the dishes. And you even helped me with experiments in the wind tunnel! It really made the transition when moving to Lund so much easier. Renee &co. My sister and her family Edwin, Roman, Manu and Rosa. Living in Sweden makes me not visiting you enough, sorry for that. You are very dear to me, and it was great that you came to visit us so close after Rosa was born. Eric, Karin and Linda, thank you for being part of my family, especially during the great Christmas dinners!

Mam, I know it is not nice if your son moves to another country, but that has made the times that you came to visit us so much more special. It was great to go sight seeing in Skåne with you and Huub. You are a great mother to me, and your support and guidance throughout the years made me the person I am today, so I think this book also your creation. Huub, thank you for being in my mother's life, and as a result of that also in mine. Your decisiveness in whatever you do and your positive view on life are inspiring, and an important lesson to me. Pap, you have supported me always in everything I did, and then I mean literally everything… Luckily I chose to become a scientist and not a bank robber. But when I think about it, me becoming a scientist is also very much your doing. Your curiosity in the world around you, resulting in your broad knowledge of so many aspects of art and science, did not only made you always win with Triviant. It triggered my own curiosity in the world (maybe initially to beat you with Triviant), and this was the basis for my scientific career. Mary and Josan, my parents in law. Already quite a few years you are my second set of parents and I would like to thank you very much for your support, and sorry for dragging your daughter with me all the way to Sweden.

Lieke, I love you! You are the most important person in my life, and without you this all would have never been possible. I really mean this. You are so generous in supporting me in my career, not only by moving with me to Lund, or giving comments on talks or manuscripts, but mainly by just being there and believing in me. During my PhD studies, we have built a great family with our son Max, and we are still in the middle of the building process… Max, it will take a couple of years before you can read this, still I would like to thank you for the half year of parental leave, where I could focus on you instead of vortices. Although you will not remember it, in fact I am certain you have already forgotten it, let me tell you: It was a great time!

List of contributions to the papers

Paper I. The study was planned by F.T.M., L.C.J., G.R.S. and A.H. The PIV experiments were performed by F.T.M. and R.B. The kinematics experiments were performed by L.C.J. and M.W. The PIV data was analyzed by F.T.M., L.C.J. and G.R.S. The kinematics data was analyzed by L.C.J. and M.W. The results were discussed by F.T.M., L.C.J., G.R.S. and A.H. The manuscript was written by F.T.M., L.C.J., G.R.S. and A.H.

Paper II. The study was planned by F.T.M., L.C.J. and A.H. The experiments were performed by F.T.M. The data was analyzed by F.T.M. The results were discussed by F.T.M., L.C.J. and A.H. The manuscript was written by F.T.M., L.C.J. and A.H.

Paper III. The study was planned by A.H., F.T.M., R.v.B., L.C.J. and G.R.S. The experiments were performed by F.T.M. and R.v.B. The data was analyzed by F.T.M. The results were discussed by A.H., F.T.M., R.v.B., L.C.J., and G.R.S. The manuscript was written by A.H., F.T.M., R.v.B., L.C.J., and G.R.S. The bats were provided by Y.W.

Paper IV. The study was planned by F.T.M., L.C.J. and A.H. The experiments were performed by F.T.M. The data was analyzed by F.T.M. The results were discussed by F.T.M., L.C.J. and A.H. The manuscript was written by F.T.M., L.C.J. and A.H. The bats were provided by Y.W.

Paper V. The study was planned by F.T.M. and A.H. The experiments were performed by F.T.M. The data was analyzed by F.T.M. The results were discussed by F.T.M., G.R.S. and A.H. The manuscript was written by F.T.M., G.R.S. and A.H. The bats were provided by Y.W.

Paper VI. The study was planned by F.T.M., L.C.J. and A.H. The experiments were performed by F.T.M. and M.B. The data were analyzed by F.T.M., M.B. and L.C.J. The results were discussed by F.T.M., M.B. and L.C.J. The manuscript was written by F.T.M., M.B., L.C.J. and A.H.

Paper VII. The study was planned by F.T.M., L.C.J. and A.H. The experiments were performed by F.T.M., M.B. and R.v.B. The data were analyzed by F.T.M., M.B. and R.v.B. The results were discussed by F.T.M., L.C.J., M.B. and A.H. The manuscript was written by F.T.M., L.C.J., M.B. and A.H. The bats were provided by Y.W.

Leading-Edge Vortex Improves Lift in Slow-Flying Bats

F. T. Muijres,[1] L. C. Johansson,[1] R. Barfield,[1] M. Wolf,[1] G. R. Spedding,[2] A. Hedenström[1]*

Staying aloft when hovering and flying slowly is demanding. According to quasi–steady-state aerodynamic theory, slow-flying vertebrates should not be able to generate enough lift to remain aloft. Therefore, unsteady aerodynamic mechanisms to enhance lift production have been proposed. Using digital particle image velocimetry, we showed that a small nectar-feeding bat is able to increase lift by as much as 40% using attached leading-edge vortices (LEVs) during slow forward flight, resulting in a maximum lift coefficient of 4.8. The airflow passing over the LEV reattaches behind the LEV smoothly to the wing, despite the exceptionally large local angles of attack and wing camber. Our results show that the use of unsteady aerodynamic mechanisms in flapping flight is not limited to insects but is also used by larger and heavier animals.

Generating enough lift during hovering and slow forward flight is problematic according to traditional quasi–steady-state wing theory (*1, 2*). Yet several species of small flying vertebrates are adapted to foraging using this flight mode. Insects are able to hover by using a range of possible unsteady high-lift mechanisms, including rotational circulation (*3*),

clap-and-fling (*4*, *5*), wake capture (*3*, *6*), and added mass (*7*, *8*). However, arguably the most important mechanism is a leading-edge vortex (LEV) (*5*, *9–12*), which may generate up to two-thirds of the total lift in insect flight (*13*, *14*). Although unsteady lift mechanisms have been studied extensively in insects or scaled models of their flapping wings (*5*, *6*, *11–17*), vertebrates have only been studied indirectly. Such measurements derived from kinematics or wakes suggest that some birds (*18*) and bats (*19*) require additional lift for weight support, other than quasi–steady-state lift alone (*2*). A recent study of hovering hummingbirds found traces of previously shed LEVs in their wakes (*20*), and sharp-edged model wings of gliding swifts with high sweep (60°) developed stable LEVs (*21*).

We quantitatively measured the airflow, using digital particle image velocimetry (DPIV), around the wings of three individuals of Pallas' long-tongued bat, *Glossophaga soricina* (table S1), flying freely in front of a feeder in a low-turbulence wind tunnel at a forward flight speed $U_\infty = 1$ m/s (*22*). At this flight speed, the average local Reynolds number of the bat wing is $Re \approx 5 \times 10^3$ (*23*) and the Strouhal number $St \approx 1.36$ (*24*).

The DPIV image plane was orientated vertically in the freestream flow direction, and measurements were made at different span-wise locations along the wing, when the wing was positioned horizontally. At this wing position, the wing does not block the DPIV image, the wingspan is at its maximum, and the wing is two-thirds into the downstroke (*22*). Cross-stream DPIV measurements were also performed closely behind the bats (a distance of ~3 mean wing chord lengths at $U_\infty = 1.35$ m/s). From the DPIV data, we determined the two in-plane velocity components of the airflow, resulting in a planar velocity field. Spatial gradients of this planar velocity field also yield the divergence, which is a measure of the variation in out-of-plane velocity (*25*), and the vorticity, which is a measure of the local angular velocity.

From the streamwise DPIV data, the wing profile and its motion (Fig. 1, A to D) were also determined by tracking the part of the wing profile illuminated by the laser sheet (*22*). The velocity of the wing profile was used as a no-slip boundary condition in the DPIV calculations (*22*). The average wing camber is $18 \pm 3\%$ (mean $\pm$ SD, $n = 68$ observations) of the wing chord (fig. S5D), and the average effective angle of attack is $51° \pm 19°$ ($n = 68$ observations) (fig. S5F) (*22*). Both are high values for steady-state wing theory: A fixed wing at similar Re with such high camber and angle of attack would stall and lose lift (*26*).

[1]Department of Theoretical Ecology, Lund University, SE-223 62 Lund, Sweden. [2]Department of Aerospace and Mechanical Engineering, University of Southern California, Los Angeles, CA 90089–1191, USA.

*To whom correspondence should be addressed. E-mail: anders.hedenstrom@teorekol.lu.se

The vorticity field and velocity vectors around the bat wing (Fig. 1) show that the flow separates at the leading edge, generating a patch of high negative vorticity (clockwise spin). But, remarkably, behind this patch of vorticity the airflow reattaches, resulting in attached and laminar flow at the trailing edge. The vorticity patch at the leading edge of the wing was present at all measured span-wise locations but was stronger near the wingtip (Fig. 1C) than toward the wing root (Fig. 1A). Instantaneous streamlines computed from the measured streamwise flow (Fig. 1D) form a recirculating region at the vorticity patch, which also spirals inward at the core. All these facts are consistent with the presence of an attached LEV (*10*). In the neighborhood of the LEV, the divergence of the flow in the image plane is on average positive (source flow) (*25*) and small compared to the vorticity magnitude (fig. S4). Both sign and magnitude differ from theoretical expectations for LEV stabilization (*10*), which could imply that no LEV stabilizing mechanism is needed (*27*).

In some of the images (mainly distally on the wing), an area of high negative vorticity is also found near the trailing edge but without recirculation (Fig. 1D). The presence of negative vorticity near the trailing edge is associated with the outer wing making a strong rotational (pitch-up) movement before the end of the downstroke (Fig. 1D). Therefore this patch of high vorticity could be a result of rotational circulation (*3*), which is an alternative aerodynamic mechanism for enhanced lift generation.
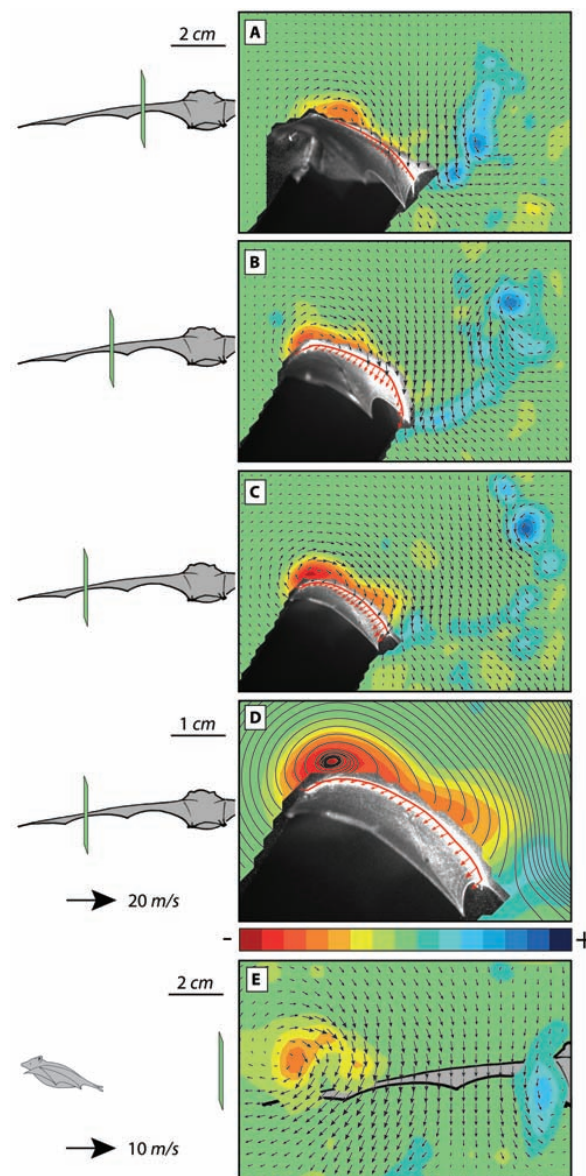

Fig. 1. Velocity and vorticity fields around a bat wing in slow forward flight (1 m/s), when the wing is positioned horizontally in the down-stroke. The vectors show the disturbance caused by the wing with the uniform mean flow (of 1 m/s) removed. (**A** to **C**) show streamwise measurements at different positions along the span. The span locations are 33, 50, and 65% of the semi-wingspan for (A), (B), and (C), respectively, as indicated on the bat silhouettes to the left. The flight direction is from right to left. Instantaneous two-dimensional streamlines of part of (C) are shown in (**D**). In (A) to (D), The bat wing and its shadow in the DPIV laser sheet are visible; the local wing profile and its relative motion are shown with a red curve and arrows. (E) Data derived from cross-stream measurements, with the position of the bat indicated by the bat silhouette. The vorticity field is scaled according to the color bar; it ranges from −1750 to +1750 s⁻¹, for (A) to (D) and from −700 to +700 s⁻¹ for (E). The velocity vectors are scaled to the reference vector at the left of the color bar for (A) to (D) and at left of (E). Space scale bars are located at left of (A) for (A) to (C), at left of (D), and at left of (E).

To investigate the contribution of the LEV to the total lift, the circulation of the LEV was determined at different span locations (Fig. 2). The average chord length and average effective wing velocity ($\overline{c} = 0.042$ m and $\overline{U}_{\text{eff}} = 4.0$ m/s) were used to nondimensionalize the circulation ($\Gamma / \overline{U}_{\text{eff}}\,\overline{c}$) (*22*). The results show that the LEV circulation increases toward the wingtip (Fig. 2), which is consistent with LEV structures found for some insects (*1*). When assuming that a LEV enhances lift by adding its own circulation to the bound circulation of a wing (*1*), the nondimensional circulation of the LEV is related to its associated lift coefficient by $C_{\text{LEV}} \approx 2 \cdot \Gamma_{\text{LEV}} / \overline{U}_{\text{eff}}\,\overline{c}$ (*22, 28*). The average nondimensional LEV circulation is about 1 (Fig. 3), which corresponds to a $C_{\text{LEV}} \approx 2$.

During the downstroke of a flapping wing, positive vorticity is generated at the trailing edge and is shed into the wake. This vorticity can be generated throughout the downstroke, and we will label it trailing-edge vorticity (TEV). According to Kelvin's theorem (*29*), the circulation of the TEV (Γ_{TEV}) is related to the bound circulation on the wing and thus to the total lift coefficient by $C_{\text{L}} \approx 2 \cdot \Gamma_{\text{TEV}} / \overline{U}_{\text{eff}}\,\overline{c}$ (*22*). The shed TEV is clearly visible in Fig. 1, A to C, as a distinct patch of positive vorticity (counterclockwise spin) to the right of the wing, called
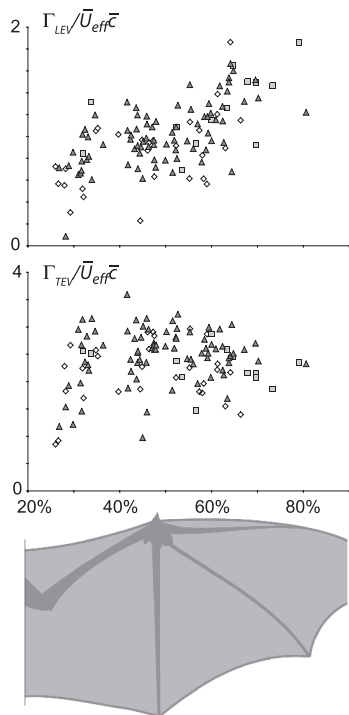
the start vortex, and a trail of positive vorticity between this start vortex and the trailing edge. Because the tip of the wing travels a larger distance during the downstroke than does the wing root, the start vortex is located further behind the wing near the wingtip (Fig. 1C) than near the wing root (Fig. 1A). This pattern of vorticity shedding is strikingly similar to that of a hawkmoth (*30*). Γ_{TEV} was determined at different span locations (Fig. 2), but no systematic variation was found. The average nondimensional Γ_{TEV} is 2.4 (Fig. 3), for an effective lift coefficient of 4.8 (*22*), which is beyond that considered to be the maximum possible for quasi–steady-state wings (*2*) at the same *Re* and aspect ratio (*26*), but is similar to results from previous studies of bats (*19*) and within the possible range of pitching and heaving plates (*31*).

As mentioned above, the nondimensional $\Gamma_{\text{LEV}} \approx 1$, which means that the LEV contributes to more than 40% of the total lift ($\Gamma_{\text{LEV}}/\Gamma_{\text{TEV}} = 0.42$) (*22*). This value is similar to LEV contributions reported for insects [hawkmoth, up to 65% (*13, 14*), and fruit fly $\approx$ 45% (*3*)] but is considerably higher than the 15% estimated from

the wake of hovering hummingbirds (*20*). The TEV minus the LEV nondimensional circulation is 1.4, resulting in a non-LEV lift coefficient of 2.8 (*22*). This value is also higher than conventional quasi–steady-state wing models at similar conditions (*26*), suggesting that other unsteady lift mechanisms may also be involved, such as rotational circulation (*3*) and delayed stall (*15*), resulting in high lift due to a high angle of attack.

To obtain an image of the three-dimensional wake structure, near-wake cross-stream DPIV measurements were performed for two bats (Fig. 1E). The vorticity field and velocity vectors show the presence of a tip vortex with negative vorticity (clockwise spin) and a weaker vortex near the wing root (root vortex) with positive vorticity (counterclockwise spin). The average tip- and root-vortex circulation were nondimensionalized using the mean wing chord length ($\overline{c}$) and the average effective wing velocity ($\overline{U}_{\text{eff}}$) determined from kinematic measurements (*22*). The average tip-vortex circulation has a similar strength as Γ_{TEV}, and the average Γ_{LEV} is 65% of the root-vortex circulation (Fig. 3).

Based on the qualitative and quantitative data, we suggest a cartoon model of the vortex system around the bat wing during the downstroke (Fig. 4). At the beginning of the downstroke, a start vortex is formed at the trailing edge of the wing. During the downstroke, this vortex travels downward and backward because of self-convection, creating a trail of vorticity between the start vortex and the trailing edge of the wing. In inviscid vortex dynamics, a line vortex must terminate either as a closed loop or at a solid surface, and so the start vortex connects to two tip and two root vortices, which grow in length during the downstroke. The tip and root vortices are connected to the wing and to the LEV. The start vortices of each wing are probably connected to each other behind the body (*19*). Because the LEV circulation strength is similar to the root-vortex circulation, these are probably connected, hence the absence of a LEV across the body. The near wake of slow-flying bats did not show a separately shed LEV (*19*), suggesting that the LEV stays attached throughout the downstroke and merges with the stop vortex.

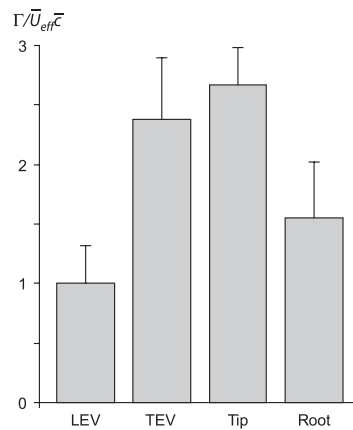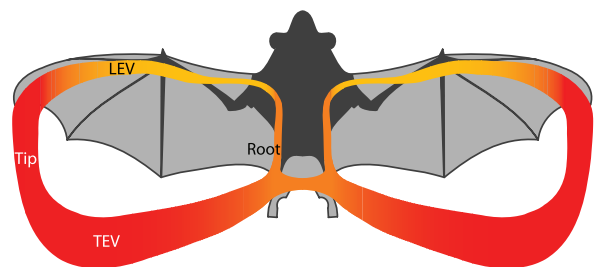For hovering and slow-flying insects, three different types of LEV systems have been proposed

Fig. 3. Mean ± SD for circulations in different parts of the wake structure during the downstroke when the wing is horizontal, at a forward speed of 1 m/s. The circulation was nondimensionalized using $\overline{c}$ and $\overline{U}_{\text{eff}}$ (fig. S5). For the LEV and TEV, *n* = 119 observations; for the tip and root vortex, *n* = 98 observations (*22*).

Fig. 2. Circulation Γ_{LEV} (**top**) and Γ_{TEV} (**bottom**) at different wing positions for three bats. The circulation was nondimensionalized using $\overline{c}$ and $\overline{U}_{\text{eff}}$ of the measured points (fig. S5). Dimonds represent bat 1, squares represent bat 2, and triangles represent bat 3.

Fig. 4. Cartoon of the primary vortex structure for a bat during the downstroke when the wing is horizontal, at a forward speed of 1 m/s. The structure consists of two closed loops, one for each wing, consisting of a LEV on top of the wing, connected to a start vortex shed in the wake via a tip vortex (Tip) and a root vortex (Root). The color coding indicates the absolute value of local circulation; yellow is low circulation and red is high circulation.

(*14*): a helical-shaped LEV starting at the inner wing, increasing in size along the wingspan, and finally connecting to the tip vortex (*9*, *27*); a cylindrical-shaped LEV that expands across the thorax and is connected to the two tip vortices (*6*, *14*); and a LEV that is connected to a small root vortex and a large tip vortex (*5*). The vortex system proposed here (Fig. 4) is most similar to the latter case.

The sharp leading edge of the bat wing probably facilitates the generation of the LEV (*21*), whereas the ability to actively change the wing shape and camber (*32*) could contribute to the control and stability of the LEV.

LEVs have now been observed in active unrestricted bat flight, with a strength that is important to the overall aerodynamics. Unsteady aerodynamic mechanisms for enhanced lift are therefore not unique to insect flight, and larger animals adapted for slow and hovering flight, such as these nectar-feeding bats, can (and perhaps must) use LEVs to enhance flight performance.

References and Notes

1. F.-O. Lehmann, *Naturwissenschaften* **91**, 101 (2004).
2. Quasi–steady-state wing theory assumes that the forces on a moving wing are equivalent to the sum of the forces on a fixed wing over a sequence of attitudes that track the wing motion. This model neglects acceleration forces and unsteady aerodynamic effects.
3. M. H. Dickinson, F.-O. Lehmann, S. P. Sane, *Science* **284**, 1954 (1999).
4. T. Weis-Fogh, *J. Exp. Biol.* **59**, 169 (1973).
5. T. Maxworthy, *J. Fluid Mech.* **93**, 47 (1979).
6. R. B. Srygley, A. L. R. Thomas, *Nature* **420**, 660 (2002).
7. C. Ellington, *Philos. Trans. R. Soc. London Ser. B* **305**, 1 (1984).
8. S. Vogel, *Life in Moving Fluids* (Princeton Univ. Press, Princeton, NJ, 1994).
9. C. P. Ellington, C. van den Berg, A. P. Willmott, A. L. R. Thomas, *Nature* **384**, 626 (1996).
10. T. Maxworthy, *J. Fluid Mech.* **587**, 471 (2007).
11. M. W. Luttges, in *Frontiers in Experimental Fluid Mechanics*, M. Gad-El-Hak, Ed. (Springer, Berlin, 1989), pp. 429–456.
12. A. L. R. Thomas, G. K. Taylor, R. B. Srygley, R. L. Nudds, R. J. Bomphrey, *J. Exp. Biol.* **207**, 4299 (2004).
13. C. van den Berg, C. P. Ellington, *Philos. Trans. R. Soc. London Ser. B* **352**, 329 (1997).
14. R. J. Bomphrey, N. J. Lawson, N. J. Harding, G. K. Taylor, A. L. R. Thomas, *J. Exp. Biol.* **208**, 1079 (2005).
15. M. H. Dickinson, K. G. Gotz, *J. Exp. Biol.* **174**, 45 (1993).
16. A. Willmott, C. Ellington, *J. Exp. Biol.* **200**, 2693 (1997).
17. C. Somps, M. Luttges, *Science* **228**, 1326 (1985).
18. U. M. Norberg, in *Swimming and Flying in Nature*, vol. 2, T. Y.-T. Wu, C. J. Brokaw, C. Brennen, Eds. (Plenum, New York, 1975), pp. 869–881.
19. A. Hedenström *et al.*, *Science* **316**, 894 (2007).
20. D. R. Warrick, B. W. Tobalske, D. R. Powers, *Nature* **435**, 1094 (2005).
21. J. J. Videler, E. J. Stamhuis, G. D. E. Povel, *Science* **306**, 1960 (2004).
22. See supporting material on *Science* Online.
23. $Re = \overline{U}_{eff}\overline{c}/\nu$ ($\overline{U}_{eff}$ is average effective wing speed, which is the sum of the flight velocity and the wing-flapping velocity; $\overline{c}$ is the average wing chord length; and ν is the kinematic viscosity of air). *Re* is the ratio between inertial and viscous aerodynamic forces and is an index of the relative instability of the fluid around an airfoil. The bats operate at a *Re* range with rather stable aerodynamic characteristics, just below the *Re* range ($10^4 \leq Re \leq 10^5$) where the aerodynamics are notoriously hard to predict and control.
24. $St = fA/U_\infty$ (*f* is wingbeat frequency and *A* is the tip-to-tip vertical excursion of the wing tip). *St* is proportional to the ratio of the average wingbeat velocity to the steady forward speed and is an indication of the unsteadiness and efficiency of vortex generation.
25. For an incompressible fluid, the divergence in a planar velocity field is related to the change in out-of-plane flow velocity. When the divergence is positive, the fluid works as a fluid source in the planar velocity field, decreasing the out-of-plane velocity. When it is negative, it is a fluid sink, which increases the out-of-plane velocity.
26. E. V. Laitone, *Exp. Fluids* **23**, 405 (1997).
27. J. M. Birch, M. H. Dickinson, *Nature* **412**, 729 (2001).
28. J. M. Birch, W. B. Dickson, M. H. Dickinson, *J. Exp. Biol.* **207**, 1063 (2004).
29. J. D. Anderson, *Fundamentals of Aerodynamics* (McGraw-Hill, Singapore, 1991).
30. R. Bomphrey, N. Lawson, G. Taylor, A. Thomas, *Exp. Fluids* **40**, 546 (2006).
31. D. A. Read, F. S. Hover, M. S. Triantafyllou, *J. Fluids Struct.* **17**, 163 (2003).
32. S. M. Swartz, M. S. Groves, H. D. Kim, W. R. Walsh, *J. Zool.* **239**, 357 (1996).
33. We thank R. von Busse and Y. Winter for their support. This work was supported by grants from the Swedish Research Council, the Swedish Foundation for International Cooperation in Research and Higher Education, the Knut and Alice Wallenberg Foundation, the Crafoord Foundation, the Magnus Bergvall Foundation, and the Royal Physiographical Society.

Supporting material

Materials and Methods

Bat training and wind tunnel setup

Three Pallas' long-tongued bats (*Glossophaga soricina*) were trained to fly at a feeder, providing honey-water, suspended from the ceiling of a low-turbulence wind tunnel (*S1*, Fig. S1). The wind tunnel airspeed was set to a constant velocity of 1 m/s (0.94 ± 0.05 m/s, mean $\pm$ SD, N = 25). Honey-water was administered to the feeder using a manually operated syringe. When not feeding, the bats roosted on a net in the wind tunnel settling chamber, 6 m upstream of the test-section. The bats fed spontaneously by flying downstream into the test-section, approaching the feeder via a U-turn from the downstream direction. The bats were individually identified using the position camera videos and the digital particle image velocimetry (DPIV) images (Fig. S2). The bats were clock-shifted 12 h so their active (dark) period coincided with daytime working hours. Since *G. soricina* is a tropical bat, the wind tunnel temperature was kept at 22-27 °C. Morphological data for the bats used in this study are shown in Table S1.

Digital Particle Image Velocimetry setup

A custom DPIV setup was used, using a double-pulsed laser (Quanta Ray PIV II, dual head Nd:YAG) running at a repetition rate of 10 Hz. The air was seeded by filling the wind tunnel with fog (particle size 1 µm). A CCD array camera (Redlake Megaplus II ES 4020) operating in binning mode (1024x1024 pixels) captured pair-wise images, separated by $\delta t = 200$ µs. The images were transferred via a digital interface (DVR Express 1.23, IO Industries) directly to a parallel SCSI disk array hosted on a PC. A Correlation Image Velocimetry (CIV) algorithm was used to calculate particle image displacements (*S2*). Uncertainty in estimation of the velocity field is approximately ±1% and in the vorticity field ±10% (*S3*).

Laser sheet positions

The velocity components *u*, *v* and *w* in streamwise (*x*), spanwise (*y*) and vertical (*z*) direction were measured in combinations of vertical-streamwise (Fig S1A) and vertical-spanwise (called cross-stream; Fig S1B) imaging planes.

The streamwise [*x-z*] image plane (Fig S1A) was used to investigate the Leading Edge Vortex (LEV) and Trailing Edge Vortex (TEV) strength and topology. The illumination plane was positioned vertical and parallel with the flow-direction, at the same streamwise location as the feeding bat. Using a mirror, the laser-sheet was directed from above and slightly from behind, so the air above the wing and the upper surface of the wing is illuminated, and a shadow is formed below the wing (Fig. S2). DPIV images were taken when the bat wing was positioned horizontally in the downstroke. At this wing position the wing does not block the DPIV image, the wingspan is at its maximum and the wing is two-thirds into the downstroke (67% ± 14%, N=9). The bats were repositioned with respect to the image plane in spanwise (*y*) direction by moving the feeder in the *y*-direction. A position camera filming from a downstream position was used to determine the exact location of the wing with respect to the image plane. The feeder is designed so the head of the bat was shielded from the laser light when feeding.

The cross-stream [*y-z*] plane was a vertical, span-wise laser sheet with approximately 3 mm thickness in the *x*-direction, positioned approximately 10 cm (~ 3 chord lengths) downstream from the wing trailing edge of a feeding bat (Fig S1B). The cross-stream image plane was used to determine the wing tip- and root-vortex strength and topology (*S4*).

The total data-set consisted of 121 cross-stream and 119 streamwise images at different spanwise locations. Combining the streamwise and cross-stream DPIV data enabled us to generate a three-dimensional picture of the aerodynamics around the wing of a slow flying bat.

Wing shape, attitude and movement

For the streamwise measurements the bat wing was visible in the DPIV image pairs: the wing profile was locally illuminated by the laser sheet (Fig. S2). By tracking the locally illuminated wing profile (using a custom-written manual tracking system), we were able to determine the local wing profile, attitude and movement parameters from the DPIV image pairs (Fig. S3).

The profile and attitude parameters are (Fig. S3A): the *camber line* function $z'=f(x')$, with the *x'*-axis parallel to the chord line (see Fig. S3A*)*; the chord length *c*; the maximum camber *camber$_{max}$*; the geometrical angle of attack α_{geo}. The movement parameters are (Fig. S3B): the velocity distribution over the wing $(u,v)=g,h(x'/c)$; the average effective wing velocity U_{eff} (which is vector sum of the forward velocity of the bat U_∞ and the average flapping velocity of the wing $\overline{U}=(\overline{u},\overline{v})$); the effective angle of attack α_{eff} (which is the angle between the effective wing velocity vector U_{eff}, and the mean chord line of the wing The results are shown in Fig. S5.

Masking and filtering

For the streamwise CIV calculations, a mask was created over the part of the images where the bat wing was blocking the laser, in order to reduce errors in the CIV calculations. In Fig. S4 the bat and background are visible at the location of the mask. The images were also filtered to remove parts of the bat and feeder in the background of the non-masked part of the image (Fig. S2), using a high-pass filter (medfilt2, Matlab 2006a, box-size: 15x15).

No-slip Boundary Conditions

The streamwise raw correlation data were post-processed by removing erroneous vectors and by applying a two-dimensional, patched smoothing thin-shell spline routine (*S5*). The local wing profile and wing velocity distribution as determined from the DPIV image pairs (Fig. S3) are used in the smoothing routine as a no-slip boundary condition (*S6*). The no-slip boundary condition consists of 20 velocity vectors evenly distributed over the wing profile: the (*u,v*) vectors in Fig. S3. The spline functions in independent patches covering the wing surface thus have the local wing velocity as their end condition and the interpolated velocity gradients close to the membrane are more likely to be correct, on average, even though the measurements do not resolve the boundary layer itself.

Circulation calculations

The circulation (Γ) was estimated by integrating the vorticity over all contiguous grid points above a threshold value 20% of the maximum vorticity in all the measurements. For the TEV circulation measurements a square search area was selected from the trailing edge of the wing to the upper right corner of the PIV image, for the LEV circulation the search area consisted of a 10x10 grid point box centered on the LEV center. The tip- and root-vortex circulation were calculated in a square search box of 20x20 grid points centered on the vortex centers. The results are shown in Fig. S5.

Kinematics

Kinematics measurements were performed to determine wing kinematics parameters, using two synchronized high-speed cameras (Redlake MotionScope PCI500, operating at 250 Hz sampling rate and shutter speed of 1/1250 s) to record the bats from side and dorsal views, respectively (Fig. S1). Infrared illumination was used to avoid disturbing the bats and to minimize interference with the DPIV measurements. The two-dimensional coordinates of the digitalized measurement points in each view were merged into a three-dimensional coordinate system using the linear transformation coefficients derived from a calibration cube (*S7*).

The kinematics data were used to derive the effective wing velocity at the horizontal wing position U_{eff}, the wingbeat frequency f and the wingbeat vertical tip-to-tip amplitude A. The variables were used for non-dimensionalizing the cross-stream wake data (e.g. Γ / $U_{eff} c$) and for calculating the Reynolds number $Re = U_{eff} c$ / ν and the Strouhal number $St = f A / U_{\infty}$.

Lift predictions

General lift-circulation correlation

The lift generated by a wing is related to the amount of circulation around the wing by $L^{'}(y) = \rho \, U_{eff}(y) \, \Gamma(y)$, where $L^{'}$ is the lift per unit wingspan, ρ is the air density, U_{eff} is the effective wing velocity and Γ is the circulation around the wing at a certain wingspan location y. The corresponding lift-coefficient is $C_l(y) = 2 \, \Gamma(y) / U_{eff}(y) \, c(y)$. In steady state conditions the circulation around the wing is called the bound circulation, but in cases with unsteady aerodynamics behavior the circulation around the wing can also include the LEV circulation (Γ_{LEV}).

LEV lift

In our setup we were able to measure the attached LEV circulation, which can be used to calculate the lift that could potentially be generated by the LEV (*S8*): $L^{'}_{LEV}(y) = \rho \, U_{eff}(y) \, \Gamma_{LEV}(y)$, and its corresponding LEV lift-coefficient $C_{LEV}(y) = 2 \, \Gamma_{LEV}(y) / U_{eff}(y) \, c(y)$.

Total lift

Kelvin's theorem states that, in a closed system and when viscous dissipation is negligible, the total sum of circulation is constant, meaning that the circulation around the wing is equal and opposite in sign to the circulation of its wake (*S9*). For our setup this means that, when assuming that the lift of the wing at the beginning of the downstroke is

zero, the lift generated by the wing is proportional to the circulation of the trailing edge vorticity (Γ_{TEV}) shed from the wing, written as $L'(y) = \rho\, U_{eff}(y)\, \Gamma_{TEV}(y)$ and $C_l(y) = 2\, \Gamma_{TEV}(y) \,/\, U_{eff}(y)\, c(y)$.

Table S1: Morphology of the three individual Pallas' long-tongued bats (*Glossophaga soricina*) used in this study. The symbols for the different individuals correspond to the data points in Fig. S5.

Bat	*#1 (◇)*	*#2 (▢)*	*#3 (▵)*	*Mean ± SD*
weight *W* [*g*]	10.6	10.6	10.4	**10.5 ± 0.1**
Wing span *b* [*cm*]	24.0	24.1	24.4	**24.2 ± 0.2**
Wing surface *S* [*cm²*]	100.7	96.3	80.4	**92.9 ± 10.7**
Mean chord length *c* [*cm*]	4.19	3.99	3.30	**3.85 ± 0.47**
Aspect ratio *AR* = *b²/S* [-]	5.73	6.03	7.39	**6.35 ± 0.88**
Wing loading *W/S* [*kg/m²*]	1.05	1.10	1.29	**1.14 ± 0.13**
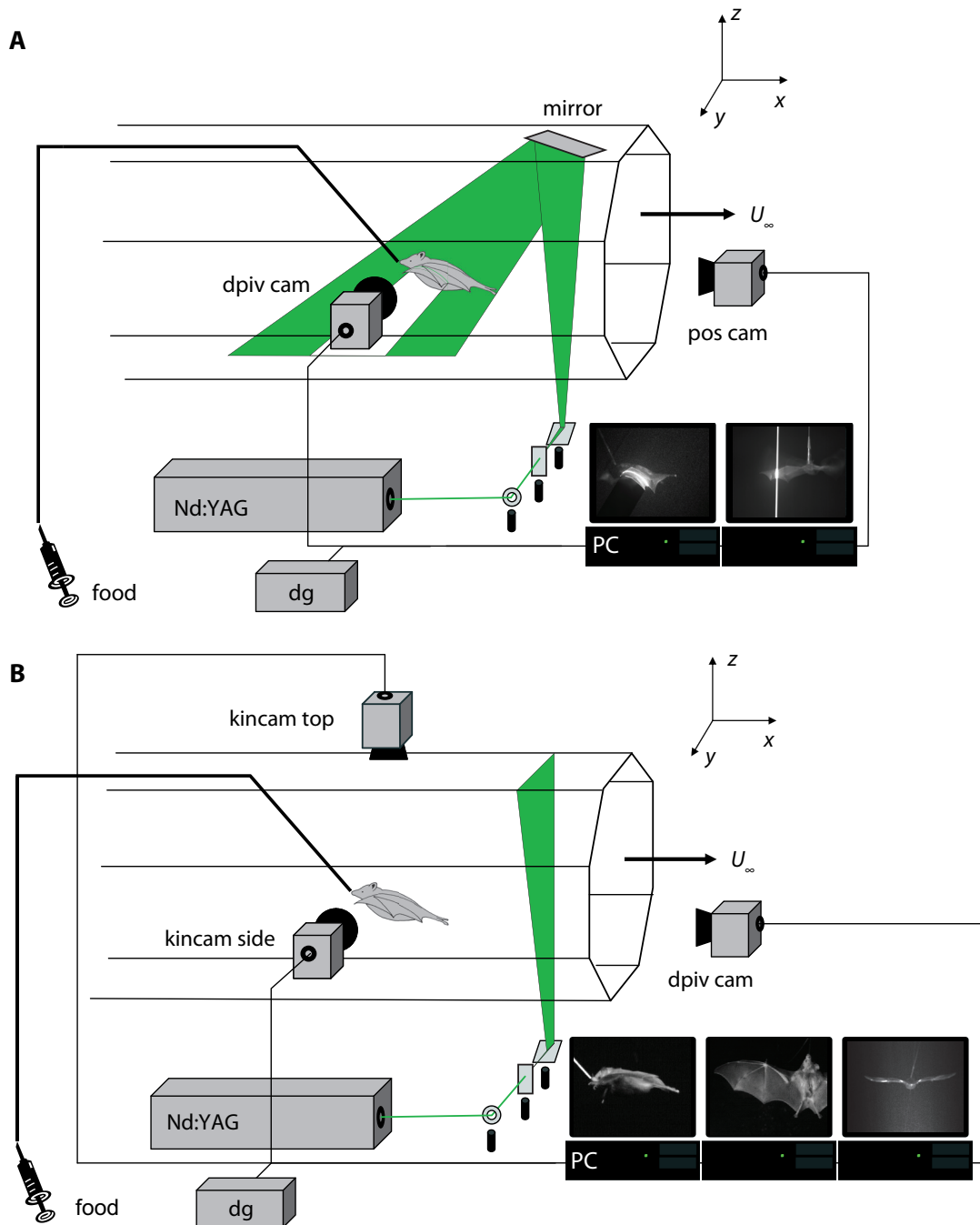
Figure S1: the experimental setup in the wind tunnel test section, studying the aerodynamics around the wing of a slow flying bat. The pulsed laser (*Nd:YAG*) generates a paired light sheet in the wind tunnel test section. Smoke particles illuminated by the light sheet are captured by the CCD array camera (*DPIV cam*) and stored on the hard disk (*PC*). In the streamwise setup (A), the laser light sheet is redirected by a mirror and positioned around the bats wing. A position camera (*pos cam*), located downstream, is used to determine the wing position with respect to the laser. In the cross-stream setup (B) two high speed cameras (*kincam*) are used to film the bats for kinematics analysis. The setup is synchronized by a digital delay generator (*dg*). The bat (silhouette) is flying at the feeder, which provides the bat with honey-water (*food*) through a syringe.
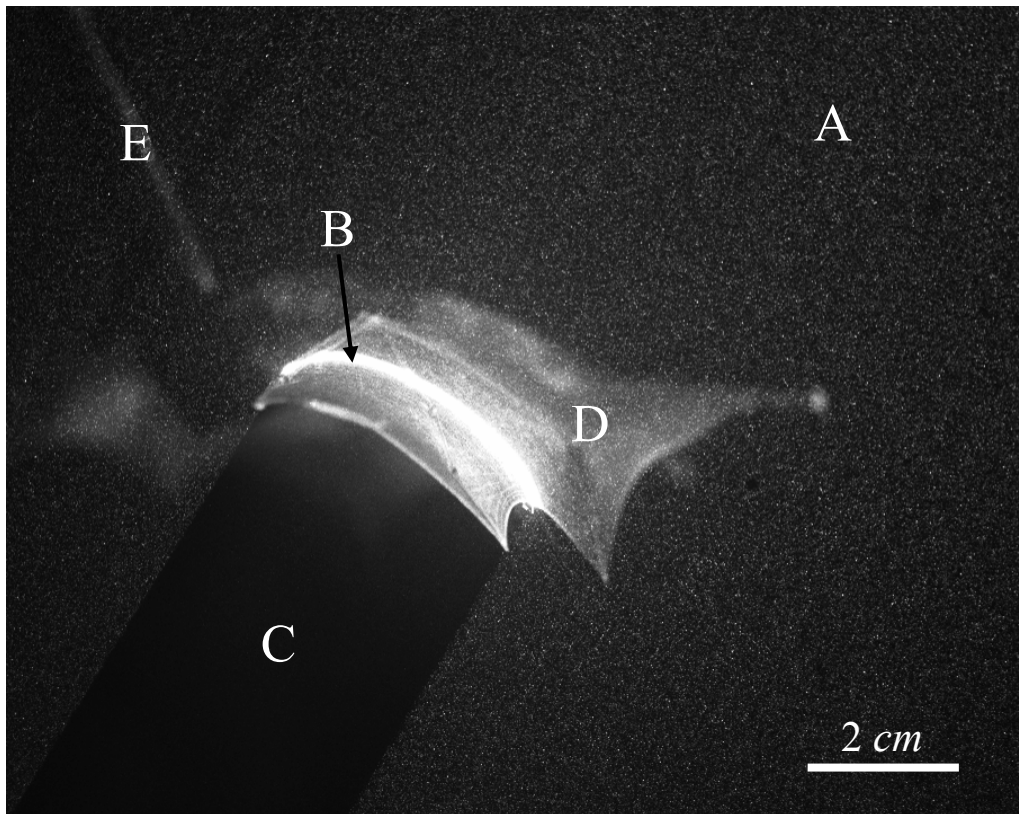
Figure S2: a raw side view DPIV image. In the images the illuminated seeding particles (smoke) are visible as white dots (A). The bat wing is illuminated locally by the laser (B), which enables us to track the wing profile and movement (see Fig. S3 for the tracking results). Below the wing a shadow is created (C), where the seeding is not illuminated. The bat (D) and feeder tube (E) are seen in the background, these are filtered out to improve the DPIV correlation. The air is moving from the left to the right and a scale bar (2 cm) is in the bottom right corner of the image.
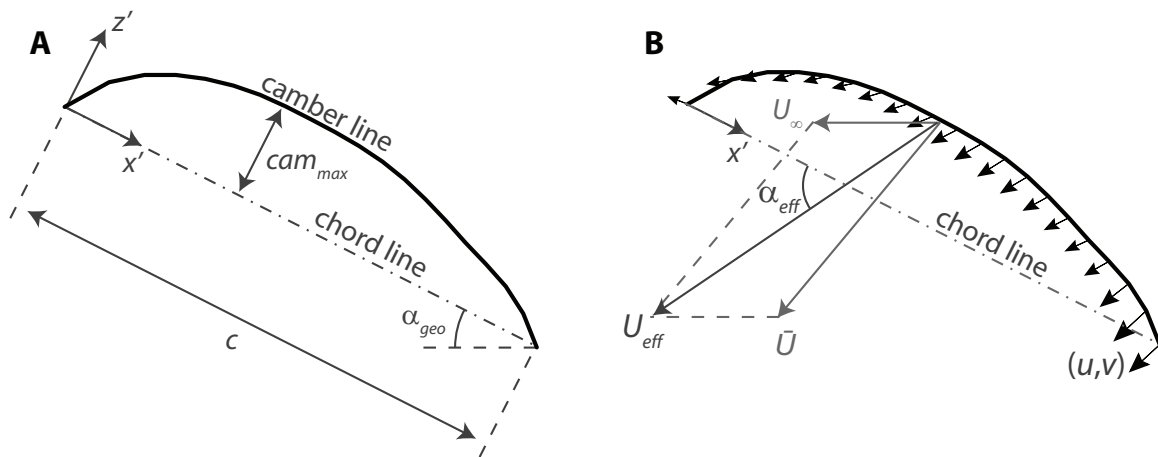
Figure S3: schematic image of the batwing profile from Fig. S2, with the different profile, attitude and movement parameters. In panel A the profile and attitude parameters are shown: the camber line function *z' = f(x')*, with the *x'*-axis parallel to the *chord line*; the wing chord length *c*; the maximum camber *cam$_{max}$*; and the geometrical angle-of-attack α_{geo}. In panel B the movement parameters are shown: The velocity distribution over the flapping wing *(u,v) = g,h(x')*; the effective wing velocity U_{eff}, which is a function of the forward velocity of the wing U_∞ and the average flapping velocity of the wing $\bar{U}$; the effective angle-of-attack α_{eff}, which is the angle between U_{eff} and the *chord line*.
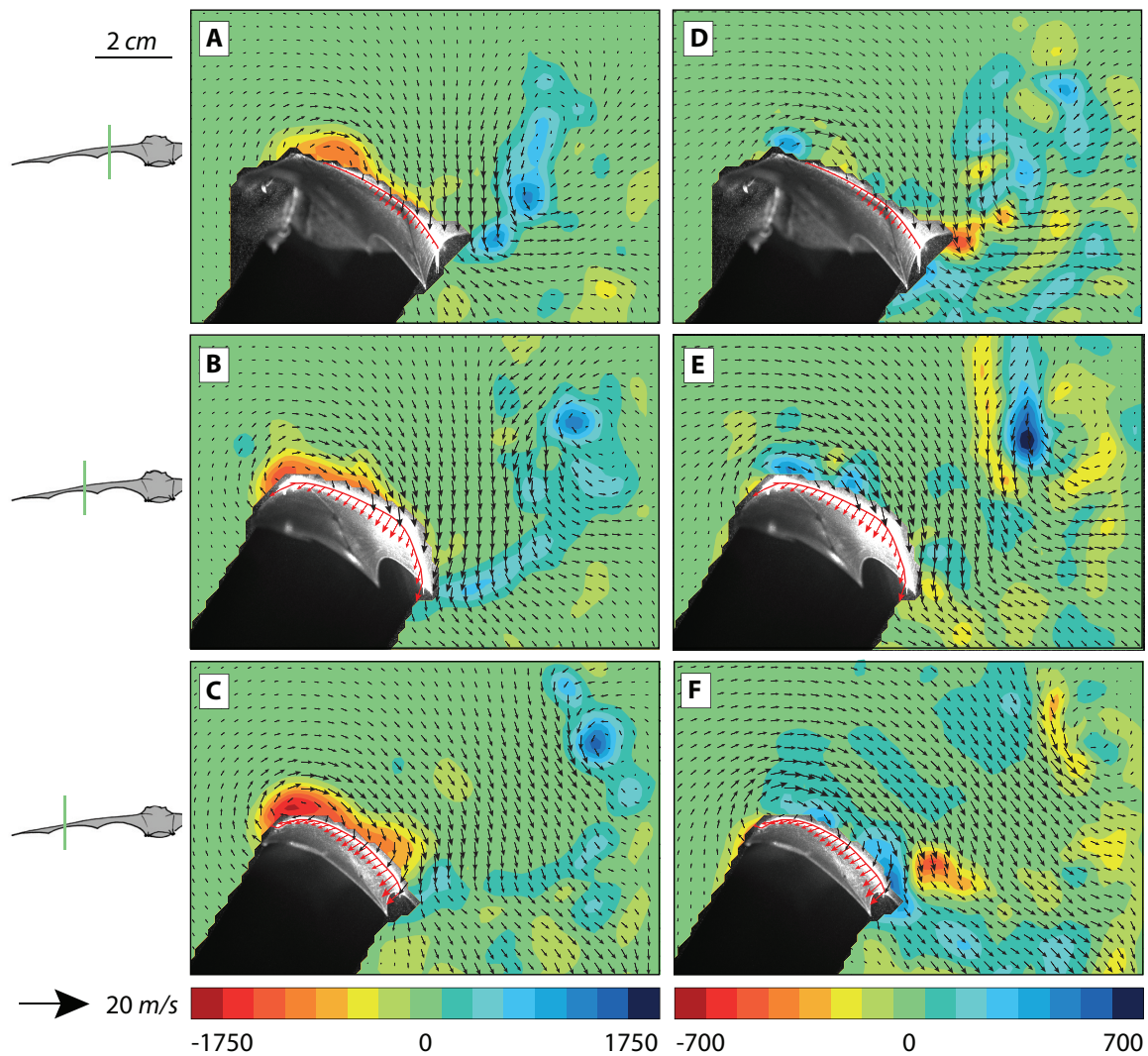
Figure S4. Velocity, vorticity (for A to C) and divergence (for D to F) fields around a bat wing at slow forward flight (1 m/s), when the wing is positioned horizontally in the downstroke. The spanwise wing-locations are indicated on the bat silhouettes to the left of the images, and are 33%, 50% and 65% of the semi-wingspan for the first, second and third row respectively. The flight direction is from the right to left. For A to C the vectors show the disturbance caused by the wing with the uniform mean flow (of 1 m/s) removed. The vectors in D to F show the total flow velocity including the uniform mean flow. The bat wing and its shadow in the DPIV laser sheet are visible in the images; the local wing profile and its relative motion are shown with a red curve and arrows. The vorticity and divergence field are scaled in equal steps according to the color bars below the images. The velocity vectors are scaled to the reference vector left of the color bar. The space scale bar is located left of image A.
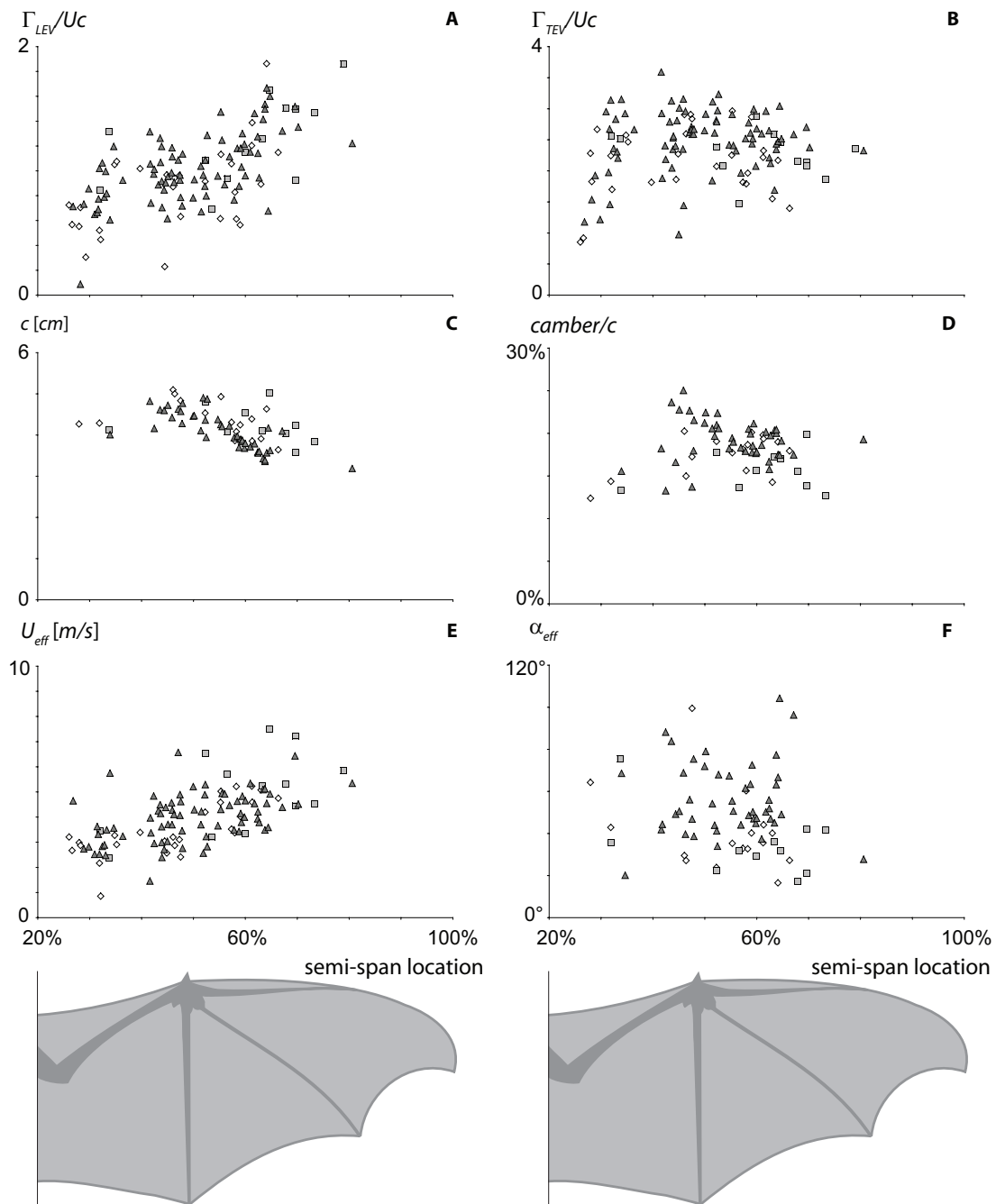
Figure S5. Aerodynamic and wing kinematic parameters at different semi-spanwise wing locations for three bats with the wing positioned horizontally in the downstroke. Panel A and B (top row) show the aerodynamic parameters: non-dimensional LEV circulation ($\Gamma_{LEV} / \overline{U}_{eff}\overline{c}$) and non-dimensional TEV circulation ($\Gamma_{TEV} / \overline{U}_{eff}\overline{c}$); panel C and D (middle row) show the wing profile parameters: the chord length of the wing (*c*) and the maximum camber in percentage of chord length (*camber/c*); panel E and F (bottom row) show the kinematics data: effective wing velocity (U_{eff}) and the effective angle of attack (α_{eff}). ◇ represent data for bat 1 from Table S1, ▫ represent bat 2 and ▵ represent bat 3.

References and Notes

S1. C. J. Pennycuick, T. Alerstam, A. Hedenstrom, *J. Exp. Biol.* **200**, 1441 (1997).

S2. A. M. Fincham, G. R. Spedding, *Exp. Fluids* **23**, 449 (1997).

S3. G. R. Spedding, A. Hedenström, M. Rosén, *Exp. Fluids* **34**, 291 (2003).

S4. A. Hedenstrom *et al.*, *Science* **316**, 894 (2007).

S5. G. R. Spedding, E. J. M. Rignot, *Exp. Fluids* **15**, 417 (1993).

S6. According to the no slip boundary condition, the air close to the wing surface has the same velocity as the wing. Therefore, in the DPIV calculations the velocity vectors of the air close to the wing are set to the local velocity of the wing.

S7. H. Hatze, *J. Biomechanics* **21**, 533 (1988).

S8. F.-O. Lehmann, *Naturwissenschaften* **91**, 101 (2004).

S9. J. D. Anderson, *Fundamentals of Aerodynamics*, (McGraw-Hill, Singapore, 1991).

Wing Twist Stabilizes Leading Edge Vortex in Slow-Flying Birds

Florian T. Muijres, L. Christoffer Johansson and Anders Hedenström

Department of Biology, Ecology Building, Lund University, SE-223 62 Lund, Sweden

To generate enough lift, most insects and hovering hummingbirds use a leading-edge vortex (LEV) during both the wing downstroke and upstroke. Avian hoverers, which only produce lift during the downstroke, have been proposed to also use some kind of unsteady aerodynamic mechanism to enhance lift. Using particle image velocimetry we show that an avian hoverer, the Pied flycatcher, uses attached LEVs to increase lift by 49%. This lift enhancement is three times higher than in hummingbirds to compensate for the inactive upstroke in flycatchers. The LEV strength is reduced towards the wing tip, which is caused by spanwise wing twist and upward bending of the primary feathers. We suggest this is a LEV stabilization mechanism preventing separation of the particularly strong LEVs in avian hovering.

Animals belonging to all extant flying taxa (*1-3*) and even some plant seeds (*4*) use leading edge vortices (LEVs) to enhance aerodynamic lift production during flight, making the LEV the most widely used unsteady aerodynamic mechanism (*5, 6*). The presence of LEVs has been demonstrated in two types of animal flight, being in hovering or slow flight with fast flapping wings (*5*) and in gliding flight with highly swept wings (*7*). The former is represented by insects (*1, 8, 9*), hummingbirds (*3*) and small nectar feeding bats (*2*). In this case, the wing typically operates at high angles-of-attack ($>20º$, *10*) to generate flow separation at the leading edge of the wing (*6*), and at low Reynolds numbers ($Re\sim10^2$-10^4, *10*) to enable the flow to re-attache to the wing. This results in the generation of a separation bubble, also known as an attached LEV (*5, 6*). For flapping wings, also a sufficiently low Rossby number ($Ro\sim1$) is required for LEV stability (*11*).

In gliding flight, LEVs have been found in a model resembling a gliding swift with highly swept wings and sharpened leading edges (*12*). The high wing sweep restricts growth of the LEV due to a high spanwise flow, similar to the mechanism found on sharp-edged delta wings (*6, 7*). One character that animal wings with LEVs have in common is that they all have a sharp leading edge compared to more conventional wing profiles. It is assumed that this sharp leading edge is of primary importance for generating the flow separation required for a LEV (*6*), although LEVs have been found on a mechanical flapper based on a conventional bird with rounded leading edge wings (*13*).

Insects, hummingbirds and small bats use normal hovering, where lift forces are generated throughout the complete wingbeat, i.e. during both downstroke and upstroke (*14*). Other than hummingbirds, most conventional birds use asymmetric or avian hovering
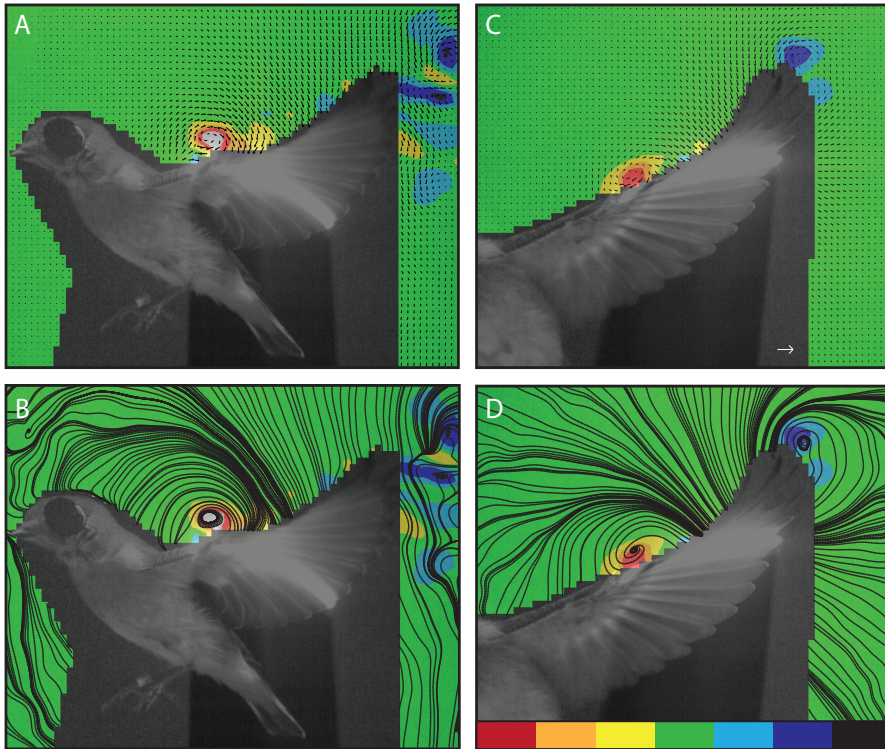
Fig. 1. Vorticity field, velocity vectors (top row) and instantaneous streamlines (bottom row) around the wing of a flycatcher flying at 1 m/s. The forward flight speed has been substracted from the velocity field. Panel **A** and **B** show the airflow on top of the arm wing part of the avian wing, while panel **C** and **D** show fluid motions above the hand wing part. The bird, wearing goggles to protect its eyes, is seen in the masked area of the PIV image. The velocity vectors are scaled relative to the white reference vector of 5 m/s in panel **C**, the vorticity field is scaled according to the color bar below panel **D**, which ranges from -1500 s^{-1} to 1500 s^{-1}.

where lift is mainly produced during the downstroke (*15, 16*). During the upstroke (recovery stroke), the wing is made inactive by folding the wing and spreading the primary feathers to minimize aerodynamic forces (*16, 17*). To compensate for the inactive upstroke, lift forces during the downstroke should be higher in avian hovering compared to normal hovering, and thus the use of some unsteady aerodynamic mechanism to enhance lift is also expected in avian hovering (*16*). However, most avian wings have a rounded leading edge at the inner wing section (arm wing), which would argue against the use of a LEV. The hand section of the wing does have a sharp leading edge (*15*).

Here, we study the flow dynamics around the wing of an avian hoverer with a typical avian wing, the Pied Flycatcher (*Ficedula hypoleuca*), flying freely in a wind tunnel at a speed of 1 m/s. At this flight speed the flap frequency f = 13.9 Hz, downstroke ratio R_{ds} = 0.50, downstroke based effective Re_{eff} = 1.2×10^4 (*10*), the downstroke based Strouhal number St_{ds} = 0.70 (*10, 18*), and the downstroke and wingtip based Rossby number Ro_{tip} = 2.8 (*10, 11*). The flycatcher is a small (14*g*) insectivorous passerine, which hunts insects mainly on the wing while hovering or flying slowly. We measured the flow dynamics using time-resolved stereoscopic Particle Image Velocemetry (PIV)

in two planes. A vertical streamwise plane directed at the wing of the flycatcher, and a transverse vertical plane in the near wake, 20cm (4-5*c*) downstream of the bird. From the streamwise PIV data we determined the flow dynamics closely above the wing surface, the corresponding effective wing velocity U_{eff} and the effective angle-of-attack α_{eff} of the local wing profile throughout the downstroke at 4 wing positions [two arm wing sections: inner wing and mid wing; two hand wing sections: outer wing and wing tip (Fig. S2)] for flycatcher 1 (Table S1) (*10*). Using the transverse near wake PIV data the wing tip vortex circulation is measured throughout the downstroke of the wing, for 28 wingbeats of two flycatchers (Table S1) (*10, 19*).

The vorticity field above the flycatcher wing shows that the flow separates from the wing at the leading edge, resulting in a patch of high vorticity above the wing near the leading edge. This patch of high vorticity is present at all the measured spanwise locations, but it is stronger at the arm wing (Fig. 1A and B) than at the hand wing section (Fig. 1C and D). The induced velocity field between the wing surface and the high vorticity patch show reversed or retrograde flow (Fig. 1A and Fig. 1C), and instantaneous streamlines, based on the velocity field, show the presence of a recirculation region at the patch of high vorticity

Fig. 2. (**A**) LEV circulation measurements and linear trend lines throughout the downstroke for the different wing sections (see legend in **A**). Visible in the background is the tip vortex circulation distribution ($\Gamma_{tip}(\tau)$) throughout the downstroke, consisting of the average distribution (dotted line), and the sliding 95% confidence interval (grey bar around dotted line). (**B**) average and standard error of the tip vortex circulation and of the LEV circulation at the four different wing sections. (**C**) average and standard error of the effective wing velocity for the four different wing sections. (**D**) average and standard error of the effective angle-of-attack of the local wing profile for the four different wing sections.
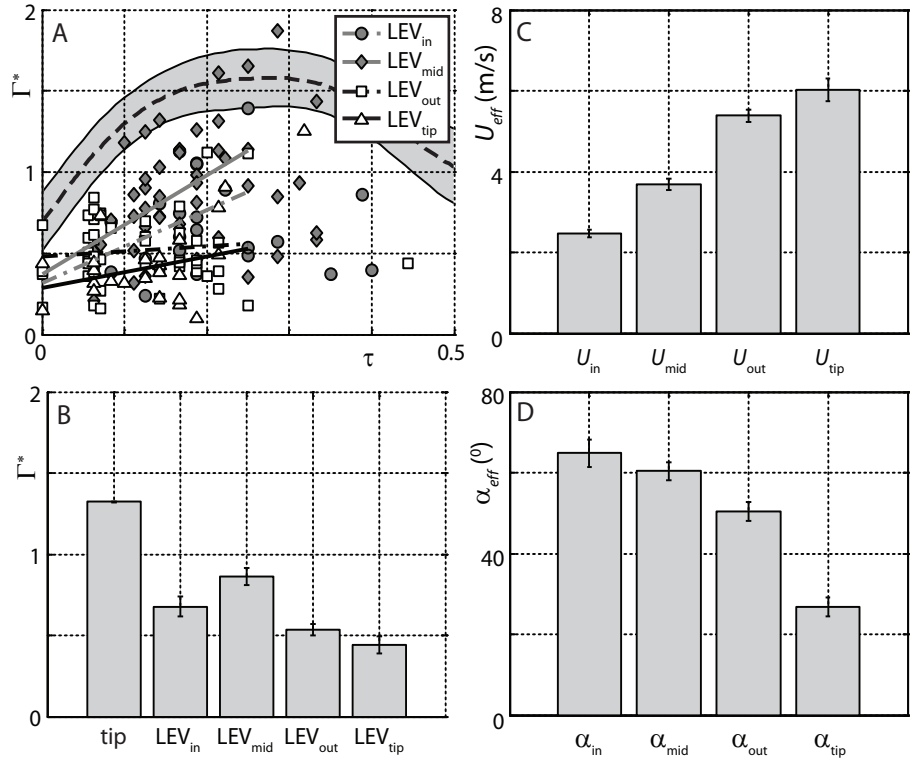
(Fig. 1B and Fig. 1D). All these flow characteristics are consistent with the presence of an attached LEV along the complete wingspan, despite the combination of high Ro_{tip} and high Re_{eff} in flycatchers (*11*).

The temporal circulation distribution throughout the downstroke was determined for the tip vortex and for the LEV at the four different spanwise locations (Fig. 2A) (*10*). All circulation measurements where normalized by $\Gamma^* = \Gamma / \overline{U}_{eff} c$, where $\overline{U}_{eff}$ =4.14 m/s is the average effective wing speed (Fig. 2C) and c is the average wing cord length (Table S1) (*10*). Γ^*_{LEV} increases with normalized time [$\tau = t / T$, where T is the wingbeat period], at least up to mid downstroke (τ =0.25), and the increase is stronger at the arm wing section than at the hand wing (Fig. 2A).

When assuming that the tip vortex circulation is equal to the average circulation about the wing (*20*), the lift coefficient of the wing is related to the normalized tipvortex circulation by $C_L = 2\,\Gamma^*_{tip}$ (*7, 10*). When assuming that the LEV circulation contributes to the total circulation around the wing, the increase in lift coefficient due to the presence of the LEV is $\Delta C_{LEV} = 2\,\Gamma^*_{LEV}$ (*2, 10*). The average normalized tipvortex circulation throughout the downstroke is $\overline{\Gamma}_{tip}$ =1.32 (Fig. 2B), which corresponds to a downstroke

average lift coefficient of $\overline{C}_L$ = 2.64, and a good lift to weight ratio of L/W = 0.96 [based on the effective span b_{eff} = 0.88b (*10*)]. $\overline{C}_L$ = 2.64 is significantly lower than the $\overline{C}_L$ = 5.3 predicted for hovering flycatchers based on kinematics analysis (*16*), but high enough to require the usage of a LEV (*21*). Subtracting $\overline{C}_{LEV}$ from $\overline{C}_L$ results in a non-LEV lift coefficient of $\overline{C}_{Lbound}$ =1.34. This value is consistent with steady-state aerodynamics (*21*), which indicates that the LEV could be the only high-lift mechanism required in slow flying flycatchers. Note that these are averages, meaning that maximum instantaneous C_L values can be expected to be higher.

Comparing Γ^*_{LEV} with Γ^*_{tip} (Fig. 2B) shows that the LEV contributes about 49% of the average lift production. This is lower than the 65% found in a model hawkmoth (*22*), slightly higher than the 45% found in a model fluitfly (*8*) and the 40% found in similarly sized bats (*2*), and much higher than the 16% in hummingbirds (*3*). The difference in LEV strength in the flycatcher compared to that in hummingbird could be due to the difference in upstroke function. The hummingbird generates 25% of its total lift during the upstroke (*23*), while the flycatcher has an inactive upstroke (*16*). To compensate for this inactive upstroke, the flycatcher needs to generate more lift during the downstroke, which can be achieved by

producing a stronger LEV. Since the use of a strong LEV is aerodynamically inefficient (*11*), this should result in lower aerodynamic flight efficiency in avian hovering compared to normal hovering.

For the flycatcher, the LEV strength was highest at the arm wing section and lowest near the wingtip (Fig. 2B and Fig. S2), which is different from the spanwise LEV distribution observed in all previously studied animals, where Γ^*_{LEV} consistently increases towards the wingtip (*1, 2, 9, 12, 24-26*). The fact that the strongest LEV was generated by the arm wing part, which has a relatively rounded leading edge, confirms that a sharp leading edge is not required for LEV generation in bird (*13*). At the middle wing section where Γ^*_{LEV} was highest (Fig. 2B) flycatchers have, similar to other passerines, an alula. Especially at low flight speeds, this alula is deflected (*15, 16*) and could therefore be involved in the onset of flow separation required for the LEV. It has been argued that the alula does the opposite and prevents separation (*27*), although this was proposed before LEVs in animal flight were discovered.

Based on the combination of Ro_{tip}=2.8 and Re_{eff} = 1.2×10^4 for slow-flying flycatchers one expects that the LEV should burst and separate near the wing tip (*11*), as has been found in a bird inspired mechanical flapper with a spanwise constant wing profile (*13*). Since neither LEV bursting nor LEV separation have been observed along the complete wingspan of the flycatcher, some LEV stabilizing mechanism is expected. The average α_{eff} decreases along the wing span for flycatchers, and α_{eff} is particularly low near the wing tip (Fig. 2D), which is correlated with the spanwise reduction of the LEV strength (Fig. 2B). The spanwise decrease in α_{eff} is achieved by a combination of two mechanisms. The animal twists the wing to reduce α_{eff} (*15*) and the primary and secondary feathers bend up passively and aero-elastically at the trailing edge of the wing (*16*). This mechanism is very similar to a mechanism found in a mechanical insect wing flapper, where lift forces could be controlled by modulating trailing edge flexibility, and which was assumed to be a result of controlling LEV strength (*28*). Therefore, we suggest that wing twist is an – at least partially aero-elastic – LEV stabilizing mechanism which reduces LEV strength near the wing tip to prevent bursting and separation of the particularly strong LEV in avian hovering.

References

(1) C. Ellington, C. van den Berg, A. Willmott, and A. Thomas, "Leading-edge vortices in insect flight," *Nature* **384**, 626 (1996).

(2) F. T. Muijres, L. C. Johansson, R. Barfield, M. Wolf, G. R. Spedding, and A. Hedenström, "Leading-Edge Vortex Improves Lift in Slow-Flying Bats," *Science* **319**, 1250 (2008).

(3) D. R. Warrick, B. W. Tobalske, and D. R. Powers, "Lift production in the hovering hummingbird," *Proceedings of the Royal Society B: Biological Sciences*, **276**, 3747 (2009).

(4) D. Lentink, W. B. Dickson, J. L. van Leeuwen, and M. H. Dickinson, "Leading-Edge Vortices Elevate Lift of Autorotating Plant Seeds," *Science* **324**, 1438 (2009).

(5) S. Sane, "The aerodynamics of insect flight," *J Exp Biol* **206**, 4191 (2003).

(6) F. Lehmann, "The mechanisms of lift enhancement in insect flight," *Naturwissenschaften* **91**, 101 (2004).

(7) J. D. Anderson, *Fundamentals of Aerodynamics* (McGraw-Hill, New York, 1991).

(8) M. Dickinson, F. Lehmann, and S. Sane, "Wing Rotation and the Aerodynamic Basis of Insect Flight," *Science* **284**, 1954 (1999).

(9) R. Srygley and A. Thomas, "Unconventional lift-generating mechanisms in free-flying butterflies," *Nature* **420**, 660 (2002).

(10) See supporting material.

(11) D. Lentink and M. H. Dickinson, "Rotational accelerations stabilize leading edge vortices on revolving fly wings," *Journal of Experimental Biology* **212**, 2705 (2009).

(12) J. Videler, E. Stamhuis, and G. Povel, "Leading-Edge Vortex Lifts Swifts," *Science* **306**, 1960 (2004).

(13) T. Y. Hubel and C. Tropea, "The importance of leading edge vortices under simplified flapping flight conditions at the size scale of birds," *J Exp Biol* **213**, 1930 (2010).

(14) D. E. Alexander, *Nature's Flyers: Birds, Insects, and the Biomechanics of Flight.* (JHU Press, Baltimore, 2004).

(15) U. M. Norberg, *Vertebrate flight: mechanics, physiology, ecology and evolution.* (Springer-Verlag, Berlin, 1990).

(16) U. M. Norberg, "Hovering flight in the pied flycatcher (*Ficedula hypoleuca*)," *Swimming and Flying in Nature* **2**, 869 (1975).

(17) R. A. Norberg, "Function of vane asymmetry and shaft curvature in bird flight feathers; inference on flight ability of Archaeopteryx," in *The beginnings of birds. International Archaeopteryx Conference in Eichstätt*, pp. 303–318 (1985).

(18) M. Wolf, L. C. Johansson, R. von Busse, Y. Winter, and A. Hedenström, "Kinematics of flight and the relationship to the vortex wake of a Pallas' long tongued bat (*Glossophaga soricina*)," *J Exp Biol* **213**, 2142 (2010).

(19) F. T. Muijres, L. C. Johansson, Y. Winter, and A. Hedenström, "Comparative aerodynamic performance of flapping flight in two bat species using time-resolved wake visualization," *Journal of The Royal Society Interface*, doi: 10.1098/rsif.2011.0015, 2011.

(20) P. G. Saffman, *Vortex dynamics*. (Cambridge University Press, Cambridge, 1995).

(21) E. Laitone, "Wind tunnel tests of wings at Reynolds numbers below 70 000," *Experiments in Fluids* **23**, 405 (1997).

(22) C. van den Berg and C. Ellington, "The vortex wake of a 'hovering' model hawkmoth," *Philosophical Transactions of the Royal Society B: Biological Sciences* **352**, 317 (1997).

(23) D. Warrick, B. Tobalske, and D. Powers, "Aerodynamics of the hovering hummingbird," *Nature* **435**, 1094 (2005).

(24) T. Maxworthy, "Experiments on the Weis-Fogh mechanism of lift generation by insects in hovering flight. Part 1. Dynamics of the 'fling'," *J. Fluid Mech.* **93**, 47 (1979).

(25) J. Birch and M. Dickinson, "Spanwise flow and the attachment of the leading-edge vortex on insect wings," *Nature* **412**, 729 (2001).

(26) R. Bomphrey, N. Lawson, N. Harding, G. Taylor, and A. Thomas, "The aerodynamics of *Manduca sexta*: digital particle image velocimetry analysis of the leading-edge vortex," *J Exp Biol* **208**, 1079 (2005).

(27) W. Nachtigall and B. Kempf, "Vergleichende Untersuchungen zur flugbiologischen Funktion des Daumenfittichs (Alula spuria) bei Vögeln," *Zeitschrift fur Vergleichende Physiologie* **71**, 326 (1971).

(28) L. Zhao, Q. Huang, X. Deng, and S. P. Sane, "Aerodynamic effects of flexibility in flapping wings," *Journal of The Royal Society Interface* **7**, 485 (2010).

Supporting material

Materials and methods

Experimental animals and wind tunnel

Three juvenile Pied Flycatchers (*Ficedula hypoleuca*) were captured and trained to fly freely in the Lund university low-turbulence wind tunnel (Fig. S1) (*S1*). For the experiments the wind tunnel was set to the required forward flight speed of $U = 1$ m/s. A flycatcher was allowed to perch on a hand held wooden perch in the test section of the wind tunnel. When the perch was lowered, the flycatcher would take off. If the bird would fly steadily in a position right above the perch, experimental measurements were performed, after which the perch was raised again to let the bird rest. If, on the other hand, the bird would fly away, the perch was not presented until the bird would return to the area above the perch. By this procedure the birds were conditioned to fly at the appropriate position.

The airflow around the birds was measured using Particle Image Velocimetry system (PIV) in two planes: a vertical transverse plane (*y-z*) in the near wake of the animal (±20cm, 4-5 wing cords downstream); and a vertical streamwise plane (*x-z*) positioned above the wing, called the on-wing setup (Fig. S1). For the transverse experiments, only two out of the three individuals would perform the steady flights, while only one would fly steadily during the on-wing experiments. Therefore, all transverse data were collected from flycatcher 1 and flycatcher 2, while all on-wing data were collected from flycatcher 1 (Table S1). Before and after each experimental session

the weight of the animal was measured using an electric balance. These and other morphological data for the experimental animals are shown in Table S1. During the on-wing experiments the flycatcher was provided with a custom-made pair of goggles, made of red filter material to protect the eyes from stray light from the laser. After all the experiments were finished, the birds were released back into the wild.

Particle Image Velocimetry setup

A high-speed (200Hz) stereoscopic Particle Image Velocimetry system (PIV) was used for airflow measurements (Fig. S1). The PIV system consists of two synchronized, double frame, CMOS-cameras (HighSpeedStar3; 1024×1024 pixels) in stereo setup and a 200 Hz double pulsed 50 mJ Laser (Litron LPY732 series, Nd:YAG, 532 nm), controlled by the Lavision PIV software package DaVis (LaVision, DaVis 7.2.2.110).

For the PIV experiments the air was seeded by filling the wind tunnel with fog (particle size 1µm). These fog particles were illuminated by the laser sheet. For each measurement, 100 pairwise images (1/2 s at 200 Hz, image size ~20x20cm and $dt = 200$-270 µs) of the illuminated particles were recorded by each CMOS-camera and stored on a computer. Simultaneously, a high-speed (250 Hz) digital video camera captured the animal to monitor its movement. For the transverse near wake PIV measurements, the laser sheet was positioned in the {*y-z*} plane, and for the on-wing measurements the laser sheet was orientated in the {*x-z*} plane (Fig. S1).
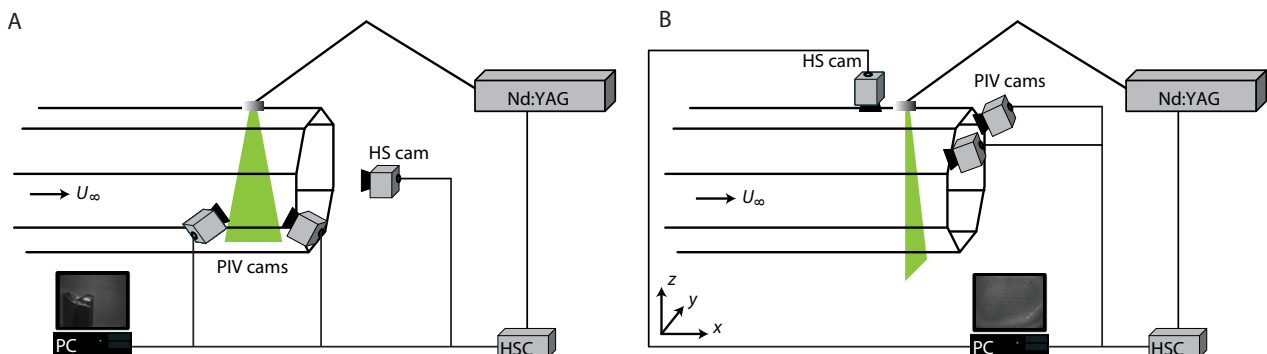
Fig. S1. experimental setup consisting of a low-speed low-turbulence wind tunnel, a high-speed stereo PIV setup and a high-speed video camera (HS cam). For the on-wing experiments (A), the laser sheet is positioned in a streamwise orientation (in x-z plane). For the near wake experiments (B), the laser sheet was positioned in a transverse orientation (in y-z plane). The laser (Nd:YAG) and PIV cameras (PIV cams) were synchronized at 200 Hz using a high-speed control box (HSC). The trigger signal of the PIV system was used to also trigger the video camera (HS cam).

Table S1. Morphological data the flycatchers used in the experiment, consisting of Mass M, wing span b, wing surface area S, mean cord length $c = S/b$, aspect ratio based on the complete wingspan $AR = b^2/S$, aspect ratio based on the span of a single wing $AR_{wing} = b_{wing}^{2}/S_{wing}$ and wing loading $Q = Mg/S$, with g the gravitational constant.

individual	M (kg)	b (m)	S (m²)	c (m)	AR (-)	AR_{wing} (-)	Q (N/m²)
Flycatcher 1	0.0148	0.235	0.0106	0.045	5.2	2.3	13.7
Flycatcher 2	0.0141	0.235	0.0105	0.045	5.3	2.3	13.2

Particle Image Velocimetry analysis

For the on-wing PIV analysis, the useful image pairs were selected manually. These were the images where the fluid movements above the wing was not blocked by the wing, and where the animal was not seen in the background. The selected on-wing PIV images were pre-processed to reduce errors in the PIV calculations. Background noise was filtered out using a high-pass filter (medfilt2, Matlab 7.7.0.471, R2008b, box-size 15x15), and a mask was created over the part of the image where the bird was visible.

The PIV images were analysed using the Lavision PIV software package DaVis (LaVision, DaVis 7.2.2.110). For the transverse data, we used a multi-pass normalized stereo cross-correlation (64x64 and 32x32, 50% overlap, Whittaker reconstruction), followed by a smoothing {3x3}. For the on-wing data, we used a multi-pass normalized cross-correlation (32x32 and 16x16, 50% overlap, Whittaker reconstruction), followed by a smoothing {3x3}. The resulting velocity fields (on-wing: $\{u, w\}$; transverse: $\{u, v, w\}$) were imported into a custom-made PIV analysis program (Matlab 7.7.0.471, R2008b), in which the vorticity field was calculated (transverse: streamwise vorticity ω_x; on-wing: spanwise vorticity ω_y), and vortex circulation could be calculated.

Vortex circulation was calculated by selecting manually a patch of high vorticity. Within this patch, vorticity was integrated over all the PIV node points with vorticity values above the threshold $|\omega|_{min}$ (transverse: $|\omega|_{min} = 60$ s⁻¹; on-wing: $|\omega|_{min} = 100$ s⁻¹). The vorticity distribution outside the $|\omega|_{min}$ iso-line is assumed to have a normal Gaussian distribution, so the total circulation of a vortex was estimated as $\Gamma = (1 + |\omega|_{min} /|\omega|_{max}) \Gamma_{measured}$, where $\Gamma_{measured}$ is the measured circulation above the threshold $|\omega|_{min}$, and $|\omega|_{max}$ is the maximum absolute vorticity in the vortex area (*S2*).

Tip vortex distribution

The transverse vorticity fields were used to determine the circulation distribution of the tip vortex throughout the downstroke. For each PIV frame within a data-set the tip vortex was identified, and its circulation $\{\omega_x\}$ and position $\{y,z\}$ was measured. Based on the vertical distribution of the tip vortex, each PIV frame was given a normalized time-stamp $\tau = t/T$, where t is the time within the wingbeat and T is the wingbeat period. The PIV frame with the highest location of the tip vortex, representing the start of the downstroke, was given time stamp $\tau = 0$, and the PIV frame with the lowest location of the tip vortex represents the end of the downstroke ($\tau = R_{ds} = 0.5$, where R_{ds} is the downstroke ratio). For the PIV frame in between $\tau = 0$ and $\tau = 0.5$, the time stamp was linearly interpolated.

The average temporal distribution throughout the downstroke of the tip vortex circulation $\Gamma_{tip}(\tau)$ (Fig. 2A) was determined by fitting a smoothing spline (Matlab, csaps smoothing parameter = 1-10⁻³) through the $\Gamma_{tip}(\tau)$ data points for all the measured wingbeats. The relative deviation of the data points from the average spline was estimated by calculating a sliding 95% confidence interval from a sliding window of 28 local data points, where 28 is the amount of wingbeats analyzed (*S3*). The average tip vortex circulation within the downstroke $\overline{\Gamma}_{tip}$ (Fig. 2B) was determined as the average of all measured $\Gamma_{tip}(\tau)$ values.

Leading edge vortex distributions

The on-wing vorticity fields were used to determine the LEV circulation distribution along the span and throughout the downstroke. For each PIV frame with a visible LEV its circulation Γ_{LEV} was measured. This was mostly for the PIV frames belonging to the first half of the downstroke of the wing, because the PIV images for the second half of the downstroke were often not suitable for analysis, since or the bird was visible in the background or the upwards bended tip
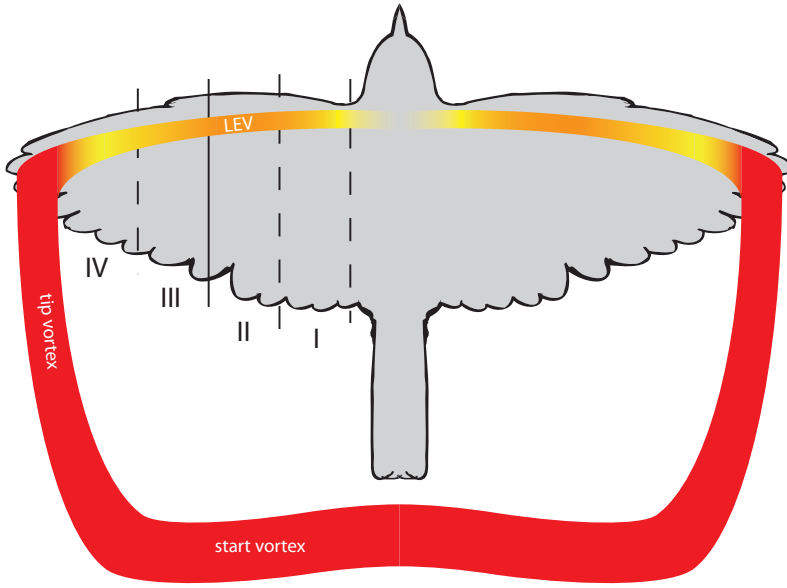
Fig. S2. cartoon of the top view of a slow flying flycatcher during mid downstroke. The four wing sections as used in the on-wing PIV analysis are indicated as (I) inner wing, (II) mid wing, (III) outer wing, and (IV) wing tip. I and II are arm wing sections which have a conventional rounded leading edge, and III and IV are hand wing sections which have a sharp leading edge. The primary vortex structures at mid downstroke are shown in color, where red equals high absolute circulation and yellow equals low circulation. The vortex structure consists of a start vortex, two tip vortices and a LEV above each wing. The LEV is strongest at arm section II and weakest at hand section IV.

feathers would block the area above the wing.

Based on the wing movement, which was visible in the PIV images, the normalized time stamp τ for each PIV frame was determined by identifying the PIV frame with the highest wingtip position ($\tau = 0$), and the PIV frame with the lowest wingtip position ($\tau = R_{ds} = 0.5$). For the PIV frame in between $\tau = 0$ and $\tau = 0.5$, the time stamp was linearly interpolated. Each PIV frame with a visible LEV was given a spanwise location, defined as the location where the laser hits the leading edge of the wing. Four different locations were discriminated, two arm wing sections (inner wing and mid wing) and two hand wing sections (outer wing and wing tip), see Fig. S2. For each wing section, the temporal variation of the LEV circulation $\Gamma_{LEV}(\tau)$ was estimated using a linear polynomial (polyfit, Matlab). Since the resolution of $\Gamma_{LEV}(\tau)$ measurements was low for $\tau > 0.25$, the linear polynomial was restricted to the first half of the downstroke.

Effective wing velocity and effective angle-of-attack

For each on-wing PIV frame where a LEV was present, the position and in-plane wing velocity of the local wing profile was estimated using DaVis (LaVision, DaVis 7.2.2.110). Since the images were overexposed at the area where the PIV laser hits the wing, the local wing profile was identified by masking the whole image, except for the overexposed area. For the masked image, we used a multi-pass normalized stereo cross-correlation (32x32 and 16x16, 50% overlap, Whittaker reconstruction) to determine the in-plane velocity distribution along the wing profile. U_{eff} was determined as the vector sum of the average in-plane wing velocity vector $\{u,w\}$ and the forward flight speed U. The leading and trailing edge of the wing was determined as the location of the velocity vector with the highest and lowest x-value, respectively. The local wing cord was defined as a straight line between leading edge and trailing edge. The effective angle-of-attack α_{eff} was determined as the angle between the U_{eff} vector and the cord line (*S4*). Note that induced air movements are ignored.

Based on the average U_{eff} for all measurements, the effective Reynolds number and downstroke based Strouhal number (*S5*) were determined as

$$Re_{eff} = U_{eff}c/\nu$$

and

$$St_{ds} = \frac{w_{ds}/2}{(U + u_{ds})}$$

where c is the mean wing cord length (Table S1), ν is the kinematic viscosity of air, w_{ds} is the downstroke average vertical wing velocity component, and u_{ds} is the downstroke average horizontal wing velocity component. The wingtip based Rossby number is determined by (*S6*)

$$Ro_{tip} = \sqrt{\left(\frac{1}{2St_{ds}}\right)^2 + 1}\ AR_{wing}$$

where AR_{wing} is the aspect ratio of a single wing (Table S1).

Lift force estimates

The lift force produced by a wing is related to the amount of circulation about the wing (Γ) by $L = \rho\,U\,b\,\Gamma$, where ρ is the air density, U is the wing speed, and b is the wing span ($S7$). The corresponding lift coefficient is $C_L = 2\,\Gamma/Uc$, where c is the mean cord length of the wing.

Kelvin's theorem states that, in a closed system and when viscous dissipation is negligible, the total sum of circulation is constant ($S7$). So, the circulation around a wing Γ has the same strength but opposite sign as the circulation in its wake. In inviscid vortex dynamics, a vortex must terminate at a solid surface ($S8$), so the wake circulation is connected to the wing. When assuming that this streamwise vorticity rolls up completely into the tip vortices, the tip vortex circulation at τ can be assumed equal to the total circulation around the wing at τ, and the $\Gamma_{tip}(\tau)$ distribution can be used to estimate $C_L(\tau)$.

The lift-to-weight ratio is estimated by ($S3$)

$$L/W = R_{ds}\,\rho\,\overline{U}_{eff}\,\overline{b}_{eff}\,\overline{\Gamma}_{tip}/M\,g$$

where R_{ds} is the downstroke ratio, $\overline{U}_{eff}$ is the average effective wing velocity within the downstroke, $\overline{b}_{eff}$ is the downstroke average horizontal wingspan of the flapping wing, $\overline{\Gamma}_{tip}$ is the downstroke average tip vortex circulation, and $W=Mg$ is the weight of the flycatcher.

If a wing has an attached LEV, the total circulation around the wing is equal to the sum of the bound circulation (Γ_{bound}) and the LEV circulation (Γ_{LEV}). Thus, the increase in C_L due to the presence of the LEV can be estimated by $\Delta C_{LEV} = 2\,\Gamma_{LEV}/U_{eff}c$ ($S4$).

References

(*S1*) C. J. Pennycuick, T. Alerstam, and A. Hedenström, "A new low-turbulence wind tunnel for bird flight experiments at Lund University, Sweden," *J Exp Biol* **200**, 1441 (1997).

(*S2*) G. R. Spedding, M. Rosen, and A. Hedenström, "A family of vortex wakes generated by a thrush nightingale in free flight in a wind tunnel over its entire natural range of flight speeds," *J Exp Biol* **206**, 2313 (2003).

(*S3*) F. T. Muijres, L. C. Johansson, Y. Winter, and A. Hedenström, "Comparative aerodynamic performance of flapping flight in two bat species using time-resolved wake visualization," *Journal of The Royal Society Interface*, doi: 10.1098/rsif.2011.0015, 2011.

(*S4*) F. Muijres, L. Johansson, R. Barfield, M. Wolf, G. Spedding, and A. Hedenström, "Leading-Edge Vortex Improves Lift in Slow-Flying Bats," *Science* **319**, 1250 (2008).

(*S5*) M. Wolf, L. C. Johansson, R. von Busse, Y. Winter, and A. Hedenström, "Kinematics of flight and the relationship to the vortex wake of a Pallas' long tongued bat (Glossophaga soricina)," *J Exp Biol* **213**, 2142 (2010).

(*S6*) T. Y. Hubel and C. Tropea, "The importance of leading edge vortices under simplified flapping flight conditions at the size scale of birds," *J Exp Biol* **213**, 1930 (2010).

(*S7*) J. D. Anderson, *Fundamentals of Aerodynamics*. (McGraw-Hill, New York, 1991).

(*S8*) P. G. Saffman, *Vortex dynamics*. (Cambridge University Press, Cambridge, 1995).

RESEARCH ARTICLE

High-speed stereo DPIV measurement of wakes of two bat species flying freely in a wind tunnel

**Anders Hedenström · F. T. Muijres · R. von Busse ·
L. C. Johansson · Y. Winter · G. R. Spedding**

Abstract Previous studies on wake flow visualization of live animals using DPIV have typically used low repetition rate lasers and 2D imaging. Repetition rates of around 10 Hz allow ∼1 image per wingbeat in small birds and bats, and even fewer in insects. To accumulate data representing an entire wingbeat therefore requires the stitching-together of images captured from different wingbeats, and at different locations along the wing span for 3D-construction of wake topologies. A 200 Hz stereo DPIV system has recently been installed in the Lund University wind tunnel facility and the high-frame rate can be used to calculate all three velocity components in a cube, whose third dimension is constructed using the Taylor hypothesis. We studied two bat species differing in body size, *Glossophaga soricina* and *Leptonycteris curasoa*. Both species shed a tip vortex during the downstroke that was present well into the upstroke, and a vortex of opposite sign to the tip vortex was shed from the wing root. At the transition between upstroke/downstroke, a vortex loop was shed from each wing, inducing an upwash. Vorticity iso-surfaces confirmed the overall wake topology derived in a previous study. The measured dimensionless circulation, Γ/Uc, which is proportional to a wing section lift coefficient, suggests that unsteady phenomena play a role in the aerodynamics of both species.

A. Hedenström (✉) · F. T. Muijres · L. C. Johansson
Department of Theoretical Ecology, Lund University,
Ecology Building, 223 62 Lund, Sweden
e-mail: Anders.Hedenstrom@teorekol.lu.se

R. von Busse · Y. Winter
Department of Biology, Bielefeld University,
33501 Bielefeld, Germany

G. R. Spedding
Department of Aerospace and Mechanical Engineering,
University of Southern California, Los Angeles,
CA 90089-1191, USA

Present Address:
G. R. Spedding
Department of Mechanical and Aeronautical Engineering,
University of Pretoria, Pretoria 0002, South Africa

1 Introduction

Flapping flight in vertebrates has resisted simple analysis, because of the time-varying shape of elastic actuators and their complex interaction with the surrounding fluid. Early models therefore discarded these facts altogether by representing the animal, bird or bat, by mass and wing span alone (Pennycuick 1968, 1975; Norberg 1990). Even though this approach allows predictions for cruising flight performance (Pennycuick 1989; Hedenström 2002), it does not capture any details of the kinematics and associated time-varying force production and cannot be used to predict performance during maneuvering or hovering flight. On the other hand, the early vortex wake theory of bird flight was based upon a minimum of kinematic details, even if the assumptions about the wake geometry itself were more realistic than the actuator disk and momentum jet models (Rayner 1979a, b). Experiments originally focused upon kinematic analyses of wing motions (Brown 1948; Norberg 1976; Aldridge 1986). Eventually, with improved experimental techniques for quantitative wake flow visualization (Spedding et al. 1984; Spedding 1987a, b), the conceptual image of the wake structure began to improve (if not always simplify), now that it was based on actual evidence. Digital particle image velocimetry (DPIV) techniques have been applied to freely flying birds in wind

tunnels (Spedding et al. 2003a, b; Warrick et al. 2005; Hedenström and Spedding 2008) to yield more refined models of the wake geometry and its variation with forward flight speed, wing geometry and kinematics. The same techniques have also been applied to the small Glossophagine bats, and reveal some notable differences in wake geometry compared with birds (Hedenström et al. 2007).

To date, quantitative wake data of flying vertebrates have come from rather low repetition rates lasers (5–10 Hz), and the three-dimensional wake structure over one wingbeat cycle is assembled from large numbers of separate images, obtained from large numbers of separate wingbeats. Previous studies have also derived primarily from stacks (in space or time) of 2D data, with two out of three velocity components available in any one plane. Nevertheless, the use of DPIV methods has considerably strengthened our understanding of wake topology and aerodynamics of vertebrate flapping flight in recent years (e.g. Hedenström and Spedding 2008), and continued rapid technological advances are likely to propel the scientific progress further still (see Spedding and Hedenström 2009, this issue). Here we report on the first high-speed stereo-3D DPIV measurements, and thus 3D velocity profiles, of bat flight in the Lund University wind tunnel using two species of Glossophagine bats. The main objective was to investigate whether the wake topology derived from high-speed wake sampling conforms to previous conclusions derived from low-speed sampling (Hedenström et al. 2007). A second objective was to compare the scaling of wake properties from two species of bats with different body weight, aspect ratio and wing loading.

2 Materials and methods

2.1 Experimental animals

Two species of nectarivorous bats, *Glossophaga soricina* and *Leptonycteris curasoae*, were trained to fly in front of a thin metal tube (feeder) providing honey water in the test section of a low-turbulence wind tunnel. For these experiments, two individuals each of *G. soricina* and *L. curasoae* were used. The morphology of the four bats is summarised in Table 1. Wing span and wing area were measured from top-view images obtained at flight speeds 5–6 m/s captured, when the wings are positioned horizontally during the downstroke. At this flight speed, the body angle is near horizontal. Wing span and wing area were measured using ImageJ (http://rsb.info.nih.gov/ij/) with the length of the radius as reference length (Table 1). Body mass was measured with an electronic balance before and after each experimental session, and the mean values are shown in Table 1.

Since bats are nocturnal and mainly active in the dark, they were clock-shifted by 12 h, so their active feeding period coincided with researchers' working schedule. Before experiments, the bats were released into the wind tunnel, where they roosted on a net inside the settling chamber 6 m upstream from the test section. When a bat decided to feed, it would fly with the wind towards the test section, increasing the speed between the settling chamber and the test section through the contraction, and would then make a U-turn inside the test section to approach the feeder from the downstream direction. The requirement of making this U-turn inside the test section area (1.22×1.08 m) limits the maximum flight speed range that can be studied to approximately 7–8 m/s.

2.2 Wind tunnel

The Lund University wind tunnel is a closed-loop, low-speed, low-turbulence wind tunnel crafted for studies of animal flight. The overall design and baseline characteristics are described in Pennycuick et al. (1997). The background turbulence is about 0.03% (Spedding et al. 2009), which makes this tunnel suitable for repeatable quantitative measurements at the moderate values of wing chord-based Reynolds number that are characteristic of small birds and bats (see below). All airspeeds (U) refer to the equivalent airspeed defined as

$$U_{\mathrm{eq}} = \sqrt{2q/\rho_0},$$

Table 1 Morphological properties of the four bats used in this study, body mass (m), wing span (b), wing area (S), mean wing chord (c), aspect ratio (AR $= b^2/S$), wing loading ($Q = mg/S$), and f is wing beat frequency

Bat	m (kg)	Femur length (mm)[a]	Wing length (m)	b (m)	S (m²)	c (m)	AR	Q (N)	f (Hz)
Glossophaga soricina, male (#1)	0.0101	34.6	0.101	0.233	0.00879	0.038	6.2	11.3	14.9
Glossophaga soricina, female (#5)	0.0095	34.9	0.097	0.230	0.00860	0.037	6.2	10.9	14.9
Leptonycteris curasoae, male (#97)	0.0216	50.3	0.149	0.335	0.01576	0.047	7.1	13.4	10.4
Leptonycteris curasoae, female (#18)	0.0236	51.0	0.144	0.323	0.01529	0.047	6.8	15.1	9.9

[a] Used as reference length on images for estimating wing length, wing span and wing area

where ρ_0 is the assumed air density at sea level in the International Standard Atmosphere (1.225 kg/m^3) and q ($=\rho U^2/2$) is the dynamic pressure at the measured air density during an experiment. During this study, ρ varied between 1.16 and 1.20 kg/m^3, and the temperature was 19–24°C. The bats were studied at forward flight speeds 1–7 m/s, but the main results in this paper are based on observations at 4 m/s. The Reynolds number based on airspeed ($Re = Uc/v$, where c is the mean chord length of the wing and v is the kinematic viscosity) ranged from $Re = 0.26–1.81 \times 10^4$ in *G. soricina* to $Re = 0.32–2.27 \times 10^4$ in *L. curasoae*. At $U = 4$ m/s, the speed for which we present most of the data in this paper, $Re = 1.03 \times 10^4$ and 1.30×10^4, respectively. This difference in Re is aerodynamically not significant. The bats are small in comparison with the test section [wing span (b)/tunnel diameter (B): $b/B < 0.28$) and so interactions with the side walls are ignored.

2.3 Stereo DPIV

The flow field was measured over an approximately 20×20 cm^2 area using two CMOS-cameras (High-SpeedStar3; $1,024 \times 1,024$ pixels) and frame grabber PCI boards in the host computer. The cameras were equipped with 60 mm lenses (Micro Nikkor, f2.8) on Scheimpflug mounts. Two alignments of the light sheet were used: (1) the vertical [xz] plane is aligned with the free-stream, with the cameras mounted on opposite sides outside the test section (Fig. 1a), and (2) the [yz] plane is normal to U, and the cameras are mounted in the open part of the test section (Fig. 1b), viewing obliquely from above and behind onto

Fig. 1 Experimental set-up for visualizing wakes of bats flying in the Lund University wind tunnel. The pulsed laser (Nd:YAG) generates a light sheet in the wind tunnel test section. Image pairs of densely-distributed fog particles, illuminated by the light sheet, are captured by the two CMOS cameras (DPIV cam) and stored on the host PC. The light sheet is positioned by the use of an optical arm and either aligned parallel to U (**a**) or perpendicular to U (**b**). The position camera monitors the flight behaviour and position of the bat with respect to the light sheet. The triggering of image acquisition and laser pulses is synchronized by a high speed controller box (HSC). Honey water is provided through a syringe and thin plastic tubing to a metal tube of 3 mm diameter
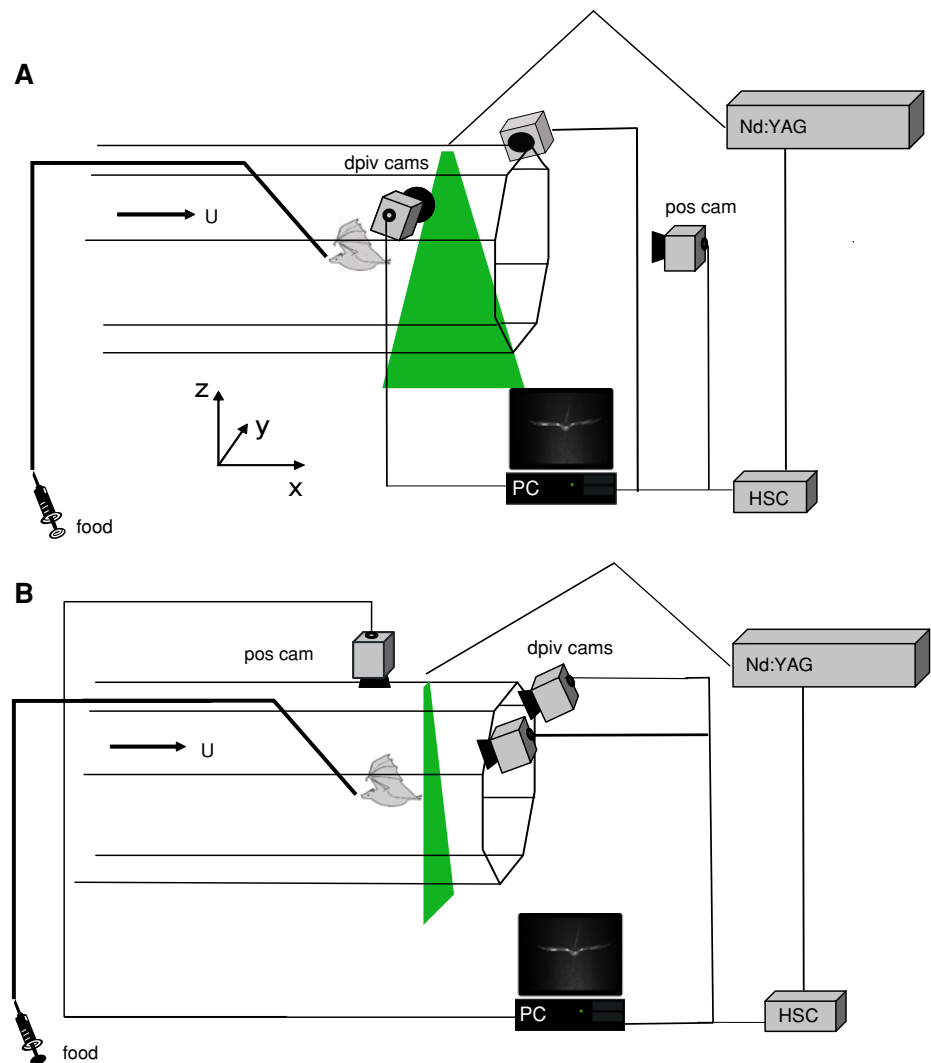
the light sheet. The feeder was about 20 cm upstream of the center of the light sheet, and the distance from the wing tip to the imaging plane varied between 16 and 18 cm, which is 3.4–4.7c, or 0.5–0.8b. At $U = 4$ m/s, the vortex travel time from the wing tip to the imaging plane was about 0.04 s, which is 0.4–0.6T_w, where T_w is the time for one wingbeat cycle. The whole tunnel was filled with a thin fog (particle size 1 μm), which was illuminated in slices by a pulsed 50 mJ Laser (Litron LPY732 series, Nd:YAG, 532 nm) at 200 Hz repetition rate. The PIV cameras have band pass filters (530 $\pm$ 5 nm) to minimize stray light from other sources. An independent camera monitored the position and flight behaviour of the bat in relation to the light sheet. This position-monitor camera was positioned on the top of the test section in the transverse light sheet configuration (Fig. 1b), and in the first diffuser downstream from the test section in the streamwise light sheet configuration (Fig. 1a). For both transverse [yz] and streamwise [xz] data, the left wing and body were imaged.

2.4 DPIV analysis

2.4.1 The DPIV system and calibration

The DPIV data are captured and analyzed using the DaVis software package from LaVision (Davis 7.2.2.110). It is calibrated using a calibration plate (20 $\times$ 20 cm^2, type 22), in combination with the DaVis Stereo PIV self-calibration algorithms to compensate for misalignments between the laser sheet and the calibration plate. Background flow DPIV measurements were performed for monitoring the pixel displacement magnitudes and possible peak-locking errors, and the time difference between the laser pulses was adjusted to optimise the available velocity bandwidth. The background flow was also used to determine the flight speed at low wind tunnel speed settings ($U \leq 2$ m/s), since at these low speeds, the conventional wind tunnel monitor system (using the static pressure difference before and after the contraction immediately upstream from the test section) is inaccurate. At low speeds, the spatial variation (RMS within the 20 $\times$ 20 cm^2 measurement area) was less than 2.5% of the mean velocity ($n = 6$). The temporal velocity variations are on average of 2.25% of the mean velocity ($n = 3$), with a maximum time difference between the measurements of 1 h.

2.4.2 Data acquisition

The bat flight data were captured by manual triggering. When a bat was flying steadily in front of the feeder, the laser shutter was opened and a sequence of 50 frames was captured by the DPIV cameras. Simultaneously (using a synchronization signal), a 1 s video sequence of the flying bat and laser pulses was recorded using a 250 Hz frame-rate digital video camera (Fig. 1). If the bat continues to fly behind the feeder, the triggering routine can be repeated. This procedure typically generates DPIV data for up to two (*L. curasoae*) and three (*G. soricina*) consecutive wingbeats per trigger event.

2.4.3 Analysis

The DPIV data were analyzed using the DaVis software. The images were pre-processed to reduce systematic errors due to background noise, for example, when a bat is visible in the background. A multi-pass stereo cross-correlation was used (64 $\times$ 64 and 32 $\times$ 32, 50% overlap), and the results were post processed using a correlation peak ratio deletion scheme (peak ratio < 1.01), a median vector field filter, and a false vector rejection criterion of vector magnitudes, $|v| > 1.5$ times the neighbourhood RMS, and recalculation for $|v| > 2$ times the local RMS, and a single 3 $\times$ 3 smoothing average.

The computed $\{u, v, w\}$ velocity components in x- (streamwise), y- (spanwise) and z- (vertical) directions were used to calculate the vorticity components, $\{\omega_x, \omega_y, \omega_z\}$ normal to the planes [yz, zx, xy], respectively. For example, the streamwise vorticity, $\omega_x = \partial w/\partial y - \partial v/\partial z$, is determined by the $\{v, w\}$ velocity gradients in the [yz] plane. The circulation of identified vortex structures was also measured in selected planes using procedures described in Spedding et al. (2003b).

The DPIV data were compiled into a 3D spatial matrix (x, y, z), by concatenating the results from consecutive DPIV frames, and converting the time difference between the frame pairs into a streamwise displacement ($\Delta x = U\Delta t$). When doing this, one assumes that wake displacements are dominated by mean flow convection, and that no strong vortex wake evolution/kinematics occurs at and after the measurement point.

Although the data are assembled into a single 3D cube, the original data acquisition planes (where the in-plane velocity estimation errors are smaller than the out-of-plane components) have some particular interest in the analysis. The streamwise [xz] planes are parallel to U, and to g. The drag is defined as the aerodynamic force component parallel to U, and the lift is defined as normal to U, which is parallel to g here. The u and w disturbance velocities are therefore the leading contributors to estimates of D and L. Invoking quite reasonable assumptions for far-field flows shows that they are the only components of significance (see Spedding and Hedenström 2009, this volume). These points were noted in the original bird flight DPIV studies (Spedding et al. 2003b) and the [xz] plane data can be compared directly with them.

The [yz] plane, normal to U, is where the v and w components of velocity can be most accurately estimated

Fig. 2 Colour-coded vorticity fields and velocity vector fields from ▶ two bats flying in a wind tunnel. The images show the [yz] plane of the left wing and body for one *Glossophaga soricina* (**a–e**) and one *Leptonycteris curasoae* (**f–j**), both flying at $U = 4$ m/s. The individual bats are the males (#1 and #97) of Table 1. The distance from the bat to the [yz] imaging plane varied between 3.4 and 4.7 chord lengths. The *panels* represent sub-periods of a wing stroke as follows (*top–bottom*): beginning of downstroke, mid downstroke, end of downstroke, mid upstroke and end of upstroke. The colour scale symmetrically maps the streamwise vorticity, ω_x, (s^{-1}) from -280 (*blue*) to $+280$ (*red*) in steps of 40 s^{-1}. The {v,w}-component velocity vectors are scaled to the reference at 5 m/s at *bottom right*. The *closed curves* show the path of the wing tip for an average wingbeat and the *dots* show the centers of the wing tip vortices with the *grey dot* showing the current frame. The *panels* represent a real area of 17.5 × 17.5 cm

together. When this plane is far from the disturbance source, then the only significant disturbance velocities will be the v and w components in the wake itself (u will be much smaller), and inviscid theory can be used to estimate the induced drag of a wake oriented parallel to U and passing through this plane. This plane is called the Trefftz plane in aeronautics. If all the three components of velocity are available in this plane, then both the lift and drag can be computed, using only this information. It is tempting to invoke all [yz] planes as Trefftz planes, but they must be large, far from the body and the wake must be normal to them for the original analysis to hold.

3 Results

3.1 Wake structure and implications for aerodynamic force generation on the wing

Figure 2 shows a time sequence of [yz] planes at $x/c \approx 5$ (from set-up in Fig. 1b), behind the body and left wing through one complete wing stroke at $U = 4$ m/s, for one individual each of *G. soricina* and *L. curasoae* (hereafter *G. s.* and *L. c.*). The path of the wingtip is shown by a continuous line and the centers of the tip vortices are shown as black dots with the current centre of the wing tip vortex shown in grey. At the beginning of the downstroke, some weak streamwise vorticity is seen in *G. s.* (Fig. 2a), while in *L. c.*, the tip vortex is already visible (blue patch, Fig. 2f), together with a counter-rotating vortex shed from the wing root (yellow patch, Fig. 2f). By mid downstroke, there are prominent wing tip vortices as well as wing root vortices in both species (Fig. 2b, g). At this stage, there is a clear downwash between the opposite-signed shed vortices, with magnitude (mean ± SD) 1.47 ± 0.63 m/s ($n = 18$) and 1.27 ± 0.47 m/s ($n = 25$) in *G. s.* and *L. c.*, respectively (n is the number of vectors between tip- and toot-vortices). The larger sample size in *L. c.* is due to the longer
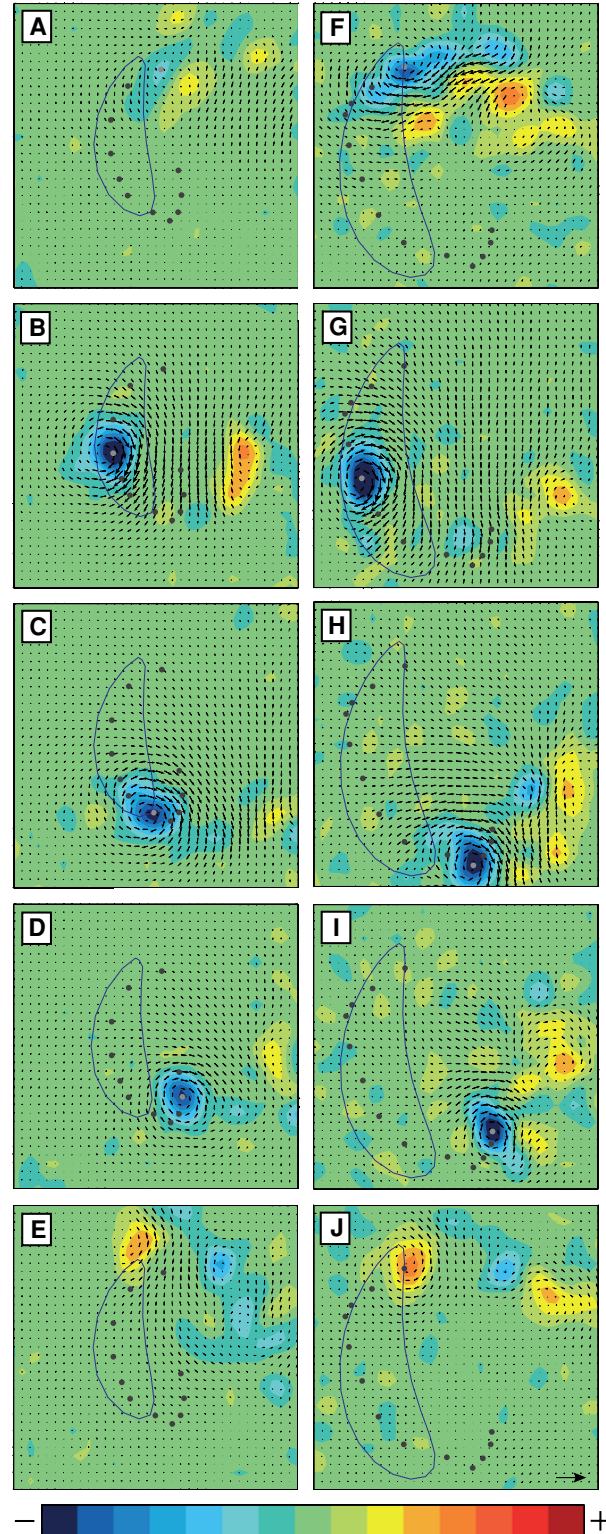
wingspan compared with *G. c.* At mid downstroke, the wing span has its maximum horizontal extent, and the horizontal distance, l_y, between tip and root vortices for
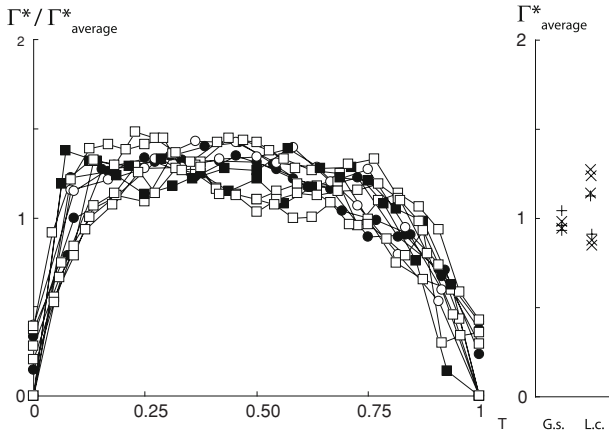
Fig. 3 Normalised circulation, $\Gamma^*_{average} = \Gamma/Uc$, of the wingtip trailing vortex, realtive to the mean value of the sequence. Mean values for individual wingbeats are given in the *panel* to the *right*. The *symbols* represent *Glossophaga soricina* (*circles*; *open* and *filled symbols* denote different individuals) and *Leptonycteris curasoae* (*squares*) followed over a number of wing strokes. The wingbeat period was 0.067 and 0.099 s for *Glossophaga soricina* and *Leptonycteris curasoae*, respectively

G. s. and *L. c.* is 7.9 and 12.2 cm, respectively. Normalised by the wing semispan, $2l_y/b = 0.69$ and 0.74, respectively.

At the end of the downstroke, the tip vortex has the same circulation magnitude as at mid downstroke, but it is now shed from a position closer to the body midline as the wing tips are moved towards each other below the body (Fig. 2c, h). At the beginning of the upstroke, the wing is being flexed and at mid upstroke, the tip vortex is still present, although it is closer to the body midline than it was at mid downstroke. Notice that there is still an induced downwash about halfway into the upstroke (Fig. 2d, i), indicating that the wing is generating lift also during the upstroke up to this point. Towards the end of the upstroke, the tip vortex vanishes, but instead, there is shedding of a vortex dipole inducing an upwash and hence an associated negative lift (Fig. 2e, j). The root vortex appears weaker during the upstroke in *G. s.* than in *L. c.* (Fig. 2c, d vs. h, i). In most cases, the centre of the tip vortex is inboard of the wing-tip trace, except for about one quarter into the downstroke in *L. c.* (Fig. 2).

The circulation, Γ is a measure of the integrated vorticity magnitude in a region. The normalised circulation of the tip vortices, $\Gamma^* = \Gamma/Uc$, is plotted as a function of T ($T = t/T_w$, where T_w is the wing beat period, and t is counted from the beginning of each downstroke) stroke at $U = 4$ m/s in Fig. 3. Γ^* increases rapidly after the beginning of the downstroke ($T < 0.1$), and then varies only little between 1.2–1.8 well into the upstroke ($T \approx 0.75$), after which it drops to almost zero at the end ($T = 1$) of the upstroke. The pattern and magnitude of the circulation variation throughout a wing stroke are very similar between the two species, although one individual *L. c.* (the female) appears to show somewhat larger variation.

3.2 Three-dimensional wake topology

As the wake is sampled at 200 Hz, the $[yz](t)$ image sequence can be used to generate iso-surfaces of constant streamwise vorticity (ω_x) over one wing stroke. $\omega_x(x, y, z)$ was assembled from time sequences of data, such as Fig. 2, using the previously-noted transform rule $\Delta x = U\Delta t$, and ω_x iso-surfaces are shown in Fig 4. The iso-values of ω_x are $\pm$mean $|\omega_x|$ (red positive, blue negative). The bat is flying from left to right and obliquely towards the observer, and the iso-surfaces show the streamwise vorticity that trails the bat wing and body during the course of a little over one wingbeat. The tip vortex shed by the right wing is blue, circulating clockwise when viewed downstream from the bat, and the root vortex is red, rotating in the opposite, anti-clockwise direction. Their counterparts in mirror image behind the left wing are opposite in direction of rotation and colour. The downstroke generates a prominent tip vortex in both *G. s.* and *L. c.* A wing root vortex of opposite sign is also present during the downstroke in both species. At the end of the upstroke, an inverted vortex dipole, whose cross-section was shown in Fig. 2e and j, can be seen in the top right of both Fig. 4a and b. The wingtip trailing vortex gradually loses strength and falls below the visualization threshold towards the end of the upstroke, but we should remember that the visualized component is ω_x (and not $|\omega|$), so although the connecting start and stop vortices, which are primarily ω_y, are not visible, their presence (as required by Helmholtz's conservation laws) is known from the full vorticity vector data, and from plots of $\omega_y(x, z)$. Here, however, the vortex loops appear as disconnected vortex strands of ω_x.

3.3 Wake defect maps

Figure 5 shows the normalized streamwise velocity, $(u - U)/U$. Since drag and thrust are associated with deceleration and acceleration of the mean streamwise velocity, U, then a region of $(u - U)/U < 0$ might be interpreted to contribute a net drag and $(u - U)/U > 0$, a net thrust. Then the integrated sum of these regions, taken over a suitable control volume, will be zero for any self-propelled body in steady motion. This is a rather over-simplified picture, especially for such a complex flow, and so close to the wings and body (see Spedding and Hedenström 2009, this volume, for conditions for estimating mean forces from wake velocity distributions), but as a first order approximation, we may assert that maps of $(u - U)/U$ show where the major contributors to thrust and drag are located on the bat, through their imprint in the cross-plane wake. The trailing tip vortex has a velocity defect towards its centre in both species. This
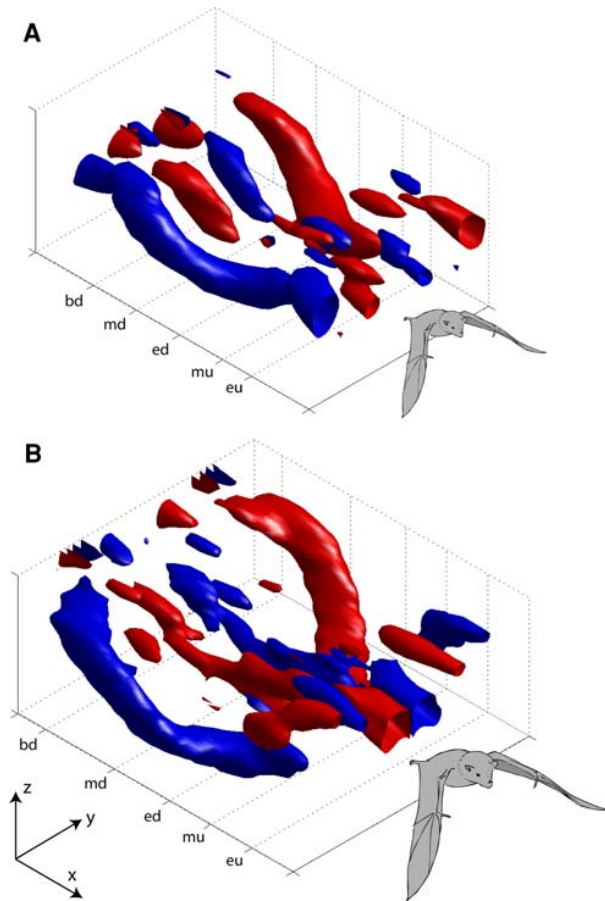
Fig. 4 Iso-surfaces of normalized constant streamwise vorticity ($\omega_x^* = \omega_x/|\varpi_x|$) during just over one wing stroke of (**a**) *Glossophaga soricina* (#1) and (**b**) *Leptonycteris curasoae* (#97). The iso-values are normalized of $\omega_x^* = \pm 1.0$ (*red* is positive; *blue* is negative). The data cubes are oriented, so the bat is flying obliquely to the right and towards the viewer. The larger centrally trailing tubes therefore mark the streamwise vorticity shed at the wing root. Approximate time-marks are: *bd* (beginning of downstroke), *md* (mid downstroke), *ed* (end of downstroke), *mu* (mid upstroke), *eu* (end of upstroke). The *data boxes* are scaled as $(x, y, z) = (400, 260, 180)$ mm in (**a**) and $(x, y, z) = (400, 345, 180)$ mm in (**b**)

is consistent with an axial flow along the vortex core towards the wing, as also noted in the kestrel wake by Spedding (1987b), and based also on 3D velocity fields. The strongest accelerated wake flow appears inboard of the tip vortex, between it and the wing root. At the body, the flow is again decelerated in this cut, at this stage of the wingbeat. Figure 6 shows that this is true for most of the wingbeat, for both bats.

4 Discussion

4.1 Aerodynamically-equivalent flight speeds

This paper describes the wakes of two species of bats flying at the same speed, $U = 4$ m/s, which is in the middle of the
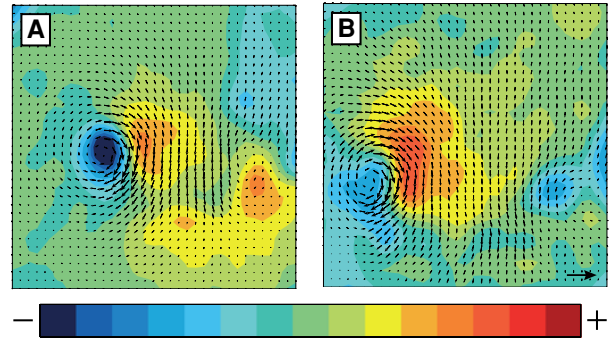

Fig. 5 $(u - U)/U$ at mid downstroke of (**a**) *Glossophaga soricina* (#1)and (**b**) *Leptonycteris curasoae* (#97). The *colour bar* runs from $(u - U)/U = -0.35$ to 0.35 in steps of 0.05 m/s. The $\{v,w\}$-component velocity vectors are scaled to the reference at 5 m/s at *bottom right*. The *panels* represent a real area of 17.5×17.5 cm

speed range of small bats (Lindhe Norberg and Winter 2006). In a comprehensive study of insect flight, Ellington (1984) used the advance ratio $J = U/2\Phi fR$, where Φ is stroke angle (in radians), f is wingbeat frequency and R is wing length, to describe the force asymmetry between downstroke and upstroke and defined hovering as including slow forward speed with $J < 0.1$. Here $J = 1.08$ for both for *G. s.* and *L. c.* The related Strouhal number, $St = fA/U$, where A is the vertical peak-to-peak amplitude of the wingtip, evaluates to 0.47 and 0.43 for *G. s.* and *L. c.*, respectively. The similar values of both J and St show that the flight speeds are aerodynamically-equivalent for the two bat species, even though they are of different size.

St measures the mean wingtip speed relative to the forward speed (it is one half of this ratio; Spedding et al. 2008) and so at $U = 4$ m/s, the tip and forward speeds have a similar magnitude. Since the wingtip speed fluctuates considerably during each wingbeat cycle, then we may expect time-varying aerodynamic force components to be non-negligible, simply based on such values of St.

4.2 The loading and unloading wing cycle

The circulation of the wingtip trailing vortex varies smoothly through the downstroke/upstroke transition and continues to be measurable, with the same sign, until close to the end of the upstroke. At the same time, a downwash induced between the wingtip and wing root sections supports the notion that the upstroke is aerodynamically active for about half its duration, at which point, the circulation falls to zero and the wing is aerodynamically unloaded. This cycle of wing loading and unloading through the wingbeat is quite consistent with previous interpretations (Hedenström et al. 2007) based on multiple 2D DPIV planes. The agreement of the 3D data with multiple 2D slices from hundreds of different wingbeats is gratifying.
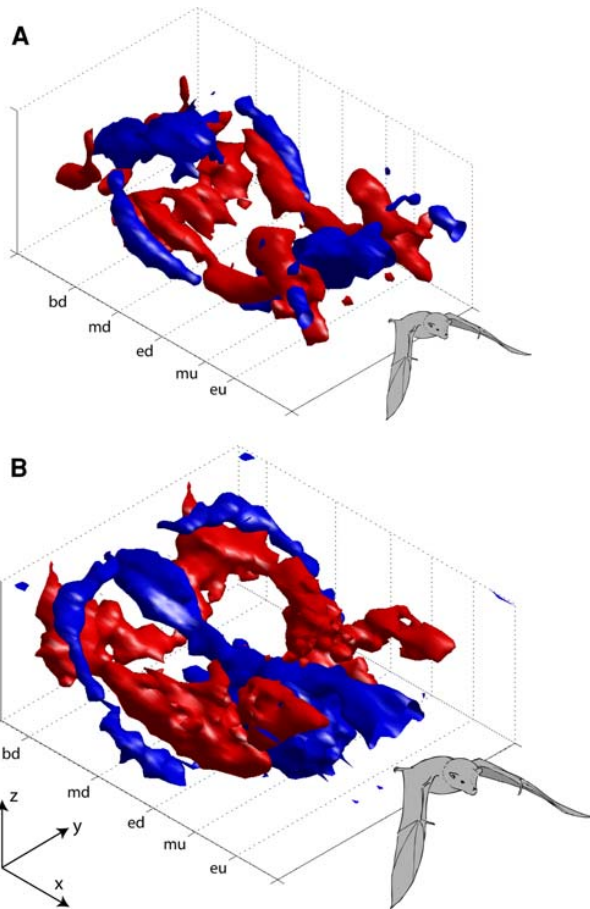
Fig. 6 $(u − U)/U$ (x, y, z) for one wing beat of (**a**) *Glossophaga soricina* (#1) and (**b**) *Leptonycteris curasoae* (#97). Orientation and time-marks as in Fig. 4. The threshold values used were $(u − U)/U = ±0.25$ in (**a**) and $±0.3$ in (**b**). The *data boxes* are scaled as $(x, y, z) = (400, 260, 180)$ mm in (**a**) and $(x, y, z) = (400, 345, 180)$ in (**b**)

4.3 Pseudo-3D data

It is not only the wing loading/unloading cycle that can be confirmed in the 3D data, but also the observations of wing root vortices and of the shedding of inverted vortex loops at the end of the upstroke. These phenomena were newly observed in bats and make their wake signatures qualitatively different from those of birds (Hedenström et al. 2007). The 3D reconstructions in Figs. 4 and 6 are reasonable if the transformation $\Delta x = U\Delta t$ is reasonable. The wake evolves in both space and time, and one can only substitute one for the other provided the intervals are short compared with spatial or temporal evolution time-scales. This is often known as the 'frozen-flow' hypothesis: would the wake really be frozen in place as it convects through the measurement volume? The streamwise extent of the reconstructed wake, $X_w = UT_w$, where T_w is the wingbeat period, and here $X_w/c = 7.2$ for *G. s.* and 8.3 for *L. c.*

A comparison of near and far wakes in *G. s.* at $x = 3.2c$ and $19c$ (Johansson et al. 2008) shows that the qualitative and quantitative wake properties vary rather little with x and so the frozen flow assumption is tenable.

4.4 Drag, thrust and power

The power required to move at steady speed U is just DU, where D is the total drag that must be overcome to move through the surrounding fluid. In steady, unaccelerated flight, the total drag is balanced by the total thrust and the net horizontal momentum flux in the wake is zero. Although the wake is often touted as the footprint of the flying animal, which must contain a record of all the forces experienced by the wings and body, the causes and traces of drag and thrust are not necessarily separable. There are two major contributors to drag in a three-dimensional lifting system—the induced drag due to the downwash induced by the trailing vortices, and the viscous drag due to friction and pressure drag on all exposed surfaces. The induced drag is an inviscid component, and will be non-zero on all parts of the flyer that generate lift (and hence shed trailing vortices). The largest part of that, by far, can be expected to be from the wings, but especially in light of the complex root vortex shedding, it will be interesting to see how and when body lift makes a contribution to the induced drag.

The viscous drag is not predicted by any tractable theory, so it is always estimated from empirical performance curves, usually from polar plots of lift coefficient versus drag coefficient. There is a very significant uncertainty in its estimation, especially for complex systems like flapping bat wings. Given this practical problem, it is tempting to look to the wake structure for alternative measures of drag. Thus far, animal wake analyses have assumed that the total drag of the flying animal is balanced by a thrust that can be calculated from the geometry of the vortex wake (e.g. Spedding et al. 2003b; Hedenström et al. 2006; Henningsson et al. 2008). Thus the wake geometry, which is essentially an inviscid construct of line vortices in a potential flow, can be estimated to give a certain net forward impulse. This is then assumed to balance a viscous drag over one wingbeat, whose signature has not been explicitly measured, but which is assumed to trail behind the wings and body without disrupting the primary trailing vortex system.

It may be reasonable to further localize these forces. The wake directly downstream of the body presumably contains the drag signature of the body, and the measurement of a three-dimensional, mean streamwise velocity defect could be used to estimate the body drag. It is tempting therefore to look to data such as Fig. 6, which contains the velocity defect map for one wingbeat, for a complete solution to the

drag estimation problem. Indeed, blue and red blobs of momentum excess or deficit seem to be located in separate regions, and so while their sum must be zero, the different parts might be countable. It seems plausible that most thrust comes from the outer part of the wing, and that most drag comes from the body, as deduced from Fig. 6. However, it is far from clear that the pressure fluctuations can be ignored at $x = 3$–$5c$ in this highly unsteady wake, and it is also not clear whether appropriate far-field boundary conditions can be assumed. Furthermore, there is a uniqueness problem when the propulsor is a source of both thrust and drag, because there are an infinite number of combinations of negative and positive momentum flux that could have given rise to any given positive or negative net result. Teasing out these force components will be a significant challenge, but at least the data that one requires (such as Figs. 4, 6) are now becoming available.

4.5 Unsteady aerodynamics

Based on values of the Strouhal number alone ($St \approx 0.4$–0.5), we expect that unsteady aerodynamic forces are likely to be non-negligible. Wake measurements here show that $\Gamma/Uc \approx 1$ for both bat species and if this is interpreted as one half of a local lift coefficient (Rosén et al. 2007), then the wings apparently have time-averaged $C_L \approx 2$. A local wing section sees the vector sum of U and its local flapping speed, and not just U, and if the tip speed and mean speed have the same magnitude, then the corrected speed will be $\sqrt{2}U$ and the implied average C_L becomes 1.4. This is close to the upper limit that could be expected from moderate aspect ratio wings at this Re (Laitone 1997; Lyon et al. 1997; Spedding et al. 2008). *G. s.* has been shown to develop a significant fraction of its lift in near hovering flight from an unsteady leading-edge vortex (LEV) that appears and is stable due to wing accelerations (Muijres et al. 2008). It is possible that some form of LEV persists into higher speed conditions for *G. s.*, and since it appears to be flying in a very similar regime, the same extrapolation is as likely to hold for *L. c.* also.

5 Conclusion

The higher temporal resolution and availability of the third velocity component allows wake reconstructions for flying animals of greater detail and reliability than before. Nevertheless, it is notable how the new wake data are very consistent with previous reconstructions based on the painstaking assembly of multiple, separately-acquired data planes. We look forward to make new flight models based on these more comprehensive data, and to explore the challenges in estimating force coefficients from the 3D, unsteady wake.

References

Aldridge HDJN (1986) Kinematics and aerodynamics of the greater horseshoe bat, *Rhinolophus ferrumequinum*, in horizontal flight at various flight speeds. J Exp Biol 126:479–497

Brown RHJ (1948) The flight of birds. The flapping cycle of the pigeon. J Exp Biol 25:322–333

Ellington CP (1984) The aerodynamics of hovering insect flight. III. Kinematics. Phil Trans R Soc B 305:41–78

Hedenström A (2002) Aerodynamics, evolution and ecology of bird flight. Trends. Ecol Evol 17:415–422

Hedenström A, Spedding GR (2008) Beyond robins: aerodynamic analyses of animal flight. J R Soc Interface 5:595–601

Hedenström A, Rosén M, Spedding GR (2006) Vortex wakes generated by robins *Erithacus rubecula* during free flight in a wind tunnel. J R Soc Interface 3:263–276

Hedenström A, Johansson LC, Wolf M, von Busse R, Winter Y, Spedding GR (2007) Bat flight generates complex aerodynamic tracks. Science 316:894–897

Henningsson P, Spedding GR, Hedenström A (2008) Vortex wake and flight kinematics of a swift in cruising flight in a wind tunnel. J Exp Biol 211:717–730

Johansson LC, Wolf M, von Busse R, Winter Y, Spedding GR, Hedenström A (2008) The near and far wake of Pallas' long tongued bat (*Glossophaga soricina*). J Exp Biol 211:2909–2918

Laitone EV (1997) Wind tunnel tests of wings at Reynolds numbers below 70 000. Exp Fluids 23:405–409

Lindhe Norberg UM, Winter Y (2006) Wing beat kinematics of a nectar-feeding bat, *Glossophaga soricina*, flying at different flight speeds and Strouhal numbers. J Exp Biol 209:3887–3897

Lyon CA, Broeren AP, Giguere P, Gopalarathnam A, Selig MS (1997) Summary of low-speed airfoil data, vol 3. Soartech, Virginia Beach

Muijres FT, Johansson LC, Barfield R, Wolf M, Spedding GR, Hedenström A (2008) Leading-edge vortex improves lift in slow-flying bats. Science 319:1250–1253

Norberg UM (1976) Aerodynamics, kinematics, and energetics of horizontal flapping flight in the long-eared bat *Plecotus auritus*. J Exp Biol 65:179–212

Norberg UM (1990) Vertebrate flight. Springer, Berlin

Pennycuick CJ (1968) Power requirements for horizontal flight in the pigeon *Columba livia*. J Exp Biol 49:527–555

Pennycuick CJ (1975) Mechanics of flight. In: Farner DS, King JR, Parkes KC (eds) Avian Biology, vol 5. Academic Press, New York, pp 1–75

Pennycuick CJ (1989) Bird flight performance: a practical calculation manual. Oxford University Press, Oxford

Pennycuick CJ, Alerstam T, Hedenström A (1997) A new low-turbulence wind tunnel for bird flight experiments at Lund University, Sweden. J Exp Biol 200:1441–1449

Rayner JMV (1979a) A vortex theory of animal flight. Part 2. The forward flight of birds. J Fluid Mech 91:731–763

Rayner JMV (1979b) A new approach to animal flight mechanics. J Exp Biol 80:17–54

Rosén M, Spedding GR, Hedenström A (2007) Wake structure and wingbeat kinematics of a house-martin *Delichon urbica*. J R Soc Interface 4:659–668

Spedding GR (1987a) The wake of a kestrel (*Falco tinnunculus*) in gliding flight. J Exp Biol 127:45–57

Spedding GR (1987b) The wake of a kestrel (*Falco tinnunculus*) in flapping flight. J Exp Biol 127:59–78

Spedding GR, Hedenström A (2009) PIV-based investigations of animal flight. Exp Fluids. doi:10.1007/s00348-008-0597-y

Spedding GR, Rayner JMV, Pennycuick CJ (1984) Momentum and energy in the wake of the a pigeon (*Columba livia*) in slow flight. J Exp Biol 111:81–102

Spedding GR, Hedenström A, Rosén M (2003a) Quantitative studies of the wakes of freely flying birds in a low turbulence wind tunnel. Exp Fluids 34:291–303

Spedding GR, Rosén M, Hedenström A (2003b) A family of vortex wakes generated by a thrush nightingale in free flight in a wind tunnel over its entire natural range of flight speeds. J Exp Biol 206:2313–2344

Spedding GR, Hedenström A, McArthur J, Rosén M (2008) The implications of low-speed fixed-wing aerofoil measurements on the analysis and performance of flapping bird wings. J Exp Biol 211:215–223

Spedding GR, Hedenström A, Johansson C (2009) A note on wind-tunnel turbulence measurements with DPIV. Exp Fluids 46:527–537. doi:10.1007/s00348-008-0578-1

Warrick DR, Tobalske BW, Powers DP (2005) Aerodynamics of the hovering hummingbird. Nature 435:1094–1097

Comparative aerodynamic performance of flapping flight in two bat species using time-resolved wake visualization

Florian T. Muijres[1],*, L. Christoffer Johansson[1], York Winter[2] and Anders Hedenström[1]

[1]*Animal Flight Laboratory, Department of Biology, Lund University, Sölvegatan 37, 223 62 Lund, Sweden*
[2]*Cognitive Neurobiology, Humboldt University, and NeuroCure Centre of Excellence at the Charité Universitätsmedizin Berlin, Dorotheenstrasse 94, 10117 Berlin, Germany*

Bats are unique among extant actively flying animals in having very flexible wings, controlled by multi-jointed fingers. This gives the potential for fine-tuned active control to optimize aerodynamic performance throughout the wingbeat and thus a more efficient flight. But how bat wing performance scales with size, morphology and ecology is not yet known. Here, we present time-resolved fluid wake data of two species of bats flying freely across a range of flight speeds using stereoscopic digital particle image velocimetry in a wind tunnel. From these data, we construct an average wake for each bat species and speed combination, which is used to estimate the flight forces throughout the wingbeat and resulting flight performance properties such as lift-to-drag ratio (L/D). The results show that the wake dynamics and flight performance of both bat species are similar, as was expected since both species operate at similar Reynolds numbers (Re) and Strouhal numbers (St). However, maximum L/D is achieved at a significant higher flight speed for the larger, highly mobile and migratory bat species than for the smaller non-migratory species. Although the flight performance of these bats may depend on a range of morphological and ecological factors, the differences in optimal flight speeds between the species could at least partly be explained by differences in their movement ecology.

Keywords: bats; flight; aerodynamics; wind tunnel; particle image velocimetry; vortex wake

1. INTRODUCTION

Bat wings are known to be extremely flexible compared with wings of members of the two other taxa of actively flying animals, birds and insects. The bat wing consists of thin and highly compliant membranes spanned between stiffeners, consisting of elongated finger bones [1,2]. This gives the potential for fine-tuned active control to optimize aerodynamic performance throughout the wingbeat. As a result of this, the bat airframe solution is often associated with high manoeuvrability, but has also been associated with reduced energetic flight efficiency compared with birds [3–5]. However, bat wings are thin when compared with bird wings and resemble cambered flat plates rather than standard wing profiles. In a steady state configuration, such cambered flat plates outperform standard wing profiles at the Reynolds numbers (Re) relevant for bats and birds ([6,7]; $2.0 \times 10^4 \leq Re \leq 7.0 \times 10^4$, $Re = Uc/\nu$, where U is the speed of the wing through the air, c is the mean chord length of the wing and ν is the kinematic viscosity of air). There is, however, a large variation in wing size and morphology among bat species, which is related to variation in ecology [8,9]. The available data on flapping bat wing performance are too limited to draw any general conclusions on how bat wing performance varies between different bat species as a result of physical scaling laws, morphology or due to differences in their ecology.

Here, we compare the aerodynamic performance of two bat species, *Glossophaga soricina* and *Leptonycteris yerbabuenae*. Both species are New World nectar-feeding bats of the family Glossophaginae, which have similar morphology and life-history strategy [9]. We recognize two main differences between these species, their size and their movement ecology [9].

Leptonycteris yerbabuenae is about twice the weight of *G. soricina*. Based on this difference in weight we expect that characteristic flight speeds (e.g. minimum

*Author for correspondence (florian.muijres@teorekol.lu.se).

Table 1. Morphological data for the bats used in the experiment. Mass M, wing span b, wing surface area S, mean cord length $c = S/b$, aspect ratio $AR = b^2/S$ and wing loading $Q = Mg/S$, where g is the gravitational constant.

bat (species, gender)	M (kg)	b (m)	S (m²)	c (m)	AR (−)	Q (N m⁻²)
G. soricina, male	0.0101	0.233	0.00879	0.038	6.2	11.3
G. soricina, female	0.0095	0.230	0.00860	0.037	6.2	10.8
L. yerbabuenae, male	0.0216	0.335	0.01576	0.047	7.1	13.4
L. yerbabuenae, female	0.0236	0.323	0.01529	0.047	6.8	15.1

power speed and maximum range speed [10]) are higher for *L. yerbabuenae* than for *G. soricina*. According to isometric scaling laws for animal flight [9,10], this difference should be in the order of $U^*_{\text{char}} \sim (M^*)^{1/6}$, where U^*_{char} is the characteristic flight speed ratio and M^* is the mass ratio for the two bat species.

As for movement ecology, *G. soricina* is a resident species, which has a relatively small home range in which it both roosts and feeds. Its mean recapturing area is only 200 m² [11]. On the other hand, *L. yerbabuenae* makes long commuting flights between its roosting and feeding sites, travelling around 100 km every night [12]. Also, *L. yerbabuenae* migrates annually up to 1000–1600 km between southern Mexico and southern Arizona [13], which is among the longest known migration routes in bats.

On the basis of these ecological differences, one can assume that evolutionary selection pressure for efficient fast-forward flight should be stronger for *L. yerbabuenae*, and selection pressure for efficient hovering and slow flight should be stronger for *G. soricina* [9]. Thus, our hypothesis is that, when controlling for the differences in weight, optimal flight speeds for *L. yerbabuenae* should be significantly higher than for *G. soricina* ($U^*_{\text{char}} > (M^*)^{1/6}$). A second hypothesis is that we do not expect the general wake morphology of the two studies species to differ. This is based on the large similarities between the wake morphology of *G. soricina* and *L. yerbabuenae* at a flight speed of 4 m s⁻¹ [14], and the similarities in wake morphology with a much larger bat, *Cynopterus brachyotis* [15,16].

To test these hypotheses, we studied the aerodynamic performance of both bat species flying freely in a wind tunnel across a range of flight speeds using time-resolved stereoscopic particle image velocimetry (PIV). The experimental set-up is described in Hedenström *et al.* [14], which is a methods paper showing preliminary data for these bats flying at a forward flight speed of 4 m s⁻¹. Here, we present a complete experimental dataset for these bats, over a flight speed range from 2 to 7 m s⁻¹. Using the time-resolved PIV data, we construct an average vortex wake based on multiple wingbeats for each species and flight speed combination [17]. From these average vortex wakes, we determine the flight force distribution throughout the wingbeat and measures of flight performance, such as the lift-to-drag ratio L/D. The resulting wake dynamics, temporal force production and flight performance measures are compared between the two nectar-feeding bat species, and with flight performance data of birds.

2. METHOD

2.1. Study animals

The flight kinematics of *G. soricina* is described in Norberg & Winter [18] and Wolf *et al.* [19], and of *L. yerbabuenae* in R. von Busse, L. C. Johansson, Y. Winter & A. Hedenström (2011, unpublished data). The downstroke-to-upstroke ratio of both species is consistent across the studied flight speed range (2–7 m s⁻¹), being 0.52 ± 0.01 (mean $\pm$ s.d. $n = 14$) for *G. soricina* and 0.51 ± 0.01 ($n = 16$) for *L. yerbabuenae*. The Strouhal number ($St = f\,A/U_\infty$, where U_∞ is the forward flight speed, f is the flapping frequency and A is the tip-to-tip vertical flapping amplitude of the wing tip) for *G. soricina* ranges from 0.67 at 2 m s⁻¹ to 0.25 at 7 m s⁻¹, while for *L. yerbabuenae*, it ranges from 0.68 at 2 m s⁻¹ to 0.23 at 7 m s⁻¹. In this study the Re number range is $0.5 \times 10^4 \le Re \le 1.7 \times 10^4$ for *G. soricina*, and $0.6 \times 10^4 \le Re \le 2.1 \times 10^4$ for *L. yerbabuenae*. Of each bat species, a male and a female bat were used in our experiments, of which the morphological characteristics are shown in table 1.

Since the Re range and the relation between the Strouhal number and flight speed are very similar between these two species, we assume that the wake dynamics scales similar with flight speed for both species. Therefore, we will directly compare the flight dynamics of the two species at each flight speed.

2.2. Experimental set-up

The experimental set-up (electronic supplementary material, figure S1) was the same as the set-up described in Hedenström *et al.* [14], in which preliminary wake data were presented (the wake at 4 m s⁻¹). The bats were trained to fly at a feeder in the test section of the Lund low-turbulence wind tunnel [20], at wind tunnel speeds $U_\infty = 2$–7 m s⁻¹, with 1 m s⁻¹ increments. An intermediate speed of 2.5 m s⁻¹ was included because a large change in kinematics was observed between 2 and 3 m s⁻¹ for *G. soricina* [19]. The PIV system image plane (approx. 20×20 cm) was positioned 20 cm downstream from the feeder. The PIV system consists of a transversely positioned $\{y,z\}$ plane (for the coordinate system see electronic supplementary material, figure S1) laser light sheet, generated by a 200 Hz pulsed 50 mJ Laser (Litron LPY732 series, Nd : YAG, 532 nm), and two synchronized, double frame, CMOS-cameras (High-SpeedStar3; 1024×1024 pixels) in stereo set-up. The system is controlled by the Lavision PIV software

package DaVis (LaVision, DaVis 7.2.2.110). When a bat was flying steadily in front of the feeder, a sequence of 50 PIV measurements (1/4 s at 200 fps) of the wake was recorded. Simultaneously, a synchronized kinematics camera filmed the feeding bat from above at 250 Hz, which was used to determine the animal's behaviour, position, attitude and wing morphology.

2.3. Particle image velocimetry analysis

The PIV images were analysed using DaVis (7.2.2.110), as described in Hedenström *et al.* [14] (multi-pass stereo cross-correlation {64 × 64 and 32 × 32, 50% overlap}, followed by a smoothing {3 × 3}). The resulting three-component transverse PIV data ({u, v, w} velocity matrix) are imported into a custom-made Matlab (7.7.0.471, R2008b) PIV analysis program, in which the location, vorticity and circulation of different vortices within a PIV frame can be measured. We have not determined if the patches of high vorticity that we call vortices are indeed vortices in the strict fluid-dynamics sense [21]. However, for convenience, we will refer to them as vortices in the rest of this paper.

The circulation Γ of a vortex is estimated by determining a vortex area of which the edge is defined by the $|\omega|_{min} = 60 \text{ s}^{-1}$ vorticity iso-line. The threshold vorticity $|\omega|_{min}$ is determined by the maximum vorticity caused by measurement uncertainties for the worst case with $U_\infty = 7 \text{ m s}^{-1}$, estimated from background flows of an empty wind tunnel. The vortex circulation ($\Gamma_{measured}$) was determined by integrating the stream-wise vorticity (ω_x) across the vortex area. Assuming that the vorticity in the vortex has a normal Gaussian distribution, the tails outside the cut-off ($|\omega| < |\omega|_{min}$) were added to determine the total vortex circulation as [22]

$$\Gamma = \left(1 + \frac{|\omega|_{min}}{|\omega|_{max}}\right)\Gamma_{measured}, \qquad (2.1)$$

where $|\omega|_{max}$ is the absolute peak vorticity of the vortex. The location of the vortex is defined as the location of the peak vorticity $|\omega|_{max}$.

The analysed PIV frames were given a normalized time stamp, τ, defined as

$$\tau = \frac{t}{\Pi}, \qquad (2.22)$$

where Π is the wingbeat period and t is the time of measurement in relation to the start of the downstroke within each wingbeat. The start of the downstroke ($t = 0$) is defined as the PIV frame when the tip vortex is at the highest vertical position (highest value in z-direction). By assuming that the wake convects downstream with the forward flight speed U_∞, the PIV frame time stamps can be converted into a stream-wise spatial value (along the x-axis) as

$$x = U_\infty t. \qquad (2.3)$$

Using the x values for the collection of PIV frames of a single wingbeat, and assuming that the vortex wake interactions are negligible within the time scale of one wingbeat period Π, a {x,y,z} wake matrix of this wingbeat is constructed. From this wake matrix a
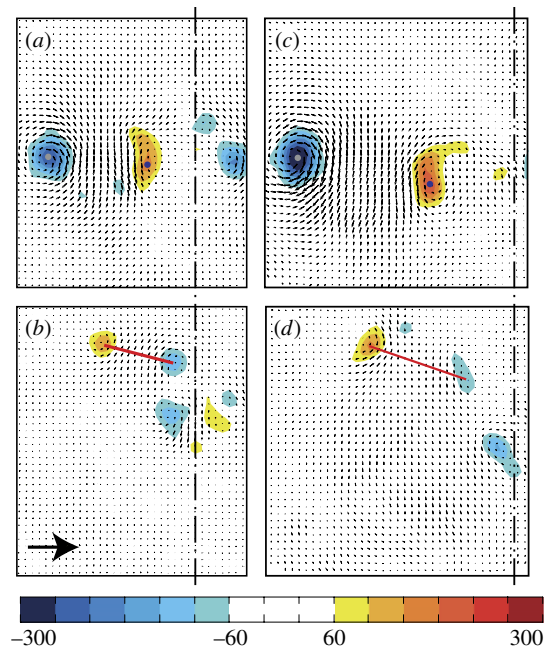

Figure 1. Transverse PIV frames (y–z) behind the bats flying at 6 m s^{-1}. (a,c) Downstroke for *G. soricina* and *L. yerbabuenae*, respectively, while (b,d) the equivalent upstrokes. The symmetry line behind the bat body is indicated by the black vertical dot-dash line. The in-plane velocity vectors are shown, and the surface colour shows the stream-wise vorticity. During the downstroke, the tip-vortex is visible as the dark blue areas indicated with a grey dot in the centre, and the root vortices are the orange areas indicated with a blue dot. During the upstroke, the reversed vortex dipole is visible as the blue and red vorticity patch connected with a red bar. The vorticity colour bar ranges from −300 to 300 s^{-1}, while vorticity below the threshold of ±60 s^{-1} is not shown. The reference velocity vector on the bottom left corner of (e) is equal to 10 m s^{-1}. Panel sizes are 175 mm by 205 mm for *G. soricina* and 200 mm by 205 mm for *L. yerbabuenae* (width by height).

three-dimensional vortex wake can be constructed by creating iso-surfaces of the stream-wise vorticity.

Hedenström *et al.* [14] identified three main wake structures for *G. soricina* and *L. yerbabuenae* flying at 4 m s^{-1}, being the tip vortex, root vortex and the reversed vortex dipole (see also [15,23,24]). If present in the PIV frame, all these vortex types are measured using the Matlab PIV analysis program. For each measured vortex, the peak vorticity (ω_{max}), circulation (Γ), location of the peak vorticity ({x, y, z}) and time stamp (τ) are stored in a database. For each individual and flight speed combination, at least five flight sequences (on average 11 wingbeats) were analysed.

3. VORTEX WAKE MODEL OF FLYING BATS

The three main wake structures for *G. soricina* and *L. yerbabuenae* flying at 4 m s^{-1}, being the tip vortex, root vortex and reversed vortex dipole [14,23], are found in the wake of these bats throughout the complete flight speed range (figures 1 and 2), and are
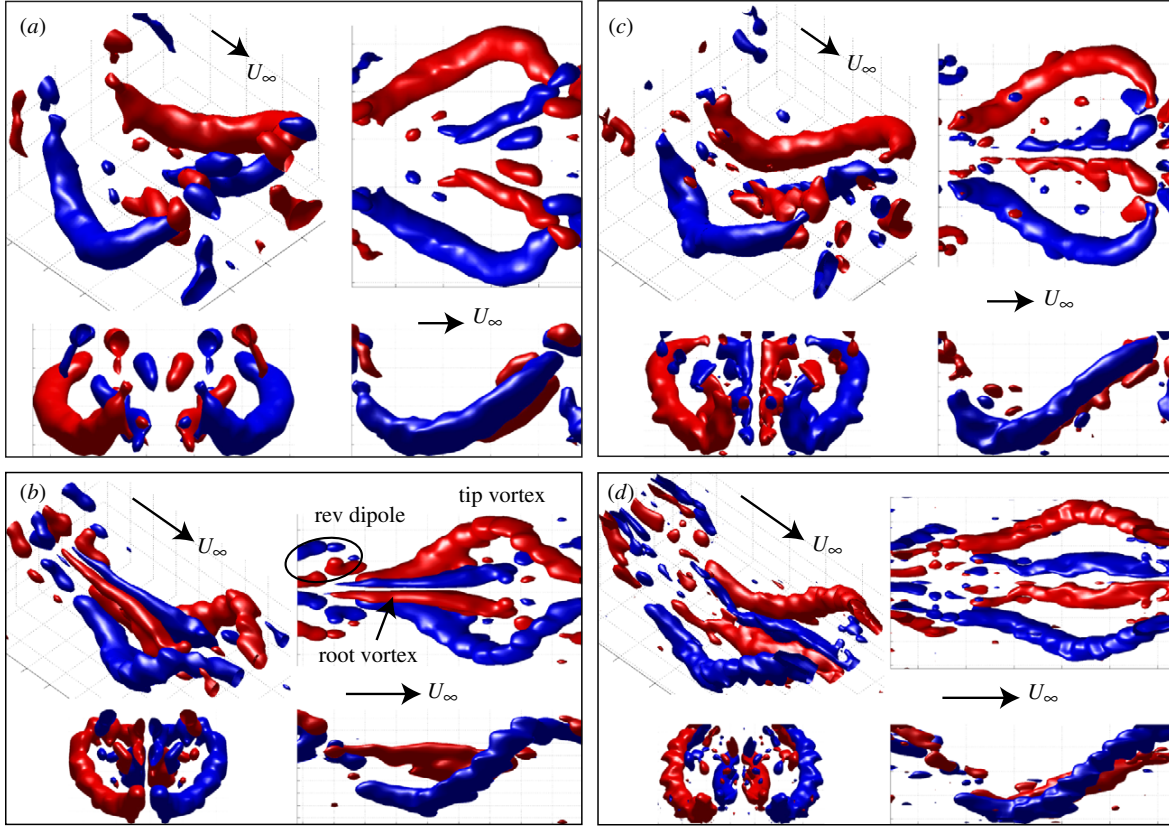
Figure 2. Different views of iso-surfaces of the stream-wise component of vorticity in the wake of a flying *G. soricina* and *L. yerbabuenae* for a whole wingbeat. The red tube-like iso-surfaces show positive stream-wise vorticity and the blue iso-surfaces show negative stream-wise vorticity. The different panels are: (*a*) male *G. soricina* at $3.2\,\mathrm{m\,s^{-1}}$, isovalue: $\omega_{\mathrm{iso}} = 54\,\mathrm{s^{-1}}$; (*b*) female *G. soricina* at $6.1\,\mathrm{m\,s^{-1}}$, isovalue: $\omega_{\mathrm{iso}} = 36\,\mathrm{s^{-1}}$; (*c*) male *L. yerbabuenae* at $3.3\,\mathrm{m\,s^{-1}}$, isovalue: $\omega_{\mathrm{iso}} = 53\,\mathrm{s^{-1}}$; (*d*) female *L. yerbabuenae* at $6.3\,\mathrm{m\,s^{-1}}$, isovalue: $\omega_{\mathrm{iso}} = 35\,\mathrm{s^{-1}}$. Each (*a*)–(*d*) consist of four different views: perspective view (northwest); top view (northeast); front view (southwest); side view (southeast). Wind tunnel velocity vectors U_{∞} are found in the perspective view, and in between the top and side view.

therefore the vortex structures that we will use to define the wakes for both bat species. The flight forces associated with these different vortex structures can be estimated using Kelvin's theorem and inviscid vortex theory [25] as follows (for details see electronic supplementary material, 'Vortex wake model of flapping flight'):

$$
\left.
\begin{aligned}
F_{\mathrm{tip}}(\tau) &= \rho\, U_{\infty}\, b_{\mathrm{tip}}(\tau)\, \Gamma_{\mathrm{tip}}(\tau), \\
F_{\mathrm{root}}(\tau) &= \rho\, U_{\infty}\, b_{\mathrm{root}}(\tau)\, \Gamma_{\mathrm{root}}(\tau) \\
\text{and} \qquad F_{\mathrm{rev}}(\tau) &= \rho\, U_{\infty}\, d_{\mathrm{rev}}(\tau)\, \Gamma_{\mathrm{rev}}(\tau),
\end{aligned}
\right\}
\tag{3.1}
$$

where ρ is air density, $\Gamma_{\mathrm{tip}}(\tau)$ is the circulation of the tip vortex and $\Gamma_{\mathrm{root}}(\tau)$ is the circulation of the root vortex. $\Gamma_{\mathrm{rev}}(\tau)$ is the circulation of the reversed vortex dipole, defined as the mean value of the inner and outer vortex of the vortex dipole (respectively, $\Gamma_{\mathrm{rev}}^{+}$ and $\Gamma_{\mathrm{rev}}^{-}$)

$$
\Gamma_{\mathrm{rev}} = \frac{(|\Gamma_{\mathrm{rev}}^{+}| + |\Gamma_{\mathrm{rev}}^{-}|)}{2}.
\tag{3.2}
$$

The $b_{\mathrm{tip}}(\tau)$ is the distance between the tip vortices of the left and right wing at τ, which is equal to twice the y-directional distance between the tip vortex to the body centreline (figure 1), $b_{\mathrm{root}}(\tau)$ is the distance between the root vortices, $d_{\mathrm{rev}}(\tau)$ is the width of the reversed vortex dipole (defined as the horizontal component of the red bar in figure 1*b,d*). Thus, we ignored the sideway forces (in y-direction), as these forces will cancel out owing to the symmetry of the left and right wing during steady flight.

The lift and thrust components of the forces in equation (3.1) can be determined by

$$
\left.
\begin{aligned}
L(\tau) &= F(\tau)\cos(\bar{\gamma}(\tau)) \\
\text{and} \qquad T(\tau) &= F(\tau)\sin(\bar{\gamma}(\tau)).
\end{aligned}
\right\}
\tag{3.3}
$$

Note that this is the lift (L) of the whole flying animal, defined as the force vertical and perpendicular to U_{∞}, similar to L of a helicopter, and thrust (T) is defined as the force component of F that is parallel to U_{∞}. $\bar{\gamma}(\tau)$ is the mean instantaneous forward tilt angle of the specific vortex force, which can be determined from the vortex sheet orientation (for details see electronic supplementary material,

'vortex wake model of flapping flight'). The mean vortex sheet angle for the tip- and root-vortex structures were estimated as

$$\overline{\gamma}(\tau) = \frac{\gamma(\tau) + \gamma_{\text{body}}(\tau)}{2} = \frac{(1 - (A_{\text{body}}/A))}{2}\gamma(\tau), \quad (3.4)$$

where $\gamma(\tau)$ is the tip- or root-vortex angle, A_{body}/A is the ratio between the vertical body movement amplitude and the vertical wing movement amplitude at the vortex position (see electronic supplementary material, 'vortex wake model of flapping flight'). There is a minus sign in front of A_{body}/A because the body movement is in anti-phase compared with the wing movement (the body moves up when the wing moves down). Kinematics analysis showed that throughout the flight speed range $A_{\text{body}}/A_{\text{tip}} = 0.055 \pm 0.006$ for *G. soricina* (based on data presented by [19]), and $A_{\text{body}}/A_{\text{tip}} = 0.059 \pm 0.009$ for *L. yerbabuenae* (based on R. von Busse, L. C. Johansson, Y. Winter & A. Hedenström 2011, unpublished data). Since the relative body movement is consistent between species and flight speeds, $A_{\text{body}}/A_{\text{tip}} = 0.06$ is used in equation (3.4) for all flight speeds and both species. The body to root vortex movement is determined as $A_{\text{body}}/A_{\text{root}} = A_{\text{body}}/A_{\text{tip}} \times A_{\text{tip}}/A_{\text{root}}$. Since the root vortex cannot directly be linked to a certain wing section, $A_{\text{tip}}/A_{\text{root}}$ is determined using the vertical paths of the tip and root vortices. For the reversed vortex dipole, the mean vortex angle is equal to the mean $\gamma(\tau)$ of the outer and inner vortex of the dipole. The angle of each vortex structure ($\gamma(\tau)$) can be determined from the horizontal vortex path as

$$\gamma(\tau) = \tan^{-1}\left(\frac{\mathrm{d}z(\tau)}{\mathrm{d}x}\right) = \tan^{-1}\left(\frac{\mathrm{d}\tau}{\mathrm{d}x}\frac{\mathrm{d}z(\tau)}{\mathrm{d}\tau}\right)$$
$$= \tan^{-1}\left(\frac{1}{U_{\infty}\Pi}\frac{\mathrm{d}z(\tau)}{\mathrm{d}\tau}\right). \quad (3.5)$$

We tested the sensitivity of the lift and thrust estimates on the wake angle assumptions in equation (3.4) by alternatively assuming no vertical body movement ($\gamma_{\text{body}} = 0$), instead of a 6 per cent anti-phase body movement. This resulted in a mean reduction in lift force of $0.4 \pm 0.1\%$ of the total lift, and a mean thrust force increase of $5.6 \pm 0.4\%$ of the total thrust.

The total lift and thrust for a flying bat are determined by summing up the different components (note that each single wing generates a reversed vortex dipole)

$$\left.\begin{array}{l} L(\tau) = L_{\text{tip}}(\tau) + L_{\text{root}}(\tau) + 2\,L_{\text{rev}}(\tau) \\ \text{and} \quad T(\tau) = T_{\text{tip}}(\tau) + T_{\text{root}}(\tau) + 2\,T_{\text{rev}}(\tau) \end{array}\right\} \quad (3.6)$$

From the $L(\tau)$ and $T(\tau)$ distribution of the flying bat, the mean effective lift and thrust for one wingbeat can be determined by integrating $L(\tau)$ and $T(\tau)$ throughout

the wingbeat as

$$\left.\begin{array}{l} L = \int_{\tau=0}^{1} L(\tau)\mathrm{d}\tau \\ \text{and} \quad T = \int_{\tau=0}^{1} T(\tau)\mathrm{d}\tau. \end{array}\right\} \quad (3.7)$$

For a steady flying bat, the mean effective lift L should be equal to the weight of the bat ($L = -W$), while the mean thrust should be equal to the mean drag produced by the whole animal ($T = -D$). Hence, by comparing L with the body weight of the bat, the validity of the vortex wake model can be tested. The lift-to-drag ratio, which is an important value for flight efficiency, can be determined by $L/D = L/-T$.

To compare $F(\tau)$, $L(\tau)$ and $T(\tau)$ for both bat species, we have normalized them using the weight of the animal

$$\left.\begin{array}{l} F^*(\tau) = \dfrac{F(\tau)}{W}, \\[4pt] L^*(\tau) = \dfrac{L(\tau)}{W} \\[4pt] \text{and} \quad T^*(\tau) = \dfrac{T(\tau)}{W}, \end{array}\right\} \quad (3.8)$$

where W is the weight of the bat. The vertical movement of the different vortex structures, required to determine the force angle, is normalized by:

$$z^*(\tau) = \frac{z(\tau)}{b/2}. \quad (3.9)$$

where b is the wingspan (table 1).

4. STATISTICS

4.1. Average wingbeat wake

The average wingbeat wake is defined, for each species and flight speed combination, by determining the average $F^*(\tau)$ and $z^*(\tau)$ distribution of the tip vortex, root vortex and the reversed vortex dipole [17]. With these characteristics the average wake for each species and speed combination can be modelled and analysed. The distributions were determined by fitting a cubic smoothing spline (Matlab, csaps, smoothing parameter $= 1-10^{-3}$) through the data points of the different PIV measurements. To ensure that the mean wingbeat splines are periodic, meaning that the slope and position of each spline is the same at $\tau = 0$ and at $\tau = 1$, the data points were multiplied twice and distributed over three wingbeat periods ($-1 \leq \tau \leq 2$). The mean wingbeat is described by the middle sub-spline ($0 \leq \tau \leq 1$). The relative deviation of the data points from the mean was estimated using a sliding 95% confidence interval, determined from a sliding window of 20 local data points, where the value of 20 corresponds to the average amount of wingbeats used to construct the mean wingbeat.

4.2. Temporal force distribution

To determine any between-species differences in the temporal force distributions we used a mixed linear model, for each flight speed separately. The

normalized tip-vortex force estimates $F_{\text{tip}}^*(\tau)$ for each PIV measurement at a certain flight speed was set as dependent variable, with *species* as fixed factor. *Individual* was nested within *species*, *sequence* nested within *individual* and *wingbeat* nested within *sequence*, were set as random variables. τ is used as a covariate and was included as τ, τ^2, τ^3 and τ^4, which corresponds to fitting a fourth-order polynomial to the data. The two species were allowed to vary in the different coefficients in the polynomial by adding the interaction between species and τ and any higher orders of τ. Since we do not have an *a priori* hypothesis about how F_{tip}^* should vary with τ, we first tested the fourth-order polynomial and successively removed the highest order non-significant combination. To allow for a better fit of the rather low-order polynomials (without affecting any differences between the species), the data were time shifted $\tau^* = \tau + \Delta\tau$ so that the minimum value of F_{tip}^* coincided with $\tau^* = 0$.

4.3. Maximum lift-to-drag ratio and its corresponding flight speed

To determine any between species differences in the lift-to-drag polars $(L/D(U_\infty))$, while controlling for difference in weight of the bats, the flight speeds are normalized. We normalized U_∞ for *G. soricina* with the unit speed ($U_\infty^* = U_\infty/U_{\text{char}}$ with $U_{\text{char}} = 1$), so we normalized U_∞ for *L. yerbabuenae* by $U_{\text{char}} = (M^*)^{1/6}$.

Since the L/D estimates are based on average wingbeats, error estimates are lost in the $L/D(U_\infty^*)$ distributions. Therefore, a jack-knife method was used to evaluate the variation in the $L/D(U_\infty^*)$ estimates, for each species–speed combination separately [26]. For a certain species–speed combination all the measured flight sequences are consecutively removed and replaced. At each removal L/D is estimated, resulting in a distribution of N L/D estimates per species–speed combination, with N being the amount of sequences measured at that species–speed combination. Through the resulting $L/D(U_\infty^*)$ distribution a third-order polynomial is fitted, for each species separately, which is used to estimate the maximum lift-to-drag ratio $(L/D_{\max})$ and the corresponding flight speed $(U_{L/D_{\max}}^*)$. The variation in $L/D_{\max}$ and $U_{L/D_{\max}}^*$ was determined using the covariance matrix of the polynomial error. From the covariance matrix, we sampled 10 000 sets of polynomial coefficients resulting in 10 000 estimates of $L/D_{\max}$ and $U_{L/D_{\max}}^*$ per species. These distributions were used to determine the 95% confidence interval of the $L/D_{\max}$ and $U_{L/D_{\max}}^*$ estimates.

5. RESULTS AND DISCUSSION

5.1. Wake topology

The overall vortex wake topology for one wingbeat for both *G. soricina* and *L. yerbabuenae* flying at $U_\infty = 3$ and 6 m s^{-1} is shown in figure 2. In the iso-surface vorticity wake plots both the tip- and root vortices are distinguishable throughout almost the complete wingbeat (figure 2). Also the reversed vortex dipole is visible at the end of the upstroke and start of the downstroke, although they are more prominent at 6 m s^{-1} than at 3 m s^{-1} (best seen on the left side of the top views in figure 2). It is assumed that the reversed vortex dipole consists of the inner and outer vortices of a closed vortex loop, called the reversed vortex loop [23]. The spanwise parts of the vortex loop (the parts along the y-axis) are not visible because figure 2 shows only stream-wise vorticity, which is also the reason why no start or stop vortices are visible. The wake patterns for both species are qualitatively strikingly similar. The same structures are visible in both species, and only minor differences are present, such as the position of the root vortices at 3 m s^{-1} and the relative strength of the reversed vortex dipole.

The vortex wake topology described here is similar to the wakes earlier described for bats [14–16,23,24]. When comparing the bat wake data with bird wake data at similar time resolution [17,27], it can be concluded that the bat wake topology is more complex than for birds that have weaker root vortices and no reversed vortex dipoles (cf. [27]).

5.2. Lift and drag estimates

To investigate if the similarities and differences in the vortex wakes of the different bat species have also quantitative merit, the average force distribution over the wingbeats were constructed for each species and speed combination (figure 3 and electronic supplementary material, figures S4 and S5). From these two distributions, the lift and thrust components for each wake structure were determined using equations (3.3)–(3.5) (electronic supplementary material, figures S6 and S7), and by adding these (equation (3.6)) the total lift $(L^*(\tau))$ and thrust $(T^*(\tau))$ distributions were determined (figure 4 and electronic supplementary material, figure S8). By integrating $L^*(\tau)$ and $(T^*(\tau)$ throughout the wingbeat (equation (3.7)), the mean effective lift-to-weight ratio (L/W) and thrust-to-weight ratio (T/W) were determined.

To test the accuracy of our vortex wake model, we focus on the L/W (figure 5a). Across the flight speed range $L/W = 0.97 \pm 0.03$ for *G. soricina* and $L/W = 0.93 \pm 0.05$ for *L. yerbabuenae*, which are sufficiently close to 1, suggesting that the flight force estimate based on the model and measurements are reasonable (cf. [15]).

If assuming that the estimated mean thrust generated throughout the average wingbeat equals drag of the flying bat, we can determine the effective lift-to-drag ratio $L/D = -L/T$ for the bats (figure 5b). From the statistical analysis of the $L/D(U_\infty^*)$ distribution, we find that both the maximum lift-to-drag ratio $(L/D_{\max})$ and the corresponding normalized flight speed $(U_{L/D_{\max}}^*)$ are significantly different between the species (electronic supplementary material, figure S9). For *L. yerbabuenae* the maximum lift-to-drag ratio $(L/D_{\max} = 6.93$ (6.77–7.11, 95% confidence interval)) is
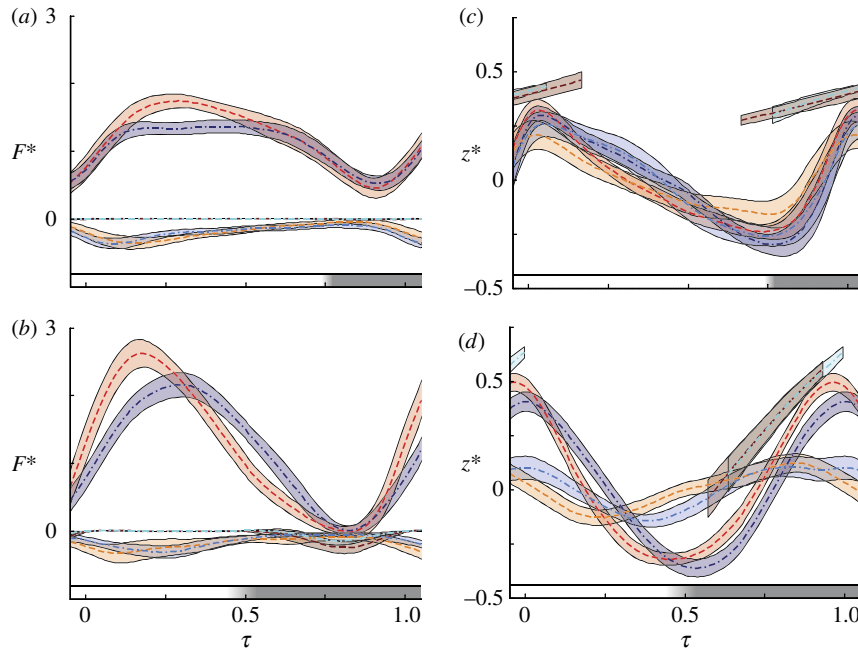
Figure 3. $F^*(\tau)$ and $z^*(\tau)$ distributions for the different wake structures throughout the wingbeat of *G. soricina* and *L. yerbabuenae*, consisting of the average spline and the 95% confidence interval. (*a*) $F^*(\tau)$ at $2\,\mathrm{m\,s^{-1}}$, (*b*) $F^*(\tau)$ at $6\,\mathrm{m\,s^{-1}}$, (*c*) $z^*(\tau)$ at $2\,\mathrm{m\,s^{-1}}$, and (*d*) $z^*(\tau)$ at $6\,\mathrm{m\,s^{-1}}$. The results for the different species and wake structures are colour-coded as follows: red dashed lines, *G. soricina* tip vortex; orange dashed lines, *G. soricina* root vortex; brown dashed lines, *G. soricina* reversed vortex loop; dark blue dashed-dotted lines, *L. yerbabuenae* tip vortex; light blue dashed-dotted lines, *L. yerbabuenae* root vortex; turquoise dashed-dotted lines, *L. yerba-buenae* reversed vortex loop. The white-grey colour bars at the bottom of each panel show the downstroke (white) and upstroke (grey) section of the wingstroke. The gradient indicates the difference in the downstroke/upstroke transition between the two species, where *G. soricina* has a consistently earlier transition.
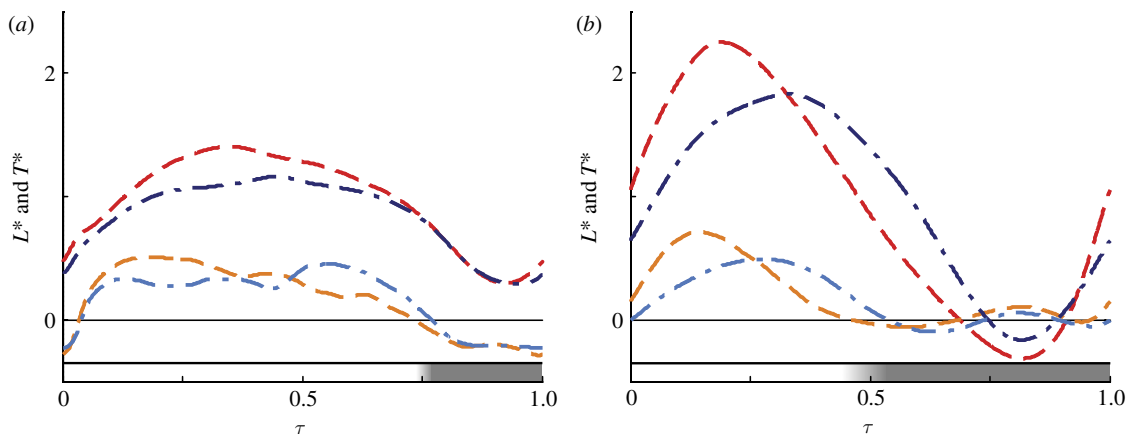
Figure 4. The overall $L^*(\tau)$ and $T^*(\tau)$ distribution throughout the average wingbeat for *G. soricina* and *L. yerbabuenae* at (*a*) 2 m s^{-1} and (*b*) 6 m s^{-1}. The results of $L^*(\tau)$ and $T^*(\tau)$ for the different species are colour-coded as follows: red dashed lines, *G. soricina* L^*; orange dashed lines, *G. soricina* T^*; dark blue dashed-dotted lines, *L. yerbabuenae* L^*; light blue dashed-dotted lines, *L. yerbabuenae* T^*. The white-grey colour bars at the bottom of each panel show the downstroke (white) and upstroke (grey) section of the wingstroke. The gradient indicates the difference in the downstroke/upstroke transition between the two species, where *G. soricina* has a consistently earlier transition.

lower and occurs at a higher flight speed ($U^*_{L/D_{\max}} = 4.39$ (4.18–4.57)) than for *G. soricina* ($L/D_{\max} = 7.54$ (7.44–7.65) and $U^*_{L/D_{\max}} = 3.45$ (3.42–3.49)). The differences in $U^*_{L/D_{\max}}$ between the species are in line with our prediction that the highly mobile *L. yerbabuenae* should fly more efficiently at fast-forward flight speeds, while the more stationary *G. soricina* should fly more efficiently at hovering and slow flight speeds. Since both species operate

at similar Re, the difference in $L/D_{\max}$ is not expected, but can partly be explained by the fact that $L/D_{\max}$ for *L. yerbabuenae* is underestimated using the third-order polynomial fit (figure 5*b* and electronic supplementary material, figure S9).

To the best of our knowledge, this is the first direct estimate of L/D for flapping flight of bats, but the values are similar to L/D for a gliding dog-faced bat
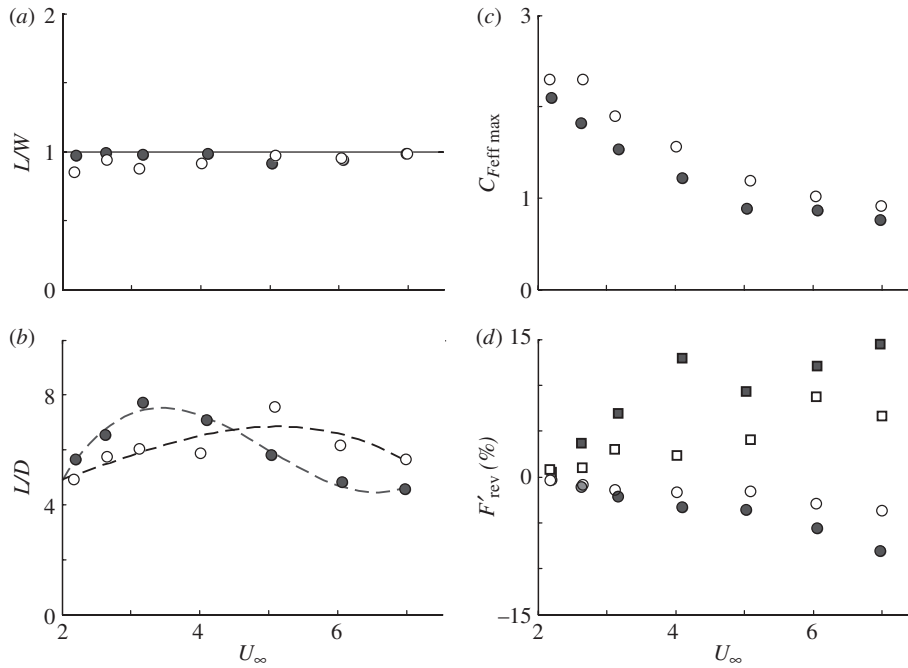
Figure 5. Aerodynamic measures in relation to forward flight speed in *G. soricina* and *L. yerbabuenae*. (*a*) The lift-to-weight ratio L/W; (*b*) the lift-to-drag ratio L/D; (*c*) the maximum effective force coefficient $C_{F\text{eff max}}$. The filled circles represent data for *G. soricina* and the open circles for *L. yerbabuenae*. (*d*) The relative contribution of the reversed vortex dipole on L (filled and open circles) and T (filled and open squares), defined as $L'_{\text{rev}} = L^*_{\text{rev}}/L^* \times 100\%$ and $T'_{\text{rev}} = T^*_{\text{rev}}/T^* \times 100\%$.

Rousettus aegyptiacus ([28]; figure 6). L/D at the largest measured flight speed ($U_\infty = 7\,\text{m s}^{-1}$) for *G. soricina* ($L/D = 6.0$) and *L. yerbabuenae* ($L/D = 6.8$) are compared with L/D of flapping birds (figure 6), for details on the L/D calculations [30]. For the flapping birds a positive correlation can be distinguished between L/D and Re. Our bats operate at the low end of this Re range, and when taking the L/D–Re correlation into account, the bats perform similar to birds, which seem to confirm that thin flexible bat wings performs relatively well at low Re [6,35]. If bat wings, in general, are more optimized for lower Re than birds, this would suggest that migrating bats should fly at lower flight speeds than birds, which could be one explanation for why bats migrate less and in general shorter distances than birds [36].

5.3. Force dynamics throughout the average wingbeat

The results of the analysis of how $F^*_{\text{tip}}(\tau)$ varies over the wingbeat in the two species (table 2 and electronic supplementary material, figure S10) show that for all speeds except $3\,\text{m s}^{-1}$, we find significant differences between the two bat species. This corresponds well with the fact that the 95% confidence intervals of $F^*_{\text{tip}}(\tau)$ for the two species do not overlap for at least part of the wingbeat (figure 3*a,b* and electronic supplementary material, figure S4), except for the force distribution at $3\,\text{m s}^{-1}$ (electronic supplementary material, figure S4*c*).

The main difference in $F^*_{\text{tip}}(\tau)$ between the species is that the force production is more equally distributed throughout the wingbeat for *L. yerbabuenae* than for *G. soricina*, resulting in a consistently lower maximum $F^*_{\text{tip}}(\tau)$ value for *L. yerbabuenae*. The tip vortex vertical movement throughout the wingbeat does not vary much with speeds or between species (figure 3*c,d* and electronic supplementary material, figure S5).

The root vortex force $F^*_{\text{root}}(\tau)$ is much smaller than that of the tip vortex, but it is not negligible. The vertical movement of the root vortex throughout the wingbeat varies a lot between the different flight speeds (figure 3*c,d* and electronic supplementary material, figure S5). The root vortex follows the tip vortex movement closely at the lowest flight speed (figure 3*c*), while it moves very little up and down at the highest speed (figure 3*d*). This is because, at higher speeds, the root vortex is shed from the inner wing or from the tail membrane (figure 2*b*), while at low flight speeds, the root vortex is shed further out on the wing (figure 2*a*). This means that, at low flight speeds, the outer wing generates most of the aerodynamic forces, probably because the effective airflow over the outer wing is higher than at the inner wing and body.

The force contribution of the reversed vortex dipole ($F^*_{\text{rev}}(\tau)$) is small compared with that of the tip and root vortex. At the lowest flight speed it is negligibly small (figure 3*a*), while for the higher speeds it is only present at the upstroke, where F^*_{rev} is of similar size as that of the other vortex forces. $F^*_{\text{rev}}(\tau)$ is consistently larger for *G. soricina* than for *L. yerbabuenae*. The vertical movement of the reversed vortex dipole throughout the wingbeat is similar for the two bat species (figure 3*c,d* and electronic supplementary material, figure S5).
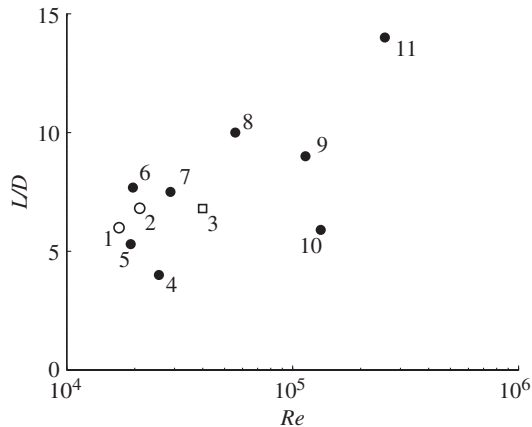
Figure 6. Maximum lift-to-drag ratio for bats and birds versus the Reynolds number. The different data points are—flapping bats (open circles): (1) *G. soricina*, (2) *L. yerbabuenae*; gliding bat (open squares): (3) dog-faced bat *Rousettus aegyptiacus* [28]; birds (filled circles): (4) Budgerigar *Melopsittacus undulatus* [29], (5) Blackcap *Sylvia atricapilla L.* [27], (6) Common swift *Apus apus* [17], (7) Robin *Erithacus rubecula* [30], (8) black-billed magpie *Pica pica* [31], (9) European starling *Sturnus vulgaris* [32], (10) pigeon *Columba livia* [33], (11) bar-headed goose *Anser indicus* [34].

The detailed contribution of the different vortex structures to the total lift and thrust production throughout the wingbeat is found in the electronic supplementary material (figures S6 and S7). By summing the lift and thrust of these different wake structures, the total lift and thrust distribution throughout the wingbeat was estimated (figure 4 and electronic supplementary material, figure S8). For both bat species, the majority of lift and thrust are generated during the downstroke at all flight speeds. However, during the upstroke, the lift and thrust production varies significantly with flight speed. At flight speeds below 4–$5\,\mathrm{m\,s^{-1}}$ the lift production is positive and the thrust production is negative (drag production) during the upstroke, while for higher speeds a small amount of negative lift in combination with positive thrust is generated during part of the upstroke (figure 4 and electronic supplementary material, figure S8). This combination of positive thrust and negative lift during the upstroke is a result of the reversed vortex dipole (electronic supplementary material, figure S7).

To be able to compare the force estimates with data of steady wings, we determined the maximum effective flight force coefficient defined as

$$C_{F,\mathrm{eff,max}} = \frac{F_{\max}}{1/2\rho\,U_{\infty,\mathrm{eff}}^2\,S}, \qquad (5.1)$$

where $F_{\max}$ is the maximum force throughout the wingbeat, S is the wing area (table 1), $U_{\infty,\mathrm{eff}}$ is the effective free-stream flight velocity. The effective free-stream velocity is a function of the forward flight speed and the flapping movement of the wing, which can be estimated from Lentink & Gerritsma [37] as

$$U_{\infty,\mathrm{eff}} \approx U_\infty \times \sqrt{(4\times St_{\mathrm{mean}})^2 + 1}, \qquad (5.2)$$

where St_{mean} is the mean Strouhal number of the wing, which we assume to be half the wing tip Strouhal number

($St_{\mathrm{mean}} = St/2$). $C_{F,\mathrm{eff,max}}$ is higher for *L. yerbabuenae* than for *G. soricina* (figure 5c), which could be explained by the larger wing loading for *L. yerbabuenae* (table 1). The maximum possible lift coefficient for steady wings is generally regarded as about $C_L = 1.6$ [6] (for steady wings $C_L = C_F$), indicating that for *G. soricina* unsteady aerodynamic mechanisms, like a leading edge vortex [38], are expected to be present at flight speeds up to at least $3\,\mathrm{m\,s^{-1}}$, while for *L. yerbabuenae* unsteady aerodynamic mechanisms can be expected at speeds up to at least $4\,\mathrm{m\,s^{-1}}$.

5.4. Reversed vortex dipole

To determine the influence of the reversed vortex dipole on the flight forces, we consider how the different wake structures contribute to lift and thrust production throughout the wingbeat (electronic supplementary material, figures S6 and S7). The reversed vortex dipole is present at the end of the upstroke [3,14,15,23], and generates negative lift in combination with positive thrust (figure 5d; see also [24]). The relative contribution of the reversed vortex dipole to the total lift and thrust production (respectively, L'_{rev} and T'_{rev}) varies almost linear with flight speed (figure 5d) resulting in a negligibly small contribution at the lowest speeds, but a significant contribution at the highest speeds.

Taken together, as a result of the vortex dipole, there is a positive total thrust during part of the upstroke for the highest flight speeds (figure 4 and electronic supplementary material, figure S8), and this thrust production is higher for *G. soricina* than for *L. yerbabuenae* (figure 5d). The L/D results show that the thrust requirements at these high flight speeds are higher than at medium flight speeds, as well as higher for *G. soricina* than for *L. yerbabuenae* (figure 5a). This suggests that the reversed vortex dipole is generated by the bat wing mainly to generate extra thrust, which is accompanied with some negative lift. A similar mechanism has been described as optimal for a flapping wing with a relatively large thrust requirement [39,40], where also both thrust and negative lift are generated by the outer part of the wing during the upstroke.

The reversed vortex dipole, resulting in negative lift and positive thrust, is generated by the bats by moving the outer wing upwards during the end of the upstroke resulting in $U_{\infty,\mathrm{eff}}$ with a downward component, and by positioning the outer wing at a negative effective angle of attack, α_{eff} ([19], R. von Busse, L. C. Johansson, Y. Winter & A. Hedenström 2011, unpublished data).

5.5. Concluding remarks

We determined the vortex wake dynamics for the average wingbeat of two microchiropteran bat species, from which we estimated the temporal flight force distributions and average flight performance, across a range of flight speeds from near hover to cruising flight speed. The results for *G. soricina* are similar to the results described by Hedenström *et al.* [23] and

Table 2. p-values for the $F_{\text{tip}}^*(\tau)$ polynomial analysis at the measured flight speeds (U_∞). The p-values in bold are significant.

U_∞	$2\,\mathrm{m\,s^{-1}}$	$2.5\,\mathrm{m\,s^{-1}}$	$3\,\mathrm{m\,s^{-1}}$	$4\,\mathrm{m\,s^{-1}}$	$5\,\mathrm{m\,s^{-1}}$	$6\,\mathrm{m\,s^{-1}}$	$7\,\mathrm{m\,s^{-1}}$
intercept	**0.0257**	0.1532	0.4157	**0.0064**	**<0.0001**	**0.0002**	**0.0014**
species	0.5719	0.1607	0.2037	0.2042	**<0.0001**	**0.0112**	0.1362
time (τ)	**<0.0001**	**<0.0001**	**<0.0001**	**<0.0001**	**<0.0001**	**<0.0001**	**<0.0001**
τ^2	**<0.0001**	**<0.0001**	**<0.0001**	**<0.0001**	**<0.0001**	0.1386	**0.0096**
τ^3	**0.0063**	**<0.0001**	**<0.0001**	**<0.0001**	0.3051	**<0.0001**	**<0.0001**
τ^4	0.0648	—	**0.0130**	—	0.4055	**<0.0001**	**<0.0001**
$\tau \times$ species	0.4313	**<0.0001**	0.7344	**0.0002**	**<0.0001**	**<0.0001**	**<0.0001**
$\tau^2 \times$ species	0.4913	**0.0002**	0.7210	**0.0003**	**<0.0001**	**0.0002**	**<0.0001**
$\tau^3 \times$ species	0.1203	**<0.0001**	0.8531	**0.0011**	**0.0008**	**0.0289**	**0.0010**
$\tau^4 \times$ species	**0.0464**	—	0.9916	—	**0.0147**	0.3339	**0.0306**

Johansson *et al.* [24], but the present high-speed stereo PIV analysis allowed us to present more detailed wakes.

The wake pattern and associated measures are strikingly similar between the two species, which is in line with the fact that the bats operate at similar *St* and *Re* and our prediction based on the similar wake patterns of *G. soricina* and *L. yerbabuenae* in a previous study [3,14], and similarities with a larger megachiropteran bat flying at higher *Re* [15]. Still, a few differences in the wake dynamics of the two bat species could be unravelled. The main difference was in the timing of the force production. *G. soricina*, generated the highest flight force during the first half of the downstroke, while *L. yerbabuenae* generated lower forces more evenly throughout the downstroke and into the beginning of the upstroke. A typical wing has an optimal force coefficient ($C_{F,\text{opt}}$) at which the relative drag is lowest. This $C_{F,\text{opt}}$ occurs generally at moderate values of C_F, indicating that a wing at $C_{F,\text{opt}}$ should operate at relatively high speeds to generate significant/enough forces (figure 5c, [25]). If this is also the case for bat wings, a fast flying *L. yerbabuenae* could operate at this $C_{F,\text{opt}}$ for a larger fraction of the wingstroke, resulting in more efficient flight at high speeds than *G. soricina*.

A direct estimate of the flight efficiency for these bat species are the determined L/D values. When controlling for differences in weight between the species, the speed at which L/D is maximum ($U_{L/D_{\max}}^*$) was significantly higher for *L. yerbabuenae* than for *G. soricina*. This is in line with our prediction that the more mobile and migratory species *L. yerbabuenae* should fly more efficiently at higher flight speeds, and that the residential species *G. soricina* should fly more efficiently at low flight speeds. Although the difference in flight performance between the two species may depend on a range of morphological and ecological factors, the agreement with the predictions from the species relative mobility suggests a hypothesis to be further tested in future comparative studies.

REFERENCES

1 Norberg, U. M. 1970 Functional osteology and myology of the wing of *Plecotus auritus* Linnaeus (Chiroptera). *Ark. Zool.* **33**, 483–543.

2 Swartz, S. M., Groves, M. D., Kim, H. D. & Walsh, W. R. 1996 Mechanical properties of bat wing membrane skin. *J. Zool.* **239**, 357–378. (doi:10.1111/j.1469-7998.1996.tb05455.x)

3 Hedenström, A., Johansson, L. C. & Spedding, G. R. 2009 Bird or bat: comparing airframe design and flight performance. *Bioinspir. Biomim.* **4**, 015001. (doi:10.1088/1748-3182/4/1/015001)

4 Johansson, L. C., Wolf, M. & Hedenström, A. 2010 A quantitative comparison of bird and bat wakes. *J. R. Soc. Interface* **7**, 61–66. (doi:10.1098/rsif.2008.0541)

5 Vaughan, T. A. & Bateman, G. C. 1970 Functional morphology of the forelimb of mormoopid bats. *J. Mammal.* **51**, 217–235. (doi:10.2307/1378472)

6 Laitone, E. 1997 Wind tunnel tests of wings at Reynolds numbers below 70 000. *Exp. Fluids* **23**, 405. (doi:10.1007/s003480050128)

7 Schmitz, F. W. 1967 *Aerodynamics of the model airplane.* USA: Translation Branch, Redstone Scientific Information Centre, Research and Development Directorate, US Army Missile Command.

8 Baagøe, H. J. 1987 The Scandinavian bat fauna: adaptive wing morphology and free flight in the field. In *Recent advances in the study of bats* (eds M. B. Fenton, P. Racey & J. M. V. Rayner), pp. 57–74. Cambridge: Cambridge University Press.

9 Norberg, U. M. & Rayner, J. M. V. 1987 Ecological morphology and flight in bats (Mammalia; Chiroptera): wing adaptations, flight performance, foraging strategy and echolocation. *Phil. Trans. R. Soc. Lond. B* **316**, 335–427. (doi:10.1098/rstb.1987.0030)

10 Pennycuick, C. J. 2008 *Modelling the flying bird.* Amsterdam: Elsevier.

11 Heithaus, E. R., Fleming, T. H. & Opler, P. A. 1975 Foraging patterns and resource utilization in seven species of bats in a seasonal tropical forest. *Ecology* **56**, 841–854. (doi:10.2307/1936295)

12 Horner, M. A., Fleming, T. H. & Sahey, C. T. 1998 Foraging behaviour and energetics of a nectar-feeding bat, *Leptonycteris curasoae* (Chiroptera: Phyllostomidae). *J. Zool.* **244**, 575–586. (doi:10.1111/j.1469-7998.1998.tb00062.x)

13 Wilkinson, G. S. & Fleming, T. H. 1996 Migration and evolution of lesser long-nosed bats *Leptonycteris curasoae*, inferred from mitochondrial DNA. *Mol. Ecol.* **5**, 329–339.

14 Hedenström, A., Muijres, F. T., Busse von, R., Johansson, L. C., Winter, Y. & Spedding, G. R. 2009 High-speed stereo PIV measurement of wakes of two bat species flying freely in a wind tunnel. *Exp. Fluids* **46**, 923–932. (doi:10.1007/s00348-009-0634-5)

15 Hubel, T. Y., Riskin, D. K., Swartz, S. M. & Breuer, K. S. 2010 Wake structure and wing kinematics: the flight of the lesser dog-faced fruit bat, *Cynopterus brachyotis. J. Exp. Biol.* **213**, 3427–3440. (doi:10.1242/jeb.043257)

16 Hubel, T., Hristov, N. I., Swartz, S. M. & Breuer, K. S. 2009 Time-resolved wake structure and kinematics of bat flight. *Exp. Fluids* **46**, 933–943. (doi:10.1007/s00348-009-0624-7)

17 Henningsson, P., Muijres, F. T. & Hedenström, A. 2010 Time-resolved vortex wake of a common swift flying over a range of flight speeds. *J. R. Soc. Interface* (doi:10.1098/rsif.2010.0533)

18 Norberg, U. M. & Winter, Y. 2006 Wingbeat kinematics of a nectar-feeding bat, *Glossophaga soricina*, flying at different flight speeds and Strouhal numbers. *J. Exp. Biol.* **209**, 3887–3897. (doi:10.1242/jeb.02446)

19 Wolf, M., Johansson, L. C., von Busse, R., Winter, Y. & Hedenstrom, A. 2010 Kinematics of flight and the relationship to the vortex wake of a Pallas' long tongued bat (*Glossophaga soricina*). *J. Exp. Biol.* **213**, 2142–2153. (doi:10.1242/jeb.029777)

20 Pennycuick, C., Alerstam, T. & Hedenström, A. 1997 A new low-turbulence wind tunnel for bird flight experiments at Lund University, Sweden. *J. Exp. Biol.* **200**, 1441–1449.

21 Batchelor, G. K. 2000 *An introduction to fluid dynamics.* Cambridge: Cambridge University Press.

22 Spedding, G. R., Rosen, M. & Hedenström, A. 2003 A family of vortex wakes generated by a thrush nightingale in free flight in a wind tunnel over its entire natural range of flight speeds. *J. Exp. Biol.* **206**, 2313–2344. (doi:10.1242/jeb.00423)

23 Hedenström, A., Johansson, L. C., Wolf, M., Busse von, R., Winter, Y. & Spedding, G. R. 2007 Bat flight generates complex aerodynamic tracks. *Science* **316**, 894–897. (doi:10.1126/science.1142281)

24 Johansson, L. C., Wolf, M., Busse von, R., Winter, Y., Spedding, G. R. & Hedenström, A. 2008 The near and far wake of Pallas' long tongued bat (*Glossophaga soricina*). *J. Exp. Biol.* **211**, 2909–2918. (doi:10.1242/jeb.018192)

25 Anderson, J. D. 1991 *Fundamentals of aerodynamics.* USA: McGraw-Hill/University of Michigan.

26 Shao, J. & Tu, D. 1995 *The jackknife and bootstrap.* Berlin, Germany: Springer.

27 Johansson, L. C. & Hedenström, A. 2009 The vortex wake of blackcaps (*Sylvia atricapilla L.*) measured using high-speed digital particle image velocimetry (PIV). *J. Exp. Biol.* **212**, 3365–3376. (doi:10.1242/jeb.034454)

28 Pennycuick, C. J. 1971 Gliding flight of the dog-faced bat *Rousettus Aegyptiacus* observed in a wind tunnel. *J. Exp. Biol.* **55**, 833–845.

29 Tucker, V. A. 1968 Respiratory exchange and evaporative water loss in the flying budgerigar. *J. Exp. Biol.* **48**, 67–87.

30 Hedenström, A., Rosén, M. & Spedding, G. R. 2006 Vortex wakes generated by robins *Erithacus rubecula* during free flight in a wind tunnel. *J. R. Soc. Interface* **3**, 263–276. (doi:10.1098/rsif.2005.0091)

31 Boggs, D., Jenkins, F. & Dial, K. 1997 The effects of the wingbeat cycle on respiration in black-billed magpies (*Pica pica*). *J. Exp. Biol.* **200**, 1403–1412.

32 Biewener, A. A., Dial, K. P. & Goslow, G. E. 1992 Pectoralis muscle force and power output during flight in the starling. *J. Exp. Biol.* **164**, 1–18. (doi:10.1016/0022-0981(92)90132-T)

33 Pennycuick, C. J. 1968 Power requirements for horizontal flight in the pigeon *Columba Livia. J. Exp. Biol.* **49**, 527–555.

34 Ward, S., Bishop, C. M., Woakes, A. J. & Butler, P. J. 2002 Heart rate and the rate of oxygen consumption of flying and walking barnacle geese (*Branta leucopsis*) and bar-headed geese (*Anser indicus*). *J. Exp. Biol.* **205**, 3347–3356.

35 Song, A., Tian, X., Israeli, E., Galvao, R., Bishop, K., Swartz, S. & Breuer, K. 2008 Aeromechanics of membrane wings with implications for animal flight. *AIAA J.* **46**, 2096–2106. (doi:10.2514/1.36694)

36 Fleming, T. H. & Eby, P. 2003 Ecology of bat migration. In *Bat ecology*, pp. 156–208. Chicago, IL: University of Chicago Press.

37 Lentink, D. & Gerritsma, M. 2003 Influence of airfoil shape on performance in insect flight. *33rd AIAA Fluid Dynamics Conference and Exhibit.* See http://www.aiaa.org.

38 Muijres, F. T., Johansson, L. C., Barfield, R., Wolf, M., Spedding, G. R. & Hedenström, A. 2008 Leading-edge vortex improves lift in slow-flying bats. *Science* **319**, 1250–1253. (doi:10.1126/science.1153019)

39 Hall, K. C. & Hall, S. R. 1996 Minimum induced power requirements for flapping flight. *J. Fluid Mech. Digit. Arch.* **323**, 285–315.

40 Hall, K. C. & Hall, S. R. 2002 A rational engineering analysis of the efficiency of flapping flight. In *Fixed and flapping wing aerodynamics for micro air vehicle application. Progress in astronautics and aeronautics*, vol. 195, pp. 249–274. New York, NY: Academic Press.
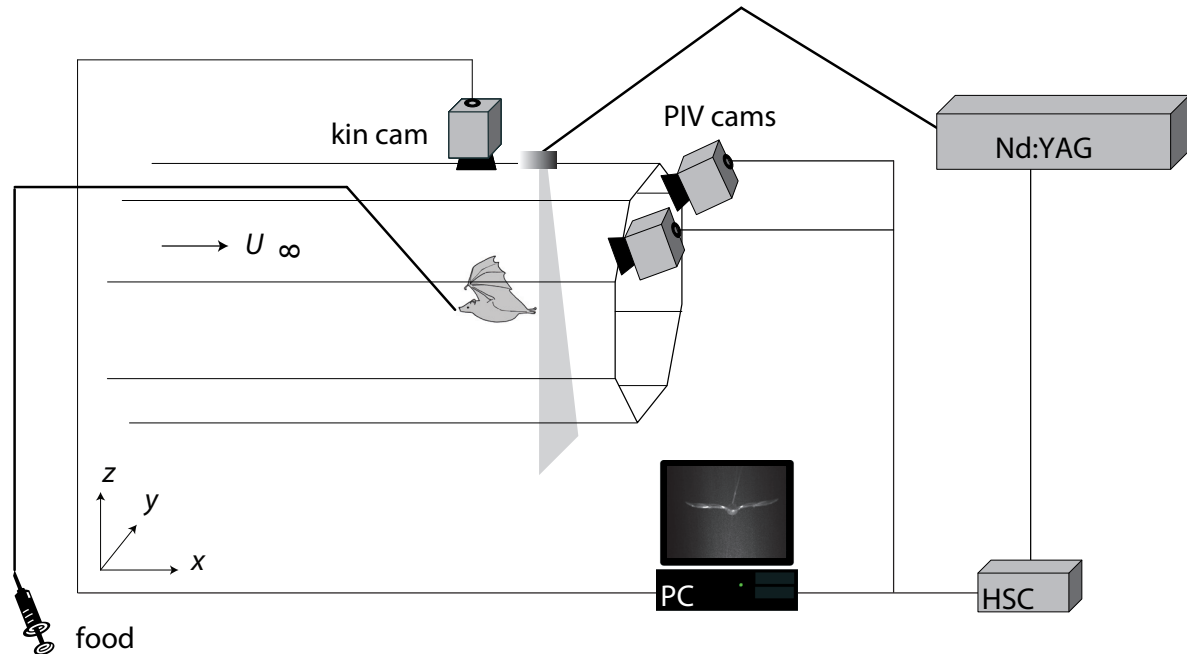
Data Supplement

Experimental setup

Figure S1. Experimental setup consisting of a wind tunnel, a stereoscopic Particle Image Velocimetry (PIV) system, and a high-speed video camera (kin cam). The bat flies in front of the feeder, 20 cm downstream from the feeder tip the laser light sheet is positioned in a transverse (y-z) plane. The two stereo PIV cameras (PIV cams) sample data at 200Hz in a 20x20 cm domain. From the top a synchronized high-speed kinematics camera films the flying bat.

Vortex wake model of flapping flight

When a wing encounters an airflow it will start to produce lift (Figure S2). As a result of this it will shed a vortex, the start vortex (Γ_{start} in Figure S2*a*) from the trailing edge of the wing. According to Kelvin's theorem (e.g. Anderson 1991), the start vortex circulation at a certain spanwise location (along the *y*-axis) is directly related to the lift production of the wing at that location (*L'(y)*), by

$$L'(y) = \rho\, U_\infty\, \Gamma_{start}\,(y) \; , \hspace{3cm} \text{(S1)}$$

where ρ is the air density and U_∞ is the forward flight speed.
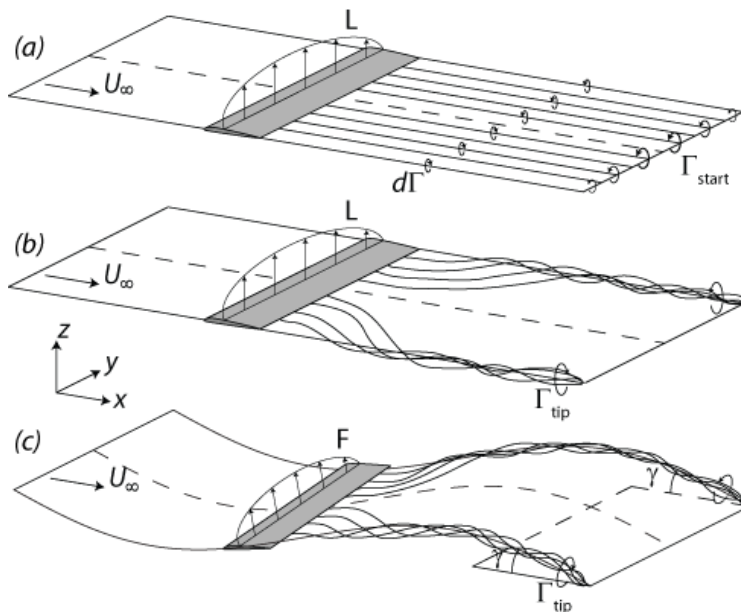

Figure S2. Lift production by a wing with an elliptical lift distribution. *(a)* **a hypothetical case where the parallel streamwise vortex lines do not interact while travelling into the wake. The vortex lines have a circulation equal to the local change in start-vortex circulation** $d\Gamma_{start}$**;** *(b)* **due to vortex interactions the streamwise vortex lines bundle into a single tip vortex with circulation** Γ_{tip}**;** *(c)* **a heaving foil with continuously changing lift force, as a result of this the tip vortex circulation** Γ_{tip} **and orientation also vary with time.**

When ignoring viscosity, vortex theory prescribes that vortex circulation is conserved in a fluid, which means that a vortex must form a ring or extend to the boundaries of a fluid (at ∞ or at a surface). Since the only surface in this system is the wing, each spanwise change in start vortex circulation will introduce a vortex line that connects the start vortex to the wing surface (streamwise vortex lines in Figure S2*a*). The strength of this vortex line at position *y* will be equal to the change in start vortex circulation at *y*, called *dΓ(y)*. By measuring *dΓ(y)* in the wake, the lift per span (*L'*) distribution across the wing span could be determined using

$$L'(Y) = \rho U_\infty \int_{y=0}^{Y} d\Gamma(y)\, dy \,.$$
(S2)

In practice though, the circulation distribution *dΓ(y)* will interact when travelling from the wing into the wake by rolling up into distinct vortices, such as the well known tip vortex (Figure S2*b*). This means that information about the spanwise lift distribution is lost and only the average lift of the whole wing can be determined by measuring the circulation of these compact wake vortices.

Let us assume a simple steady wing system where the complete circulation distribution has rolled up into two tip vortices (Figure S2*b*). The lift generated by this wing can be determined from the tip vortex by

$$L = \rho\, U_\infty\, b_{tip}\, \Gamma_{tip} \,,$$
(S3)

where b_{tip} is the tip vortex span and Γ_{tip} is the circulation of the tip vortex (e.g. Anderson 1991).

Until now we have only considered a wing moving steadily forward, but if the wing starts to heave sinusoidally (Figure S2*c*), both the effective wing speed and the angle-of-attack will vary continually over time, resulting in a temporal variation of wing forces. This means that start or stop vorticity is continually shed from the wing, causing the tip vortex circulation to also vary with time. Consequently the temporal force distribution *F(t)* for the heaving wing can be determined by measuring the temporal tip vortex strength distribution as

$$F(t) = \rho\, U_\infty\, b_{tip}\, \Gamma_{tip}\, (t) \;. \tag{S4}$$

Notice that, in equation (S4), *L* has been replaced by *F*, since for a heaving wing the force generated by the wing does not have to be perpendicular to the free-stream direction, but rather perpendicular to the local free-stream velocity $U_{\infty,eff}$, which is a function of U_∞ and the heaving motion U_{heave}. The angle with which the force is tilted forward or backwards at *t* can be determined by measuring the angle of the wake shed from the wing at time *t*, $\gamma(t)$ (Figure S2*c* and Figure S3). The lift and thrust components of *F* are

$$\begin{aligned} L(t) &= F(t)\cos(\gamma(t)) \\ T(t) &= F(t)\sin(\gamma(t)) \end{aligned} \tag{S5}$$

Note that this is the lift (*L*) of the whole flying animal, defined as the force vertical and perpendicular to U_∞, similar to *L* of a helicopter. This *L* can be very different from the instantaneous lift produced by the wing throughout the wingbeat (Wang 2004). Thrust (*T*) is defined as the force component of *F* that is parallel to U_∞.
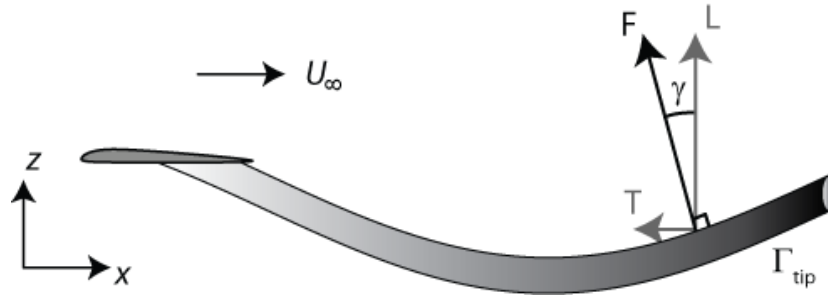
Figure S3. Side view of a hypothetical tip vortex behind a flapping wing. The force *F* generated by the flapping wing is directed perpendicular to the orientation of the vortex system. The effective lift component of this force *L* is directed perpendicular to the free-stream airflow U_∞, while the thrust component *T* is directed parallel to U_∞.

The wing motion of a flying bat is by far more intricate than that of the above described heaving wing (Figure S2*c*), but the model can easily be adapted further to include some of the characteristics of bat flight. The main difference between the heaving wing in Figure S2*c* and a steadily flying bat is that a bat has a body fuselage, which stays relatively steady, and that the wings flap by rotation around the shoulder joint and changes span by flexing the arm wing. This means that, for bats, the tip vortex span b_{tip} in equation (S4) varies throughout the wingbeat, and so for bats we have

$$F(t) = \rho \, U_\infty \, b_{tip}(t) \, \Gamma_{tip}(t) \, , \tag{S6}$$

where $b_{tip}(t)$ is the time varying tip vortex span, which can be estimated from the tip vortex location. Also, for flapping flight of bats, the instantaneous wake angle varies along the span and is not equal to the tip vortex angle $\gamma_{tip}(t)$.

The mean angle of the vortex system behind the bat can be estimated by taking the average of the vortex system angle at the tip vortex and at the body by

$$\bar{\gamma}(t) = \frac{\gamma_{tip}(t) + \gamma_{body}(t)}{2} = \frac{(1 - {A_{body}}/{A_{tip}})}{2}\gamma_{tip}(t) \tag{S7}$$

where $\gamma_{tip}(t)$ is the tip vortex angle at t, ${A_{body}}/{A_{tip}}$ is the ratio between the vertical body movement amplitude and the vertical wingtip movement amplitude. The vertical movement at the body should be measured at the quarter cord point at the wing-body intersect, since this can be assumed to be the aerodynamic centre of that wing section (Anderson 1991). There is a minus sign in front of ${A_{body}}/{A_{tip}}$ because the body movement is typically in anti-phase compared to the wing movement (the body moves up when the wing moves down).

The tip vortex angle can be estimated from the vertical tip vortex location distribution $z_{tip}(t)$ by

$$\gamma_{tip}(t) = \tan^{-1}\left(\frac{dz_{tip}(t)}{dx}\right) = \tan^{-1}\left(\frac{dt}{dx}\frac{dz_{tip}(t)}{dt}\right) = \tan^{-1}\left(\frac{1}{U_\infty}\frac{dz_{tip}(t)}{dt}\right). \tag{S8}$$

References

Anderson, J.D., 1991. *Fundamentals of Aerodynamics*, McGraw-Hill.

Wang, Z., 2004. The role of drag in insect hovering. *J Exp Biol*, 207(23), pp.4147-4155.

Wolf, M. et al., 2010. Kinematics of flight and the relationship to the vortex wake of a Pallas' long tongued bat (Glossophaga soricina). *J Exp Biol*, 213(12), pp.2142-2153.
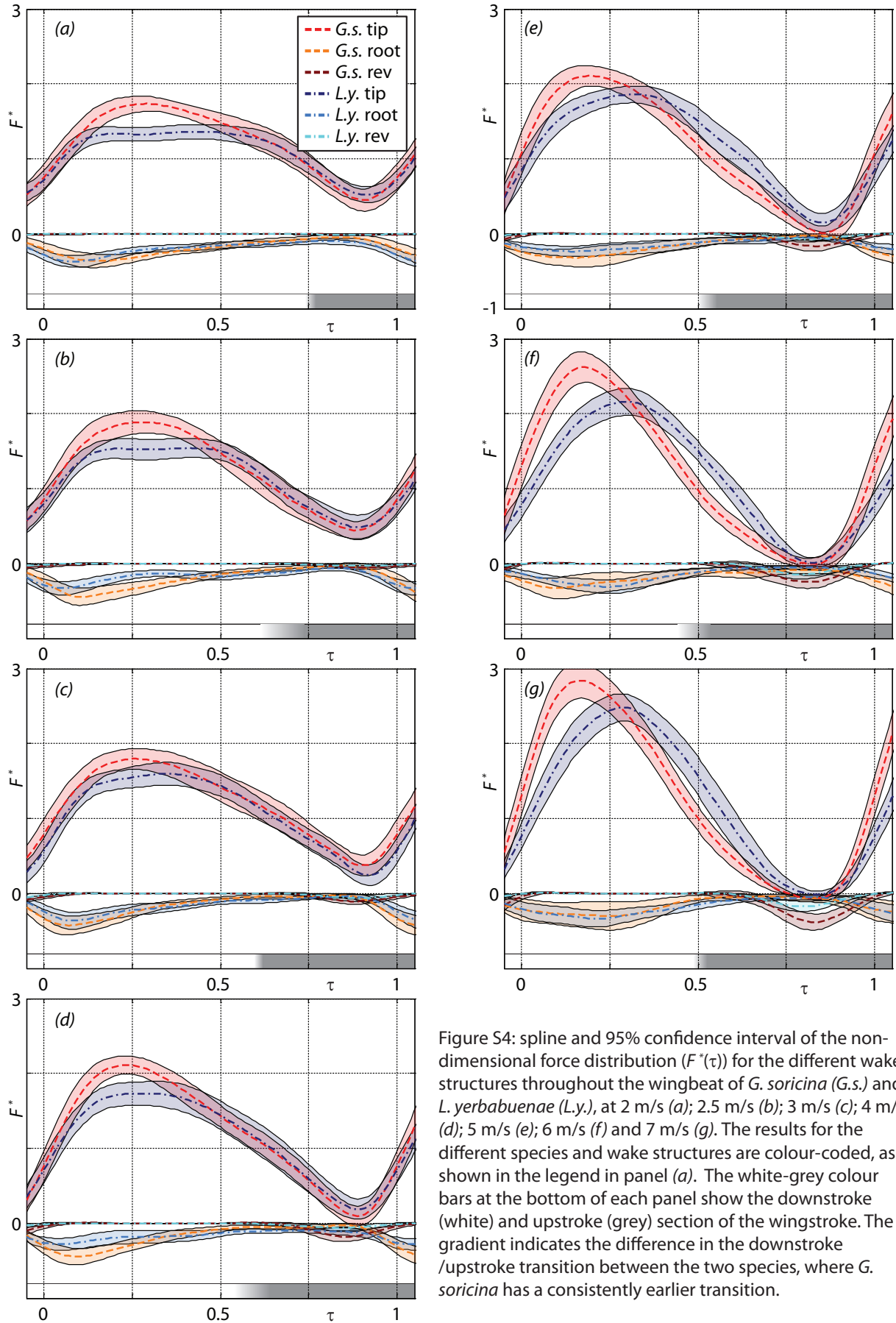
Figure S4: spline and 95% confidence interval of the non-dimensional force distribution ($F^*(\tau)$) for the different wake structures throughout the wingbeat of *G. soricina (G.s.)* and *L. yerbabuenae (L.y.)*, at 2 m/s *(a)*; 2.5 m/s *(b)*; 3 m/s *(c)*; 4 m/s *(d)*; 5 m/s *(e)*; 6 m/s *(f)* and 7 m/s *(g)*. The results for the different species and wake structures are colour-coded, as shown in the legend in panel *(a)*. The white-grey colour bars at the bottom of each panel show the downstroke (white) and upstroke (grey) section of the wingstroke. The gradient indicates the difference in the downstroke/upstroke transition between the two species, where *G. soricina* has a consistently earlier transition.
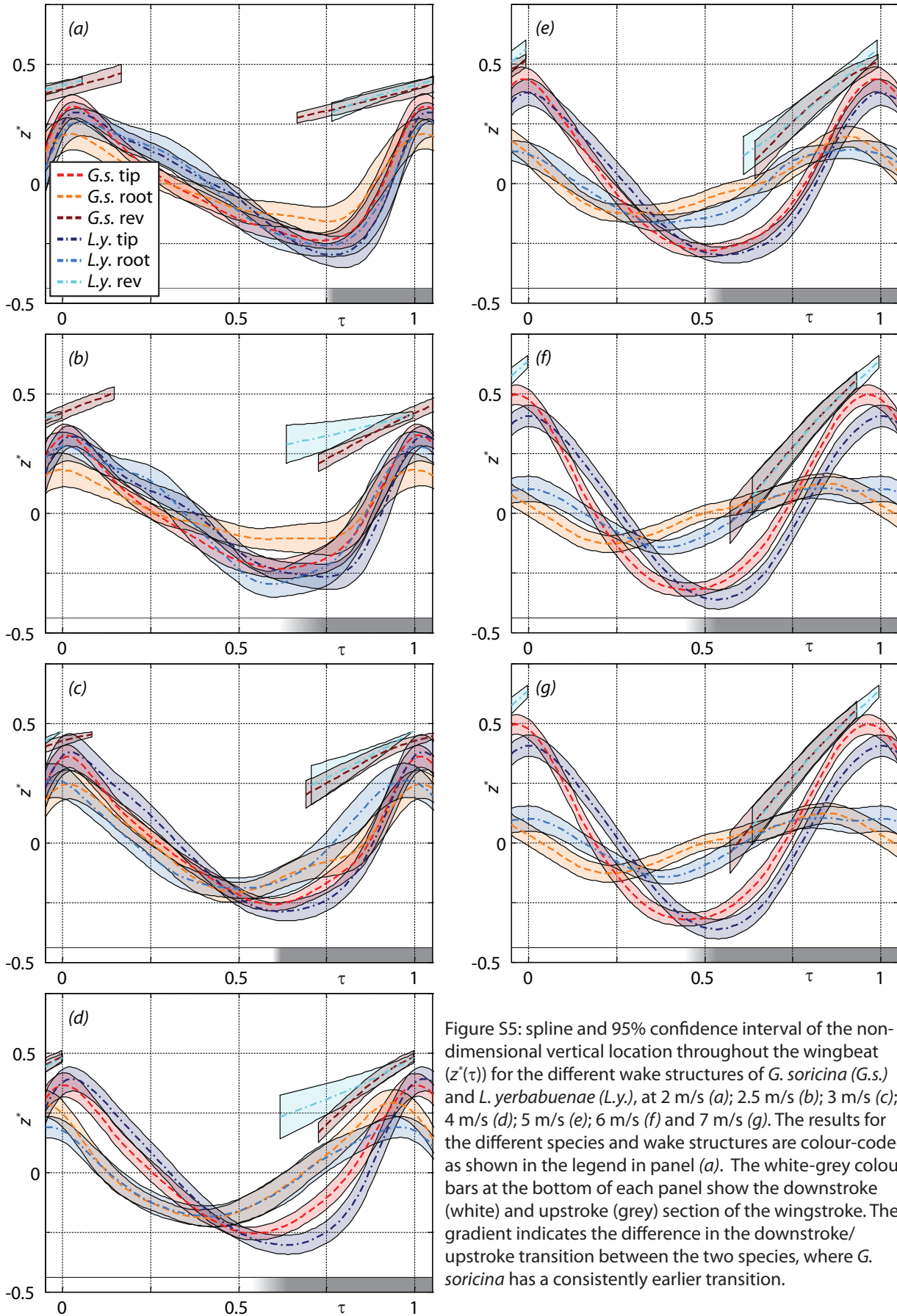
Figure S5: spline and 95% confidence interval of the non-dimensional vertical location throughout the wingbeat ($z^*(\tau)$) for the different wake structures of *G. soricina (G.s.)* and *L. yerbabuenae (L.y.)*, at 2 m/s *(a)*; 2.5 m/s *(b)*; 3 m/s *(c)*; 4 m/s *(d)*; 5 m/s *(e)*; 6 m/s *(f)* and 7 m/s *(g)*. The results for the different species and wake structures are colour-coded, as shown in the legend in panel *(a)*. The white-grey colour bars at the bottom of each panel show the downstroke (white) and upstroke (grey) section of the wingstroke. The gradient indicates the difference in the downstroke/upstroke transition between the two species, where *G. soricina* has a consistently earlier transition.
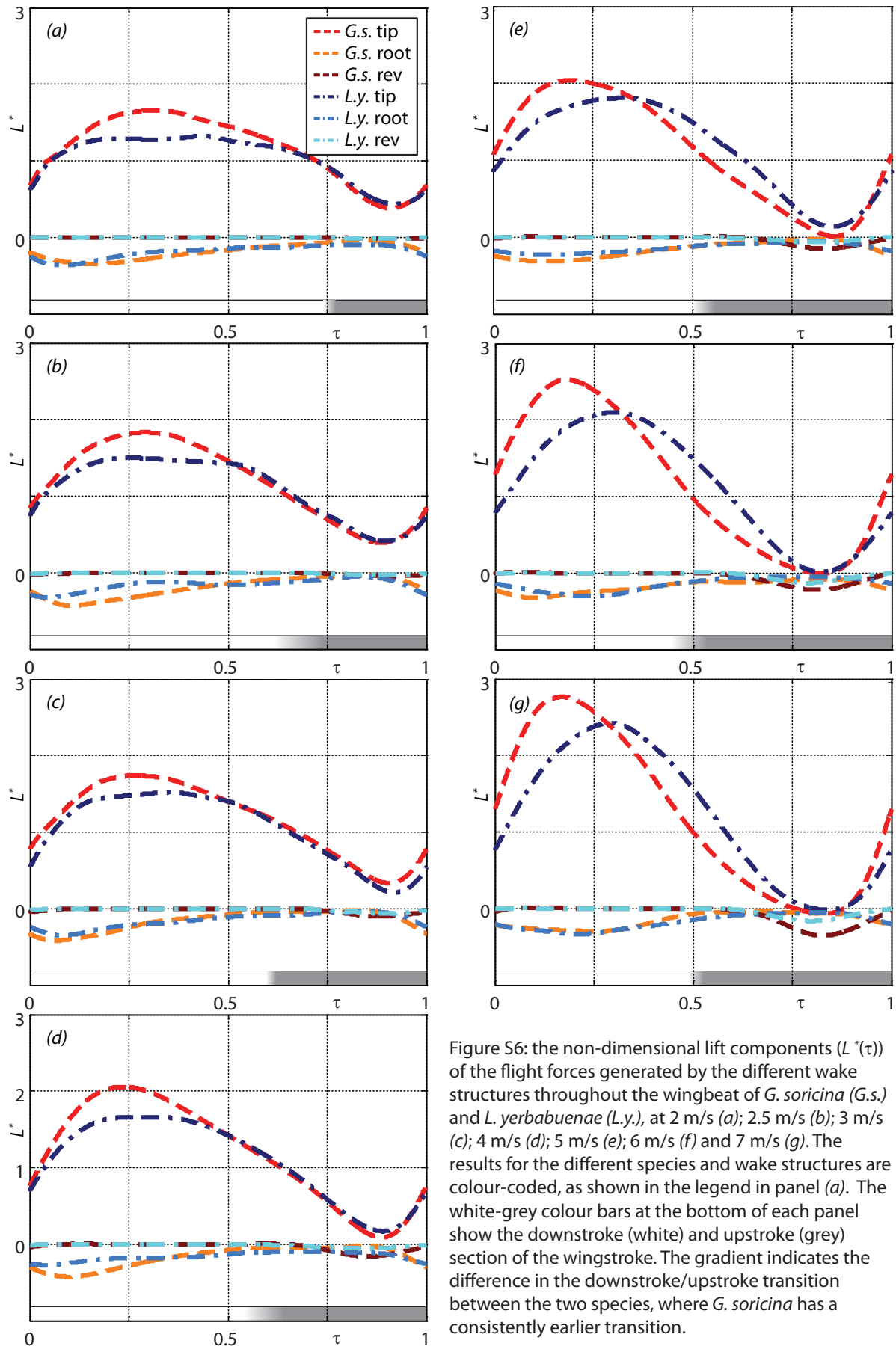
Figure S6: the non-dimensional lift components ($L^*(\tau)$) of the flight forces generated by the different wake structures throughout the wingbeat of *G. soricina (G.s.)* and *L. yerbabuenae (L.y.),* at 2 m/s *(a)*; 2.5 m/s *(b)*; 3 m/s *(c)*; 4 m/s *(d)*; 5 m/s *(e)*; 6 m/s *(f)* and 7 m/s *(g)*. The results for the different species and wake structures are colour-coded, as shown in the legend in panel *(a)*. The white-grey colour bars at the bottom of each panel show the downstroke (white) and upstroke (grey) section of the wingstroke. The gradient indicates the difference in the downstroke/upstroke transition between the two species, where *G. soricina* has a consistently earlier transition.
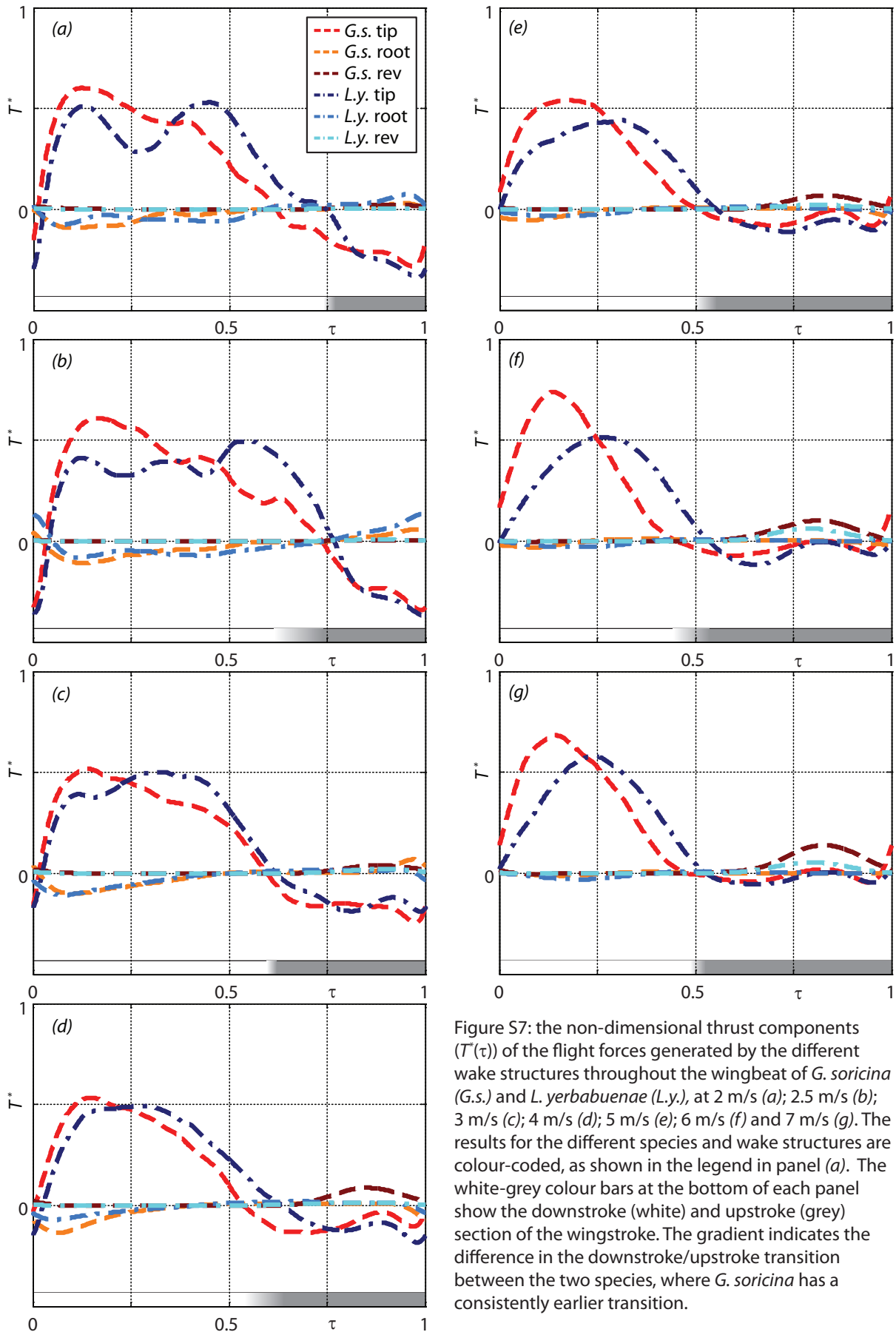
Figure S7: the non-dimensional thrust components ($T^*(\tau)$) of the flight forces generated by the different wake structures throughout the wingbeat of *G. soricina (G.s.)* and *L. yerbabuenae (L.y.)*, at 2 m/s *(a)*; 2.5 m/s *(b)*; 3 m/s *(c)*; 4 m/s *(d)*; 5 m/s *(e)*; 6 m/s *(f)* and 7 m/s *(g)*. The results for the different species and wake structures are colour-coded, as shown in the legend in panel *(a)*. The white-grey colour bars at the bottom of each panel show the downstroke (white) and upstroke (grey) section of the wingstroke. The gradient indicates the difference in the downstroke/upstroke transition between the two species, where *G. soricina* has a consistently earlier transition.
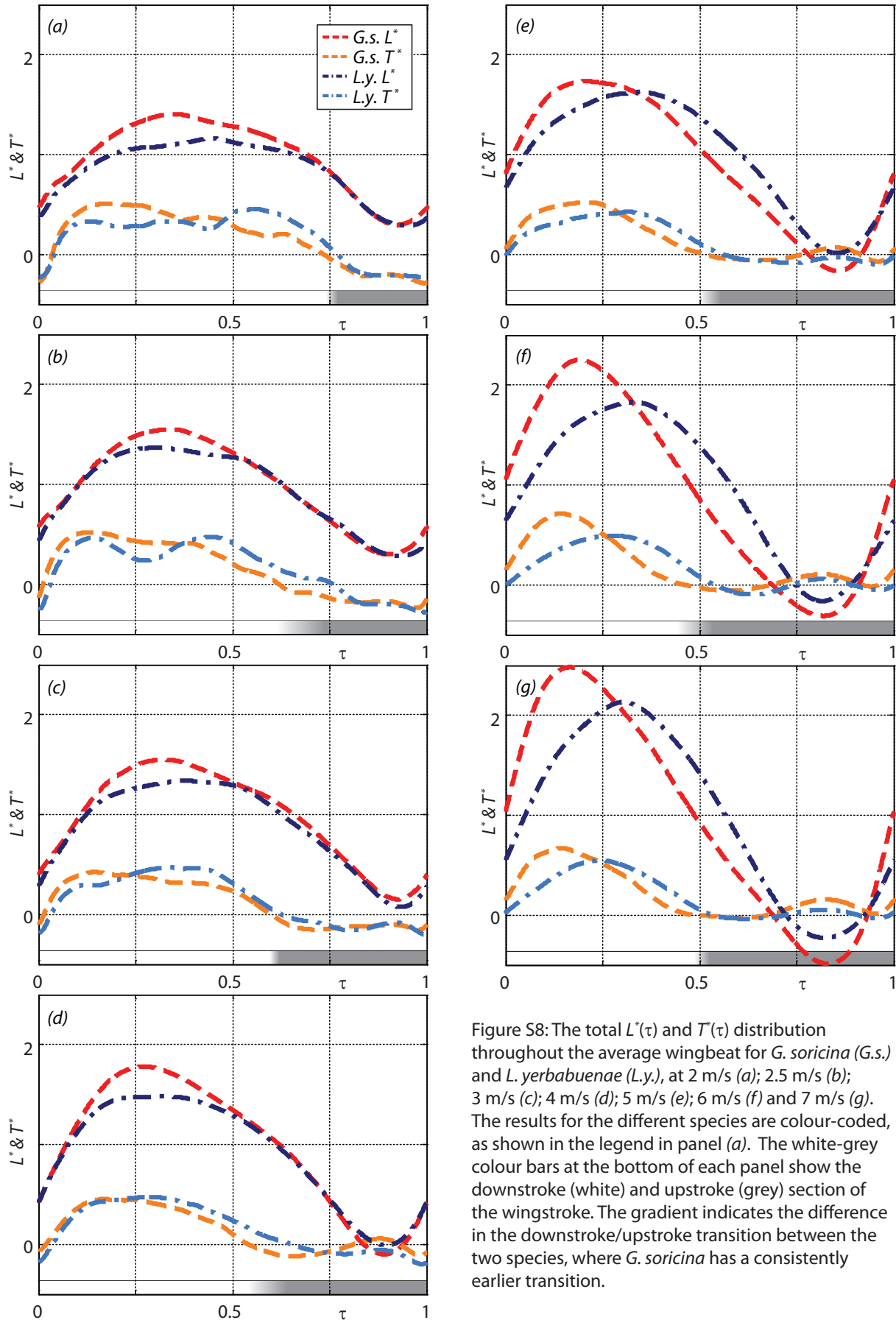
Figure S8: The total $L^*(\tau)$ and $T^*(\tau)$ distribution throughout the average wingbeat for *G. soricina (G.s.)* and *L. yerbabuenae (L.y.)*, at 2 m/s *(a)*; 2.5 m/s *(b)*; 3 m/s *(c)*; 4 m/s *(d)*; 5 m/s *(e)*; 6 m/s *(f)* and 7 m/s *(g)*. The results for the different species are colour-coded, as shown in the legend in panel *(a)*. The white-grey colour bars at the bottom of each panel show the downstroke (white) and upstroke (grey) section of the wingstroke. The gradient indicates the difference in the downstroke/upstroke transition between the two species, where *G. soricina* has a consistently earlier transition.
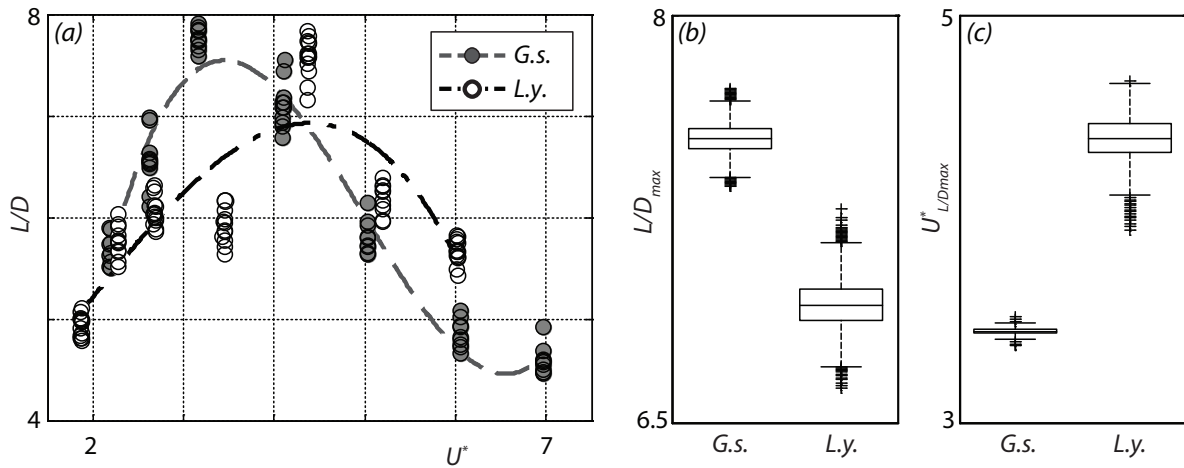
Figure S9: *(a)* the lift-to-drag ratio (*L/D*) estimates from the Jackknife analysis versus the normalized flight speed (*U**), together with the corresponding third order *L/D(U*)* polynomials. The closed symbols represent data for *G. soricina* (*G.s.*) and the open symbols for *L. yerbabuenae* (*L.y.*), as indicated in the legend; *(b)* boxplot of the *L/D$_{max}$* distribution for the two bats ; *(c)* boxplot of the *U*$_{L/Dmax}$* distribution for the two bats.
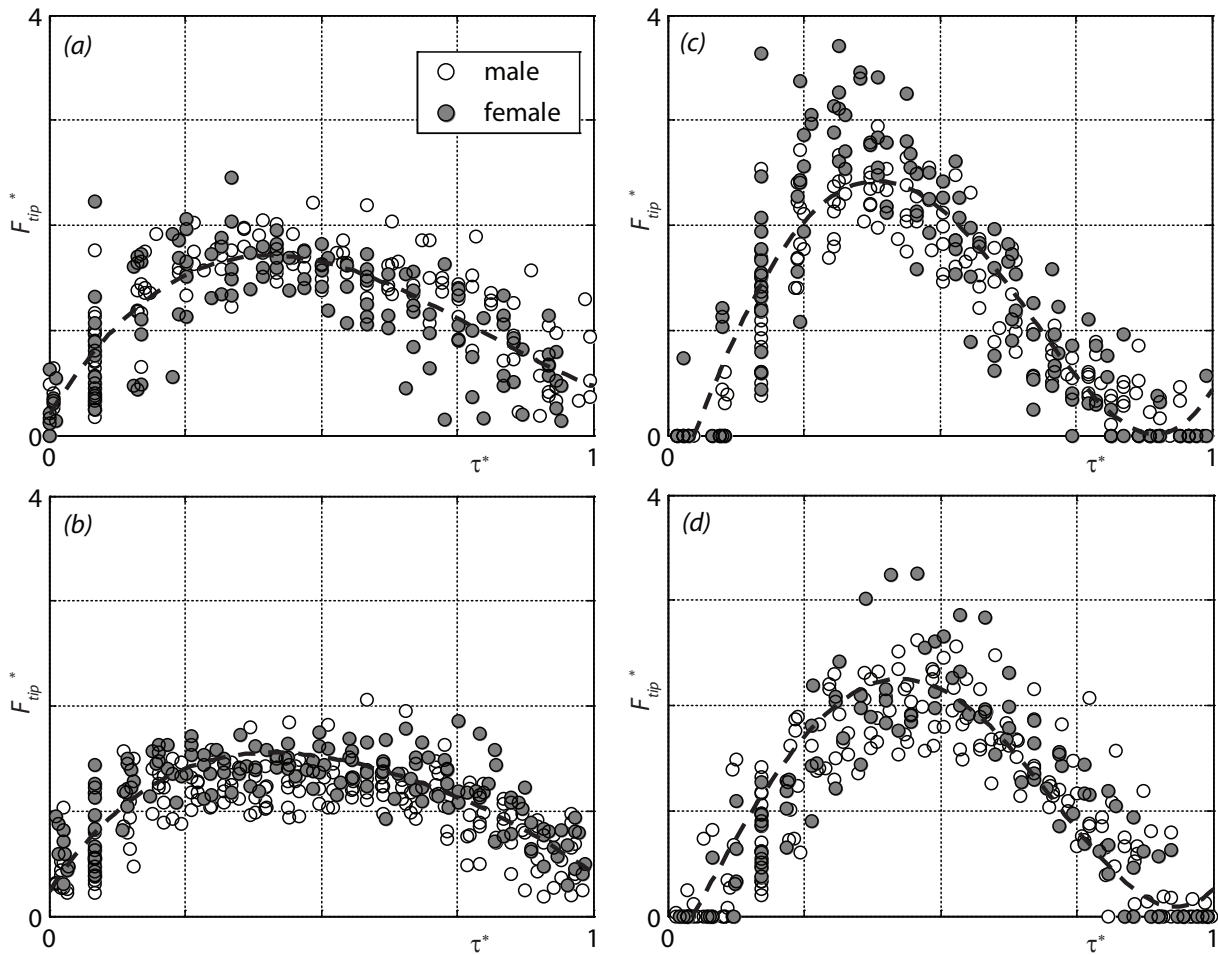
Figure S10: normalized tip vortex force (*F*$_{tip}$*(τ*)) of all measured PIV data points for *G. soricina* flying at 2 m/s *(a)* and 6 m/s *(c)* and *L. yerbabuenae* at 2 m/s *(b)* and 6 m/s *(d)*. Open symbols represent data from the male bats and closed symbols represent data from the female bats, see legend in *(a)*. The time variable is phase shifted (τ*=τ+Δτ) so that the minimum value of *F$_{tip}$** coincided with τ* = 0. The black dotted lines represent the 4th order polynomials resulting from the statistical analysis.

Actuator disk model and span efficiency of flapping flight in bats based on time-resolved PIV measurements

Florian T. Muijres[1], Geoffrey R. Spedding[2], York Winter[3] and Anders Hedenström[1]

[1]*Department of Biology, Ecology Building, Lund University, SE-223 62 Lund, Sweden*
[2]*Department of Aerospace and Mechanical Engineering, University of Southern California, Los Angeles, CA 90089-1191, USA*
[3]*Cognitive Neurobiology, Humboldt University, and NeuroCure Center of Excellence at the Charité Universitätsmedizin Berlin, Dorotheenstrasse 94, 10117 Berlin, Germany*

All animals flap their wings in powered flight to provide both lift and thrust, yet few human-engineered designs do so. When combined with flexible wing surfaces, the resulting unsteady fluid flows and interactions in flapping flight can be complex to describe, understand and model. Here, a simple modified actuator disk is used in a quasi-steady description of the net aerodynamic lift forces on several species of bat whose wakes are measured with time-resolved PIV. The model appears to capture the time-averaged and instantaneous lift forces on the wings and body and could be used as basis for comparing flapping flight efficiency of different animal species and micro-air vehicle designs.

1 Introduction

Flapping flight is often assumed to be more manoeuvrable compared to steady flight with fixed or constantly rotating wings, but evidence on transport efficiency (e.g. L/D_{max}) is more mixed (Hall & Hall 1996; Hall et al. 1998; Wang 2008). A reduction in efficiency for flapping flight compared to steady wings is often explained using quasi-steady aerodynamic theory, where a steady wing can operate constantly at an optimal angle of attack, while a flapping wing needs to deviate from this optimum (Wang 2008). In a recent study, though Pesavento & Wang (2009) showed that for a 2D numerical model of a fruitfly wing, the flapping wing can be more efficient than the equivalent steady wing, due to unsteady wing-wake interactions at stroke reversal. Hall et al. (1998) use a viscous extension of the Betz criterion for optimal propellers to find the minimum power required for a

flapping wing generating a prescribed lift and thrust. Due to a trade-off between efficient lift production and efficient thrust production, the flapping wing is slightly less efficient than an equivalent constant rotating wing (propeller).

Just a few human-engineered aircraft flap their wings to power flight, often being flapping Micro Air Vehicles (MAVs, e.g. *www.delfly.nl*). Most flapping MAVs are inspired by flying animals, and also operate at Reynolds numbers (*Re*) similar to those of birds and bats ($10^3 \le Re \le 10^5$, $Re = Uc/\nu$, where *U* is the wing velocity, *c* is the mean chord length and n is the kinematic viscosity of air). In this *Re* range the aerodynamics are hard to predict and control, because the laminar boundary layer on a wing can easily separate, and reattach after it has become turbulent (Lissaman 1983). This behavior is very sensitive to small changes in freestream turbulence, ambient noise (Grundy et al. 2001) and wing geometry and flexibility (Spedding et al 2008).

Active flapping of biological or bio-inspired wings leads to further complications as the wing geometry changes can be significant fractions of the total wingbeat amplitude, and the deformations themselves are coupled with the time-dependent aerodynamic forces. An example of a highly flexible flapping wing configuration is that of the bat, which has flexible membranous wings (Pennycuick 1971, 1973, 2008b; Swartz et al. 1996). When flapping, the wings deform continuously (Wolf et al. 2010; Swartz et al. 2007), under passively and active control (Hedenström et al. 2009). At slow flight speeds (at Strouhal number $St = 1.36$, $St = f A /U_\infty$, where *f* is the wingbeat frequency, *A* is the vertical flapping amplitude of the wingtip, and U_∞ is the forward flight speed), the Pallas' Long-tongued bat (*Glossophaga soricina*) deforms and controls its wing in such a way that, during each downstroke, a Leading Edge Vortex (LEV) is generated, which enhances lift during the downstroke by up to 40% of the total (Muijres et al. 2008).

This complex flow near the wing surface as well as the time-varying fluid-structure interactions are hard to measure and model, and so most aerodynamic measurements on flapping animal flight have focussed on far wake measurements (Spedding & Hedenström 2009). In the most common configuration, a three-dimensional model of the vortex wake of the flapping animals is assembled by identifying coherent vortex structures over a far wake domain that spans a streamwise distance equivalent to one wingbeat. By measuring the circulation of the various patches of vorticity the gross, time-averaged forces within a wingbeat can be estimated (Spedding et al. 2003a,b). This approach has improved our understanding of flapping animal flight significantly (Hedenström et al. 2006, 2007; Spedding et al. 2003a), but the 3D wake structure must be assembled by combining measurements from multiple wingbeats, with relatively poor resolution in the spanwise direction (normal to the plane of each slice). Moreover, the assemblage is constructed from only two velocity components, and the third, or its spatial gradient is inferred from vorticity conservation laws.

Recently, high speed stereo PIV systems have become available for animal flight research, with which the wake dynamics can be analyzed at a high temporal resolution (Hedenström et al. 2009; Hubel et al. 2009). In these studies the wake is generally sampled using a transverse (vertical spanwise) PIV image at a typical frequency of 200 Hz. From the high-speed transverse PIV data the three-dimensional vortex wake is assembled by identifying coherent streamwise vortex structures (Hubel et al. 2010), such as the tip vortex, from which the time varying flight forces can be estimated (Henningsson et al. 2010; Johansson & Hedenström, 2009; Muijres et al. 2011). With these methods the temporal resolution is increased and the potential effect of the researcher's interpretation is reduced, resulting in more objective wake models. But, since the forces generated by the flapping wing are typically modelled using tip vortex circulation, spanwise force distributions can not be determined.

A very simple model of flapping animal flight is the actuator disk (Ellington, 1984; Norberg et al. 1993; Pennycuick 1968), which has originally been developed to estimate helicopter rotor performance (Gessow & Myers 1952). For this model, an actuator disk is defined as a circular surface with diameter equal to the wingspan, or alternatively equal to the width of the wake area behind the flying animal. These actuator disk models are very useful for estimating the average lift force and power for flapping flight, but can not be used for more detailed analysis since variations in induced velocities as a result of wingbeat kinematics are ignored.

In this study we present a modified actuator disk model for forward flapping flight, which is adapted

Table 1 Morphological data and typical flight speeds for the experimental bats.

Bat (species, gender)	M (kg)	b (m)	S (m²)	W/b (N/m)	U_{mp} [a] (m/s)	U_{mr} [b] (m/s)
G. soricina, male	0.0101	0.233	0.00879	0.425	3.26	5.09
G. soricina, female	0.0095	0.230	0.00860	0.405	3.27	5.01
L. yerbabuenae, male	0.0216	0.335	0.01576	0.633	3.70	5.39
L. yerbabuenae, female	0.0236	0.323	0.01529	0.717	3.67	5.56

The mass M was measured before and after each experiment. The wing span b, and wing surface area S were determined at mid downstroke, using the kinematics data. The span loading W/b is used to scale the induced power estimates. The minimum power speed U_{mp}, and maximum range speed U_{mr} are estimated from the morphological data following Norberg & Rayner (1987)

[a] $U_{mp} = 6.58 \, M^{0.422} \, b^{-0.479} \, S^{-0.148}$

[b] $U_{mr} = 8.71 \, M^{0.423} \, b^{-0.498} \, S^{-0.144}$

for use with near-wake time-resolved PIV data of freely flying animals, using bats as a case in point. Here, the actuator disk area depends directly on the wake topology, and the measured induced downwash velocities within this modified disk are used to get a first-order estimate of the vertical impulse generated by the flapping wing both along the wingspan and throughout the wingbeat. From this the temporal lift force distribution is determined, as well as the induced power and the span efficiency factor. This approach enables us to estimate the performance of flapping flight at high spatial and temporal resolution, without having to model the fluid-structure interactions of the flexible wing, nor the highly unsteady fluid-dynamics near the wing surface itself.

2 Methods
2.1 Experimental animals

Two bat species were studied, the Pallas' Long-tongued bat (*Glossophaga soricina*, from here on called *G. soricina* and the Lesser Long-nosed bat (*Leptonycteris yerbabuenae*, from here on called *L. yerbabuenae*). Both species are small to medium sized new-world nectar feeding bats of the subfamily *Glossophaginae*, and both are capable of hovering flight, which they habitually do when feeding from flowers. *L. yerbabuenae* is about twice the weight of *G. soricina* (Table 1), and is a migratory species, while *G. soricina* is a residential species. Of each bat species, a male and a female bat were used in the experiments. Relevant morphological data together with the estimated minimum power speed U_{mp} and maximum range speed U_{mr} (Norberg & Rayner 1987) for these bats are given in Table 1. Since U_{mp} and U_{mr} are similar for both bat species, we will directly compare the results for both species at the

same flight speed.

In flapping flight, the airspeed that a flapping wing encounters is generally higher than the forward flight speed, due to the flapping motion of the wing. When assuming a sinusoidal flapping motion, this average effective free-stream speed ($U_{\infty,eff}$) can be estimated by (e.g. Lentink & Gerritsma 2003)

$$U_{\infty,eff} = U_\infty \sqrt{St^2 + 1}. \tag{1}$$

$U_{\infty,eff}$ is based on the forward flight speed and the flapping motion of the wing, but any induced fluid motion is ignored, hence the addition of 'free-stream'. For *G. soricina* St can be estimated by $St=1.26 \, U_\infty^{0.85}$ (Wolf et al. 2010), while, for *L. yerbabuenae* it may be approximated by $St=1.28 \, U_\infty^{-0.90}$ (R. von Busse, L.C. Johansson, Y. Winter & A. Hedenström, unpublished data). We will use the effective free-stream velocity $U_{\infty,eff}$, instead of the commonly used U_∞, as the general velocity scaling parameter (e.g. for Re and C_L). At the flight speeds range studied (2 m/s < U_∞ < 7 m/s) the Reynolds number range, based on $U_{\infty,eff}$ and c is in the order of $1\times10^4 < Re_{eff} < 2\times10^4$ for both bat species. This is a similar range to local effective Reynolds numbers of wings of small birds (Rosén et al. 2007).

2.2 Experimental setup

Experiments were performed in the Lund University low-turbulence, low-speed wind tunnel (Pennycuick et al. 1997, Fig.1). The experimental setup used in this study is the same as described in Hedenström et al. (2009), where preliminary data for this study were presented. The bats were trained to fly in front of a feeder in the test section of the wind tunnel, at a speed ranging from U_∞ = 2 m/s to 7 m/s, in increments of
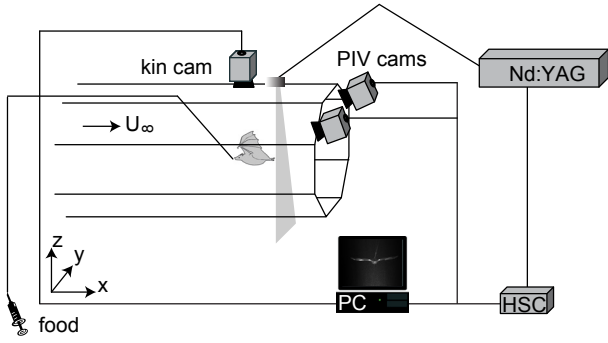
Fig. 1 The experimental setup consists of a high-speed stereo PIV setup, synchronized with a top-view high-speed kinematics camera in a wind tunnel. The position of the bat is controlled using a manually operated feeder system

1 m/s, with an extra step at 2.5 m/s. 20 cm downstream from the feeder a 20x20 cm² PIV image plane was positioned, resulting in an average distance between the trailing edge of the bat wing and the image plane of approximately 10 cm (2–3 *c*, Fig 1). A rectangular coordinate system is defined with *x* running in the streamwise direction, *y* the spanwise direction and *z* is positive opposing the direction of gravitational acceleration, {*u, v, w*} are the velocity components in these directions. The origin of the coordinate system is at the PIV image plane, directly downstream from the feeder. The high-speed stereo PIV system consisted of a transverse laser sheet (aligned in the *y-z* plane), generated by a 200 Hz pulsed 50 mJ Laser (Litron LPY732 series, Nd:YAG, 532 nm), and two CMOS-cameras (HighSpeedStar3; 1024×1024 pixels). The system was controlled using DaVis software (LaVision 7.2.2.110).

For the experiments, the wind tunnel was set to the required forward flight speed, while the bats were roosting in the settling chamber. When a bat wanted to eat, it flew with the wind downstream into the test section, made a U-turn and approached the feeder from downstream. While the bat was judged to be flying steadily at the feeder, a sequence of 50 frame pairs were acquired at a sample rate of 200Hz. The ¼ s period is equal to three to four wingbeats. The time separation between PIV frames (δ*t*) was set so mean pixel displacements in the wake of the bat were in the order of 3.5, and not close to an integer value to reduce peak locking. It ranged from δ*t*=200 μs at 2 m/s to δ*t*=100 μs at 7 m/s.

Simultaneously with the PIV recording, the bat was filmed from above with a NAC HotShot 1280

video camera, (640x512 pixels, 250 Hz sampling rate and shutter speed 1/250 s, Fig.1). The video sequences were used to identify the individual and to determine the bat's position, attitude, basic wing kinematics and morphological data.

2.3 Analysis

The PIV images were analyzed using Davis (Lavision 7.2.2.110), as described in (Hedenström et al. 2009). A multi-pass stereo cross-correlation (64x64, 32x32, 50% overlap) was used, and the data were post-processed using a 3x3 smoothing average, resulting in an in-plane spatial resolution of the velocity vectors of 5.1 mm. The resulting velocity fields were interrogated using a custom Matlab (7.7.0.471, R2008b) program where the velocity components {*u, v, w*} at the image plane location {*y,z*} were extracted on specified transects and stored.

For each PIV sequence the frames within one wingbeat were given a frame number $n = [1\text{-}N]$, a non-dimensional time stamp $\tau = [0\text{-}1]$ and a streamwise position $x = [0\text{-}\lambda]$, where λ is the wavelength of the wingbeat. The start (n=1) and end frames (n=N) coincide with the part of the wake generated by the start of the downstroke. The non-dimensional time stamp is defined as $\tau = t/T$, where T is the wingbeat period, and t is the moment at which the wake structure measured in PIV frame n is generated by the flapping wing, t=0 is equivalent to the start of the downstroke, and $t = T$ is the end of the upstroke. Since the flapping bat wings travel forward with respect to the PIV image plane during the downstroke, and backwards during the upstroke, a Doppler shift is present in the PIV data, resulting in an overrepresentation of the downstroke in the PIV frames. By assuming that the wing moves forward and backwards at a constant speed, the non-dimensional time stamp for PIV frame n are determined by

$$\tau = \frac{(n-1)}{N}\frac{t_{ds\,wing}}{t_{ds\,wake}} \text{ for } 1 \leq n \leq N_{du}$$

$$\tau = \frac{(n-1)}{N}\frac{t_{us\,wing}}{t_{us\,wake}} \text{ for } N_{du} \leq n \leq N$$

(2)

where N_{du} is the PIV frame at the transition from downstroke to upstroke. $t_{ds\,wing}/t_{ds\,wake}$ is the ratio between the downstroke duration of the wing and

the downstroke duration of the PIV sequence, and $t_{us\,wing}/t_{us\,wake}$ is the ratio between the upstroke duration of the wing and the upstroke duration of the PIV sequence.

If we assume that the wake convects statically downstream with the forward flight speed U_∞, the streamwise position for PIV frame n is

$$x = (n-1)U_\infty \cdot \Delta t \tag{3}$$

where Δt is the inverse of the PIV frame rate (Δt = 1/200 s). Using these x-values, the three-dimensional wake field behind the flying animal can be constructed. Each node-point within the resulting three-dimensional wake matrix consists of a position vector $\{x,y,z\}$ and the three velocity components $\{u,v,w\}$. The resolution of the wake field is, in y-and z-direction, equal to the PIV vector node point spacing Δy = 5.1 mm, and in x-direction equal to $\Delta x = U_\infty \cdot \Delta t$, which will vary from Δx = 10.0 mm at U_∞ = 2 m/s to Δx = 35.0 mm at U_∞ = 7 m/s. To compensate for the low resolution in x-direction a cubic interpolation routine is used (Matlab, interp3), resulting in a streamwise resolution in the interpolated wake matrix of 5 mm for all flight speeds. For this interpolated wake matrix the vorticity magnitude ($|\omega| = \sqrt{\omega_x^2 + \omega_y^2 + \omega_z^2}$) is calculated. Controlled tests on an artificial vortex tube of similar strength and size as for the bats, oriented in y-direction, showed that at the highest flight speeds, the interpolation routine still results in an underestimation of ω_y (e.g. vorticity of start or stop vortices).

3 The actuator disk model for flapping flight

The actuator disk model (Gessow & Myers 1952; Spalart 2003; Stepniewski & Keys 1984) is a highly simplified model for force and power estimations of constantly rotating wings, originally developed for helicopter rotors, but also adapted for flapping animal flight (Pennycuick 2008a). The basic model defines the actuator disk as a circular disk swept by the wing configuration, typically a rotor or a propeller.

Let us first assume an ideal rotor during forward flight (Fig. 2*a*). Due to wing rotation, a uniform pressure difference (Δp) is created across the propeller disk, resulting in an induced airflow with velocity vector $\overline{u} = \{u,w\}$ at the disk surface. For an ideal actuator disk the induced velocity $\overline{u}$ is often assumed to be uniform throughout the disk area, although
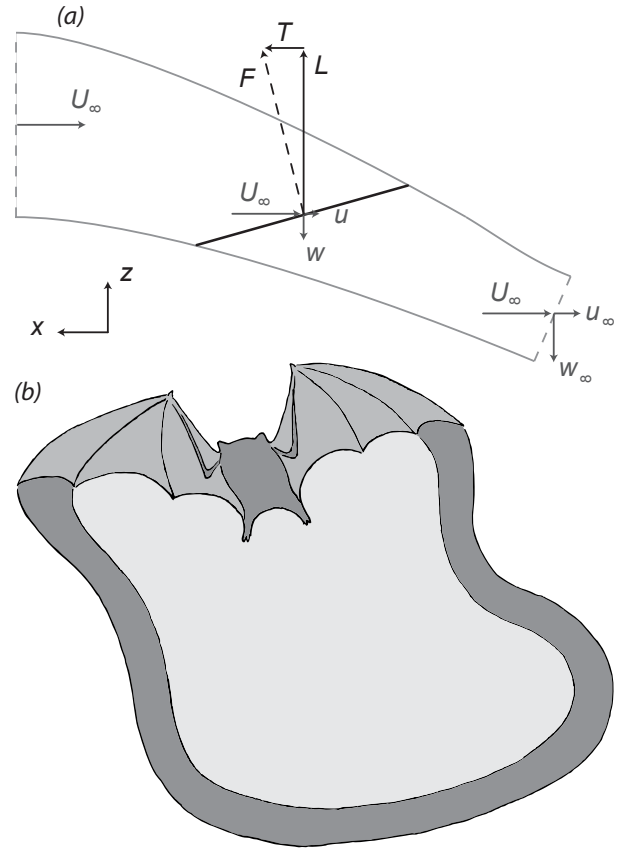

Fig. 2 *(a)* An ideal actuator disk in forward flight. A uniform pressure difference generated by the rotating disk causes air to accelerate through the disk. This results in an induced velocity change from $\overline{u}_0$ = 0 far upstream to $\overline{u}_\infty = 2\overline{u}$ far downstream, and a flight force production F with lift component L and thrust component T. *(b)* cartoon illustration of a flying bat with its actuator disk wake. The disk area is bound by the main vortex structures (start vortex, tip vortices and stop vortex). In this image the stop vortex has not yet been shed

Spalart (2003) showed that this assumption is incorrect, even for a uniform Δp. The induced velocities far upstream of the disk are zero ($\overline{u}_0$=0, Fig. 2*a*), while the induced velocities attained in the far wake $\overline{u}_\infty = \{u_\infty, w_\infty\}$ are twice the induced velocity at the disk ($\overline{u}_\infty$ = 2 $\overline{u}$). If we ignore the streamwise component of the induced velocity vector ($\overline{u} = \{w\}$), the lift force L and induced (or shaft) power generated by the propeller can be estimated as

$$L = -2\dot{m}\,w$$
$$P_{i\,ideal} = -L\,w \tag{4}$$

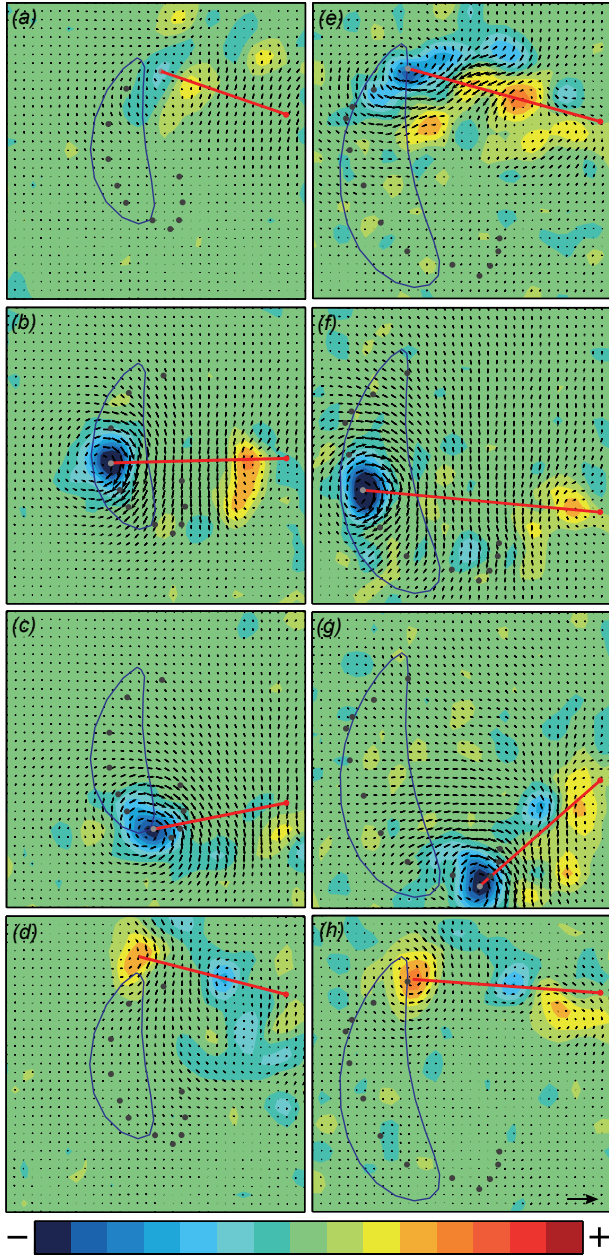where $\dot{m}$ is the mass flux through the disk, defined as

Fig. 3 Transverse PIV results for one wingbeat of both bat species flying at 4 m/s. The left panels *(a-d)* show the results for *G.soricina*, while the right panels *(e-h)* show the results for *L. yerbabuenae*, at the start of the downstroke *(a,e)*; mid-downstroke *(b,f)*; end of the downstroke *(c,g)*; end of the upstroke *(d,h)*. The arrows are the inplane velocity vectors, scaled with the reference vector of 5 m/s in panel *(h)*. The colors visualize the streamwise vorticity ω_x, scaled according to the scale bar on the bottom of the figure, with range $-300 < \omega_x < 300$. The grey dots show the tip vortex location in the different PIV frames n, with the light grey dot indicating the current frame, while the blue line shows the wingtip movement throughout the wingbeat

$$\dot{m} = \rho \, A_d \left| \overline{U}_d \right| \tag{5}$$

where ρ is the air density, A_d is the disk area, and $\overline{U}_d = \{U_\infty, w\}$ is the total velocity vector at the disk. There is a minus sign in Eq. 4 since a downwash (negative w) will result in a positive lift, and the factor 2 is due to the fact that $w_\infty = 2\,w$. $P_{i_{ideal}}$ is called the ideal induced power, since it is the power required for generating a uniform downwash within the actuator disk area, and this uniform downwash is the lowest energy solution for a given momentum flux (Stepniewski & Keys 1984).

This general actuator disk model for forward flight has been applied to animal flight (Pennycuick 1968), by defining the actuator disk of the flapping wings as a circular area with the diameter equal to the wing span, and the forces and induced power for a flying animal can directly be determined using the above described theory. This highly simplified model for flapping flight of animals can be used to determine the required power for flight and for estimating the average flight forces throughout a wingbeat, but it cannot be used for more detailed studies, such as for estimating temporal or spatial force distributions within a wingbeat.

Here, we propose a modified area for the actuator disk, which is directly based on the wake area generated by the flapping wing configuration, and which enables us to study the aerodynamics of flapping flight in more detail. Our modified actuator disk area for flapping flight is defined as the area spanned by the main vortex structures generated within one wingbeat (start, stop and tip vortices, Fig. 2b). The area can be constructed from the PIV data, by tracing the area between the two tip vortices for all PIV frames within one wing beat (PIV frame $n = [1\text{-}N]$). Throughout the modified actuator disk area, the vertical induced velocity is not assumed to be uniform, but is measured. This downwash variation can be used to analyse flapping flight in detail. The variations in streamwise direction (*x*-direction) can be used to estimate the relative contribution of various parts of the wingbeat, e.g. lift generated by the downstroke versus lift generated by the upstroke. The downwash variation in spanwise direction (*y*-direction) can be used to determine the real induced power P_i and the span efficiency e_i, as is described below. Eq. 4 and Eq. 5 are converted to implement the variation of w throughout the actuator disk as follows
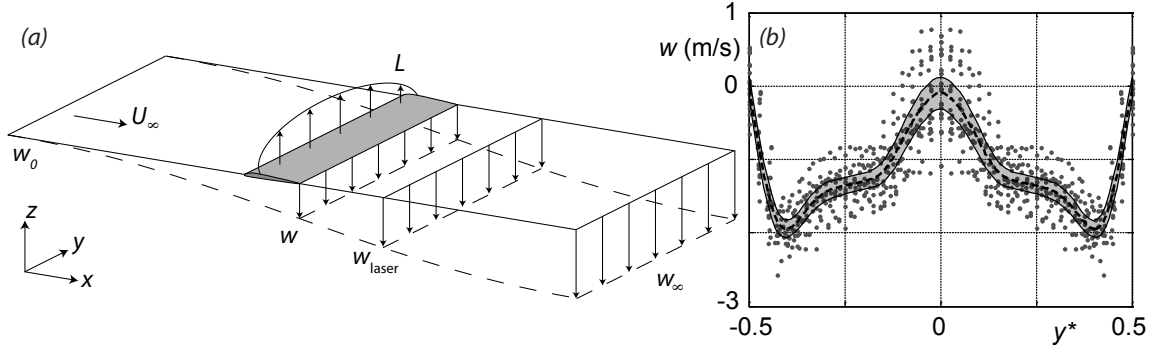
Fig. 4 *(a)* The vertical induced velocity behind a steady wing with an elliptical lift-distribution *L*. The downwash increases from $w_0 = 0$ far upstream, to $w_\infty = 2\,w$ far downstream in the wake. At the PIV laser location, we assume $w_{PIV} = w$. *(b)* The vertical induced velocity distribution $w(y^*)$ along the non-dimensionalized wake span $y^*=y/b_w$ at mid downstroke, for *G. soricina* at 4 m/s. The datapoints are determined from the PIV data of 20 analyzed wingbeats, the dotted line is the smoothing spline through these data, and the shaded area around the dotted line shows the 95% confidence interval

$$\dot{m}_z = \rho \cdot A_d \cdot w = \rho \int_0^\lambda \int_{-b_w(x)/2}^{b_w(x)/2} w(x, y)\,dy\,dx$$

$$L = -2\dot{m}_z\,w = -2\int_0^\lambda \int_{-b_w(x)/2}^{b_w(x)/2} \dot{m}_z(x, y)w(x, y)\,dy\,dx \qquad (6)$$

$$P_i = -L\,w = -\int_0^\lambda \int_{-b_w(x)/2}^{b_w(x)/2} L(x, y)w(x, y)\,dy\,dx$$

$$\dot{m}_z'(x) = \rho \int_{-b_w(x)/2}^{b_w(x)/2} w(x, y)\,dy$$

$$L'(x) = -2\int_{-b_w(x)/2}^{b_w(x)/2} \dot{m}_z'(x, y)w(x, y)\,dy \qquad (7)$$

$$P_i'(x) = -\int_{-b_w(x)/2}^{b_w(x)/2} L'(x, y)w(x, y)\,dy$$

where λ is the wavelength of the flapping wing motion defined as $\lambda = U_\infty / f$, which is equal to the extent of the actuator disk in streamwise direction (along *x*-axis). Thus, the U_∞ component in the mass flux estimate is incorporated into the disk area as λ. $b_w(x)$ is the wake width, which varies throughout the wingbeat as a result of the varying wing span due to the flapping motion. Since the downwash is not assumed uniform throughout the actuator disk in Eq. 6, the real induced power (P_i) is calculated rather than $P_{i\,ideal}$.

Note that the actuator disk model estimates only the (vertical) lift production and corresponding induced power. The thrust component of the flight forces are ignored, since we cannot distinguish streamwise induced velocities as a result of thrust production from wake defects due to drag, and since thrust forces are small compared to lift forces for these bats (Muijres et al. 2011).

If we assume that the downwash along the wingspan at streamwise location *x*, depends directly and solely on the instantaneously generated lift at the corresponding sub-section of the wingbeat, the mass flux, lift and induced power per distance travelled are

To be able to estimate the corresponding ideal induced power per distance travelled, we first need to determine the spanwise uniform vertical induced velocity ($\overline{w}(x)$) which would result in $L'(x)$ by

$$\overline{w}(x) = -\sqrt{\frac{L'(x)}{2\rho\, b_w(x)}}. \qquad (8)$$

The ideal induced power per distance travelled can now be estimated by

$$P_{i_{ideal}}'(x) = -L'(x)\overline{w}(x). \qquad (9)$$

This is the minimum required power per distance travelled to generate $L'(x)$, and which would be a result of an elliptical spanwise lift distribution (Anderson 1991; Spedding & McArthur 2010). The total ideal power for the whole wingbeat can be determined by integrating along the complete wingbeat (*x*-axis)

$$P_{i_{ideal}} = -\int_0^\lambda P_{i_{ideal}}'(x)\,dx = -\int_0^\lambda L'(x)\overline{w}(x)\,dx. \qquad (10)$$

This estimate of $P_{i_{ideal}}$ will be higher than for Eq. 4, because in Eq. 4 the downwash is assumed to be uniform throughout the complete actuator disk, while for Eq. 10 the downwash is assumed uniform only along the wingspan ($\overline{w(x)}$), and can vary throughout the wingbeat. The ratio between $P_{i_{ideal}}$ and P_i is called the span efficiency, and it is a direct estimate of efficiency reduction due to a deviation from a spanwise uniform downwash distribution (Spedding & McArthur 2010), for a complete wingbeat in forward flapping flight. Therefore, we will use the corresponding span efficiency notation proposed by Spedding & McArthur (2010), where e_i is the span efficiency due to downwash distribution

$$e_i = \frac{P_{i_{ideal}}}{P_i} \tag{11}$$

For isolated wings in steady, horizontal flight where L balances W, the induced power can be estimated from

$$P_i = D_i U_\infty = \left(\frac{W}{b}\right)^2 \frac{2}{\pi \rho U_\infty} \frac{1}{e_i} \tag{12}$$

where D_i is the induced drag, W is the weight of the flapping configuration, and b is the wing span. So, we will assume that the here estimated real induced power should scale with span loading squared $(W/b)^2$, the inverse flight speed $(1/U_\infty)$ and the inverse span efficiency $(1/e_i)$.

4 Analysis

The above described actuator disk model for forward flapping flight will be used to analyze transverse PIV results of the wake of two bat species flying steadily in a wind tunnel. Fig. 3 shows such PIV data for both species flying at 4 m/s. Throughout almost the complete wingbeat (Fig. 3a-c and Fig. 3e-g), the tip-vortex is present as the large blue patch of negative vorticity (centre marked with a grey dot), inducing a downwash behind the wing (between the tip-vortex and the position behind the body). For both bat species, the tip-vortex has changed sign (yellow/orange patch of positive vorticity) at the end of the upstroke (Fig. 3d and Fig. 3h), resulting in an upwash (negative lift) behind the outer wing. The 'vortices' in Fig. 3 are simply compact, contiguous patches of high vorticity magnitude, that for convenience are described as vortices in the remainder of this paper.

The local shape and orientation of the actuator disk at each PIV frame is defined as a straight line from the centre of the tip-vortex to the position behind the body (red lines in Fig. 3). The actuator disk line for PIV frame n is called actuator disk segment n with local semi-span $b_w(n)/2$. By mirroring the results along the z-axis at the body centre-line, the complete local actuator disk segment n with local span $b_w(n)$ is defined. By adding the actuator disk segments for all PIV frames within one wingbeat, and using the x-variable for each PIV frame for the streamwise distribution, the actuator disk for the complete wingbeat is defined.

Each PIV vector node point along an actuator disk segment n is marked using an index m along the spanwise y-axis, and the vertical induced velocity at each node point $w_{PIV}(n,m)$ is used as input for the actuator disk model calculations. Since the PIV image plane is positioned downstream of the bat, the measured downwash velocities $w_{PIV}(n,m)$ will be higher than at the actuator disk (in this case at the bat wing, Fig. 4a), but since the distance between wing and PIV plane is small (2-3 c) we can assume that these differences are small, and we will assume $w_{PIV} = w$. One could argue that far-wake measurements (where $w = w_\infty$) would avoid this uncertainty, but we can assume that spanwise downwash distributions in the far wake would deviate significantly from that at the wing due to wake interactions (Johansson et al. 2008).

For each individual bat and flight speed combination, at least 5 flight sequences were analyzed, which consisted on average of 11 wingbeats. From the wake data for each species and flight speed combination a single average actuator disk was determined, resulting in an average wake based on at least 20 wingbeats. The average actuator disk is constructed by dividing the actuator disk in streamwise direction into $\overline{N}$ elements, where $\overline{N}$ is the mean number of PIV frames per wingbeat for the analyzed wingbeats. Within each element ($\overline{n} = [1 - \overline{N}]$), the average spanwise downwash distribution was determined by fitting a cubic smoothing spline (Matlab, csaps, smoothing parameter = $1\text{-}10^{-4}$) through the $w(\overline{n},m)$ datapoint distribution (Fig. 4b). The relative deviation of the $w(\overline{n},m)$ node points from the average spline were estimated using a sliding 95% confidence interval (Fig. 4b), determined from a sliding window of 20 local datapoints (which is
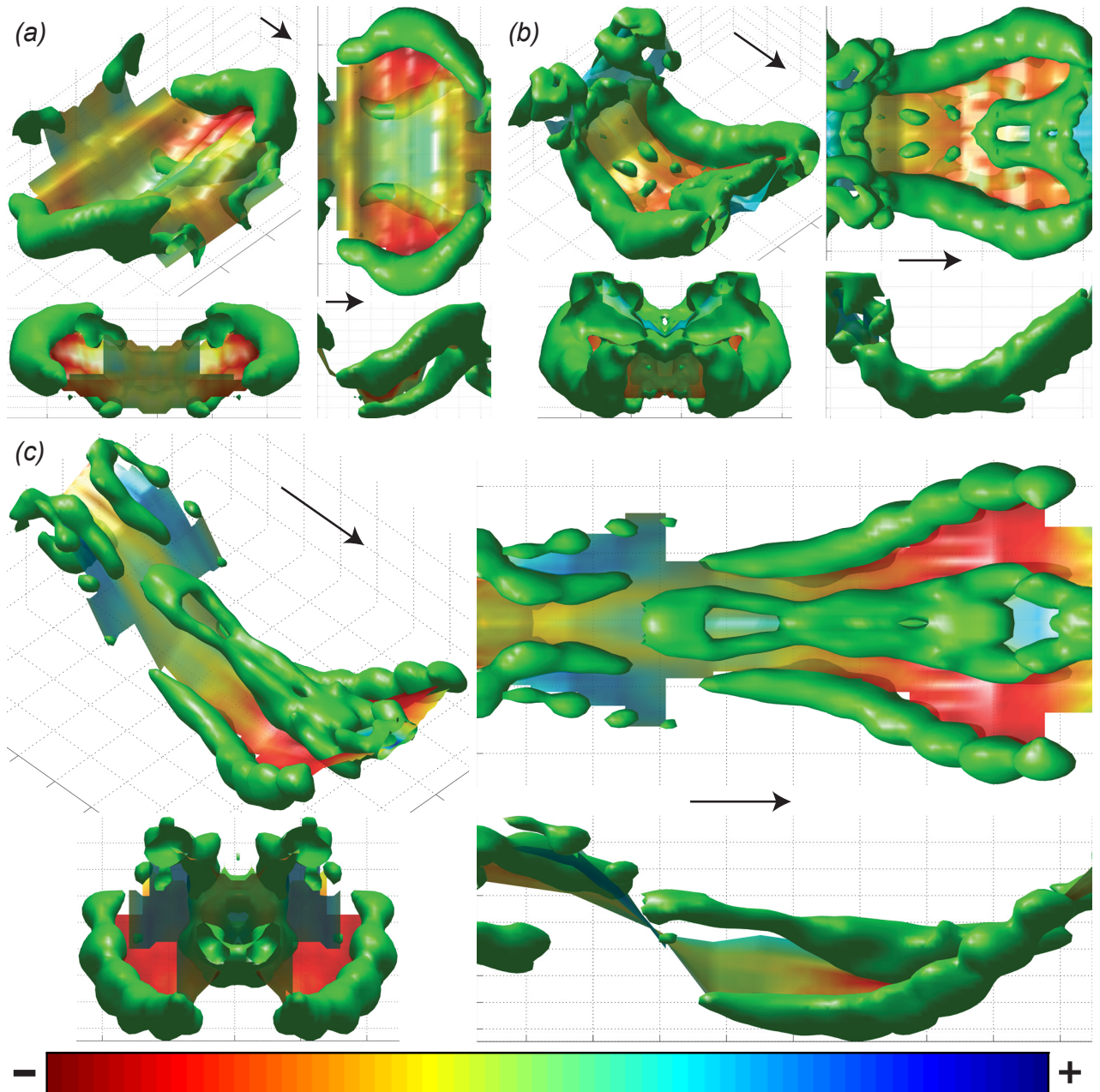
Fig. 5 Vortex-wake and actuator disk surface for a single wingbeat of *G. soricina* flying at different flight speeds. The vortex wake is visualized using green iso-surfaces of constant absolute vorticity $|\omega|$. The actuator disk surface encircled by the vortex structures is color-coded using the vertical induced velocity w according to the colour bar on the bottom of the figure. The different panels show the wake at *(a)* $U_\infty = 2$ m/s, with iso-value $|\omega|_{iso} = 200$ s⁻¹, and colour bar range -2.6 m/s < w < 2.6 m/s; *(b)* $U_\infty = 4$ m/s, $|\omega|_{iso} = 125$ s⁻¹, -2.6 m/s < w < 2.6 m/s; and *(c)* $U_\infty = 7$ m/s, $|\omega|_{iso} = 125$ s⁻¹, -1.7 m/s < w < 1.7 m/s. Each panel consists of 4 different views: (NW) perspective view; (NE) top view; (SW) front (upstream) view; (SW) side view; in perspective view and between top and side view wind tunnel velocity vectors are shown

equal to the minimum amount of wingbeats used to determine the average actuator disk).

The resulting spline function for each segment $\overline{n}$ was directly used to determine the lift and power contribution using Eq. 7-10. The actuator disk's total lift and total induced power was determined by summing the $\overline{N}$ elements

Table 2 P-values for the normalized lift estimate (*L/W-1*), the normalized induced power (P_i *(b/W)²*), and the span efficiency e_i.

	L/W-1		P_i (b/W)²	$P_{i\,ideal}$ (b/W)²	e_i
	G. soricina	*L.yerbabuenae*			
Intercept	0.2016	**0.0092**	**0.0011**	**0.0012**	**<0,0001**
Species	-	-	0.0891	0.0674	**0.0295**
U_∞	0.1213	**0.0005**	-	-	0.7873
U_∞ x *species*	-	-	-	-	**0.0018**
$1/U_\infty$	-	-	**0.0001**	**0.0002**	-
$1/U_\infty$ x *species*	-	-	0.3499	0.1608	-

P-values in bold are significant

$$L = \Delta x \sum_{n=1}^{\overline{N}} L'(\overline{n})$$

$$P_i = \Delta x \sum_{n=1}^{\overline{N}} P'_i(\overline{n}) \qquad . \qquad (13)$$

$$P_{i_{ideal}} = \Delta x \sum_{n=1}^{\overline{N}} P'_{i_{ideal}}(\overline{n})$$

The effective span efficiency e_i for each average wingbeat was determined from $P_{i\,ideal}$ and P_i using Eq. 11.

To test how the lift, power and span efficiencies vary with flight speed and between the two bat species we used mixed linear models. Since the bats fly steadily at the feeder, the total lift should be equal to the weight of the animals. Therefore, *L* is non-dimensionalized as *L/W*, and *L/W-1* is set as the dependent variable in the mixed linear model, for each species separately. U_∞ is set as a covariate. To control for differences in P_i due to differences in span loading between the individuals (Eq. 12), $P_i(b/W)^2$ is set as the dependent variable in the mixed linear model. Since $P_i(b/W)^2$ should scale with $1/U_\infty$ (Eq. 12), $1/U_\infty$, *species*, and '$1/U_\infty$ x *species*' are set as covariates. For the span efficiency test e_i is set as the dependent variable, and *species*, U_∞ and interaction between *species* and U_∞ are used as covariates.

5 Results
5.1 Wake topology and actuator disk area

Actuator disks constructed using the PIV data for *G. soricina* at three flight speeds are shown in Fig. 5 as the multicoloured surfaces spanned between the wake vortices. The vortex wake is visualized using green iso-surfaces of constant absolute vorticity $|\omega|$ in the three-dimensional interpolated wake field {*x,y,z*}.

The actuator disk surface spanned between the main vortices is colour-coded using the vertical induced velocity strength.

The vorticity magnitude iso-surfaces confirm previous wake structure descriptions for bats (Hedenström et al. 2007; Hubel et al. 2010; Muijres et al. 2011), but unrestricted from having only the streamwise vorticity component. At the lowest flight speed (U_∞ = 2 m/s, Fig. 5*a*), a start vortex is generated by each wing at the beginning of the downstroke. Each start vortex connects to the tip-vortex and a vortex which is probably shed from the root of the wing. Therefore, this vortex is called the root vortex (Hedenström et al. 2007; Muijres et al. 2011). Between each tip- and root vortex, so behind the outer wing, the downwash is largest (see actuator disk surfaces in Fig. 5*a*), while between the root vortices (behind the body) hardly any downwash is present. Both the tip and root vortices are present throughout the whole downstroke, but their strength drops below the iso-surface threshold at the start of the upstroke. During the upstroke no strong vortex structure is present, indicating that the upstroke is relatively inactive at 2 m/s.

At the medium flight speed (U_∞ = 4 m/s, Fig. 5 *b*), the vortex structure during the downstroke is very similar to that at U_∞ = 2 m/s, while during the upstroke, the wake is very different from that at U_∞ = 2 m/s. During the first part of the upstroke the tip vortices are still present at 4 m/s. They disappear at the second half of the upstroke, after which two small vortex loops appear, one behind each wing, resulting in an upwash at this part of the wake. Since these vortex loops generate an upwash, resulting in negative lift, they are denoted as reversed vortex loops. Reversed vortex dipoles were also noted by Hedenström et al.

Fig. 6 Results from the actuator disk analysis for *G. soricina* (*filled symbols*) and *L. yerbabuenae* (*open symbols*) throughout the measured flight speed range, see legend in panel (*e*). (*a*) The lift to weight ratio *L/W*. (*b*) the wingbeat average lift coefficient C_L. (*c*) datapoints and statistical trend lines of the real induced power P_i (*circle with solid line*) and ideal induced power $P_{i\,\text{ideal}}$ (*square with dotted line*). (*d*) the span efficiency e_i.


(2007), Johansson et al. (2008), Hubel et al. (2010) and Muijres et al. (2011), but here we can confirm that each reversed vortex dipole is in fact part of a vortex loop.

At the highest flight speed (U_∞ = 7 m/s, Fig. 5*c*) the same wake structures are present as at 4 m/s, but the relative strength of the structures are different. At U_∞ = 7 m/s, the root vortices are present throughout almost the complete wingbeat, resulting in a reduction in downwash behind the body, also during the upstroke. The reversed vortex loops are stretched out along a large part of the wingbeat, resulting in more upwash and more negative lift. The start vortices and the spanwise part of the reversed vortex loops are not visible in Fig. 5*c*, which could be because the spanwise vorticity ω_y is underestimated, or because the spanwise vortices are stretched out in streamwise direction due to the higher flight speed (Johansson et al. 2008), resulting in maximum vorticity values below the iso-surface threshold.

5.2 Wingbeat average lift production

The overall uncertainty of the actuator disk model for forward flapping flight was estimated by comparing the calculated lift with the known weight of the bats. The lift-to-weight ratio, *L/W*, for *G. soricina* is not significantly different from one (*L/W* = 0.98 ± 0.10, mean ± SD), but for *L. yerbabuenae* it is (*L/W* = 0.87 ± 0.13), as is the variation with speed (Table 2 and Fig.6*a*). Fig.6*b* shows the average lift-coefficient, C_L, throughout the wingbeat for the same data as in Fig. 6*a*, defined as

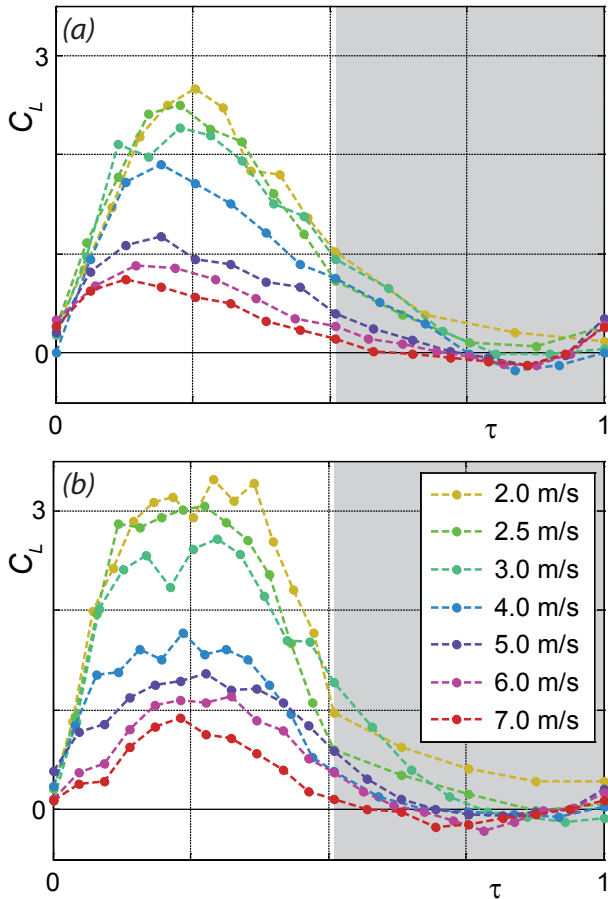$$C_L = \frac{L}{1/2\,\rho\,U_{\infty,eff}^{\,2}\,S} \tag{14}$$

113
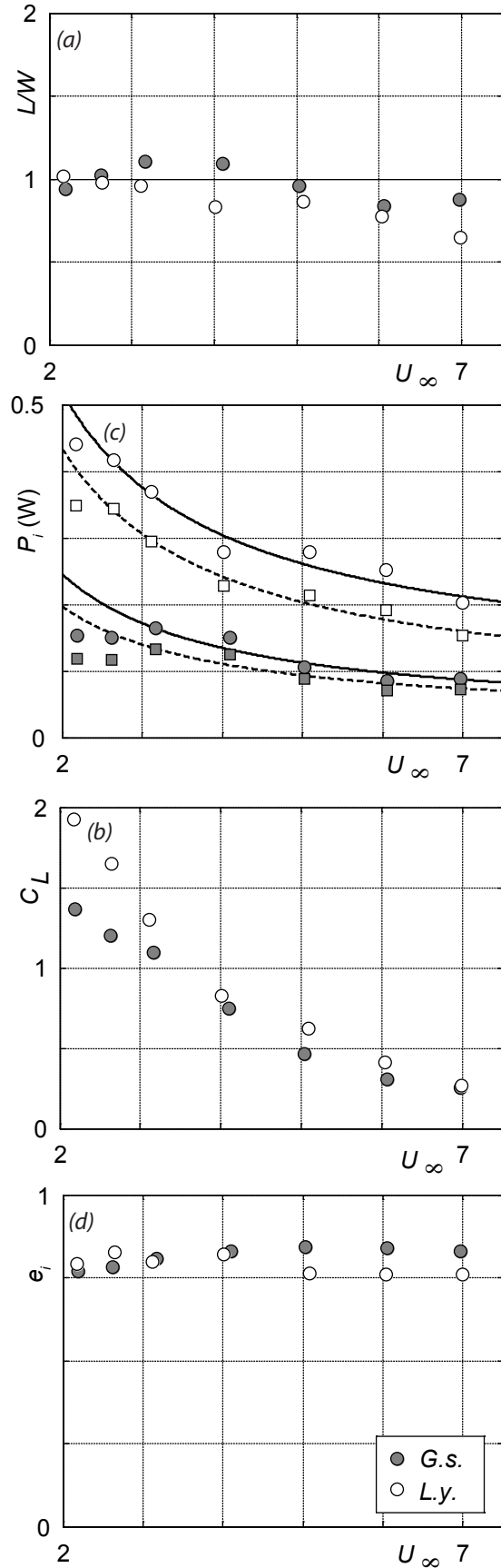
Fig. 7 The temporal C_L distributions throughout the wingbeat for different flight speeds, as indicated in the legend in panel *(b)*. Panel *(a)* shows $C_L(\tau)$ for *G. soricina*, while panel *(b)* shows $C_L(\tau)$ for *L. yerbabuenae*. The grey area in both panels indicate upstroke

5.3 Temporal C$_L$ distribution throughout the wingbeat

$C_L(\tau)$, for each species-speed combination, is determined from the $\overline{N}$ different spanwise downwash distributions using Eq. 7 and Eq. 14 (Fig. 7). For both bat species, the majority of the lift is generated during the downstroke, while for $U_\infty = 4$ m/s and faster, negative lift ($C_L < 0$) is generated during part of the upstroke. Clear differences in the temporal lift distribution between the bat species can be distinguished. For *G. soricina*, lift increases rapidly at the start of the downstroke, reaching a maximum peak around $\tau = 0.2$, whereafter C_L directly decreases. For *L. yerbabuenae*, C_L stays relatively constant at its maximum value throughout a large part of the downstroke ($\tau = [0.2, 0.35]$), after which it decreases more rapidly.

5.4 Spanwise downwash distribution

The downwash distributions along the non-dimensional wake span ($y^* = y/b_w$) for different parts of the wingbeat (start of the downstroke, $\tau = 0$; mid downstroke, $\tau = 0.25$; end of the downstroke, $\tau = 0,50$; mid upstroke, $\tau = 0.75$) are shown in Fig. 8, for both bat species, at $U_\infty = 2$ m/s, 4 m/s and 7 m/s, respectively. For all flight speeds, the downwash is highest (most negative w) during mid downstroke, with its local spanwise maximum at the outer wing ($y^* = 0.4$). $w(y^*)$ decreases towards the inner wing and drops to zero behind the body. During the uptroke a clear upwash is present behind the outer wings at $U_\infty = 4$ m/s and 7 m/s, while no upwash is observed at the lowest flight speed (2 m/s). The upwash behind the outer wings, resulting in negative lift, is primarily induced by the reversed vortex loops. Sometimes, an upwash is also present behind the body, notably for *L. yerbabuenae*.

Fig. 9 shows the spanwise downwash distribution for all measured flight speeds, at mid downstroke ($\tau = 0.25$, Fig. 9*a-b*) and at mid upstroke ($\tau = 0.75$, Fig. 9*c-d*). At mid downstroke the downwash distribution is quite similar for all flight speeds, while at mid upstroke the downwash distribution varies much more with flight speeds. For the lowest flight speeds ($U_\infty < 3$ m/s) a downwash is present along the complete wingspan during the upstroke, while at the higher speeds ($U_\infty > 3$ m/s) an upwash is present behind the outer wing, where the reversed vortex loops are located. Also, especially for *L. yerbabuenae*, an upwash is present behind the body at multiple flight speeds, as previously noted.

5.5 Induced power and span efficiency

Using the modified actuator disk model the induced power for flapping flight was estimated (Fig.6*c* and Table 2). Both the real and ideal normalized induced power $P_i(b/W)^2$ vary significantly with $1/U_\infty$, but not between species (Fig. 6*c* and Table 2). At the lowest speeds, P_i is lower than expected from Eq. 12, indicating relatively high flight efficiency at low flight speeds.

The average span efficiency throughout the measured flight speed range is estimated as $e_i = 0.81 \pm 0.03$ for *G. soricina* and $e_i = 0.79 \pm 0.03$ for *L. yerbabuenae* (see also Fig.6*d*). e_i does vary significantly between the two bat species, but not with U_∞ (Table 2).
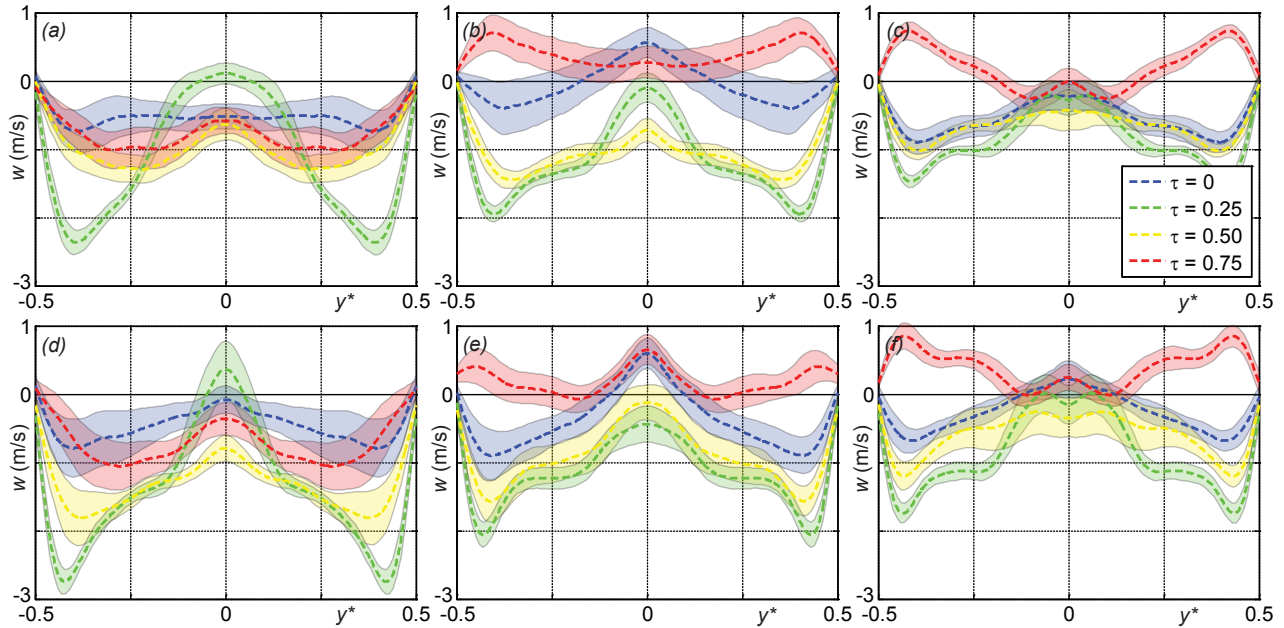
Fig. 8 Average spanwise downwash distributions $w(y^*)$, with 95% confidence interval, at different moments within the wingbeat. The top panels show data for *G. soricina* at 2 m/s *(a)*, 4 m/s *(b)* and 7m/s *(c)*, while the bottom panels *(d-f)* show the equivalent data for *L. yerbabuenae*. Each panel shows the downwash at four points within the wingbeat: start of the downstroke ($\tau = 0$); mid downstroke ($\tau = 0.25$); end of the downstroke ($\tau = 0.5$); mid upstroke ($\tau = 0.75$), see legend in panel *(c)*

6 Discussion

A modified actuator disk model for forward flapping flight was constructed from time-resolved sequences of cross-stream PIV data from the near-wake of two bat species flying freely in a wind tunnel over a speed range 2 -7 m/s. Across this speed range, the mean calculated lift-to-weight ratio, *L/W*, for *G. soricina* does not differ from one (*L/W* = 0.98 ± 0.10, Table 2), but for *L. yerbabuenae*, *L/W* is less than one (*L/W* = 0.87 ± 0.13, Table 2), especially at the higher speeds (Fig. 6*a*). The fact that the induced downwash was measured in the near wake of the flying bats instead of at the wing, cannot explain the deficit in *L/W* for *L. yerbabuenae*, since this should rather result in an over-estimation of lift (Fig.4*a*). For the actuator disk model developed here, streamwise induced velocities were ignored, since they could not be separated from wake defects due to drag. This probably results in an underestimation of the total mass flux (Eq. 5 and Fig. 2*a*). Since thrust forces can be assumed largest at the highest flight speeds (Muijres et al., 2011), and *L/W* is lowest at the highest flight speeds, one can assume that the underestimation of *L/W* is due to ignoring streamwise induced velocities.

The wingbeat average C_L estimate (Fig.6*a*) shows

that the bats generated relatively high C_L values at low flight speeds ($C_L > 1$ at $U_\infty < 3$ m/s), which is high for steady-state wings (Laitone 1997) but not uncommon for flapping wings (Hedenström & Spedding 2008; Muijres et al. 2008; Sane 2003).

The spanwise distribution of the vertical induced velocity behind the flying bats shows that these bats use the outer wing to generate the major part of the lift. The outer wing generates most lift because here, due to the flapping motion, both the angle-of-attack and the effective wing velocity are higher compared to the inner part of the wing (Wolf et al. 2010). Behind the body, induced velocity *w* is close to zero for large parts of the wingstroke, and even sometimes an upwash is present, resulting in negative lift generated by the body. This negative lift is probably generated by the wing membrane between the hind legs of the bats (*uropatagium*), and could be used for pitch control similar to the function of a horizontal tailplane in conventional airplanes. At the last part of the upstroke a 'reversed vortex loop' is generated by each wing (Fig.5), which also results in negative lift.

There are multiple hypotheses for explaining the presence of the reversed vortex loops. Reversed vortex loops could be generated due to limitations in the

Fig. 9 Average spanwise downwash distributions $w(y^*)$ for the complete measured flight speed range. *(a)* downwash at mid downstroke ($\tau=0.25$) for *G. soricina*; *(b)* downwash at mid upstroke ($\tau=0.75$) for *G. soricina*; *(c)* downwash at mid downstroke ($\tau=0.25$) for *L. yerbabuenae*; *(d)* downwash at mid upstroke ($\tau=0.75$) for *L. yerbabuenae*. The different speeds are colour coded as shown in panel *(b)*
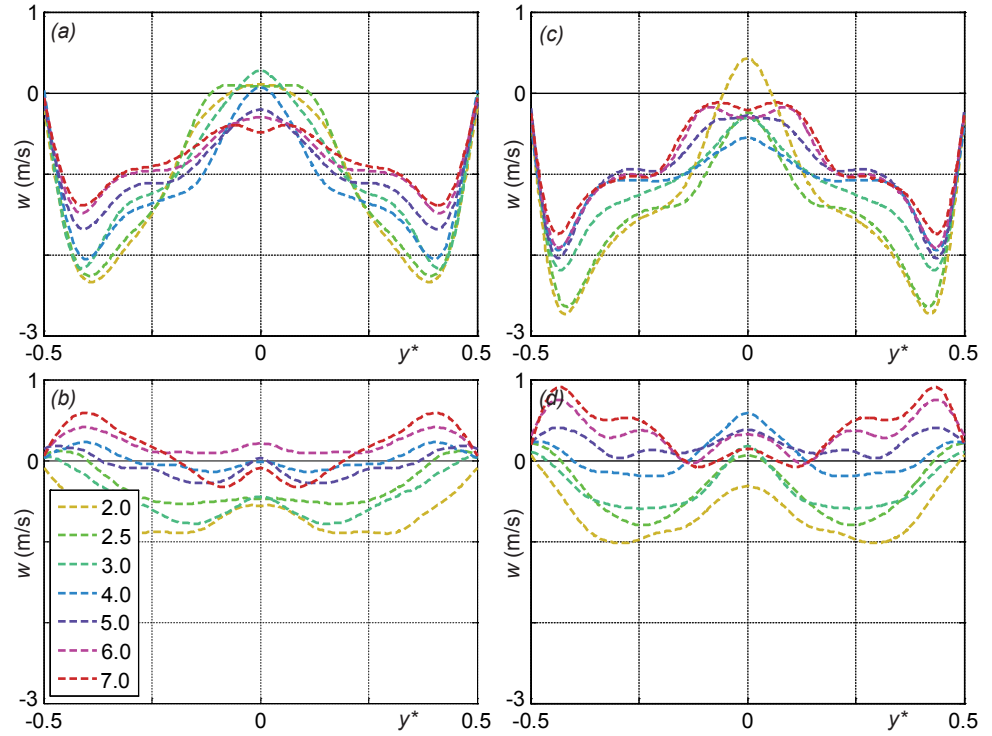
membranous wing morphology and wing kinematics (Hedenström et al. 2007), and/or could be used for maneuverability and stability control (Johansson et al. 2008), or the reversed vortex loops could be used for thrust generation with negative lift as a by-product (Muijres et al., 2011). The pattern of the induced velocities as a result of the reversed vortex loops is strikingly similar to the wake pattern at the equivalent part of the wingbeat and wing section of an optimal flapping wing with a relatively high thrust requirement (lift-to-drag ratio L/D = 5, Hall et al. 1998, similar to the L/D values estimated for these bats, Muijres et al. 2011). The optimum is the wingbeat kinematics with the lowest power requirement for the prescribed lift and thrust production. For L/D = 5, the optimal flapping wing generates thrust in combination with negative lift at the outer part of the wing during the upstroke (Hall et al. 1998). Since one can assume that thrust requirements increase with increasing flight speed, and the upwash at the reversed vortex loop for the bats also increase with flight speed, the results support the last hypothesis for explaining the presence of the reversed vortex loops.

When controlling for span loading, the induced power estimate did not differ significantly between the two bat species (Table 2). At the lowest flight speeds the induced power, P_i, was lower than expected

from Eq. 12 (Fig.6c). This can be explained by the fact that at the lowest flight speeds the difference between U_∞ and $U_{\infty\,eff}$ is largest. e.g. at U_∞ = 2 m/s the wings operate effectively at an average speed of $U_{\infty,eff}$= 3.26 m/s. Indirect support for this result comes from respirometry measurements of flying *G. soricina*, where metabolic rate of hovering was similar to that of forward flight (Winter 1998).

Norberg et al. (1993) used an ideal actuator disk model in combination with hot-wire anemometry measurements to estimated the induced power and span efficiency for *G. soricina* during hovering flight. Our induced power estimate for *G. soricina* at a speed of 2 m/s (P_i = 0.153 W) is similar to their estimate for hovering flight (P_i = 0.147 W), while our ideal power estimate ($P_{i\,ideal}$ = 0.118 W) is higher than $P_{i\,ideal}$ = 0.094 W estimated by Norberg et al. (1993). This difference in $P_{i\,ideal}$ results in a higher span efficiency estimated here for *G. soricina* at 2 m/s (e_i = 0.77), than e_i = 0.64 estimated by Norberg et al. (1993). The difference in ideal induced power can be explained by the fact that in the present study the ideal induced power presumes only a spanwise uniform downwash at each time step (Eq. 8-10), instead of a uniform downwash throughout the complete wingbeat as assumed in Norberg et al. (1993). Since e_i is defined as the factor describing the deviation from a uniform

spanwise downwash (Spedding & McArthur 2010), we would argue that assuming a spanwise uniform downwash distribution for the $P_{i\ ideal}$ calculation results in a better estimate for the true span efficiency.

The average estimations of the span efficiency throughout the flight speeds range for both bat species (e_i = 0.81±0.03 for *G. soricina* and e_i = 0.79±0.03 for *L. yerbabuenae*), are somewhat lower than estimates from other animal flight studies (gliding kestrel, e_i = 0.96, Spedding 1987; desert locust at mid downstroke, e_i = 0.85 to 0.89, Bomphrey et al. 2006), similar to values assumed in bird flight models (e_i = 0.83, Pennycuick 2008a), but high compared to the highest estimate of e_i for a steady Eppler 387 wing at similar *Re* (e_i = 0.76, Spedding & McArthur 2010). The fact that gliding kestrels have higher e_i could mean that birds have inherently higher span efficiency, but also that gliding flight results in higher e_i than flapping flight, although the results by Spedding & McArthur (2010) indicate the opposite. The span efficiency for the desert locust was estimated using a similar technique as that used here (Bomphrey et al. 2006). However, the span efficiency was estimated at mid downstroke only, while the span efficiencies reported here are the average e_i for the whole wingbeat. We have estimated e_i at mid-downstroke at 0.79 ± 0.06 for *G. soricina* and 0.79±0.04 for *L. yerbabuenae*, suggesting that desert locusts would have higher e_i than bats, at least at mid-downstroke. This difference may be a consequence of the relatively low downwash behind the body of bats as a result of low body lift and creating an unfavorable spanwise downwash distribution (Fig. 9*a-b*).

The above comparison shows that bat flight has relatively low span efficiency compared to other flying animals, possibly due to relatively low body lift in bats. But, since this is the first empirical estimate of the span efficiency throughout a complete wingbeat we cannot conclusively distinguish relative flight efficiency of bat compared to birds and insects from general flapping flight efficiency compared to steady wings. Therefore, a future comparison with similar data from birds, insects and mechanical flappers would be very informaIn conclusion, we show here how the modified actuator disk model together with high-speed PIV data can be used to obtained high-resolution temporal and spanwise downwash distribution of flapping flight. The method works without the need to model or measure complex wing-wake interactions. By applying this approach we can derive key aerodynamic properties of flapping flight such as the temporal lift distribution, the induced power and the span efficiency. The induced power and the span efficiency for *G. soricina* at the lowest flight speed are similar to that of previous estimates for a hovering *G. soricina* (Norberg et al. 1993).

References

Anderson, J. D. (1991). *Fundamentals of Aerodynamics*. McGraw-Hill, New York

Bomphrey, R. J., Taylor, G. K., Lawson, N. J., & Thomas, A. L. (2006). Digital particle image velocimetry measurements of the downwash distribution of a desert locust Schistocerca gregaria. *Journal of The Royal Society Interface*, *3*: 311 -317

Ellington, C. P. (1984). The Aerodynamics of Hovering Insect Flight. V. A Vortex Theory. *Philosophical Transactions of the Royal Society of London. Series B, Biological Sciences*, *305*: 115-144

Gessow, A., & Myers, G. C. (1952). *Aerodynamics of the helicopter*. F. Ungar Pub. Co, New York

Grundy, T. M., Keefe, G. P., & Lowson, M. V. (2001). 'Effects of Acoustic Disturbances on Low Re Aerofoil Flows. *fixed and flapping wing aerodynamics for Micro Air Vehicle Applications*, *195*: 91–112

Hall, K. C., Pigott, S. A., & Hall, S. R. (1998). Power requirements for large-amplitude flapping flight. *Journal of Aircraft*, *35:* 352–361

Hall, K. C., & Hall, S. R. (1996). Minimum Induced Power Requirements for Flapping Flight. *Journal of Fluid Mechanics Digital Archive*, *323*: 285-315

Hedenström, A., Johansson, L., Wolf, M., von Busse, R., Winter, Y., & Spedding, G. (2007). Bat Flight Generates Complex Aerodynamic Tracks. *Science*, *316*: 894-897

Hedenström, A., Rosén, M., & Spedding, G. R. (2006). Vortex wakes generated by robins Erithacus rubecula during free flight in a wind tunnel. *Journal of The Royal Society Interface*, *3*: 263-276

Hedenström, A., Muijres, F., von Busse, R., Johansson, L., Winter, Y., & Spedding, G. (2009). High-speed stereo DPIV measurement of wakes of two bat species flying freely in a wind tunnel. *Experiments in Fluids*, *46*: 923-932

Hedenström, A., & Spedding, G. (2008). Beyond robins: aerodynamic analyses of animal flight. *Journal of The Royal Society Interface*, *5*: 595-601

Henningsson, P., Muijres, F. T., & Hedenström, A. (2010). Time-resolved vortex wake of a common swift flying over a range of flight speeds. *Journal of The Royal Society Interface*. doi:10.1098/rsif.2010.0533

Hubel, T., Hristov, N., Swartz, S., & Breuer, K. (2009). Time-resolved wake structure and kinematics of bat flight. *Experiments in Fluids*, *46*: 933-943

Hubel, T. Y., Riskin, D. K., Swartz, S. M., & Breuer, K. S. (2010). Wake structure and wing kinematics: the flight of the lesser dog-faced fruit bat, Cynopterus brachyotis. *J Exp Biol*, *213*: 3427-3440

Johansson, L. C., & Hedenström, A. (2009). The vortex wake of blackcaps (Sylvia atricapilla L.) measured using high-speed digital particle image velocimetry (DPIV). *J Exp Biol*, *212*: 3365-3376

Johansson, L. C., Wolf, M., von Busse, R., Winter, Y., Spedding, G. R., & Hedenström, A. (2008). The near and far wake of Pallas' long tongued bat (Glossophaga soricina). *J Exp Biol*, *211*: 2909-2918

Laitone, E. (1997). Wind tunnel tests of wings at Reynolds numbers below 70 000. *Experiments in Fluids*, *23*: 405

Lentink, D., & Gerritsma, M. (2003). Influence of airfoil shape on performance in insect flight. *33rd AIAA Fluid Dynamics Conference and Exhibit*

Lissaman, P. (1983). Low-Reynolds-Number Airfoils. *Annual Review of Fluid Mechanics*, *15*: 223-239

Muijres, F., Johansson, L., Barfield, R., Wolf, M., Spedding, G., & Hedenström, A. (2008). Leading-Edge Vortex Improves Lift in Slow-Flying Bats. *Science*, *319*: 1250-1253

Muijres, F. T., Johansson, L. C., Winter, Y., & Hedenström, A. (2011). Comparative aerodynamic performance of flapping flight in two bat species using time-resolved wake visualization. *Journal of The Royal Society Interface*, doi: 10.1098/rsif.2011.0015, 2011

Norberg, U. M., & Rayner, J. M. V. (1987). Ecological Morphology and Flight in Bats (Mammalia; Chiroptera): Wing Adaptations, Flight Performance, Foraging Strategy and Echolocation. *Philosophical Transactions of the Royal Society of London. B, Biological Sciences*, *316*: 335-427

Norberg, U., Kunz, T., Steffensen, J., Winter, Y., & von Helversen, O. (1993). The cost of hovering and forward flight in a nectar-feeding bat, Glossophaga soricina, estimated from aerodynamic theory. *J Exp Biol*, *182*: 207-227

Pennycuick, C. J. (1971). Gliding Flight of the Dog-Faced Bat Rousettus Aegyptiacus Observed in a Wind Tunnel. *J Exp Biol*, *55*: 833-845

Pennycuick, C. J. (1973). Wing profile shape in a fruit-bat gliding in a wind tunnel, determined by photogrammetry. *Periodicum Biologorum*, *75*: 77–82

Pennycuick, C. (1968). Power Requirements for Horizontal Flight in the Pigeon Columba Livia. *J Exp Biol*, *49*: 527-555

Pennycuick, C. J. (2008a). *Modelling the Flying Bird*. Elsevier, Amsterdam

Pennycuick, C. (2008b). Chapter 6 The Membrane Wings of Bats and Pterosaurs. In *Modelling the Flying Bird* (Vol. 5, pp. 135-160). Academic Press, New York

Pennycuick, C., Alerstam, T., & Hedenström, A. (1997). A new low-turbulence wind tunnel for bird flight experiments at Lund University, Sweden. *J. Exp. Biol. 200*: 1441-1449

Pesavento, U., & Wang, Z. J. (2009). Flapping Wing Flight Can Save Aerodynamic Power Compared to Steady Flight. *Physical Review Letters*, *103*: 118102

Rosén, M., Spedding, G., & Hedenström, A. (2007). Wake structure and wingbeat kinematics of a house-martin *Delichon urbica*. *Journal of The Royal Society Interface*, *4*: 659 -668

S. M. Swartz, M. S. Groves, H. D. Kim, & W. R. Walsh. (1996). Mechanical properties of bat wing membrane skin. *Journal of Zoology*, *239*: 357-378

Sane, S. (2003). The aerodynamics of insect flight. *J Exp Biol*, *206*: 4191-4208

Spalart, P. R. (2003). On the Simple Actuator Disk. *Journal of Fluid Mechanics*, *494*(-1), 399-405.

Spedding, G. R. (1987). The Wake of a Kestrel (Falco Tinnunculus) in Gliding Flight. *J Exp Biol*, *127*: 45-57

Spedding, G. R., Hedenström, A. H., McArthur, J., & Rosen, M. (2008). The implications of low-speed fixed-wing aerofoil measurements on the analysis and performance of flapping bird wings. *J Exp Biol*, *211*: 215-223

Spedding, G. R., Rosen, M., & Hedenström, A. (2003a). A family of vortex wakes generated by a thrush nightingale in free flight in a wind tunnel over its entire natural range of flight speeds. *J Exp Biol*, *206*: 2313-2344

Spedding, G.R., Hedenström, A. & Rosén, M., (2003b). Quantitative studies of the wakes of freely flying birds in a low-turbulence wind tunnel. *Experiments in Fluids*, 34: 291

Spedding, G. R., & McArthur, J. (2010). Span Efficiencies of Wings at Low Reynolds Numbers. *Journal of Aircraft*, *47*: 120-128

Spedding, G. R., Rosen, M., & Hedenström, A. (2003). A family of vortex wakes generated by a thrush nightingale in free flight in a wind tunnel over its entire natural range of flight speeds. *J Exp Biol*, *206*: 2313-2344

Spedding, G., & Hedenström, A. (2009). PIV-based investigations of animal flight. *Experiments in Fluids*, *46*: 749-763

Stepniewski, W. Z., & Keys, C. N. (1984). *Rotary-wing aerodynamics*. Courier Dover Publications, New York

Swartz, S. M., Iriarte-Diaz, J., Riskin, D. K., Song, A., Tian, X., Willis, D. J., & Breuer, K. S. (2007). Wing structure and the aerodynamic basis of flight in bats. In *AIAA Aerospace Science Meeting*, *42*

Wang, Z. J. (2008). Aerodynamic efficiency of flapping flight: analysis of a two-stroke model. *J Exp Biol*, *211*: 234-238

Winter, Y. (1998). Energetic cost of hovering flight in a nectar-feeding bat measured with fast-response respirometry. *J. Comp. Physiol, 168*: 434-444

Wolf, M., Johansson, L. C., von Busse, R., Winter, Y., & Hedenström, A. (2010). Kinematics of flight and the relationship to the vortex wake of a Pallas' long tongued bat (*Glossophaga soricina*). *J Exp Biol*, *213*: 2142-2153

Vortex wake, downwash distribution, aerodynamic performance and wingbeat kinematics in slow-flying Pied Flycatchers

Florian T. Muijres[1], Melissa S. Bowlin[1,2], L. Christoffer Johansson[1] and Anders Hedenström[1]

[1]*Department of Biology, Ecology Building, Lund University, SE-223 62 Lund, Sweden*
[2]*Department of Natural Sciences, University of Michigan-Dearborn, 4901 Evergreen Rd., Dearborn, MI, 48128 USA*

Many small passerines regularly hover or fly slowly when catching prey, flying in cluttered environments, or landing on a perch or nest. When flying slowly, these passerines use inclined stroke plane hovering, where they generate most of the flight forces during the downstroke, and make their wing inactive during the upstroke by retracting it close to the body. How this type of hovering relates aerodynamically to so-called 'normal' hovering used in insects and hummingbirds is not yet known. Here we present time-resolved fluid dynamics data in combination with wingbeat kinematics data for three pied flycatchers flying across a range of speeds from near hovering to their calculated minimum power speed. Flycatchers are adapted to low speed flight, which they habitually use when catching insects on the wing. From the wake dynamics data, we constructed average wingbeat wakes and determined the time-resolved flight forces, the time-resolved downwash distributions, and the resulting lift-to-drag ratios and span efficiencies. During the downstroke, slow-flying flycatchers generate a single vortex loop wake, which is much more similar to that generated by birds at higher flight speeds than it is to the double loop vortex wake in hovering hummingbirds. This wake structure results in a relatively high downwash behind the body, which can be explained by the relatively active tail in flycatchers. This results in flycatchers having higher span efficiency and lower induced drag than hummingbirds. During the upstroke, the wings of slowly flying flycatchers generated no significant forces, but the tail/body configuration added 23% to weight support. This is strikingly similar to the 25% weight support generated by hummingbird wings during the upstroke. Thus, in inclined stroke plane hovering the upstroke cannot be regarded as inactive, and the tail may be of importance for flight efficiency and possibly maneuverability.

Keywords: *Ficedula hypoleuca* bird, aerodynamic flight performance, inclined stroke plane hovering, wingbeat kinematics, wind tunnel, PIV

1 Introduction

When commuting or migrating, birds are assumed to fly near the speed yielding minimum energetic costs per unit distance travelled (called maximum range speed U_{mr}) [1,2]. Therefore, the majority of bird flight research has focused on flight performance around this flight speed [3-7]. Many small birds, however, often fly much slower, particularly those that hunt or feed on the wing or live in cluttered environments [8,9], although not much is known about flight speed distributions in the wild. Still, it can be assumed that natural selection has resulted in efficient and controlled flight at low speeds for birds that often fly at these speeds, just as it has resulted in efficient flight at migratory flight speeds for migratory birds.

Most research on hovering and slow flight in birds has been done on small specialized hoverers, such as hummingbirds [10-12]. Hummingbirds are

considered specialized hoverers because they have a relatively stiff wing which turns upside down during the upstroke, much like the wings of insects. This type of hovering is commonly called 'normal' hovering, and results in lift production throughout the entire wingbeat [13]. The wake topology for hovering hummingbirds is described as a collection of vortex loops, where each wing generates a separate vortex loop at each wing stroke (upstroke and downstroke) [11]. The tail is relatively inactive in lift production. Also, hummingbirds generate a leading edge vortex (LEV) on the wing for enhancing lift production at low flight speeds [14].

Compared to hummingbirds, little research has been done on the slow flight of more conventional birds, which use a type of hovering known as asymmetric or inclined stroke plane hovering [15,16]. Asymmetric hoverers have much more flexible wings; these wings are made inactive during the upstroke. This is done by retracting the wings and spreading the primary feathers in such a way that the air can flow through the gaps in between the feathers, resulting in low flight forces during the "feathered upstroke" [17,18]. The tail, however, can still be active during the upstroke [17].

Basic aerodynamic measurements on the slow flight of more conventional birds (Pigeon *Columba livia* at 2.5 m/s, [19] and Jackdaw *Corvus monedula* at 2.5 m/s [20]) describe the wake as a single vortex loop generated during the active downstroke, while no distinct vortex structure is found during the upstroke. More detailed aerodynamic measurements on the flapping flight of birds at higher flight speeds (near U_{mr}) have found a similar wake structure during the

downstroke, where the whole animal generates a single vortex loop, although smaller wake structures could also be distinguished [6,7]. During the upstroke, a second vortex structure is generally found; this structure is also generated by the wings and results in aerodynamic forces that contribute to weight support, but which also generate negative thrust, hence adding to drag [3,5,21].

Based on these aerodynamic data, we hypothesize that asymmetric hoverers should generate wake patterns which are more similar to the wake patterns found in more conventional birds near U_{mr} than to wake patterns found in hummingbirds. We tested this hypothesis by studying the aerodynamic flight performance of an asymmetric hoverer, the pied flycatcher (*Ficedula hypoleuca*). The pied flycatcher is a small (14*g*) insectivorous passerine which hunts insects mainly on the wing [8]. We estimated the aerodynamic flight performance of three flycatchers at a flight speed range from near hovering (2 m/s) to an intermediate flight speed of 7 m/s. This speed is called intermediate because it is close to the estimated minimum power speed U_{mp} for flycatchers (Table 1) [1]. The aerodynamic flight performance was estimated based on stereoscopic flight kinematics measurements in combination with aerodynamic wake data, measured using stereoscopic time-resolved particle image velocimetry (PIV). This technique enables us to determine the vortex wake pattern and induced downwash distribution behind the flying animal, which is used to estimate the temporal flight forces and flight performance values such as the lift-to-drag ratio (*L/D*) [22] and the span efficiency (*e_i*) [23] throughout the measured flight speed range.

Table 1 Morphological data and ecologically important flight speeds for the pied flycatchers used in the experiment. The morphological data consists of mass *M*, wing span *b*, wing surface area *S*, mean chord length *c*= *S/b*, aspect ratio *AR* = *b²/S* and wing loading *Q* = *Mg/S*, where g is the gravitational constant. The ecologically important flight speeds are the minimum power speed U_{mp} and the maximum range speed U_{mr}

individual	M (kg)	b (m)	S (m²)	c (m)	AR (-)	Q (N/m²)	U_{mp} [1] (m/s)	U_{mr} [1] (m/s)
Flycatcher #1	0.0148	0.235	0.0106	0.045	5.2	13.7	7.2	13.5
Flycatcher #2	0.0141	0.235	0.0105	0.045	5.3	13.2	7.1	13.3
Flycatcher #3	0.0137	0.236	0.0107	0.045	5.2	12.6	7.0	13.2

[1] **estimated based on *M*, *b*, *S* and body drag coefficient $C_{D\,body}$ = 0.10 using the program Flight 1.22 [25]**

2 Material and methods
2.1 Pied Flycatchers

The pied flycatcher is a small (14g) passerine. It is a long-distance migrant, with breeding sites in northern Europe and Asia and wintering grounds in western and central Africa. Flycatchers are insectivorous and commonly catch insects on the wing, by taking off from a perch to catch an insect in midair before returning to the perch [8,9]. Therefore, they are likely to be adapted to hovering and slow flight.

Three juvenile pied flycatchers (from here on called flycatchers) were used for the experiments. The mass of each flycatcher was determined before and after each experimental session, while the wing area *S* and wing span *b* were determined following [24], except that Pennycuick's 'body box' [25] was added. Based on these data, we calculated their minimum power speed and maximum range speeds following [25] (see Table 1).

2.2 Experimental setup and procedure

The experiments were performed in the Lund University low-speed low-turbulence wind tunnel [26], using a high-speed (200Hz) stereoscopic PIV system (LaVision) for wake analysis and a stereoscopic high-speed (250Hz) video camera setup for kinematics analysis (Fig. 1*a*), similar to the setup described by [27].

The PIV setup consists of a 200 Hz pulsed 50 mJ Laser (Litron LPY732 series, Nd:YAG, 532 nm) and two synchronized, double frame, CMOS-cameras (HighSpeedStar3; 1024×1024 pixels) in stereo setup. The PIV image plane is 20×20 cm in size and is positioned in the {*y*,*z*} plane (Fig. 1). The PIV system was controlled by the LaVision PIV software package DaVis (LaVision, DaVis 7.2.2.110). The kinematics camera setup consists of two synchronized CCD-cameras (Redlake MotionScope PCI 500) operating at 250Hz and infrared lights (VDI-IR60F, Video Security Inc.) for illumination. Infrared lights were used to reduce interference with the PIV system, although in this study PIV and kinematics measurements were done separately.

During the experiments, a single bird was trained to perch on a hand-held perch in the test section of the wind tunnel. When the perch was lowered, the bird took off. When the flycatcher flew steadily in the desired position (directly upstream from the PIV laser sheet), 100 PIV measurements or 1024 kinematics measurements were obtained, after which the perch was presented again to the bird.
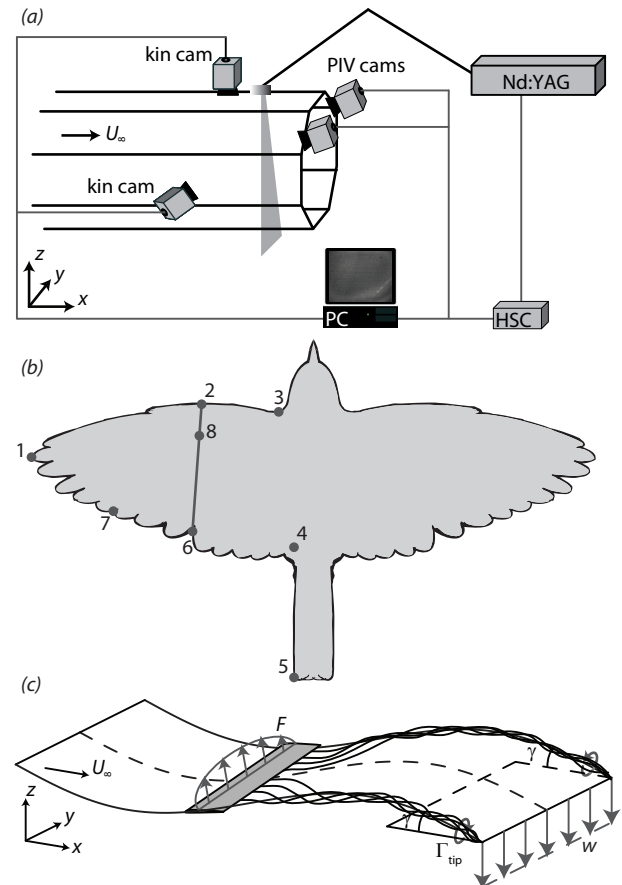

Fig. 1 (*a*) the experimental setup, consisting of a low-turbulence low-speed wind tunnel, a high-speed stereoscopic PIV system for airflow visualization, and a high-speed stereoscopic video system for flight kinematics analysis. *(b)* top view of a flycatcher with the 7 natural wing markers, being (1) the wing tip; (2) the wrist; (3) the shoulder; (4) the side of the rump; (5) the tip of the tail; (6) the indentation between the innermost primary and the outermost secondary feather; and (7) the tip of the third primary. Also, the wing chord starting at the wrist with its quarter chord point (8) is shown. *(c)* a hypothetical heaving wing with an elliptical spanwise force distribution *F*, two tip vortices with circulation Γ_{tip} and spanwise angle (γ), and spanwise uniform downwash *w*

2.3 Wingbeat kinematics analysis

The wingbeat kinematics were analyzed for flycatchers #1 and #3 at flight speeds of 2 m/s, 4 m/s and 7 m/s. For each individual and flight speed combination, at least 5 sequences (each consisting of at least 2 steady wingbeats) were filmed and analyzed using a custom-made Matlab program (Matlab 7.7.0.471 R2008a). For the analysis, 7 natural wing and body markers (Fig. 1*b*) were manually digitized and converted into three-dimensional positions $\{x,y,z\}$ using direct linear transformation (Christoph Reinschmidt Matlab routines). For each marker and flight speed combination, the average wingbeat track was constructed from all the analyzed wingbeats at that flight speed using a nested ANOVA (Matlab, anovan).

From the average wingbeat kinematics tracks, the following kinematics variables were estimated: wingbeat frequency *f*; downstroke ratio R_{ds} (defined as the ratio of the temporal downstroke period and the upstroke period of a wingbeat); span ratio *SR* (defined as the ratio between the lateral extension of the wing tip at mid upstroke and at mid downstroke); effective Reynolds number during the downstroke, defined as

$$Re_{eff} = \overline{U}_{eff} c / v \,, \qquad (2.1)$$

where *c* is the mean wing chord length, v is the kinematic viscosity of air and $\overline{U}_{eff}$ is the mean effective wing velocity. $\overline{U}_{eff}$ is the vector sum of the forward flight speed U_∞ and flapping motion of the wing, and is defined as

$$\overline{U}_{eff} = \begin{vmatrix} U_\infty + \overline{u}_{ds} \\ \overline{v}_{ds} \\ \overline{w}_{ds} \end{vmatrix}, \qquad (2.2)$$

where $\{\overline{u}_{ds}, \overline{v}_{ds}, \overline{w}_{ds},\}$ is the downstroke mean velocity vector of the wing. Induced air movements are ignored. The Strouhal number during the downstroke is defined as [28]

$$St_{ds} = \frac{\overline{w}_{ds}/2}{(U_\infty + \overline{u}_{ds})} \,. \qquad (2.3)$$

Re_{eff} and St_{ds} are based on $\overline{U}_{eff}$ at two wing positions, being at the shoulder joint and at the wingtip (Fig. 1*b*). $\overline{U}_{eff}$ is solely based on the downstroke movements, since we can assume that the wings are mainly active during this part of the wingbeat [17].

The angle-of-attack is determined for the wing (α_{wing}) and for the tail (α_{tail}). α_{wing} is defined as the angle between the wing chord from the wrist marker to the marker at the indentation between the innermost primary and the outermost secondary feather, and the local velocity vector $\overline{U}_{eff}$ at the quarter chord point (Fig. 2*a*). α_{tail} is determined as the angle between the horizontal and the tail chord from the rump marker to the tail tip marker (Fig. 1*b*). Using the same markers, we determined the tail spread angle ϕ throughout the wingbeat.

The relative vertical body movement amplitude is defined as

$$A^*_{body} = A_{body} / A_{tip} \,, \qquad (2.4)$$

where A_{body} is the vertical wingbeat amplitude of the quarter chord point at the wing-body intersection, and A_{tip} is the vertical wingtip amplitude. A^*_{body} is used in the vortex wake analysis, as described below.

2.4 PIV analysis

PIV measurements were performed for flycatcher #3 at a flight speed of 2 m/s, 4 m/s and 7 m/s, and for flycatchers #1 and #2 at all measured flight speeds (2-7 m/s, in increments of 1 m/s). We did not sample at speeds below 2 m/s because the PIV setup required a higher convection speed to capture the wake. For each measured individual and flight speed combination, at least 5 sequences (each consisting of at least 2 steady wingbeats) were measured and analyzed. Each PIV sequence, consisting of 100 PIV measurements, was analyzed with DaVis (LaVision, DaVis 7.2.2.110) using a multi-pass normalized second-order stereo cross-correlation {64×64 and 32×32, 50% overlap} with Whittaker reconstruction, followed by a {3×3} smoothing. This results in a {y,z} matrix with corresponding velocity vectors {u,v,w} for each PIV frame. The PIV frames were given a frame number *n*, a normalized time stamp τ, and streamwise location stamp *x*. The frame number range is $n = [1\text{-}N]$, with $n = 1$ for the PIV frame representing the wake at the start of the downstroke, and $n = N$ for the PIV frame at the end of the upstroke. The normalized time stamp is defined as

$$\tau = t / \Pi \,, \qquad (2.5)$$

where *t* is the time at which the PIV frame was recorded with $t = 0$ for the PIV frame representing the wake at

the start of the downstroke. Π is the wingbeat period, so the PIV frame with $\tau = 1$ represents the wake at the start of the next downstroke. Using n and τ, the PIV sequences are divided into separate wingbeats.

When assuming that the wake convects statically downstream with the forward flight speed U_∞, one can estimate the streamwise position of each PIV frame within a wingbeat as

$$x = U_\infty \ t = U_\infty \ \Pi \ \tau \ , \qquad (2.6)$$

where x ranges from 0 at the start of the downstroke to $x=\lambda$ at the end of the upstroke, where λ ($= U_\infty \Pi$) is the wingbeat wavelength. The assumption that the wake convects statically downstream is an approximation of the true wake dynamics, but the x variable is only used to qualitatively visualize the three-dimensional wake topology, and is not used for any quantitative analysis.

The PIV data for each wingbeat is stored as a four-dimensional matrix with spatial and temporal variables $\{x,y,z,\tau\}$. For each node point $\{x,y,z,\tau\}$, the three-dimensional velocity vectors $\{u,v,w\}$ are also stored, from which the streamwise vorticity is calculated as $\{\omega_x\}$. The resulting wake matrices are analyzed using a custom-made Matlab program, where two main wake characteristics were measured: the streamwise vortex wake and the spanwise downwash distributions.

For the vortex wake analysis, the different PIV frames were visualized separately, and the main wake vortices were identified (e.g. the tip vortex, Fig. 1*c*). For each of these main vortex structures, the location and time stamp $\{x,y,z,\tau\}$, streamwise peak vorticity $\{\omega_{x,max}\}$ and streamwise circulation $\{\Gamma_x\}$ were measured and stored. The vortex area was defined as the area where $\omega_x > \omega_{x,min}$, with $\omega_{x,min} = 60$ s^{-1}. This minimum value is larger than 95% of the vorticity noise as a result of the PIV calculation routine for the worst case scenario of $U_\infty = 7$ m/s, determined from PIV measurements from an empty wind tunnel. The vortex circulation is determined by integrating the vorticity throughout the vortex area. When assuming a normal Gaussian distribution of the vorticity outside the vortex area ($\omega_x < \omega_{x,min}$), the total streamwise circulation of a vortex is estimated as [5]

$$\Gamma_x = (1 + (|\omega_x|_{min}/|\omega_x|_{max})) \ \Gamma_x' \ , \qquad (2.7)$$

where Γ_x' is the streamwise circulation measured within the vortex area. In the wake of a common swift

Apus apus, three types of main vortex structures were identified [7]: the tip vortex, root vortex and tail vortex. These were also found in the wake of the flycatchers, so these vortex structures were measured and saved if present in a PIV frame.

For the spanwise downwash distribution analysis, the different PIV frames were visualized separately. In each PIV frame n, the spanwise downwash distribution was measured along a spanwise downwash line, which was defined as a straight line from the position behind the bird body to the center of the most distally positioned vortex structure (Fig. 1*c*). This structure was generally the tip vortex, but if the tip vortex was not present, the tail vortex was the most distal one, as in [7]. The vertically induced velocities w in each node point $\{y,z\}$ along this line were stored for further analysis. The collection of spanwise downwash lines in all frames within one wingbeat ($x = [0-\lambda]$) can be used to describe a downwash wake surface within the $\{x,y,z\}$ matrix, showing the downwash distribution $\{w\}$ along the span $\{y\}$ and throughout the wingbeat (along $\{x\}$ or $\{\tau\}$).

The resolution of the four-dimensional wake matrix $\{x,y,z,\tau\}$ is equal to the PIV node point resolution (5.1 mm) in the y and z directions. The temporal resolution is equal to the inverse of the frame rate of the PIV system ($\Delta t = 1/200$), resulting in a streamwise resolution of $\Delta x = U_\infty \Delta t = U_\infty /200$. Thus, Δx scales with the flight speed, ranging from $\Delta x = 10$ mm at 2 m/s to $\Delta x = 35$ mm at 7 m/s. To increase the streamwise resolution, an interpolation scheme was used where the amount of interpolation steps was equal to the flight speed. This results in an interpolated wake matrix $\{x',y,z\}$ with constant resolution of $\Delta x' = 5$ mm, throughout the complete measured flight speed range. These interpolated wake matrices are only used for qualitative analyses, as is described below.

3 Wake model for flapping bird flight
3.1 Wake topology

The wake topology for one wingbeat was visualized using the interpolated spatial wake matrix $\{x',y,z\}$ with the interpolated variables $\{w\}$ and $\{\omega_x'\}$. The vortex wake was visualized using iso-surfaces of constant spanwise vorticity $\{\omega_x'\}$ within the wake matrix. The induced velocity distribution in the wake was visualized using the downwash wake surface, where the surface is color-coded with the local vertical velocity $\{w\}$.

3.2 Vortex wake forces

The normalized aerodynamic lift forces corresponding to the different vortex wake structures (tip vortex, root vortex and tail vortex) at τ can be estimated using Kelvin's theorem and inviscid vortex theory as follows [7,22,29]

$$L_{tip}^*(\tau) = \rho U_\infty b_{tip}(\tau)\Gamma_{tip}(\tau)/Mg$$
$$L_{root}^*(\tau) = \rho U_\infty b_{root}(\tau)\Gamma_{root}(\tau)/Mg, \qquad (3.1)$$
$$L_{tail}^*(\tau) = \rho U_\infty b_{tail}(\tau)\Gamma_{tail}(\tau)/Mg$$

where ρ is the air density. $b_{tip}(\tau)$, $b_{root}(\tau)$ and $b_{tail}(\tau)$ are the vortex span of the tip vortex, root vortex and tail vortex, respectively. The forces are normalized using the weight of the flycatcher (*Mg*, where *M* is body mass and *g* is the gravitational constant). For each vortex structure, the total normalized vortex force $F^*(\tau)$ and the equivalent thrust component $T^*(\tau)$ are (Fig. 1*c*)

$$F^*(\tau) = L^*(\tau)/\cos(\bar{\gamma}(\tau))$$
$$T^*(\tau) = L^*(\tau)\tan(\bar{\gamma}(\tau)) \qquad , \qquad (3.2)$$

where $\bar{\gamma}(\tau)$ is the mean spanwise vortex sheet angle of the current vortex system (tip, root or tail vortex system). For the tail vortex system, the vortex sheet angle is assumed to be constant along the span, so $\bar{\gamma}_{tail}(\tau) = \gamma_{tail}(\tau)$, where $\gamma_{tail}(\tau)$ is the tail vortex angle at τ. For the tip and root vortex system, the mean angle is estimated as the average of the angle at the vortex (γ_{tip} or γ_{root}) and the vortex sheet angle at the body (γ_{body}) as [22]

$$\bar{\gamma}_{tip}(\tau) = \frac{\gamma_{tip}(\tau) + \gamma_{body}(\tau)}{2} = \frac{(1 - A_{body}/A_{tip})}{2}\gamma_{tip}(\tau)$$
$$\bar{\gamma}_{root}(\tau) = \frac{\gamma_{root}(\tau) + \gamma_{body}(\tau)}{2} = \frac{(1 - A_{body}/A_{root})}{2}\gamma_{root}(\tau) \qquad ,(3.3)$$

where A_{body}/A_{tip} is the ratio between the vertical wingbeat amplitude at the body and at the wingtip, which is determined in kinematics analysis ($A^*_{body} = A_{body}/A_{tip}$). The ratio between the body and root amplitude is determined by $A_{body}/A_{root} = A^*_{body} \times A_{tip}/A_{root}$. Since the root vortex cannot directly be linked to a specific wing marker, A_{tip}/A_{root} is estimated using the vertical movement of the tip vortex and root vortex, respectively [22]. There is a minus sign in front of the amplitude ratio because the body movement is in anti-phase with the wingtip and root vortex movement

(the body moves up when the wings move down). The angle for each vortex structure at τ can be estimated from the horizontal vortex path as

$$\gamma(\tau) = \tan^{-1}\left(\frac{dz(\tau)}{dx}\right) = \tan^{-1}\left(\frac{d\tau}{dx}\frac{dz(\tau)}{d\tau}\right) = \tan^{-1}\left(\frac{1}{U_\infty\Pi}\frac{dz(\tau)}{d\tau}\right). \quad (3.4)$$

The total temporal lift and thrust distributions are defined as

$$L^*(\tau) = L_{tip}^*(\tau) + L_{root}^*(\tau) + L_{tail}^*(\tau)$$
$$T^*(\tau) = T_{tip}^*(\tau) + T_{root}^*(\tau) + T_{tail}^*(\tau) \qquad . \qquad (3.5)$$

The corresponding total temporal force distribution is $F^*(\tau) = \sqrt{L^*(\tau)^2 + T^*(\tau)^2}$. By integrating these throughout the wingbeat (τ = [0-1]) the average normalized lift $\overline{L^*}$, thrust $\overline{T^*}$ and total force $\overline{F^*}$ produced within one wingbeat were determined. Since the birds were flying steadily in the wind tunnel, $\overline{L^*}$ should be equal to one (*L/W* = 1) and $\overline{T^*}$ is equal to the total normalized drag of the animal ($\overline{T^*}$ = *D/W*). The lift-to-drag ratio was determined by *L/D* = $\overline{L^*}/\overline{T^*}$ [22].

Note that lift and thrust were defined as the vertical and streamwise components of the flight forces, respectively. They can therefore be considered as the effective L^* and T^* of the whole flying animal, and L^* should not be confused with the local lift force vector at a certain wing section, which can have a different direction from L^*.

The mean and maximum force coefficient produced by the animal can be determined by

$$\overline{C}_F = \frac{2\overline{F^*}Mg}{\rho S\overline{U}_{eff}}$$
$$C_{F\max} = \frac{2F^*_{\max}Mg}{\rho S\overline{U}_{eff}} \qquad , \qquad (3.6)$$

where $\overline{F^*}$ is the downstroke average normalized flight force and F^*_{max} is the maximum flight force produced. The relative contribution of the tail vortex forces to the total lift and thrust production were defined as $L'_{tail} = (L^*_{tail}/L^*)100\%$ and $T'_{tail} = (T^*_{tail}/T^*)100\%$, respectively.

3.3 Average wingbeat wake

For each measured flight speed, an average wingbeat wake was defined, based on all the measured wingbeats at the specific flight speed [22]. The average wingbeat wake consists of the average vortex wake

and the average downwash distribution. The average vortex wake was defined as the average temporal lift distribution ($L^*(\tau)$) and normalized vertical movement ($z^*(\tau) = z(\tau)/(b/2)$) for each main vortex structure. The average downwash distribution was defined as a collection of $\overline{N}$ mean spanwise downwash distributions, where $\overline{N}$ is the mean amount of frames per wingbeat for all the measured wingbeats at a certain flight speed. All averages were determined by fitting a smoothing spline (Matlab, csaps, smoothing parameter $= 1\text{-}10^{-3}$) through the data point distributions of all

PIV measurements of a certain variable (e.g. $L^*(\tau)$ of the tip vortex) at a certain flight speed. The vortex wake splines were made periodic by copying the data points twice and distributing them across three wingbeat periods ($\tau=[(-1) - 2]$). The middle section of the resulting smoothing spline ($\tau=[0\text{-}1]$) defines the average vortex wake. The relative deviation of the data points from the average spline was estimated by calculating a sliding 95% confidence interval from a sliding window of I local data points, where I is the number of wingbeats analyzed at that flight speed.

Table 2 Wingbeat kinematics variables (mean ± standard deviation) for flycatcher #1 and #3 flying at U_∞ = 2 m/s, 4 m/s and 7 m/s. The variables are flap frequency f; downstroke ratio R_{ds}; span ratio SR; mean effective wing speed during the downstroke $\overline{U}_{eff}$ of wrist and wingtip; effective Reynolds number Re_{eff} of wrist and wingtip; downstroke based Strouhal number St_{ds} of wrist and wingtip; mean angle-of-attack ($\overline{\alpha}$), maximum angle-of-attack (α_{max}) and angle-of-attack amplitude (A_α) of both wing and tail, respectively; mean tail spread angle $\overline{\phi}$; maximum tail spread angle ϕ_{max}; normalized vertical body movement amplitude A^*_{body}

U_∞	(m/s)	2	4	7
f	(s^{-1})	12.6 ± 0.8	12.0 ± 0.4	12.1 ± 0.7
R_{ds}	(-)	0.45	0.42	0.42
SR	(-)	0.087	0.092	0.093
$\overline{U}_{eff\ wrist}$	(m/s)	2.42	4.28	7.20
$\overline{U}_{eff\ tip}$	(m/s)	5.7	6.7	9.0
$Re_{eff\ wrist}$	(-)	6.9×10^3	12.3×10^3	20.7×10^3
$Re_{eff\ tip}$	(-)	16.3×10^3	19.1×10^3	25.7×10^3
$St_{ds\ wrist}$	(-)	0.11	0.06	0.04
$St_{ds\ tip}$	(-)	0.42	0.31	0.23
$\overline{\alpha}_{wing}$[1]	(°)	34.3 ± 3.8	17.3 ± 2.3	6.0 ± 2.7
$\alpha_{wing\ max}$	(°)	40.9 ± 3.0	22.3 ± 1.3	10.6 ± 2.5
$A_{\alpha\ wing}$	(°)	46.1	25.2	12.9
$\overline{\alpha}_{tail}$	(°)	36.6 ± 7.9	19.6 ± 5.1	6.2 ± 7.1
$\alpha_{tail\ max}$	(°)	39.0 ± 4.4	26.4 ± 4.2	12.6 ± 4.2
$A_{\alpha\ tail}$	(°)	25.3	17.5	13.1
$\overline{\phi}$	(°)	21.5 ± 6.3	20.1 ± 4.0	16.9 ± 9.4
ϕ_{max}	(°)	47.6 ± 9.1	30.0 ± 4.1	12.6 ± 4.8
A^*_{body}	(-)	0.063	0.068	0.082

[1] **$\overline{\alpha}_{wing}$ is based on the downstroke part of the wingbeat, since it is assumed that the upstroke is inactive.**
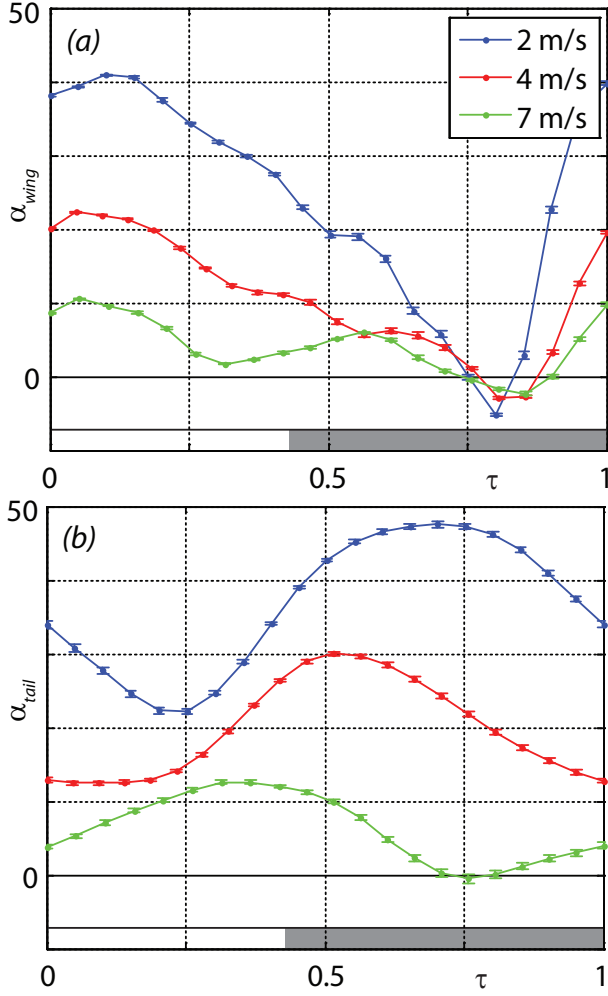
Fig. 2 effective angle-of-attack of the quarter chord point behind the wrist *(a)* and of the tail *(b)*, at flight speeds of 2 m/s, 4m/s and 7 m/s (see legend in *(a)*). The effective angle-of-attack is based on the effective local orientation and velocity of the wing or tail. The grey bar on the bottom of each panel indicates the upstroke part of the wingbeat

3.4 downwash distribution and span efficiency

The average spanwise downwash distributions determined for each mean PIV frame $n = [1 \text{-} \overline{N}]$ were used to determine the span efficiency e_i [23], which is a measure for the efficiency of lift production and is defined as [30]

$$e_i = P_{i,ideal}/P_i , \qquad (3.7)$$

where P_i is the induced power required to generate a

lift force L based on spanwise downwash distribution $w(y)$. $P_{i\,ideal}$ is the minimum required induced power to generate L based on a uniform spanwise downwash $\overline{w}$, which is the case for an elliptical spanwise lift distribution (Fig. 1*c*).

The induced power per distance travelled (P') required to generate the spanwise downwash distribution $w(y)$ for PIV frame n can be estimated by [23]

$$\dot{m}_z'(n) = \rho \int_{-b_w(n)/2}^{b_w(n)/2} w(n,y)dy$$

$$L'(n) = -2 \int_{-b_w(n)/2}^{b_w(n)/2} \dot{m}_z(n,y)w(n,y)dy , \qquad (3.8)$$

$$P_i'(n) = - \int_{-b_w(n)/2}^{b_w(n)/2} L'(n,y)w(n,y)dy$$

where $\dot{m}_z'(n)$ is the vertical mass flux per distance travelled associated with $w(n,y)$, $L'(n)$ is the lift per distance travelled, $P_i'(n)$ is the resulting induced power per distance travelled, and $b_w(n)$ is the wake span at PIV frame n, which is equal to the width (in y-direction) of the local spanwise downwash line. The minimum required induced power per distance travelled is determined by

$$P_{i\,ideal}'(n) = -L'(n)\overline{w}(n) , \qquad (3.9)$$

where $\overline{w}(n)$ is the spanwise uniform downwash resulting in the same $L'(n)$ as in equation (3.8), which is determined by

$$\overline{w}(x) = -\sqrt{\frac{L'(n)}{2\rho b_w(n)}} . \qquad (3.10)$$

By summing the induced power per distance travelled for all PIV frames $n = [1\text{-}\overline{N}]$, the total P_i and total $P_{i,ideal}$ for one wingbeat was determined [23]. From these, the wingbeat mean span efficiency for flapping flight was determined using equation [3.7].

e_i is related to the effective induced drag coefficient for flapping flight by [30]

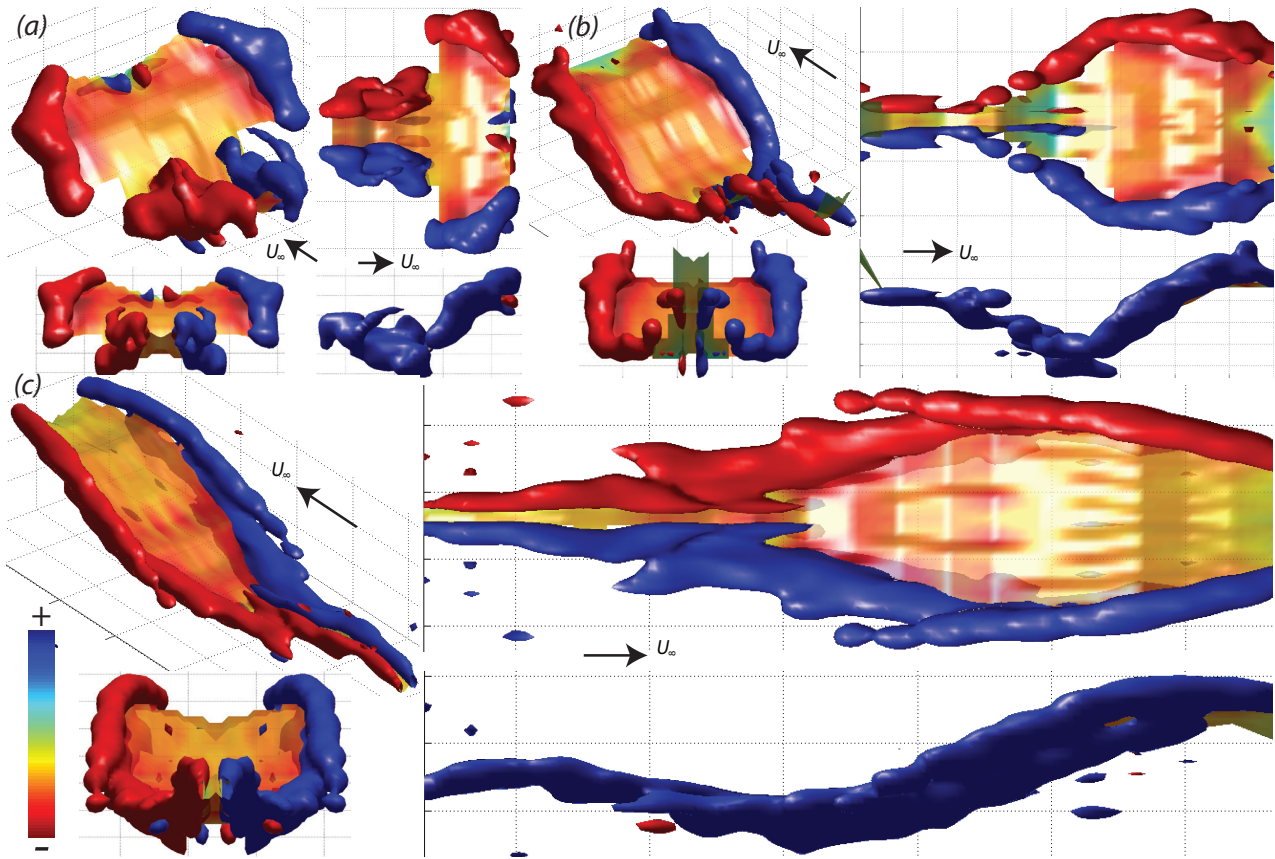$$C_{Di} = \frac{\overline{C}_F^{\ 2}}{\pi AR e_i} , \qquad (3.11)$$

Fig. 3 iso-surfaces of constant streamwise vorticity (red: $+\omega_{iso}$; blue: $-\omega_{iso}$) and the colour coded downwash distribution (see colour bar at the bottom left corner) in the wake of a flycatcher flying at *(a)* U_∞ = 3 m/s, *(b)* 5 m/s and *(c)* 7 m/s. The different panels are: *(a)* flycatcher #2, isovalue: ω_{iso} = 100 s^{-1}, maximum downwash: w_{max} = 3.8 m/s; *(b)* flycatcher #2, ω_{iso} = 100 s^{-1}, w_{max} = 2.7 m/s; *(c)* flycatcher #1, ω_{iso} = 50 s^{-1}, w_{max} = 1.7 m/s. Each panel consists of four views: perspective view (NW); top view (NE); front view (SW); side view (SE). Scaled wind tunnel velocity vectors U_∞ are shown in the perspective view, and in between the top and side view

where AR is the aspect ratio of the wings (Table 1). Since $\overline{C}_F$ is particularly high at low flight speeds (eq 3.6), C_{Di} and thus also e_i have relatively large influences on flight efficiency at low flight speeds.

4 Results
4.1 Kinematics

The kinematics variables are summarized in Table 2. Both flapping frequency and downstroke ratio decreased slightly with flight speed (Table 2). The span ratio was low and relatively constant throughout the measured flight speed range (SR = 0.091±0.003, mean ± standard deviation). The Reynolds number varied from Re_{eff} = 6.9×10^3 (based on $\overline{U}_{eff\,wrist}$ at U_∞ = 2 m/s) to Re_{eff} = 25.7×10^3 (based on $\overline{U}_{eff\,tip}$ at U_∞ = 7 m/s). The wingtip based Strouhal number

varied from St_{ds} = 0.42 at 2 m/s to St_{ds} = 0.23 at 7 m/s.

The average angle-of-attack, maximum angle-of-attack, and the angle-of-attack amplitude of both the wing and the tail were all largest at the lowest flight speed (Table 2 and Fig. 2). In the temporal occurrence of $\alpha_{max\,tail}$ a phase shift with flight speed was present. At the lowest flight speed, $\alpha_{tail,max}$ occurred at mid upstroke, at 4 m/s it occurred at the transition between downstroke and upstroke, whereas for the highest flight speed $\alpha_{tail,max}$ occurred during the second half of the downstroke (Fig. 2). The tail spread angle was highest at the lowest flight speed (Table 2).

The relative body movement A^*_{body} increased only slightly with flight speed, so the average value was used in the vortex wake analysis ($\overline{A}^*_{body}$ =0.07±0.01, Eq3.3).
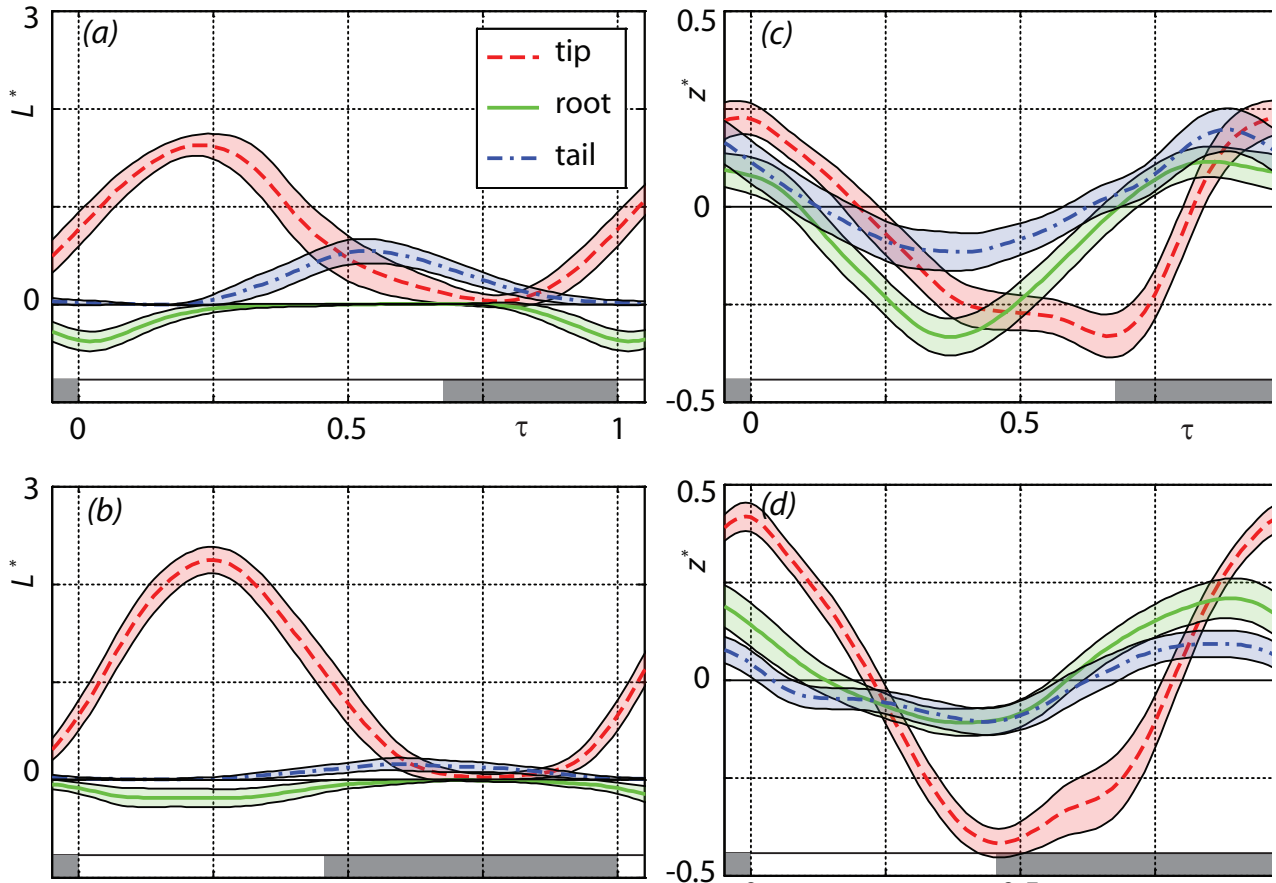
Fig. 4 Normalized vortex lift ($L^*(\tau)$) and vertical position ($z^*(\tau)$) throughout the wingbeat for the different wake structures, consisting of the average spline and 95% confidence interval. The left panels show the $L^*(\tau)$ at *(a)* 3 m/s and *(b)* 7 m/s, while the right panels show the corresponding $z^*(\tau)$ distributions. The different wake structures are colour-coded as shown in the legend in panel *(a)*. The grey colour bar at the bottom of each panel illustrates the upstroke section of the wingstroke.

4.2 Wake topology

The wake topology for the flycatchers consisted of a tip vortex, root vortex and tail vortex throughout the complete measured flight speed range (Fig. 3). For low flight speeds, at the start of the downstroke, a tip vortex and root vortex were generated behind each wing (Fig. 3*a*). Shortly after the start of the downstroke, the root vortex disappeared (its vorticity drops below the iso-surface threshold), while the tip vortex is visible until the end of the downstroke. During the upstroke, a relatively strong tail vortex with a complex shape was present.

At a flight speed of 5 m/s (Fig. 3*b*), the same vortex structures were present as at low flight speeds, although they differed in relative strength. The main differences were that, at 5 m/s, the root vortices and tail vortices were weaker, the tail vortices were simpler

in shape, and the tip vortex was still present during the first part of the upstroke. At the highest measured flight speed (7 m/s, Fig. 3*c*), the wake was similar to that at intermediate flight speeds, although at 7 m/s no root vortices could be distinguished and the wake was more drawn out due to the larger convection speed.

4.3 Vortex wake force dynamics

In the vortex force analysis we will focus on the wakes at low flight speeds (~3 m/s) and intermediate flight speeds (~7 m/s). At low flight speeds, the tip vortex generated the majority of the lift forces, although lift generated by root and tail vortices were not negligible (Fig. 4*a*). L^*_{tip} was highest during the first part of the downstroke, L^*_{tail} was highest during the transition from downstroke to upstroke, and L^*_{root} was highest during the transition from upstroke to downstroke.

At intermediate flight speeds, the root and tail vortex lift were much lower than L^*_{tip} (Fig. 4*b*). At low flight speeds, the vertical movement of the root vortex followed that of the tip vortex closely (Fig. 4*c*), while at intermediate flight speeds this connection is largely lost (Fig. 4*d*). The tail vortex movement amplitude was lower than that of the other vortices.

Comparing the amplitude of the vortex lift force and of the vertical path at the different flight speeds (Fig. 4), we observed that both increased with flight speed for the tip vortex, while they decreased with flight speed for the tail and root vortices. The total force distribution ($F^*(\tau)$) followed the same trend with flight speed as the tip vortex did (Fig. 5*a*).

4.4 Downwash distribution

For all flight speeds, the vertical induced velocities were negative throughout almost the complete wake area (downwash wake surface in Fig. 3). An upwash was only present between the root vortices, and for $U_\infty = 5$ m/s, at the start of the upstroke (Fig. 3*b*). Downwash velocities were largest at mid-downstroke and at low flight speeds (Fig. 5*b*). Also, at lower flight speeds, the spanwise downwash at mid-downstroke was more evenly distributed than at higher flight speeds. The downwash distribution at mid-upstroke was lower than at mid downstroke, and varied more between measurements, as illustrated by the larger 95% confidence interval at mid-upstroke (Fig. 5*b*).

4.5 Performance estimates

The lift-to-weight ratio based on the vortex forces was, on average, smaller than one ($L/W = 0.93 \pm 0.10$). L/D was highest at 3 m/s, while it was relatively constant for the range of $U_\infty = 5$ m/s to 7 m/s (Fig. 6*a*). Both the maximum and average C_F were highest at the lowest flight speeds (Fig. 6*c*). The tail vortex generated positive lift and negative thrust (resulting in drag, Fig. 6*d*). Both varied almost linearly with flight speed, and were highest at the lowest flight speeds ($L'_{tail} = 23\%$ at 2 m/s and $L'_{tail} = 8\%$ at 7 m/s). The span efficiency had a weak negative linear trend with flight speed (Fig. 6*b*), and the span efficiency at mid-downstroke is very similar to the average span efficiency for the wingbeat.
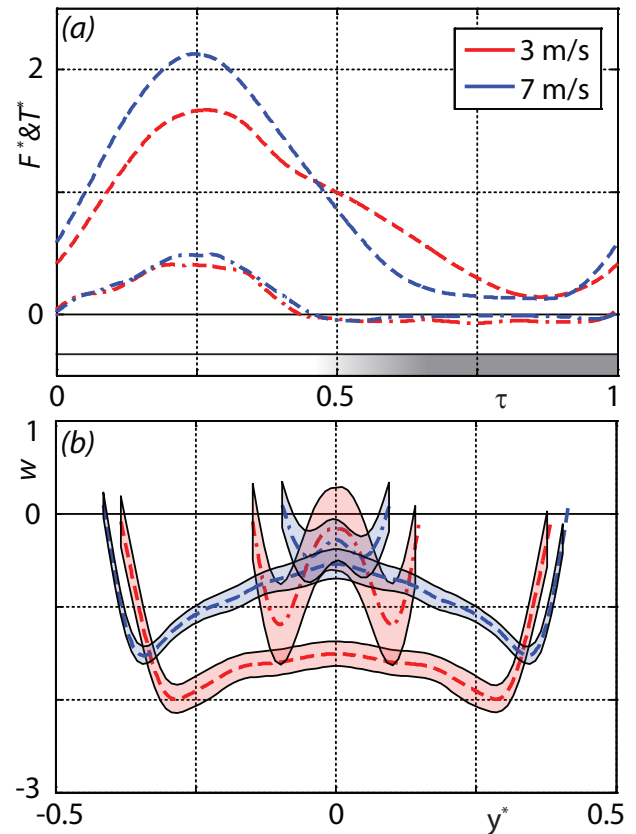

Fig. 5 *(a)* the normalized vortex force $F^*(\tau)$ (--) and corresponding thrust component $T^*(\tau)$ (-.-) throughout the wingbeat, and *(b)* the downwash distribution at mid downstroke (--) and at mid upstroke (-.-), at 3 m/s and 7 m/s, see legend in *(a)*. The grey colour bar at the bottom of panel *(a)* illustrate the upstroke section of the wingbeat, where the gradient indicates the difference between the two flight speeds and 7 m/s has an earlier transition.

5 Discussion
5.1 Wake topology

The wake topology for the flycatchers at low flight speeds (Fig. 3*a*) consisted of tip vortices throughout the complete downstroke and weak root vortices, which were only present at the start of the downstroke. This slow flight downstroke wake topology is similar to that near U_{mp}, and to the downstroke wake of blackcaps *Sylvia atricapilla* [6] and of a common swift [7] flying near U_{mp} and U_{mr}, which were determined using similar techniques and setups as used here. Thus, the flycatchers generate a single vortex loop structure during the downstroke at low flight speeds, and not two separate vortex loops as in hovering hummingbirds [11], which is consistent with our initial hypothesis.
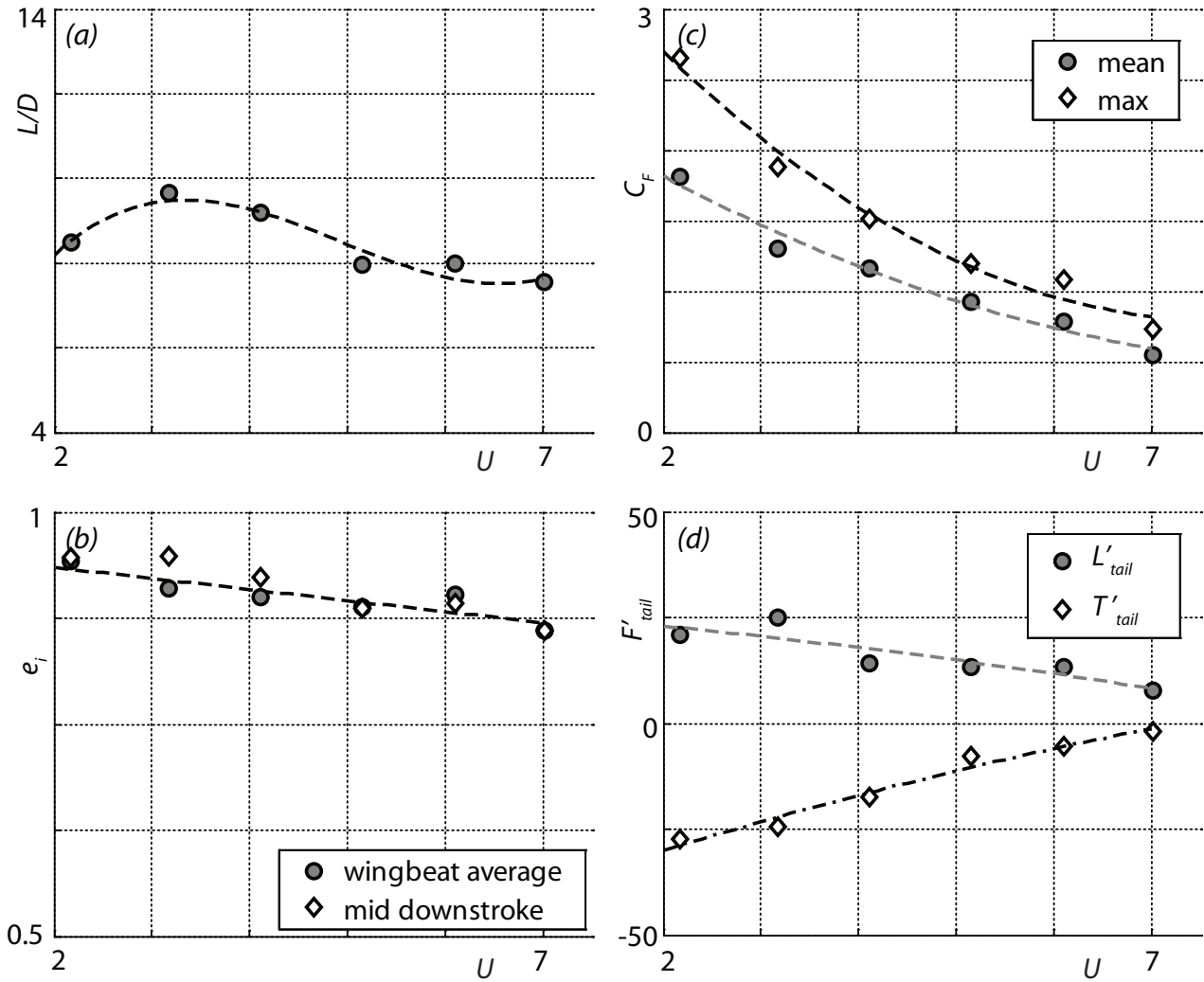
Fig. 6 Aerodynamic measurements in relation to forward flight speed. *(a)* The lift-to-drag ratio *L/D*; *(b)* the wingbeat average span efficiency (*e$_i$*, circles) and *e$_i$* at mid downstroke (diamonds); *(c)* the mean (circles) and maximum (diamonds) force coefficient based on *U$_{eff}$* at the wrist; *(d)* the relative contribution of the tail vortices on lift (circles) and thrust (diamonds).

During the upstroke, slow flying flycatchers generated strong tail vortices, while the wings were inactive. This is consisted with upstroke wakes of blackcaps [6] and swifts [7] at the lowest flight speeds they were measured at.

5.2 Forces and downwash by the wings

Since root vortices were mainly present at the start of the downstroke, and were almost completely absent at the highest measured flight speeds (Fig. 3 and Fig. 4a-b), the wings of the flycatcher appear to operate as a single wing configuration during the majority of the downstroke. This idea is also supported by the almost uniform spanwise downwash at mid downstroke

(Fig. 5b), and is very different from hovering hummingbirds, where the wings operate independently.

During the upstroke, the wings produced almost no significant lift force (Fig. 4) because the animals retracted their wings during the upstroke (*SR* = 0.091±0.003) and spread the primary feathers so air can flow through the gaps [16-18]. This mechanism appears to be very efficient in making the wings aerodynamically inactive, since hardly any vorticity is produced by the wings during the upstroke. We found only at the highest flight speed weak traces of vorticity behind the wings at the end of the upstroke (Fig. 3c).

5.3 Force and downwash by the body/ tail configuration

Although the vortex shed at the upstroke is called the tail vortex, it is probably more a result of force production by the complete body/tail configuration, since a tailless blackcap also generates vortices similar to the tail vortices we observed [6]. We still call these vortices tail vortices since they are probably shed from the rear end of the body and/or the leading edge of the delta-wing-like tail [7,31,32].

During the first part of the downstroke no tail vortices were present, but during this part of the wingbeat the tail/body configuration probably continues to generate lift [32]. This idea is supported by the fact that α_{tail} is positive during the downstroke (Fig. 2), and because no strong root vortices were present during the downstroke, as was found in the hummingbirds (inner part of the vortex loops, [11]. Thus, the fact that the wing-body-tail configuration of flycatchers operates more as a single wing than that of hummingbirds is a result of the relatively active tail/body configuration in flycatchers.

Since the wings are aerodynamically inactive during the upstroke [18], most of the lift at this point in the wingbeat cycle was generated by the tail/body configuration. This lift was highest at low flight speeds (Fig. 6*d*). At low flight speeds, the tail was also more spread (higher ϕ), operated at a higher α_{tail} and flapped more (higher $A_{\alpha\,tail}$) than at intermediate flight speeds (Table 2). At the lowest measured flight speed, the tail vortex system contributed 23% of weight support. This is strikingly similar to the 25% lift production of the wings of hovering hummingbirds during the upstroke. Hence, although flycatchers have an inactive wing during the upstroke, the tail/body configuration mostly compensates for this, when compared to hummingbirds.

The fact that the variation in both $\overline{\alpha}_{tail}$ and $\alpha_{tail\,max}$ was relatively large (Table 2), as was the 95% confidence interval of the downwash distribution during the upstroke, could also indicate that the tail is actively used for flight control [31].

5.4 Performance estimates

L/W was close to one, so we almost completely resolved the flight forces in our vortex wake model. The lift-to-drag estimates for the flycatchers near U_{mp} (L/D = 7.5 at U_∞ = 7 m/s), can be compared to L/D

estimates of other bird species (Fig. 7, see [3] for detailed calculations). There is an expected positive correlation between maximum L/D and Re, since friction drag should reduce with Re [33]. L/D for the flycatchers is similar to that of other birds operating at the same Re range; thus, these flycatchers can be assumed to be adapted to low speed flight.

At the lowest flight speed, both of the force coefficients (C_{Fmax} = 2.7 and $\overline{C}_F$ =1.8) and angles-of-attack of the wing ($\alpha_{max\,wing}$ = 40.9° and $\overline{\alpha}_{wing}$ =34.3°) for these flycatchers were well above values expected based on quasi-steady aerodynamics at this Re [34]. Thus, we can assume that at low flight speeds the flycatchers use some kind of unsteady aerodynamic mechanism [35], which has already been predicted for hovering flycatchers [17]. One likely candidate could be a leading edge vortex, which is also found in hovering hummingbirds [14] and in slow flight for similarly sized bats [36].

The fact that e_i is higher at low flight speeds (Fig. 6*b*) can be explained by the more uniformly distributed spanwise downwash (Fig. 5*b*) and the more active tail (Fig. 2*b*) at low flight speeds compared to intermediate flight speeds. To the best of our knowledge, this is the first empirical study showing span efficiency
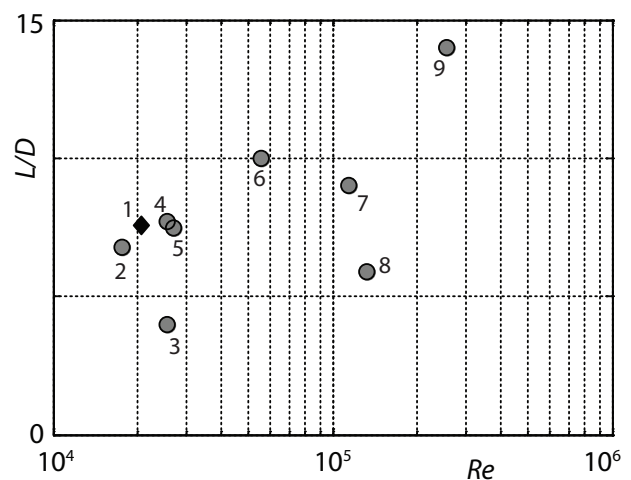

Fig. 7 maximum lift-to-drag ratio *L/D* for the flapping flight of birds versus the Reynolds number *Re* = *U c*/ν. The different data points are: (1) the pied flycatchers at 7 m/s; (2) blackcap *Sylvia atricapilla* [6] (3) budgerigar *Melopsittacus undulatus* [43]; (4) common swift *Apus apus* [7]; (5) European robin *Erithacus rubecula* [3]; (6) black-billed magpie *Pica pica* [44]; (7) European starling *Sturnus vulgaris* [45]; (8) pigeon *Columba livia* [46]; (9) bar-headed goose *Anser indicus* [47]

of flapping flight in birds. The estimated e_i near U_{mp} (e_i = 0.86 at U_∞ = 7 m/s) is similar to but slightly higher than the e_i = 0.83 assumed in bird flight models [1]. The average results (e_i = 0.90±0.03) are lower than the e_i = 0.96 estimated for a gliding kestrel [37], although they are much higher than the highest estimate for a steady model wing at a similar Re (e_i = 0.76 for an Eppler 387) [30]. Two other studies have estimated e_i for flapping animal flight using a method similar to the one used here. e_i was determined for a desert locust at mid-downstroke (e_i = 0.85-0.89) [38], and for two bat species at the same flight speeds as in this study (e_i = 0.81±0.03 for *Glossophaga soricina* and e_i = 0.79±0.03 for *Leptonycteris yerbabuenae*) [23]. e_i for the flycatcher is similar to that of the desert locust, but it is higher than e_i for the bats. The difference in e_i between bats and flycatchers can be ascribed to the relatively strong root vortices in bats, resulting in a more independent vortex structure for each wing [22,23,39,40]. These vortex structures are similar to the double vortex loop structures in hummingbirds [11], so one can assume that also hummingbirds have lower e_i than the flycatchers. Hence, flycatchers have among the highest span efficiency known in the animal kingdom; the relatively high body/tail lift production may be responsible for this high span efficiency [41,42].

5.5 Concluding remarks

Here, we studied the aerodynamics of flycatchers at flight speeds from near hovering to intermediate flight speeds. The wake topology at slow flight speeds consisted of a single vortex loop structure during the downstroke, which is much more similar to that of more conventional birds flying at higher speeds than it is to the double loop vortex wake of hovering hummingbirds. This is mainly due to the aerodynamically active tail of the flycatchers, which results in relatively high body/tail lift, a relatively uniform spanwise downwash, and probably also a higher span efficiency in the flycatchers. Although the two vortex loop system in hummingbirds should result in lower span efficiency, it has more potential for fast maneuvering, since the wings can possibly generate forces independently. The fact that, during the upstroke, the flycatcher tail generates almost the same percentage of total lift force as the hummingbird wings do, suggests that in inclined stroke plane hovering the tail is very important, and that the upstroke cannot be called inactive, although the wings certainly are.

References

1. Pennycuick CJ. *Modelling the Flying Bird* (Elsevier, Amsterdam, 2008).

2. Hedenström A, Alerstam T. Optimal Flight Speed of Birds. *Philosophical Transactions of the Royal Society of London. Series B: Biological Sciences.* **348**, 471 (1995).

3. Hedenström A, Rosén M, Spedding GR. Vortex wakes generated by robins *Erithacus rubecula* during free flight in a wind tunnel. *Journal of The Royal Society Interface* **3**, 263-276 (2006).

4. Hedenström A, Spedding G. Beyond robins: aerodynamic analyses of animal flight. *Journal of The Royal Society Interface* **5**, 595-601 (2008).

5. Spedding GR, Rosen M, Hedenström A. A family of vortex wakes generated by a thrush nightingale in free flight in a wind tunnel over its entire natural range of flight speeds. *Journal of Experimental Biology* **206**, 2313-2344 (2003).

6. Johansson LC, Hedenström A. The vortex wake of blackcaps (*Sylvia atricapilla L.*) measured using high-speed digital particle image velocimetry (DPIV). *Journal of Experimental Biology* **212**, 3365-3376 (2009).

7. Henningsson P, Muijres FT, Hedenström A. Time-resolved vortex wake of a common swift flying over a range of flight speeds. *Journal of The Royal Society Interface* (doi: 10.1098/rsif.2010.0533)

8. Davies NB. Prey selection and the search strategy of the spotted flycatcher (*Muscicapa striata*): A field study on optimal foraging. *Animal Behaviour* **25**, 1016-1033 (1977).

9. Fitzpatrick JW. Search strategies of tyrant flycatchers. *Animal Behaviour* **29**, 810-821 (1981).

10. Altshuler D, Dudley R. Kinematics of hovering hummingbird flight along simulated and natural elevational gradients. *Journal of Experimental Biology* **206**, 3139-3147 (2003).

11. Altshuler D, Princevac M, Pan H, Lozano J. Wake patterns of the wings and tail of hovering hummingbirds. *Experiments in Fluids* **46**, 835-846 (2009).

12. Tobalske B, Warrick D, Clark C, Powers D, Hedrick T, Hyder G, et al. Three-dimensional kinematics of hummingbird flight. *Journal of Experimental Biology* **210**, 2368-2382 (2007).

13. Warrick D, Tobalske B, Powers D. Aerodynamics of the hovering hummingbird. *Nature* **435**, 1094 (2005).

14. Warrick DR, Tobalske BW, Powers DR. Lift production in the hovering hummingbird. *Proceedings of the Royal Society B: Biological Sciences* **276**, 3747 -3752 (2009).

15. Alexander DE. *Nature's Flyers: Birds, Insects, and the Biomechanics of Flight* (JHU Press, London, 2004).

16. Norberg UM. *Vertebrate flight: mechanics, physiology, morphology, ecology and evolution* (Springer-Verlag, Berlin, 1990).

17. Norberg U. Hovering flight in the pied flycatcher (*Ficedula hypoleuca*). *Swimming and Flying in Nature* **2**, 869-888 (1975).

18. Norberg RA. Function of vane asymmetry and shaft curvature in bird flight feathers; inference on flight ability of *Archaeopteryx*. In: *The beginnings of birds. International Archaeopteryx Conference in Eichstätt*, (303–318, 1985).

19. Spedding GR, Rayner JMV, Pennycuick CJ. Momentum and energy in the wake of a pigeon (*Columba livia*) in slow flight. *Journal of experimental biology* **111**, 81–102 (1984).

20. Spedding GR. The wake of a jackdaw (*Corvus monedula*) in slow flight. *Journal of experimental biology* **125**, 287–307 (1986).

21. Rosén M, Spedding G, Hedenström A. Wake structure and wingbeat kinematics of a house-martin *Delichon urbica*. *Journal of The Royal Society Interface* **4**, 659-668 (2007).

22. Muijres FT, Johansson LC, Winter Y, Hedenström A. Comparative aerodynamic performance of flapping flight in two bat species using time-resolved wake visualization. *Journal of The Royal Society Interface* (doi: 10.1098/rsif.2011.0015)

23. Muijres FT, Spedding GR, Winter Y, Hedenström A. Actuator disk model and span efficiency of flapping flight in bats based on time-resolved PIV measurements. *Experiments in Fluids* (doi: 10.1007/s00348-011-1067-5).

24. Bowlin MS. Sex, Wingtip Shape, and Wing-Loading Predict Arrival Date at a Stopover Site in the Swainson's Thrush (*Catharus ustulatus*). *The Auk* **124**, 1388-1396 (2007).

25. Pennycuick CJ. *Bird flight performance: a practical calculation manual*. (Oxford University Press, Oxford; 1989).

26. Pennycuick CJ, Alerstam T, Hedenström A. A new low-turbulence wind tunnel for bird flight experiments at Lund University, Sweden. *Journal of Experimental Biology* **200**, 1441-1449 (1997).

27. Hedenström A, Muijres F, von Busse R, Johansson L, Winter Y, Spedding G. High-speed stereo DPIV measurement of wakes of two bat species flying freely in a wind tunnel. *Experiments in Fluids* **46**, 923-932 (2009).

28. Wolf M, Johansson LC, von Busse R, Winter Y, Hedenström A. Kinematics of flight and the relationship to the vortex wake of a Pallas' long tongued bat (*Glossophaga soricina*). *Journal of Experimental Biology* 213, 2142-2153 (2010).

29. Anderson JD. *Fundamentals of Aerodynamics* (McGraw-Hill, New York, 1991).

30. Spedding GR, McArthur J. Span Efficiencies of Wings at Low Reynolds Numbers. *J. Aircraft* **47**, 120-128 (2010).

31. Thomas A. On the Aerodynamics of Birds' Tails. *Philosophical Transactions of the Royal Society B: Biological Sciences* **340**, 361 (1993).

32. Tobalske B, Hearn J, Warrick D. Aerodynamics of intermittent bounds in flying birds. *Experiments in Fluids* **46**, 963-973 (2009).

33. Hoerner S. *Fluid-dynamic drag; practical information on aerodynamic drag and hydrodynamic resistance* (Hoerner, Bakersfield, California, 1965).

34. Laitone E. Wind tunnel tests of wings at Reynolds numbers below 70 000. *Experiments in Fluids* **23**, 405 (1997).

35. Sane S. The aerodynamics of insect flight. *Journal of Experimental Biology* **206**, 4191-4208 (2003).

36. Muijres F, Johansson L, Barfield R, Wolf M, Spedding G, Hedenström A. Leading-Edge Vortex Improves Lift in Slow-Flying Bats. *Science* **319**, 1250-1253 (2008).

37. Spedding GR. The Wake of a Kestrel (Falco Tinnunculus) in Gliding Flight. *Journal of Experimental Biology* **127**, 45-57 (1987).

38. Bomphrey RJ, Taylor GK, Lawson NJ, Thomas AL. Digital particle image velocimetry measurements of the downwash distribution of a desert locust *Schistocerca gregaria*. *Journal of The Royal Society Interface* **3**, 311 -317 (2006).

39. Hedenström A, Johansson L, Wolf M, von Busse R, Winter Y, Spedding G. Bat Flight Generates Complex Aerodynamic Tracks. *Science* **316**, 894-897 (2007).

40. Johansson LC, Wolf M, von Busse R, Winter Y, Spedding GR, Hedenström A. The near and far wake of Pallas' long tongued bat (*Glossophaga soricina*). *Journal of Experimental Biology* **211**, 2909-2918 (2008).

41. Csicsáky MJ. Body-gliding in the zebra finch. *Fortschr. Zool* **24**, 275–286 (1977).

42. Tobalske B, Peacock W, Dial K. Kinematics of flap-bounding flight in the zebra finch over a wide range of speeds. *Journal of Experimental Biology* **202**, 1725-1739 (1999).

43. Tucker VA. Respiratory Exchange and Evaporative Water Loss in the Flying Budgerigar. *Journal of Experimental Biology* **48**, 67-87 (1968).

44. Boggs D, Jenkins F, Dial K. The effects of the wingbeat cycle on respiration in black-billed magpies (*Pica pica*). *Journal of Experimental Biology* **200**, 1403-1412 (1997).

45. Biewener AA, Dial KP, Goslow GE. Pectoralis muscle force and power output during flight in the starling. *Journal of Experimental Biology* **164**, 1-18 (1992).

46. Pennycuick C. Power Requirements for Horizontal Flight in the Pigeon *Columba Livia*. *Journal of Experimental Biology* **49**, 527-555 (1968).

47. Ward S, Bishop CM, Woakes AJ, Butler PJ. Heart rate and the rate of oxygen consumption of flying and walking barnacle geese (*Branta leucopsis*) and bar-headed geese (*Anser indicus*). *Journal of Experimental Biology* **205**, 3347-3356 (2002).

Birds outperform bats in flight efficiency due to differences in body lift and wing upstroke

Florian T. Muijres[1], L. Christoffer Johansson[1], Melissa S. Bowlin[1,2], Rhea von Busse[1,3], York Winter[3] and Anders Hedenström[1]

[1]*Department of Biology, Ecology Building, Lund University, SE-223 62 Lund, Sweden*
[2]*Department of Natural Sciences, University of Michigan-Dearborn, 4901 Evergreen Rd., Dearborn, MI, 48128, USA*
[3]*Cognitive Neurobiology, Humboldt University, and NeuroCure Center of Excellence at the Charité Universitätsmedizin Berlin, Dorotheenstrasse 94, 10117 Berlin, Germany*

Flight is one of the most energetically costly activities in the animal kingdom[1], suggesting that natural selection should work to optimize flight performance. The similar size and flight speed of birds and bats may therefore suggest convergent aerodynamic performance[2,3]; alternatively, flight performance could be restricted by phylogenetic constraints[4]. Using time-resolved particle image velocimetry measurements of the wake of one bird and two bat species flying freely in a wind tunnel, we derived measures of aerodynamic flight efficiency. Here we show that the bird species outperforms the bats in two relevant metrics: the birds have a higher span efficiency for generating lift[5,6], and a higher effective lift-to-drag ratio, related to energetic flight efficiency[2], than the bats. We ascribe this variation in performance to differences in aerodynamic function of the body and the wing upstroke. The birds' bodies generate relatively more lift[7,8] than bats, resulting in a more uniform spanwise lift production, which in turn results in higher span efficiency[5]. During the upstroke, the bird retracts its wing, making it aerodynamically inactive[9,10,11], while the bats have a more complex wing motion, generating thrust and negative lift during the upstroke[12,13]. Despite the differences in performance, the wake morphology of both the bird and the bats resemble the optimal wake of their respective lift-to-drag ratio regimes[14,15]. Although this suggests that evolution has optimized performance relative to the respective conditions of birds and bats, the difference in flight performance have ecological consequences and may help explain why the largest birds are ten times heavier than the largest bats[16], and why bats migrate less frequently and tend to travel shorter distances than birds when they do[17,18,19].

Keywords: birds, bats, flapping flight, aerodynamic performance, wind tunnel, PIV

The independent evolution of powered flight in birds and bats begs the question of whether the apparent convergence in size, shape and flight style has resulted in the same overall flight performance, or if they differ in any respect. Most birds and bats operate in the same Reynolds number range[2,17,20] ($Re = Uc/\nu$; U is flight speed, c is wing chord and ν is kinematic viscosity of air), which indicate an overall fluid dynamic similarity[3]. Thus, any difference in flight performance would be due to variation in ecological requirements or morphology as a result of phylogenetic constraints[4]. For example, night-active bats have protruding ears required for echolocation. Bats also have wings formed by skin membranes stretched between elongated finger bones, while bird wing surfaces are formed of adjacent feathers radiating from reduced skeleton bones.

Here, we compare three individuals from one avian species and two individuals from each of two
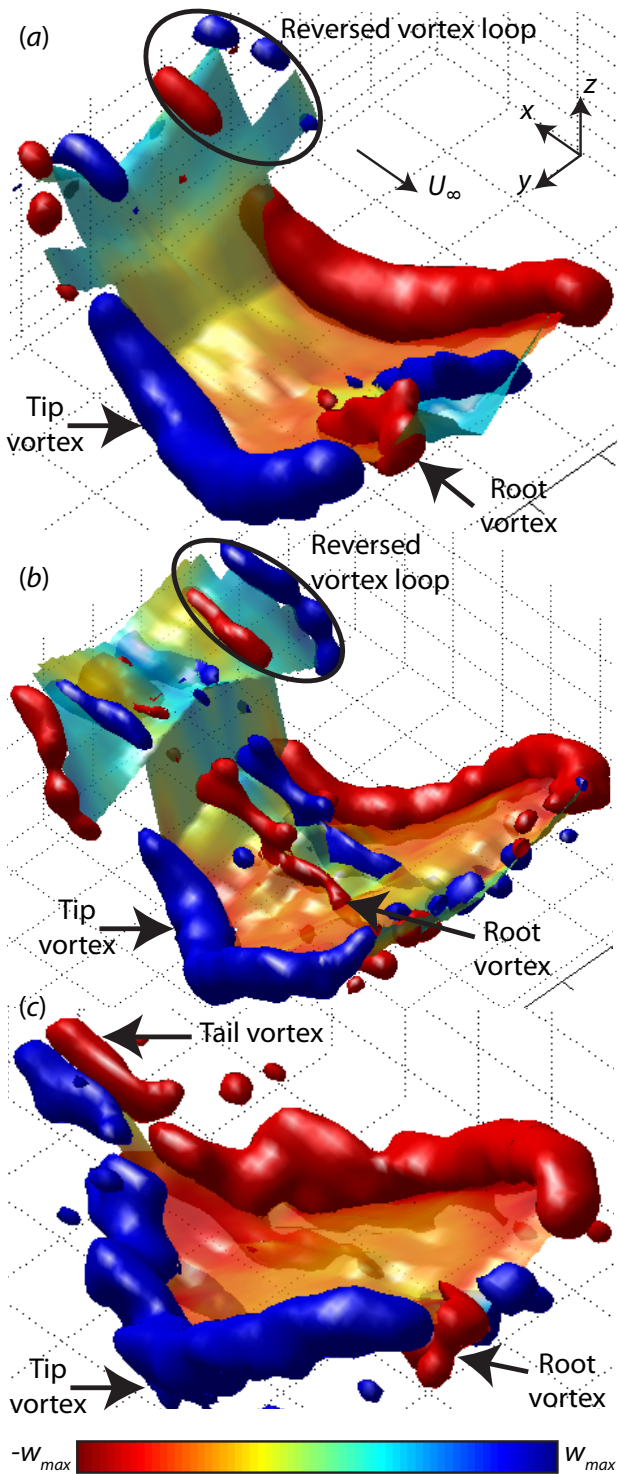
Figure 1 Wake topologies for one wingbeat of both bats and the flycatcher flying at 4 m/s

The vorticity iso-surfaces (blue: $+\omega_{x\,iso}$; red: $-\omega_{x\,iso}$) show the main vortex structures, while the colour-coded surface shows downwash w (see colour bar). *(a)* Wake of the male *G. soricina* with $\omega_{x\,iso}$ = ±60 s^{-1} and downwash scale w_{max} = 2.6 m/s; *(b)* male *L. yerbabuenae*, $\omega_{x\,iso}$ = ±75 s^{-1} and w_{max} = 2.2 m/s; *(c)* flycatcher #2, $\omega_{x\,iso}$ = ±75 s^{-1} and w_{max} = 2.6m/s. The wind tunnel velocity vector U_∞ and coordinate system {x,y,z} are in panel *(a)*

bat species flying in identical conditions in a wind tunnel, using a fluid dynamic characterization of the wake generated by these animals to derive quantitative information about the relative flight efficiency. We studied the Pied Flycatcher (*Ficedula hypoleuca*), an insectivorous migratory passerine (body mass 14 g), the Pallas' Long-tongued Bat (*Glossophaga soricina*), a nectar feeding bat (10 g), and the Lesser Long-nosed Bat (*Leptonycteris yerbabuenae*), a migratory nectar-feeding bat (22 g) (Supplementary Table S1). We compared these species since they are representative species for their respective orders, are similar in size and ecology[9,10,17], and fly at similar *Re* ($\sim$10^4)[2,3]. Although any variation in performance may be influenced by the small ecological differences between the species, phylogenetic constraints, if they exist, should have a greater effect[4].

For each species, we measured the wake dynamics using 200 Hz time-resolved stereoscopic Particle Image Velocimetry (PIV) and wingbeat kinematics using high-speed cameras in the Lund University low-turbulence wind tunnel (Supplementary Fig. S1), across flight speeds U = 2-7 m/s, with increments of 1 m/s. From these measurements, we determined the average wake topology for each species and speed combination, which we used to estimate the temporal aerodynamic force production[9,13,21], the temporal spanwise downwash distribution[6], and two derived flight performance values, the effective lift-to-drag ratio (*L/D*) and the span efficiency (e_i) (Method and Supplementary Fig. S2). *L/D* is related to the energetic flight efficiency[2], and e_i describes the aerodynamic efficiency of lift production by the wing-body configuration[5,6].

For both the bats and the bird, each wing generates a wing 'tip vortex' and a wing 'root vortex' at the start of the downstroke (Fig. 1 and Supplementary Fig. S3-S5). The tip vortices are present throughout the complete downstroke, but disappear during the upstroke. The exact timing of the disappearance varies with species and flight speed (Fig. 2*a-c*). The root vortices are mainly present during the first part of the downstroke, and are significantly weaker for the flycatcher than the bats (Fig. 2*d-f*). Also, both tip- and root-vortices are present for a shorter fraction of the wingbeat for the flycatcher than the bats (Fig. 2). For the flycatcher, but not the bats, a new vortex pair appears closer to the body about the same time as when the tip vortex disappears (Fig. 1*c*). We assume

Figure 2 Non-dimensional lift production throughout the wingbeat for the main vortex wake structures of both bats and the flycatcher The left panels show the vortex structures resulting in positive *L/W* at 2 m/s (*a*), 4 m/s (*b*) and 7 m/s (*c*), see legend in panel (*a*) The right panels show negative *L/W* at 2 m/s (*d*), 4 m/s (*e*) and 7 m/s (*f*), see legend in panel (*d*). The wingbeat upstroke fraction for the bats is marked with the grey bar on the top, and for the flycatcher with the grey bar on the bottom. Note the differences in scale between positive and negative lift.
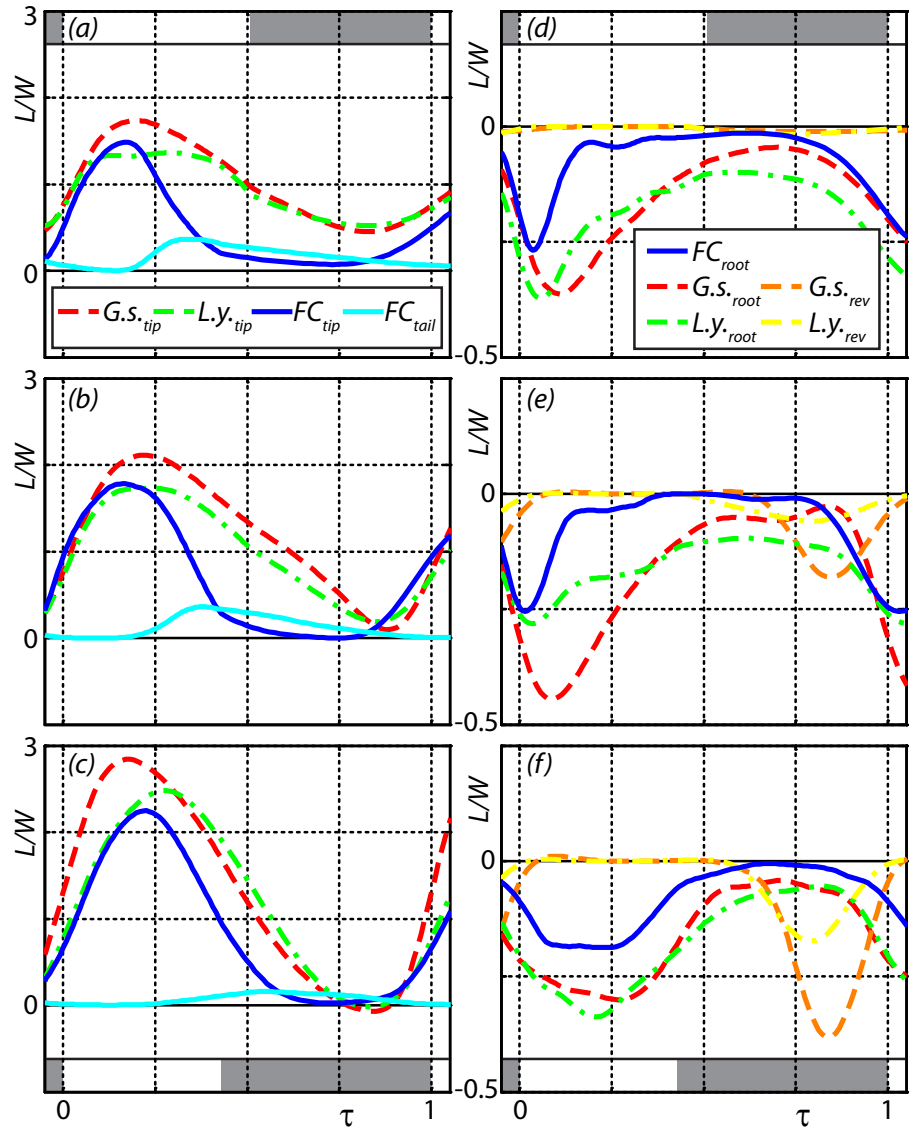
that these are shed from the body/tail configuration, so they are labelled 'tail vortices'[8,11,21]. The tail vortices are present until the end of the upstroke and add to lift (Fig. 2*a-c*)[8]. The bats, but not the flycatcher, generate a vortex loop behind each wing during the latter part of the upstroke (Fig. 1 and Supplementary Fig. S3-S5)[12,13,22,23,24]. These vortex loops result in negative lift (Fig. 2) and are therefore labelled 'reversed vortex loops'. Thus, the bats generate a more complex wake, including stronger root vortices and reversed vortex loops[12,22,23,24], than the birds[11,20,21,25].

Both *L/D* and *e_i* were significantly higher for the birds than for the bats, at all flight speeds (Fig. 3*a* and 3*d*, Supplement Table S2). From this we conclude that the birds fly more efficiently than the bats.

The drag produced by a flying animal can be

divided into drag produced by the wing (profile drag), drag produced by the body (parasite drag), and drag resulting from the downwash produced behind the animal (induced drag). The span efficiency e_i is related to the induced drag, since it is a measure of the deviation from a constant spanwise downwash distribution, which results in minimum induced drag ($e_i = 1$)[5]. Bats deviate more from a constant spanwise downwash distribution than the birds (Fig. 4), mainly due to reduced downwash behind the body (Fig. 4*a-c*), which is a result of lower body lift in bats[13]. Thus, since bats generate less body lift than birds[7,8,13], their span efficiency is lower (Fig. 3*d*), resulting in higher induced drag and lower *L/D*[3,5]. The fact that bats generate less body lift could be a result of having less streamlined bodies than birds[8],
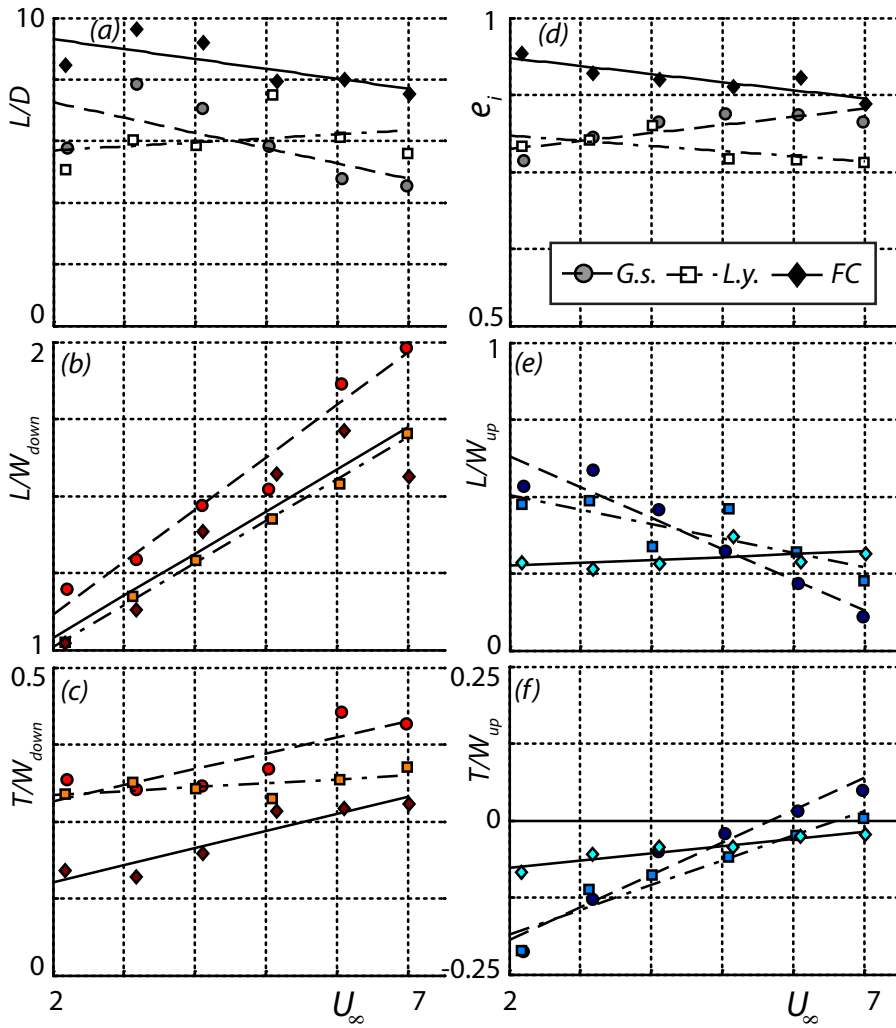
Figure 3 Flight efficiency factors and normalized force productions during downstroke and upstroke throughout the measured flight speed range
The flight efficiency factors are lift-to-drag ratio L/D (*a*) and span efficiency e_i (*d*). Force productions consist of L/W during the downstroke (*b*); L/W during the upstroke (*c*); T/W during the downstroke (*e*); and T/W during the upstroke (*f*). The data points show the measurements, the trend lines are determined by the statistical analysis. For all panels see legend in panel (*d*). Note the differences in scale between L/W and T/W.

e.g. due to the presence of protruding ears required for echolocation in bats. Since concave shapes such as ears produce more drag than most structures[26], this should also increase body drag, contributing to the lower L/D in bats.

To test how the difference in L/D for the bats and the birds affects the flight kinematics, we consider the lift (L) and thrust (T) production during the downstroke and upstroke separately (Fig. 3). Note that, for steady flight, the mean thrust throughout the wingbeat is equal to the total drag (D)[13]. During the downstroke, both the lift and thrust production for birds and bats vary similarly with flight speed (Fig. 3*b-c*), although T is significantly lower for the flycatchers (Supplement Table 2), resulting in a higher L/D estimate. During the upstroke, however, L and T scale very differently with flight speed in the birds and bats (Fig. 3*e-f*). During the upstroke, L decreases with flight speed for bats, while it increases for the birds, and

thrust production increases significantly faster with flight speed for bats than for the birds (Supplement Table 2).

In combination, the differences during the upstroke are mainly a result of the presence of reversed vortex loops in bats and tail vortices in birds (Fig. 1). The reversed vortex loops in bats are generated by the upwards moving wing when producing positive thrust and negative lift[12,13]. With increasing flight speed this negative lift and positive thrust also increase[13] (Fig. 3*e-f*). The flycatcher, on the other hand, makes its wings inactive during the latter part of the upstroke by retracting the wing and by spreading the primary wing feathers[9,10]. Therefore the birds generate primarily body lift during the latter part of the upstroke[7,27], resulting in tail vortices[8] (Fig. 2*a-c*).

Hence, there is a clear qualitative and quantitative difference in the function of the upstroke between the birds and bats, which could be directly related to

Figure 4 Spanwise downwash distributions during mid downstroke and mid upstroke for both bats and the flycatcher
The panels show $w(y^*)$ during mid-downstroke at 2 m/s (*a*), 4 m/s (*b*) and 7 m/s (*c*) and during mid-upstroke at 2 m/s (*d*), 4 m/s (*e*) and 7 m/s (*f*), see legend in panel (*f*). The dotted lines show the average downwash for all measurements and the bar around the average is the sliding 95% confidence interval.
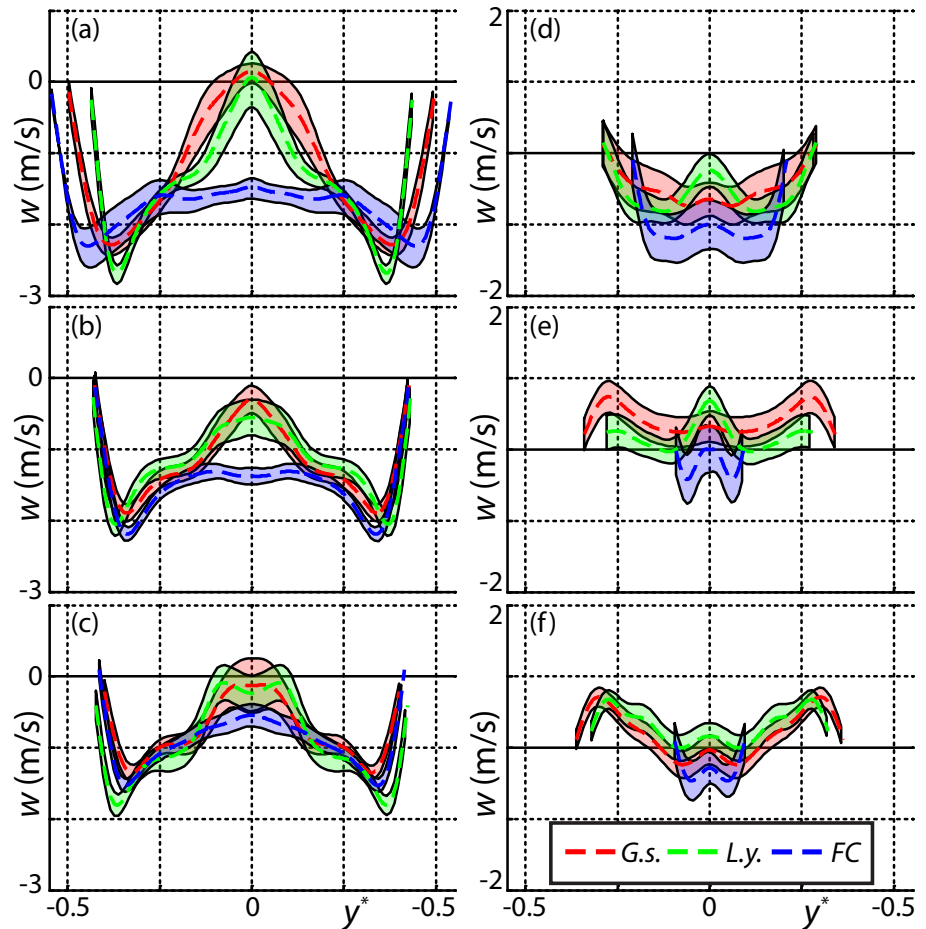
the difference in *L/D*. For large amplitude flapping wing configurations with low *L/D* (*L/D* = 5, similar to that of the bats), the energetically optimal flapping kinematics generate thrust in combination with negative lift during the upstroke (resulting in reversed vortex loops)[15], while for configurations with higher *L/*D (*L/D* = 10, similar to that of the flycatcher) the upstroke should generate positive lift[15]. So, both the flycatcher and the two bat species have a wake topology that is close to optimal for the respective *L/D* regime they operate at[14,15].

Considering the small number of species in this study, we caution against over-generalizing the results. However, previous studies have also hinted at differences in aerodynamic performance between birds and bats[28,29]. The generality of our results are further supported by results from the larger dog-faced fruit bat *Cynopterus brachyotis*[24]. Although no detailed force analysis was available for *Cynopterus brachyotis*, making a quantitative comparison impossible, their wake pattern is similar to those of our bats. This includes

the thrust and negative lift producing reversed vortex loops at the end of the upstroke and the relatively strong root vortex resulting in reduced body lift[24]. The wake topology of the flycatcher, consisting of tip-, root- and tail-vortices, is likewise similar to that of other birds[20,21,11,25], and *L/D* for the flycatcher at cruising speed (*L/D* = 7.5 at U = 7 m/s) is similar to that of a common swift *Apus apus* (*L/D* = 7.7 at *U* = 10 m/s)[21]. We re-analyzed the wake data for the blackcap (*Sylvia atricapilla*)[11] using the method presented here, to allow for a direct comparison, which yielded a *L/D* = 7.4 at *U* = 7-8 m/s that is consistent with the flycatcher data. Taken together, these studies suggest that the results presented here are typical for small to medium sized bats, passerines and even a highly aerial non-passerine bird, the swift[21].

The independent evolution of flight in birds and bats has resulted in two very different wing designs. In this study we show that the feathered wing is made inactive during the upstroke[9] and body lift is produced[7,8,27], while the membranous wing generates

significant flight forces during the upstroke[12,13]. Both wingbeat kinematics are close to optimal for the relative flight performance regime[14,15]. The different efficiency of bird and bat flight suggests that organisms may not reach the same level of performance due to phylogenetic constraints[4]. In turn, such differences may help explain ecological and morphological differences among birds and bats such as why the largest birds are ten times heavier than the largest bats[16], and why bats migrate less frequently and typically move shorter distances than birds[17,18,19].

Method
Experimental animals

For each species, we started training six individuals in the wind tunnel. For the bats, we selected the two steadiest flyers for the experiments. For the flycatchers, we used three out of six individuals. Morphological data for all experimental animals are in Supplementary Table S1.

Experiments

The experimental setup consisted of the Lund University low-turbulence, low-speed wind tunnel, a high-speed (200Hz) stereo Particle Image Velocimetry system (PIV) and two high-speed kinematics cameras running at 250 Hz (Supplementary Fig. S1)[13]. For the nectar-feeding bats, we used a honey-water feeder to position them in the tunnel. When a bat was flying steadily at the feeder, we sampled the wake behind the animal using the PIV system, and/or took a kinematics sequence. The flycatchers were trained to perch in the test-section of the wind tunnel. When the perch was lowered, the bird took off. If the bird flew steadily in the correct position, PIV measurements or kinematics measurements were performed, after which the perch was presented again.

Using this experimental procedure, we did experiments at a wind tunnel speed range of 2 m/s to 7 m/s, in increments of 1 m/s. For the bats, PIV and kinematics measurements were done at all flight speeds. For the flycatchers, kinematics were analyzed for flycatcher #1 and #3 at 2, 4 and 7 m/s, while PIV measurements were done for flycatcher #3 at 2, 4, and 7 m/s and for flycatcher #1 and #2 at all flight speeds. For each measured individual-speed combination, we analyzed both PIV and kinematics measurements for at least 5 sequences (10+ wingbeats).

Kinematics analysis

For the birds and bats, multiple natural body and wing markers were tracked manually in the videos from the two kinematics cameras. The data were converted into three-dimensional tracks using linear transformation coefficients from a calibration cube. The three-dimensional data were used to determine the wing kinematics[30]. The kinematic data were also used to determine basic morphological data.

PIV analysis

The stereo PIV data was analyzed using DaVis (LaVision, DaVis 7.2.2.110), resulting in three-dimensional velocity vectors $\{u,v,w\}$ within each node point $\{y,z\}$ in the PIV frame[13]. The PIV frames within one wingbeat were given a frame number $n=[1\text{-}N]$ ($n=1$ for the beginning of the downstroke and $n=N$ at the end of the upstroke), a non-dimensional time stamp $\tau=[0–1]$, and a streamwise position $x=[0\text{-}\lambda]$ (λ is the wingbeat wavelength). The non-dimensional time stamps are defined as $\tau=t/\Pi$, where Π is wingbeat period. t is the timing within the wingbeat where $t=0$ corresponds to the start of the downstroke, $t=\Pi$ is at the end of the upstroke, and $t=R_{ds}\Pi$ is at the end of the downstroke, where R_{ds} is the wingbeat downstroke ratio. For the frames in between, t is linearly interpolated. Assuming that the wake convects statically downstream with the forward flight speed, the streamwise position of each PIV frame is $x=(n\text{-}1)U\Delta t$, where Δt is the inverse of the PIV frame rate (1/200 Hz)[13].

The PIV results were analyzed by identifying the main vortices in the wake: the tip vortex, root vortex, tail vortex and reversed vortex loops. In each PIV frame, the position $\{x,y,z\}$ and circulation Γ of the present vortex structures were measured using a custom-made Matlab (7.7.0.471, R2008b) PIV analysis program[13]. From this, the resultant normalized aerodynamic lift of each vortex structure was calculated using basic vortex theory[3] as $L^*(\tau)=\rho\ U\ b_w(\tau)\ \Gamma(\tau)/W$, where W is the weight of the animal, ρ is the air density and $b_w(\tau)$ is the wake span determined from the y-position of the vortex structure (Supplementary Fig. S2a)[13]. The normalized thrust component of the aerodynamic force of each vortex structure is determined by $T^*(\tau)=L^*(\tau)\tan(\bar{\gamma}(\tau))$, where $\bar{\gamma}(\tau)$ is the mean streamwise vortex system angle. For the tip vortex system, it is determined

by $\overline{\gamma_{tip}}(\tau) = \frac{(1 - A_{body}/A_{tip})}{2}\gamma_{tip}(\tau)$, where $\gamma_{tip}(\tau)$ is the spanwise tip vortex angle (Supplementary Fig. S2)[13]. A_{tip} and A_{body} are the vertical wingbeat amplitude of the wingtip and body, respectively, determined from the kinematics. There is a minus sign in front of A_{body}/A_{tip} because the vertical body movement is in anti-phase with the wing movement. For the root vortex system, $\overline{\gamma_{root}}(\tau) = \frac{(1 - A_{body}/A_{root})}{2}\gamma_{root}(\tau)$, where $A_{body}/A_{root} = A_{body}/A_{tip} \times A_{tip}/A_{root}$, and A_{tip}/A_{root} is determined from the relative movement of tip and root vortex. For the reversed vortex loop and tail vortex $\overline{\gamma}(\tau) = \gamma(\tau)$ [13].

The vertical induced velocity distribution $w(y^*)$ along the normalized span y^* was measured in each PIV frame along a straight line from the position behind the animal's body centre line to the most distal vortex structure. The non-dimensional span is defined as $y^* = y/b$, where b is the wing span.

Average wingbeats

We determined the average wingbeat for a certain species-speed combination by averaging the results of all measured wingbeats for that species-speed combination, using smoothing splines[13]. The average wingbeat wake consists of the average temporal normalized lift $\overline{L}^*(\tau)$ and thrust $\overline{T}^*(\tau)$ of all vortex structures and the average spanwise and temporal downwash distribution $\overline{w}(y^*, \tau)$. The relative variation in the spanwise downwash distribution $\overline{w}(y^*, \tau)$ was estimated by determining a sliding 95% confidence interval of m local data points, with m the amount of analyzed wingbeats. The average wing kinematics were determined by averaging the kinematics for the different wingbeats using a nested ANOVA (Matlab, anovan).

Aerodynamic forces and performance

By integrating $\overline{L}^*(\tau)$ and $\overline{T}^*(\tau)$ throughout the downstroke, upstroke and complete wingbeat L/W_{down}, T/W_{down}, L/W_{up}, T/W_{up} and L/D were determined (assuming $D = T$ for steady flight). From the average spanwise and temporal downwash distribution $\overline{w}(y^*, \tau)$, the real induced power P_i and ideal induced power $P_{i\,ideal}$ were estimated[6]. P_i is the induced power for generating L and $P_{i\,ideal}$ is the minimum induced power required to generate L, based on the equivalent uniform spanwise downwash[5]. The effective span

efficiency for a complete wingbeat is defined as $e_i = P_{i\,ideal}/P_i$ [5,6].

Statistical analysis

The results for the different animals were compared using mixed linear models. L/D; e_i; L/W_{down}; T/W_{down}; L/W_{up} or T/W_{up} was the dependent variable. Covariates were *Bird/Bat*, *species(Bat)*, flight speed U, the interaction between U and *Bird/Bat*, and the interaction between U and *species(Bat)*.

References

1. Schmidt-Nielsen, K. Locomotion: energy cost of swimming, flying, and running. *Science* **177**, 222–228 (1972).
2. Tennekes, H. & Tennekes, H. *The simple science of flight: from insects to jumbo jets.* (MIT Press, Cambridge, USA, 2009).
3. Anderson, J.D. *Fundamentals of Aerodynamics.* (McGraw-Hill, New York, 1991).
4. Lauder, G.V. The argument from design. *Adaptation* 55–91 (1996).
5. Spedding, G.R. & McArthur, J. Span Efficiencies of Wings at Low Reynolds Numbers. *J. Aircraft* **47**, 120-128 (2010).
6. Bomphrey, R.J., Taylor, G.K., Lawson, N.J. & Thomas, A.L. Digital particle image velocimetry measurements of the downwash distribution of a desert locust Schistocerca gregaria. *Journal of The Royal Society Interface* **3**, 311 -317 (2006).
7. Csicsáky, M.J. Body-gliding in the zebra finch. *Fortschr. Zool* **24**, 275–286 (1977).
8. Tobalske, B., Hearn, J. & Warrick, D. Aerodynamics of intermittent bounds in flying birds. *Experiments in Fluids* **46**, 963-973 (2009).
9. Norberg, U. Hovering flight in the pied flycatcher (Ficedula hypoleuca). *Swimming and Flying in Nature* **2**, 869-888 (1975).
10. Norberg, R.A. Function of vane asymmetry and shaft curvature in bird flight feathers; inference on flight ability of Archaeopteryx. *The beginnings of birds. International Archaeopteryx Conference in Eichstätt* 303–318 (1985).
11. Johansson, L.C. & Hedenström, A. The vortex wake of blackcaps (Sylvia atricapilla L.) measured using high-speed digital particle image velocimetry (DPIV). *J Exp Biol* **212**, 3365-3376 (2009).

12. Hedenström, A. Johansson, L.C., Wolf, M., von Busse, R., Winter, Y. & Spedding, G.R. Bat Flight Generates Complex Aerodynamic Tracks. *Science* **316**, 894-897 (2007).

13. Muijres, F.T., Johansson, L.C., Winter, Y. & Hedenström, A. Comparative aerodynamic performance of flapping flight in two bat species using time-resolved wake visualization. *Journal of The Royal Society Interface,* doi:10.1098/rsif.2011.001 (2011).

14. Hall, K.C. & Hall, S.R. Minimum Induced Power Requirements for Flapping Flight. *Journal of Fluid Mechanics Digital Archive* **323**, 285-315 (1996).

15. Hall, K.C., Pigott, S.A. & Hall, S.R. Power requirements for large-amplitude flapping flight. *Journal of Aircraft* **35**, 352–361 (1998).

16. Pennycuick, C.J. *Modelling the Flying Bird.* (Elsevier, Amsterdam, 2008).

17. Norberg, U.M. & Rayner, J.M.V. Ecological Morphology and Flight in Bats (Mammalia; Chiroptera): Wing Adaptations, Flight Performance, Foraging Strategy and Echolocation. *Philosophical Transactions of the Royal Society of London. B, Biological Sciences* **316**, 335-427 (1987).

18. Alerstam, T. & Christie, D.A. *Bird migration.* (Cambridge University Press, Cambridge, 1993).

19. Fleming, T.H. & Eby, P. Ecology of bat migration. In *Bat ecology* (University of Chicago Press, Chicago, 156–208, 2003).

20. Hedenström, A., Rosén, M. & Spedding, G.R. Vortex wakes generated by robins Erithacus rubecula during free flight in a wind tunnel. *Journal of The Royal Society Interface* **3**, 263-276 (2006).

21. Henningsson, P., Muijres, F.T. & Hedenström, A. Time-resolved vortex wake of a common swift flying over a range of flight speeds. *Journal of The Royal Society Interface*, doi:10.1098/rsif.2010.0533 (2010).

22. Hedenström, A., Muijres, F.T., von Busse, R., Johansson, L.C., Winter, Y. & Spedding, G.R. High-speed stereo DPIV measurement of wakes of two bat species flying freely in a wind tunnel. *Experiments in Fluids* **46**, 923-932 (2009).

23. Johansson, L.C., Wolf, M., von Busse, R., Winter, Y., Spedding, G.R. & Hedenström, A. The near and far wake of Pallas' long tongued bat (*Glossophaga soricina*). *J Exp Biol* **211**, 2909-2918 (2008).

24. Hubel, T.Y., Riskin, D.K., Swartz, S.M. & Breuer, K.S. Wake structure and wing kinematics: the flight of the lesser dog-faced fruit bat, *Cynopterus brachyotis. J Exp Biol* **213**, 3427-3440 (2010).

25. Spedding, G.R., Rosen, M. & Hedenström, A. A family of vortex wakes generated by a thrush nightingale in free flight in a wind tunnel over its entire natural range of flight speeds. *J Exp Biol* **206**, 2313-2344 (2003).

26. Hoerner, S. Fluid-dynamic drag; practical information on aerodynamic drag and hydrodynamic resistance. (Hoerner, Bakersfield, California, 1965).

27. Thomas, A. On the Aerodynamics of Birds' Tails. *Philosophical Transactions of the Royal Society B: Biological Sciences* **340**, 361 (1993).

28. Johansson, L.C., Wolf, M. & Hedenström, A. A quantitative comparison of bird and bat wakes. *Journal of The Royal Society Interface* **7**, 61-66 (2010).

29. Hedenström, A., Johansson, L.C. & Spedding, G.R. Bird or bat: comparing airframe design and flight performance. *Bioinspiration & Biomimetics* **4**, 015001 (2009).

30. Wolf, M., Johansson, L.C., von Busse, R., Winter, Y. & Hedenström, A. Kinematics of flight and the relationship to the vortex wake of a Pallas' long tongued bat (*Glossophaga soricina*). *J Exp Biol* **213**, 2142-2153 (2010).

Supplementary Information

Table S1 Morphological data for the animals used in the experiment. Mass M, wing span b, wing surface area S, mean cord length $c = S/b$, aspect ratio $AR = b^2/S$ and wing loading $Q = Mg/S$, with g the gravitational constant.

species. (gender)	M (kg)	b (m)	S (m^2)	c (m)	AR (-)	Q (N/m^2)
G. soricina. (Male)	0.0101	0.233	0.00879	0.038	6.2	11.3
G. soricina. (Female)	0.0095	0.230	0.00860	0.037	6.2	10.8
L. yerbabuenae. (Male)	0.0216	0.335	0.01576	0.047	7.1	13.4
L. yerbabuenae. (Female)	0.0236	0.323	0.01529	0.047	6.8	15.1
Flycatcher #1	0.0148	0.235	0.0106	0.045	5.2	13.7
Flycatcher #2	0.0141	0.235	0.0105	0.045	5.3	13.2
Flycatcher #3	0.0137	0.236	0.0107	0.045	5.2	12.6

Table S2 P-values for the mixed linear model analysis of lift-to-drag ratio L/D, span efficiency e_i, normalized lift production during the downstroke L/W_{down}, normalized thrust production during the downstroke T/W_{down}, normalized lift production during the upstroke L/W_{up} and normalized thrust production during the upstroke T/W_{up}. The P-values in bold are significant

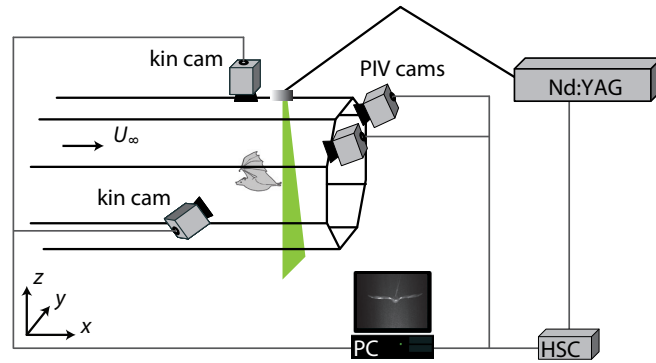|	L/D	e_i	L/W_{down}	T/W_{down}	L/W_{up}	T/W_{up}
Intercept	**<0.0001**	**<0.0001**	**<0.0001**	**<0.0001**	**<0.0001**	**<0.0001**
Bird/Bat	**0.0309**	**<0.0001**	0.9316	**0.0007**	**0.0001**	**<0.0001**
Species(Bat)	0.0792	0.0542	0.7959	0.2568	**0.0311**	0.3586
U_∞	0.0761	**0.0465**	**<0.0001**	**<0.0001**	**0.0025**	**<0.0001**
U_∞ **x** *Bird/Bat*	0.6042	**0.0202**	0.5084	0.1378	**0.0004**	**0.0001**
U_∞ **x** *species(Bat)*	0.0597	**0.0038**	0.2513	**0.0393**	**0.0186**	0.1117

Fig S1 experimental setup consisting of a low-speed low-turbulence wind tunnel, a high-speed stereo PIV setup with the laser sheet in transverse setup (in *y-z* plane) and two high-speed video cameras (kin cam). For the bats, a feeder system was used to position the animals, while for the birds a perch was used.
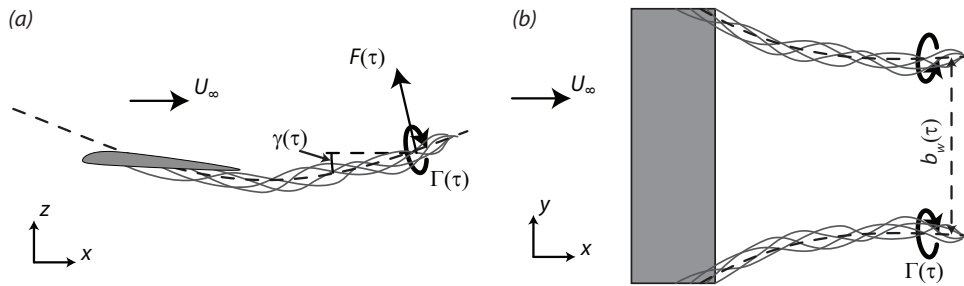

Fig S2 side *(a)* and top view *(b)* of a hypothetical flapping wing generating tip vortices with circulation $\Gamma(\tau)$ resulting aerodynamic force $F(\tau)$. The lift ($L(\tau)$) and thrust ($T(\tau)$) components of $F(\tau)$ depend on vortex angle $\gamma(\tau)$.
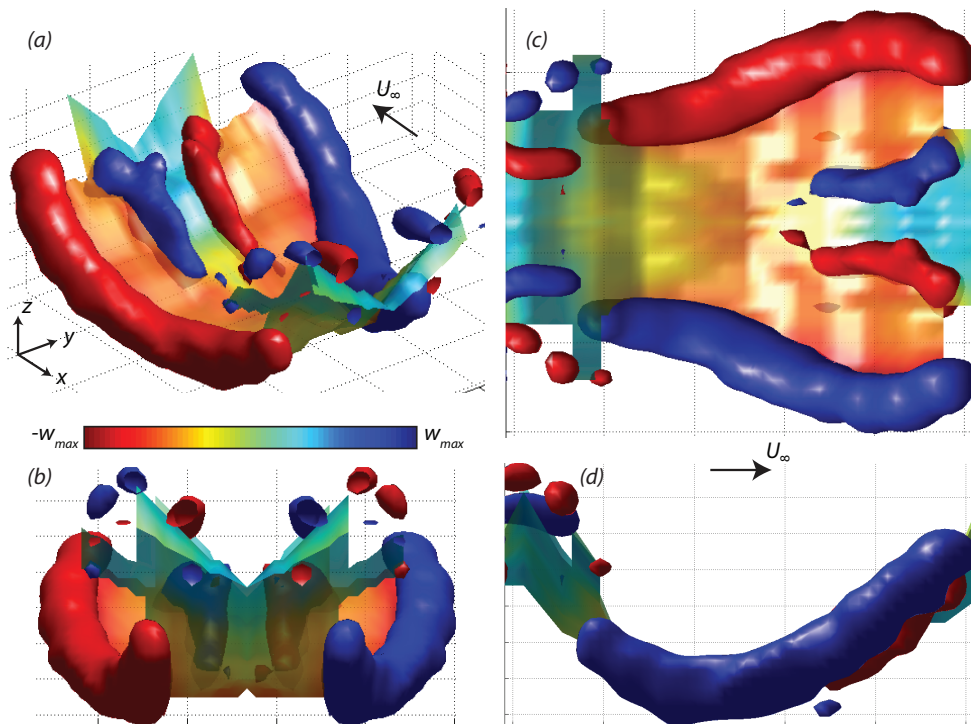

Fig S3 The wake behind the male *G. soricina* flying at 4 m/s. The wake is visualized by iso-surfaces of streamwise vorticity (blue: $\omega_{x\,iso} = 60$ s^{-1}; red: $\omega_{x\,iso} = -60$ s^{-1}) and vertical induced velocities ($w_{max} = 2.6$ m/s, see colour bar). The different views are *(a)* perspective view from upstream, *(b)* view from upstream, *(c)* top view and *(d)* side view.
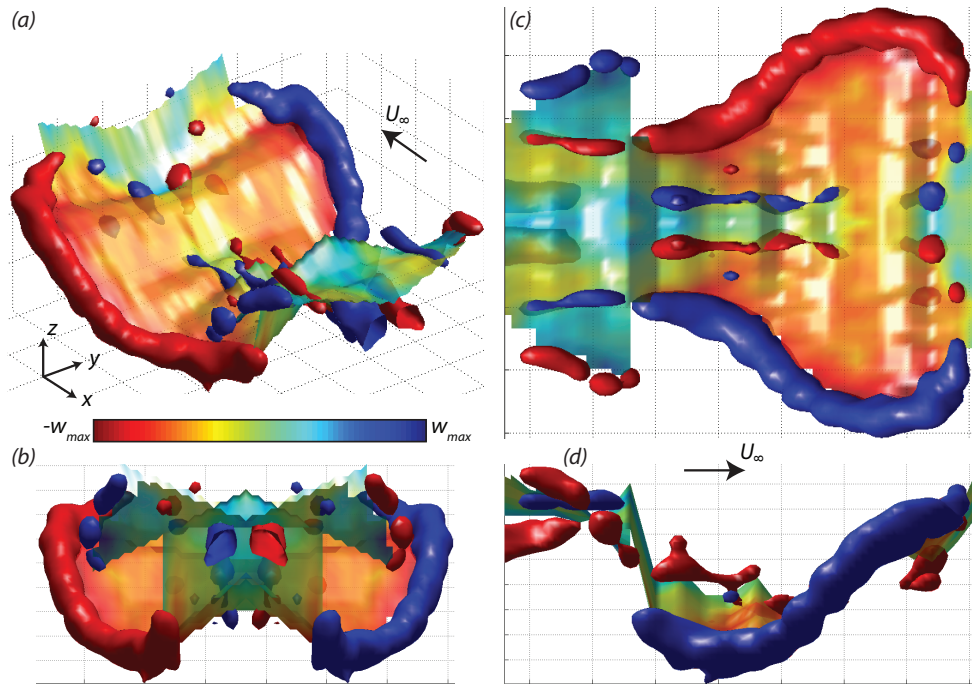
Fig S4 The wake behind the male *L. yerbabuenae* flying at 4 m/s. The wake is visualized by iso-surfaces of streamwise vorticity (blue: $\omega_{x\,iso}$ = 75 s^{-1}; red: $\omega_{x\,iso}$ = -75 s^{-1}) and vertical induced velocities (w_{max} = 2.2 m/s, see colour bar). The different views are *(a)* perspective view from upstream, *(b)* view from upstream, *(c)* top view and *(d)* side view.

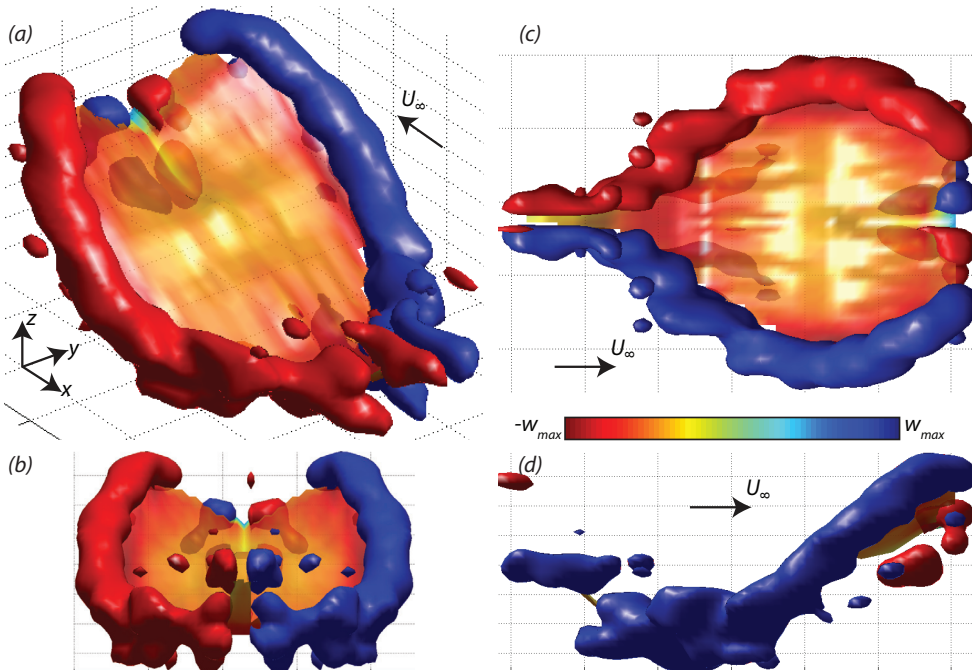Fig S5 The wake behind Pied Flycatcher #2 flying at 4 m/s. The wake is visualized by iso-surfaces of streamwise vorticity (blue: $\omega_{x\,iso}$ = 75 s^{-1}; red: $\omega_{x\,iso}$ = -75 s^{-1}) and vertical induced velocities (w_{max} = 2.6 m/s, see colour bar). The different views are *(a)* perspective view from upstream, *(b)* view from upstream, *(c)* top view and *(d)* side view.

151

The following is a list of Doctoral theses (Lund University, Sweden) from the Department of Animal Ecology (nos. 1-78, from no. 79 and onwards denoted by (A)) and Theoretical Ecology (T). (E) refers to Doctoral theses from the Department of Chemical Ecology/Ecotoxicology during the years 1988-1995.

1. CHARLOTTE HOLMQVIST. Problem on marine-glacial relicts on account on the genus *Mysis*. 6 May 1959.
2. HANS KAURI. Die Rassenbildung bei europäischen Rana-Arten und die Gültigkeit der Klimaregeln. 9 May 1959.
3. PER DALENIUS. Studies on the Oribatei (Acari) of the Torneträsk territory in Swedish Lapland. 14 May 1963.
4. INGEMAR AHLÉN. Studies on the history of distribution, taxonomy and ecology of the Red Deer in Scandinavia.
   21 May 1965.
5. STAFFAN ULFSTRAND. Bentic animal communities of river Vindelälven in Swedish Lapland. 8 May 1968.
6. SAM ERLINGE. Food habits, home range and territoriality of the otter *Lutra lutra* L. 6 May 1969.
7. GUNNAR MARKGREN. Reproduction of moose in Sweden. 17 May 1969.
8. ARNE BERGENGREN. On genetics, evolution and history of the heath-hare, a distinct population of the arctic hare, *Lepus timidus* L. 17 October 1969.
9. HåKAN HALLANDER. Habitats and habitat selection in the wolf spiders *Pardosa chelata* (O.F. Müller) and *P. pullata* (Clerck). 20 March 1970.
10. ULF SCHELLER. The Pauropoda of Ceylon. 29 May 1970.
11. LEIF NILSSON. Non-breeding ecology of diving ducks in southernmost Sweden. 2 December 1970.
12. RUNE GERELL. Distributional history, food habits, diel behaviour, territoriality, and population fluctuations of the mink *Mustela vison* Schreber in Sweden. 30 March 1971.
13. INGRID HANSSON. Skull nematodes in mustelids. 3 June 1971.
14. STURE ABRAHAMSSON. Population ecology and relation to environmental factors of *Astacus astacus* Linné and *Pacifastacus leniusculus* Dana. 3 June 1971.
15. LENNART HANSSON. Food conditions and population dynamics of Scandinavian granivorous and herbivorous rodents. 26 November 1971.
16. SVEN-AXEL BENGTSON. Ecological segregation, reproduction and fluctuations in the size of duck populations in Iceland. 21 April 1972.
17. STEN ANDREASSON. Distribution, habitat selection, food and diel activity of Swedish freshwater sculpins (*Cottus* L.). 5 May 1972.
18. KERSTIN SVAHN. Coccidian blood parasites in Lacertids. 17 May 1972.
19. RUTGER ROSENBERG. Macrofaunal recovery in a Swedish fjord following the closure of a sulphite pulp mill.
   13 April 1973.
20. SVEN ALMQVIST. Habitat selection and spatial distribution of spiders in coastal sand dunes. 25 May 1973.
21. TORSTEN MALMBERG. Population fluctuations and pesticide influence in the rook *Corvus frugilegus* L., in Scania, Sweden 1955-1970. 25 May 1973.
22. ANDERS SÖDERGREN. Transport, distribution, and degradation of organochlorine residues in limnic ecosystems (defended at the Dept of Limnology). 23 May 1973.
23. BERITH PERSSON. Effects of organochlorine residues on the whitethroat *Sylvia communis* Lath. 7 December 1973.
24. PLUTARCO CALA. The ecology of the ide *Idus idus* (L.) in the river Kävlingeån, South Sweden. 23 May 1975.
25. ÅKE GRANMO. Effects of surface active agents on marine mussels and fish. 26 May 1975.

26. BO W SVENSSON. Population ecology of adult *Potamophylax cingulatus* (Steph.) and other Trichoptera at a South Swedish stream. 15 October 1975.
27. STEN NORDSTRÖM. Associations, activity, and growth in lumbricids in southern Sweden. 6 April 1976.
28. STEN RUNDGREN. Environment and lumbricid populations in southern Sweden. 8 April 1976.
29. CHRISTIAN OTTO. Energetics, dynamics and habitat adaptation in a larval population of *Potamophylax cingulatus* (Steph.) (Trichoptera). 9 April 1976.
30. JAN LÖFQVIST. The alarm-defence system in formicine ants. 21 May 1976.
31. LARS HAGERMAN. Respiration, activity and salt balance in the shrimp *Crangon vulgaris* (Fabr.). 22 October 1976.
32. THOMAS ALERSTAM. Bird migration in relation to wind and topography. 29 October 1976.
33. LARS M NILSSON. Energetics and population dynamics of *Gammarus pulex* L. Amphipoda. 20 December 1977.
34. ANDERS NILSSON. Ticks and their small mammal hosts. 24 May 1978.
35. SÖREN SVENSSON. Fågelinventeringar - metoder och tillämpningar. (Bird censuses - methods and applications.)
    23 May 1979.
36. BO FRYLESTAM. Population ecology of the European hare in southern Sweden. 1 June 1979.
37. SVEN G NILSSON. Biologiska samhällen i heterogena miljöer: En studie på fastland och öar. (Biological communities in heterogeneous habitats: A study on the mainland and islands.) 12 October 1979.
38. BJÖRN SVENSSON. The association between *Epoicocladius flavens* (Chironomidae) and *Ephemera danica* (Ephemeroptera). 26 October 1979.
39. GÖRAN HÖGSTEDT. The effect of territory quality, amount of food and interspecific competition on reproductive output and adult survival in the magpie *Pica pica*; an experimental study. 29 February 1980.
40. JON LOMAN. Social organization and reproductive ecology in a population of the hooded crow *Corvus cornix*.
    9 April 1980.
41. GÖRGEN GÖRANSSON. Dynamics, reproduction and social organization in pheasant *Phasianus colchicus* populations in South Scandinavia. 26 September 1980.
42. TORSTEN DAHLGREN. The effects of population density and food quality on reproductive output in the female guppy, *Poecilia reticulata* (Peters). 27 February 1981.
43. AUGUSTINE KORLI KORHEINA. Environments and co-existence of *Idotea* species in the southern Baltic.
    15 May 1981.
44. INGVAR NILSSON. Ecological aspects on birds of prey, especially long-eared owl and tawny owl. 9 October 1981.
45. TORBJÖRN von SCHANTZ. Evolution of group living, and the importance of food and social organization in population regulation; a study on the red fox (*Vulpes vulpes*). 23 October 1981.
46. OLOF LIBERG. Predation and social behaviour in a population of domestic cat. An evolutionary perspective.
    11 December 1981.
47. BJÖRN MALMQVIST. The feeding, breeding and population ecology of the brook lamprey (*Lampetra planeri*).
    12 March 1982.
48. INGVAR WÄREBORN. Environments and molluscs in a non-calcareous forest area in southern Sweden. 19 March 1982.
49. MAGNUS SYLVÉN. Reproduction and survival in common buzzards (*Buteo buteo*) illustrated by the seasonal allocation of energy expenses. 26 March 1982.
50. LARS-ERIC PERSSON. Structures and changes in soft bottom communities in the southern Baltic. 23 April 1982.

51. GÖRAN BENGTSSON. Ecological significance of amino acids and metal ions, a microanalytical approach.
24 May 1982.

52. JAN HERRMANN. Food, reproduction and population ecology of *Dendrocoelum lacteum* (Turbellaria) in South Sweden. 10 December 1982.

53. BO EBENMAN. Competition and differences in niches and morphology between individuals, sexes and age classes in animal populations, with special reference to passerine birds. 8 April 1983.

54. HANS KÄLLANDER. Aspects of the breeding biology, migratory movements, winter survival, and population fluctuations in the great tit *Parus major* and the blue tit *P. caeruleus*. 29 April 1983.

55. JOHNNY KARLSSON. Breeding of the starling (*Sturnus vulgaris*). 6 May 1983.

56. CARITA BRINCK. Scent marking in mustelids and bank voles, analyses of chemical compounds and their behavioural significance. 17 May 1983.

57. PER SJÖSTRÖM. Hunting, spacing and antipredatory behaviour in nymphs of *Dinocras cephalotes* (Plecoptera).
1 June 1983.

58. INGE HOFFMEYER. Interspecific behavioural niche separation in wood mice (*Apodemus flavicollis* and *A. sylvaticus*) and scent marking relative to social dominance in bank voles (*Clethrionomys glareolus*).
9 December 1983.

59. CHRISTER LÖFSTEDT. Sex pheromone communication in the turnip moth *Agrotis segetum*. 30 November 1984.

60. HANS KRISTIANSSON. Ecology of a hedgehog *Erinaceus europaeus* population in southern Sweden. 7 December 1984.

61. CHRISTER BRÖNMARK. Freshwater molluscs: Distribution patterns, predation and interactions with macrophytes.
19 April 1985.

62. FREDRIK SCHLYTER. Aggregation pheromone system in the spruce bark beetle *Ips typographus*. 26 April 1985.

63. LARS LUNDQVIST. Life tactics and distribution of small ectoparasites (Anoplura, Siphonaptera and Acari) in northernmost Fennoscandia. 10 May 1985.

64. PEHR H ENCKELL. Island life: Agency of Man upon dispersal, distribution, and genetic variation in Faroese populations of terrestrial invertebrates. 3 June 1985.

65. SIGFRID LUNDBERG. Five theoretical excursions into evolutionary ecology: on coevolution, pheromone communication, clutch size and bird migration. 7 November 1985.

66. MIKAEL SANDELL. Ecology and behaviour of the stoat *Mustela erminea* and a theory on delayed implantation.
8 November 1985.

67. THOMAS JONASSON. Resistance to frit fly attack in oat seedlings, and ecological approach to a plant breeding problem. 13 November 1985.

68. ANDERS TUNLID. Chemical signatures in studies of bacterial communities. Highly sensitive and selective analyses by gas chromatography and mass spectrometry. 3 October 1986.

69. BOEL JEPPSSON. Behavioural ecology of the water vole, *Arvicola terrestris*, and its implication to theories of microtine ecology. 27 May 1987.

70. TORSTEN GUNNARSSON. Soil arthropods and their food: choice, use and consequences. 2 June 1987.

71. THOMAS MADSEN. Natural and sexual selection in grass snakes, *Natrix natrix*, and adders, *Vipera berus*.
4 September 1987.

72. JENS DAHLGREN. Partridge activity, growth rate and survival: Dependence on insect abundance. 4 December 1987.

73. SCOTT GILBERT. Factors limiting growth of sympatric *Peromyscus* and *Clethrionomys* populations in northern Canada. 11 December 1987.

74. OLLE ANDERBRANT. Reproduction and competition in the spruce bark beetle *Ips typographus*. 8 April 1988.

75. EINAR B OLAFSSON. Dynamics in deposit-feeding and suspension-feeding populations of the bivalve *Macoma baltica*; an experimental study. 29 April 1988.

76. JAN-ÅKE NILSSON. Causes and consequences of dispersal in marsh tits, time as a fitness factor in establishment.
11 May 1988.

77. PAUL ERIC JÖNSSON. Ecology of the southern Dunlin *Calidris alpina schinzii*. 13 May 1988.

78. HENRIK G SMITH. Reproductive costs and offspring quality: the evolution of clutch size in tits (*Parus*). 20 May 1988.

79. BILL HANSSON. (A) Reproductive isolation by sex pheromones in some moth species. An electrophysiological approach. 14 October 1988.

80. ANDERS THURÉN. (E) Phthalate esters in the environment: analytical methods, occurrence, distribution and biological effects. 4 November 1988.

81. KARIN LUNDBERG. (A) Social organization and survival of the pipistrelle bat (*Pipistrellus pipistrellus*), and a comparison of advertisement behaviour in three polygynous bat species. 10 February 1989.

82. HAKON PERSSON. (A) Food selection, movements and energy budgets of staging and wintering geese on South Swedish farmland. 6 December 1989.

83. PETER SUNDIN. (E) Plant root exudates in interactions between plants and soil micro-organisms. A gnotobiotic approach. 16 March 1990.

84. ROLAND SANDBERG. (A) Celestial and magnetic orientation of migrating birds: Field experiments with nocturnal passerine migrants at different sites and latitudes. 28 September 1990.

85. ÅKE LINDSTRÖM. (A) Stopover ecology of migrating birds. 12 October 1990.

86. JENS RYDELL. (A) Ecology of the northern bat *Eptesicus nilssoni* during pregnancy and lactation. 26 October 1990.

87. HÅKAN WITTZELL. (T) Natural and sexual selection in the pheasant *Phasianus colchicus*. 27 September 1991.

88. MATS GRAHN. (A) Intra- and intersexual selection in the pheasant *Phasianus colchicus*. 27 May 1992.

89. ANN ERLANDSSON. (A) Life on the water surface: behaviour and evolution in semiaquatic insects. 25 September 1992.

90. GUDMUNDUR A GUDMUNDSSON. (A) Flight and migration strategies of birds at polar latitudes. 2 October 1992.

91. IO SKOGSMYR. (T) Pollination biology, venereal diseases and allocation conflicts in plants. 9 October 1992.

92. ANDERS VALEUR. (E) Utilization of chromatography and mass spectrometry for the estimation of microbial dynamics. 16 October 1992.

93. LENA TRANVIK . (A) To sustain in a stressed environment: a study of soil Collembola. 27 November 1992.

94. KATARINA HEDLUND. (A) Animal-microbial interactions: The fungivorous Collembola.12 February 1993.

95. HANS EK. (E) Nitrogen acquisition, transport and metabolism in intact ectomycorrhizal associations studied by 15N stable isotope techniques.14 May 1993.

96. STAFFAN BENSCH. (A) Costs, benefits and strategies for females in a polygynous mating system: a study on the great reed warbler. 24 September 1993.

97. NOÉL HOLMGREN. (T) Patch selection, conflicting activities and patterns of migration in birds.15 October 1993.

98. ROLAND LINDQUIST. (E) Dispersal of bacteria in ground water - mechanisms, kinetics and consequences for facilitated transport. 3 December 1993.

99. JOHAN NELSON. (A) Determinants of spacing behaviour, reproductive success and mating system in male field voles, *Microtus agrestis*. 20 May 1994.

100. MARIA SJÖGREN. (A) Dispersal in and ecto-mycorrhizal grazing by soil invertebrates. 30 September 1994.

101. DENNIS HASSELQUIST. (A) Male attractiveness, mating tactics and realized fitness in the polygynous great reed warbler. 14 October 1994.

102. DORETE BLOCH. (A) Pilot whales in the North Atlantic. Age, growth and social structure in Faroese grinds of long-finned pilot whale, *Globicephala melas*. 16 December 1994.

103. MAGNUS AUGNER. (T) Plant-plant interactions and the evolution of defences against herbivores. 10 February 1995.

104. ALMUT GERHARDT. (E). Effects of metals on stream invertebrates. 17 February 1995.

105. MARIANO CUADRADO. (A) Site fidelity and territorial behaviour of some migratory passerine species overwintering in the Mediterranean area. 31 March 1995.

106. ANDERS HEDENSTRÖM. (T) Ecology of Avian Flight. 7 April 1995.

107. OLOF REGNELL. (E) Methyl mercury in lakes: factors affecting its production and partitioning between water and sediment. 21 April 1995.

108. JUNWEI ZHU. (A) Diversity and conservatism in moth sex pheromone systems. 4 May 1995.

109. PETER ANDERSON. (A) Behavioural and physiological aspects of oviposition deterrence in moths. 12 May 1995.

110. JEP AGRELL. (A) Female social behaviour, reproduction and population dynamics in a non-cyclic population of the field vole (*Microtus agrestis*).19 May1995.

111. SUSANNE ÅKESSON. (A) Avian Migratory Orientation: Geographic, Temporal and Geomagnetic Effects.
22 September 1995.

112. ADRIAN L. R. THOMAS. (A) On the Tails of Birds. 29 September 1995.

113. WENQI WU.(A) Mechanisms of specificity in moth pheromone production and response. 8 December 1995.

114. PER WOIN.(E) Xenobiotics in Aquatic Ecosystems: Effects at different levels of organisation. 15 December 1995.

115. K. INGEMAR JÖNSSON. (T) Costs and tactics in the evolution of reproductive effort. 12 April 1996.

116. MATS G.E. SVENSSON. (A) Pheromone-mediated mating system in a moth species. 30 October 1996.

117. PATRIC NILSSON. (T) On the Ecology and Evolution of Seed and Bud Dormancy. 9 May 1997.

118. ULF OTTOSSON. (A) Parent-offspring relations in birds: conflicts and trade-offs. 16 May 1997.

119. ERIK SVENSSON. (A) Costs, benefits and constraints in the evolution of avian reproductive tactics: a study on the blue tit. 6 June 1997.

120. MARIA SANDELL. (A). Female reproductive strategies and sexual conflicts in a polygynous mating system.
6 March 1998.

121. ULF WIKTANDER. (A) Reproduction and survival in the lesser spotted woodpecker. Effects of life history, mating system and age. 3 April 1998.

122. OLA OLSSON. (A) Through the eyes of a woodpecker: understanding habitat selection, territory quality and reproductive decisions from individual behaviour. 17 April 1998.

123. PETER VALEUR. (A) Male moth behaviour and perception in the pheromone plums. 24 April 1998.

124. LARS PETTERSSON. (A) Phenotypic plasticity and the evolution of an inducible morphological defence in crucian carp. 19 March 1999.

125. JOHANNES JÄREMO. (T) Plant inducible responses to damage: evolution and ecological implications. 23 April 1999.

126. ÅSA LANGEFORS. (A) Genetic variation in Mhc class IIB in Atlantic Salmon: Evolutionary and Ecological Perspectives. 10 September 1999.

127. NILS KJELLÉN. (A) Differential migration in raptors. 12 November 1999.

128. ANDERS NILSSON. (A) Pikeivory: behavioural mechanisms in northern pike piscivory. 14 January 2000.

129. JÖRGEN RIPA. (T) Population and community dynamics in variable environments. 21 January 2000.

130. BJÖRN LARDNER. (A) Phenotypic plasticity and local adaptation in tadpoles. 28 April 2000.

131. IRENE PERSSON. (A) Parental and embryonic behaviours in precocial birds. 19 May 2000.
132. ROGER HÄRDLING. (T) Evolutionary resolutions of conflicts with mates and offspring. 6 October 2000.
133. ÅSA LANKINEN. (T) Pollen competition as a target for sexual selection in plants. 17 November 2000.
134. THOMAS OHLSSON. (A) Development and maintenance of quality indicators in pheasants. 15 December 2000.
135. ANDERS KVIST. (A) Fuelling and flying: adaptations to endurance exercise in migrating birds. 20 April 2001.
136. ANNA-KARIN AUGUSTSSON. (A). On enchytraeids and naidids: Life-history traits and response to environmental stress. 23 May 2001.
137. MARIO PINEDA. (T). Evolution in Multicellular Mitotic Lineages. 31 August 2001.
138. LIV WENNERBERG. (A). Genetic variation and migration of waders. 9 November 2001
139. NICLAS JONZÉN. (T). Inference and management of populations in variable environments. 14 December 2001.
140. DAGMAR GORMSEN. (A). Colonization processes of soil fauna and mycorrhizal fungi. 21 December 2001.
141. PETER FRODIN. (T). Species interactions and community structure. 15 Mars 2002.
142. JOHAN BÄCKMAN (A). Bird Orientation: External Cues and Ecological Factors. 26 April 2002.
143. MÅNS BRUUN. (A). On starlings and farming: population decline, foraging strategies, cost of reproduction and breeding success. 7 June 2002.
144. JAKOB LOHM. (A). MHC and genomic diversity in Atlantic salmon (*Salmo salar* L.) 11 October 2002.
145. LARS RÅBERG. (A). Costs in ecology and evolution of the vertebrate immune system. 18 October 2002.
146. HELENE BRACHT JÖRGENSEN. (A). Food selection and fitness optimisation in insects. 13 December 2002.
147. MARTIN GREEN. (A). Flight strategies in migrating birds: when and how to fly. 31 January 2003.
148. BENGT HANSSON (A). Dispersal, inbreeding and fitness in natural populations. 21 February 2003.
149. MIKAEL ROSÉN. (A). Birds in the flow: Flight mechanics, wake dynamics and flight performance. 11 April 2003.
150. JONAS HEDIN. (A). Metapopulation ecology of Osmoderma eremita - dispersal, habitat quality and habitat history.
23 May 2003.
151. HELENA WESTERDAHL. (A). Avian MHC: variation and selection in the wild. 10 October 2003.
152. KEN LUNDBORG. (T). Food hoarding: Memory and social conditions - an evolutionary approach. 16 January 2004.
153. RICHARD OTTVALL (A). Population ecology and management of waders breeding on coastal meadows.
19 February 2004.
154. RACHEL MUHEIM (A). Magnetic Orientation in Migratory Birds. 20 February 2004.
155. MARIA HANSSON (A). Evolution and ecology of AhR genes in Atlantic salmon (*Salmo salar* L.). 23 April 2004.
156. MARTIN STJERNMAN (A). Causes and consequences of blood parasite infections in birds. 29 October 2004.
157. MARTIN GRANBOM (A). Growth conditions and individual quality in starlings. 19 November 2004.
158. ANNA GÅRDMARK (T). Species interactions govern evolutionary and ecological effects of population harvesting.
27 May 2005.
159. JONAS WALDENSTRÖM (A). Epidemiology and population structure of Campylobacter jejuni and related organisms in wild birds. 2 December 2005.
160. HELEN IVARSSON (T). Strategy Games: on survival and reproduction. 9 December 2005.

161. SEBASTIAN TROËNG (A). Migration of sea turtles from Caribbean Costa Rica: Implications for management.
14 December 2005.

162. EMMA SERNLAND (T). Optimal strategies and information in foraging theory. 16 December 2005.

163. MIKAEL ÅKESSON (A). Quantitative genetics and genome structure in a wild population: the use of a great reed warbler pedigree. 29 September 2006.

164. LENA MÅNSSON (T). Understanding weather effects on, in and from large herbivore population dynamics.
13 October 2006.

165. ERIK ÖCKINGER (A). Butterfly diversity and dispersal in fragmented grasslands. 17 November 2006.

166. JESSICA K. ABBOTT (A). Ontogeny and population biology of a sex-limited colour polymorphism.
23 November 2006.

167. OLOF HELLGREN (A). Avian malaria and related blood parasites: molecular diversity, ecology and evolution. 15 December 2006.

168. ANNA NILSSON (A).The problem of partial migration - the case of the blue tit. 19 January 2007.

169. PATRIK KARLSSON NYED (T). Food webs, models and species extinctions in a stochastic environment. 16 February 2007.

170. MARKUS FRANZÉN (A). Insect Diversity in Changing Landscapes. 16 May 2007.

171. MAJ RUNDLÖF (A). Biodiversity in agricultural landscapes: landscape and scale-dependent effects of organic farming. 15 June 2007.

172. OSKAR BRATTSTRÖM (A). Ecology of red admiral migration. 21 September 2007.

173. MICHAEL TOBLER (A). Maternal programming: costs, benefits and constraints of maternal hormone transfer.
5 October 2007.

174. FREDRIK HAAS (T). Hybrid zones and speciation - insights from the European Crow hybrid zone. 25 January 2008.

175. JACOB JOHANSSON (T). Evolving ecological communities in changing environment. 1 February 2008.

176. THOMAS GOSDEN (A). The Preservation of Favoured Morphs in the Struggle Between Sexes. 29 May 2008.

177. ROINE STRANDBERG (A). Migration strategies of raptors – spatio-temporal adaptions and constraints in travelling and foraging. 24 September 2008.

178. SARA S. HENNINGSSON (A). On the role of migration for the distribution of arctic birds – a circumpolar perspective. 25 September 2008.

179. JONAS KNAPE (T). Population dynamics and demography – inference from stochastic models. 6 February 2009.

180. NICLAS NORRSTRÖM (T). Artificial neural networks in models of specialization and sympatic speciation.
20 February 2009.

181. JOHAN NILSSON (A). Causes and consequences of individual variation in energy turnover rates. 17 April 2009.

182. MARTA WOLF (T). Catching the Invisible: Aerodynamic Track and Kinematics of Bat and Bird Flight. 14 May 2009.

183. JULIANA DÄNHARDT (A). On the importance of farmland as stopover habitat for migrating birds. 15 May 2009.

184. SARA NAURIN (A). Avian GEnome Evolution – Gene Expression, Gene Divergence and Sexual Dimorphism.
23 October 2009.

185. JENNIE NILSSON (T). On the origin of polymorphism – consequences of competition and predation in heterogeneous environments. 13 November 2009.

186. FABRICE EROUKHMANOFF (A). The interplay between selection and constraints on phenotypic evolution and adaptive divergence. 20 November 2009.

187. SANNA HARRIS (A). Behaviour under predation risk – antipredator strategies, behavioural syndromes and sex-specific responses in aquatic prey. 15 January 2010.

188. PER HENNINGSSON (T). Always on the wing – Fluid dynamics, flight performance and flight behavior of common swifts. 29 Januari 2010.

189. HÅKAN KARLSSON (A). There and Back Again - Nocturnal migratory behaviour of birds during spring and autumn. 8 October 2010.

190. MARY NGOZI MOLOKWU (A). Costs of foraging in a dry tropical environment. 29 October 2010.

191. MARCUS LJUNGQVIST (A). Have a fling with your neighbour, you might be less related - The use of molecular markers to estimate genetic diversity and population structure in conservation biology. 5 November 2010.

192. KRISTINA KARLSSON GREEN (A). Mating strategies and conflicts in aquatic invertebrates: consequences for evolutionary differentiation. 26 November 2010.

193. FLORIAN T. MUIJRES (T). Feathers by day, membranes by night – Aerodynamic performance in bird and bat flight. 28 April 2011.

194. MARTIN HARTVIG (T). Food Web Ecology – individual life-histories and ecological processes shape complex communities. 29 April 2011.